SYNTHESIS AND CHARACTERIZATION OF NOVEL SELF-HOSTING FLUORESCENT MATERIALS AS NON-DOPED EMITTERS FOR ORGANIC LIGHT-EMITTING DIODES

Wipaporn Kitisriworaphan

A Thesis Submitted in Partial Fulfillment of the Requirements for the

Degree of Doctor of Philosophy in Chemistry

Suranaree University of Technology

Academic Year 2019

การสังเคราะห์และพิสูจน์เอกลักษณ์ของสารเรืองแสงชนิดใหม่ที่มีตัวส่งผ่านประจุในตัวเองเพื่อใช้เป็นตัวเปล่งแสงที่ไม่มีสารเจือในอุปกรณ์ไดโอดเปล่งแสงสารอินทรีย์

นางสาววิภาพร กิติศรีวรพันธุ์

วิทยานิพนธ์นี้เป็นส่วนหนึ่งของการศึกษาตามหลักสูตรวิทยาศาสตรดุษฎีบัณฑิต
สาขาวิชาเคมี
มหาวิทยาลัยเทคโนโลยีสุรนารี
ปีการศึกษา 2562

SYNTHESIS AND CHARACTERIZATION OF NOVEL SELF-HOSTING FLUORESCENT MATERIALS AS NON-DOPED EMITTERS FOR ORGANIC LIGHT-EMITTING DIODES

Suranaree University of Technology has approved this thesis submitted in partial fulfillment of the requirements for the Degree of Doctor of Philosophy.

Thesis Examining Committee

(Prof. Dr. James R. Ketudat-Cairns)
Chairperson

(Asst. Prof. Dr. Thanaporn Manyum)
Member (Thesis Advisor)

(Prof. Dr. Vinich Promarak)
Member (Thesis Co-Advisor)

Chanokphorn Phaosiri
(Asst. Prof. Dr. Chanokporn Phaosiri)
Member

Tinnagon Keawin
(Asst. Prof. Dr. Tinnagon Keawin)
Member

(Asst. Prof. Dr. Anyanee Kamkaew)
Member

Chatchai Jothit
(Assoc. Prof. Dr. Chatchai Jothityangkoon)
Vice Rector for Academic Affairs
and Quality Assurance

(Assoc. Prof. Dr. Worawat Meevasana)
Dean of Institute of Science

วิภาพร กิติศรีวรพันธุ์ : การสังเคราะห์และพิสูจน์เอกลักษณ์ของสารเรืองแสงชนิดใหม่ที่มีตัวส่งผ่านประจุในตัวเองเพื่อใช้เป็นตัวเปล่งแสงที่ไม่มีสารเจือในอุปกรณ์ไดโอดเปล่งแสงสารอินทรีย์ (SYNTHESIS AND CHARACTERIZATION OF NOVEL SELF-HOSTING FLUORESCENT MATERIALS AS NON-DOPED EMITTERS FOR ORGANIC LIGHT- EMITTING DIODES) อาจารย์ที่ปรึกษา : ผู้ช่วยศาสตราจารย์ ดร.ธนพร แม่นยำ, 291 หน้า

งานวิจัยนี้มีวัตถุประสงค์เพื่อพัฒนาวัสดุเปล่งแสงชนิดใหม่ ไม่ว่าจะเป็นด้านการออกแบบ การสังเคราะห์ และการพิสูจน์เอกลักษณ์สารเปล่งแสงที่มีประสิทธิภาพสูงและอายุการใช้งานที่ยาวนาน งานวิจัยนี้มุ่งเน้นไปที่การออกแบบโมเลกุลและการสังเคราะห์วัสดุในอุปกรณ์ไดโอดเปล่งแสงอินทรีย์ (OLED) ที่มีโครงสร้างแบบ Donor-Acceptor-Donor เพื่อช่วยเพิ่มประสิทธิภาพในการเรืองแสง เพิ่มความเสถียรทางความร้อนและช่วยป้องกันการเรียงซ้อนกันของโมเลกุลอันเนื่องมาจากพันธะไพ โครงสร้างที่ต้องการประกอบด้วย Diketopyrrolopyrrole (DPP) Diphenyl sulfone (DPS) และอนุพันธ์ของ Benzothiazole ทำหน้าที่เป็นตัวรับอิเล็กตรอน และอนุพันธ์ของ Carbazole หรือ Tetraphenylethylene (TPE) ทำหน้าที่เป็นตัวให้อิเล็กตรอน พิสูจน์เอกลักษณ์คุณสมบัติทางแสง การเรืองแสงล่าช้าเมื่อถูกกระตุ้นด้วยความร้อน (Thermally activated delayed fluorescence) การปล่อยแสงที่เกิดจากการรวมตัว (Aggregation-induced emission) และคุณสมบัติทางไฟฟ้าเคมีของวัสดุเหล่านี้ด้วยเทคนิค UV-vis, Time-resolved fluorescence spectroscopic และ Cyclic voltammetry analyses ยิ่งกว่านั้นยังมีการรายงานการตรวจสอบการขึ้นรูปและประสิทธิภาพของอุปกรณ์โดยใช้วัสดุเหล่านี้เป็นตัวเปล่งแสงในอุปกรณ์ไดโอดเรืองแสงอินทรีย์ ผลการวิจัยพบว่าอนุพันธ์ของ Diphenyl sulfone ทั้งหมดแสดงลักษณะของการเรืองแสงล่าช้าเมื่อถูกกระตุ้นด้วยความร้อนพร้อมกับการปล่อยแสงสีน้ำเงินเข้ม อุปกรณ์ไดโอดเรืองแสงอินทรีย์ที่ขึ้นรูปโดยการระเหยด้วยความร้อนโดยใช้โมเลกุล G1DPP (**2**) เป็นตัวเปล่งแสงแสดงค่าประสิทธิภาพกระแสเท่ากับ 9.26 ค่าประสิทธิภาพของพลังงานเท่ากับ 1993 และแสดงค่าประสิทธิภาพควอนตัมภายนอกเท่ากับ 2.90 นอกจากนี้อุปกรณ์ OLED ที่ใช้โมเลกุล AIE ทั้งหมดยังแสดงประสิทธิภาพควอนตัมภายนอกที่สูงอยู่ในช่วง 3.14-4.66%

สาขาวิชาเคมี ลายมือชื่อนักศึกษา____________________
ปีการศึกษา 2562 ลายมือชื่ออาจารย์ที่ปรึกษา________________

WIPAPORN KITISRIWORAPHAN : SYNTHESIS AND CHARACTERIZATION OF NOVEL SELF-HOSTING FLUORESCENT MATERIALS AS NON-DOPED EMITTERS FOR ORGANIC LIGHT-EMITTING DIODES. THESIS ADVISOR : ASST. PROF. THANAPORN MANYUM, Ph.D. 291 PP.

DIKETOPYRROLOPYRROLE/DIPHENYL SULFONE/BENZOTHIADIAZOLE/ DENDRIMER/TADF/AGGREGATION-INDUCED EMISSION/OLED

The aim of this study is the development of new emitting materials including the design, synthesis, and characterize of high-efficiency and long-life emitters. We mainly focus on the molecular design and synthesis of the OLED materials based on the Donor-Acceptor-Donor (D-A-D) system in order to improve the emissive ability, the thermal stability of the material, and overcome π–π stacking interactions of the molecules. The desired structures were composed of diketopyrrolopyrrole (DPP), diphenyl sulfone (DPS), and benzothiazole derivatives as an acceptor and carbazole derivatives or tetraphenylethylene (TPE) as a donor. The photophysical, thermally activated delayed fluorescence (TADF), aggregation-induced emission (AIE) and electrochemical properties of these materials were characterized by UV-vis, time-resolved fluorescence spectroscopic and cyclic voltammetry analyses. Moreover, the investigation of the device fabrication and performance using these materials as an emitter is also reported. The results of this research showed that all diphenyl sulfone derivatives revealed TADF characteristics with the deep blue emission color. Thermal evaporation processed OLED using G1DPP (**2**) as an emitter exhibited an excellent current efficiency of 9.26, maximum luminance of 1993, and EQE of 2.90%. Furthermore, OLED devices based on all AIE emitters exhibited a high external quantum efficiency in the range of 3.14-4.66%.

School of Chemistry Student's Signature Wipaporn K.

Academic Year 2019 Advisor's Signature________________

ACKNOWLEDGEMENTS

I wish to express my admiration and appreciation to Prof. Dr. Vinich Promarak and Asst. Prof. Dr. Thanaporn Manyum, my advisors for their suggestions, supervision, guidance, and encouragement throughout this work.

I would like to thank the thesis committee, Asst. Prof. Dr. Chanokporn Phaosiri, Asst. Prof. Dr. Tinnakorn Keawin, Dr. Anyanee Kamkaew, and Prof. Dr. James R. Ketudat-Cairns for their valuable discussions and comments on this thesis.

A special thanks to Udon Thani Rajabhat University for financial support. Moreover, this research work was received a graduate research grant from the National Research Council of Thailand (NRCT) 2018. Gratitude is expressed to all of my teachers for showing me a different line in life as a Ph.D. student. My sincere thanks are expressed to the Smart organic materials & semiconductor devices Laboratory (SMS), Vidyasirimedhi Institute of Science and Technology (VISTEC) for all support during the laboratory work and School of Chemistry, Suranaree University of Technology for the wonderful academic environment during the course work.

My appreciation is extended to all staff of the School of Chemistry and SMS Laboratory, my friends, sisters, and brothers in the lab.

Most of all, I feel appreciate and grateful to my beloved family, mom, and dad for their inculcation and encouragement that provided me with fortitude.

Wipaporn Kitisriworaphan

CONTENTS

Page

ABSTRACT IN THAI I

ABSTRACT IN ENGLISH III

ACKNOWLEDGEMENTS V

CONTENTS VII

LIST OF TABLES XI

LIST OF FIGURES XIII

LIST OF ABBREVIATIONS XXIII

CHAPTER

I INTRODUCTION 1

- 1.1 The synthesis of organic light-emitting diodes (OLEDs) materials 1
- 1.2 The principle of OLED 7

II THE SYNTHESIS AND CHARACTERIZATION OF DPP DENDRIMERS AS EMITTERS FOR ORGANIC LIGHT-EMITTING DIODES 11

- 2.1 Introduction 11
- 2.2 Research objectives 19
- 2.3 Synthesis 19
- 2.4 Results and discussion 26

CONTENTS (Continued)

Page

2.5 Conclusion 38

III THE SYNTHESIS AND CHARACTERIZATION OF NOVEL THERMALLY ACTIVATED DELAYED FLUORESCENCE MATERIALS FOR ORGANIC LIGHT-EMITTING DIODES 39

3.1 Introduction 39

3.2 Research objectives 55

3.3 Synthesis of TADF emitters 57

3.4 Results and discussion 64

3.5 Conclusion 82

IV THE SYNTHESIS AND CHARACTERIZATION OF THERMALLY ACTIVATED DELAYED FLUORESCENCE DENDRIMERS FOR ORGANIC LIGHT-EMITTING DIODES 83

4.1 Introduction 83

4.2 Research objectives 92

4.3 Synthetic procedure 92

4.4 Results and discussion 100

4.5 Conclusion 111

V THE SYNTHESIS AND CHARACTERIZATION OF AGGREGATION-INDUCED EMISSION MATERIALS FOR ORGANIC LIGHT-EMITTING DIODES 113

5.1 Introduction 113

CONTENTS (Continued)

Page

5.2 Research objectives 121
5.3 Synthetic procedure 122
5.4 Results and discussion 130
5.5 Conclusion 144

VI EXPERIMENTAL 145
6.1 General remark 145
6.2 General procedure (GP) 146
6.3 The synthesis 149
6.4 Spectrum supplementary data 187

VII CONCLUSIONS 257

REFERENCES 261

APPENDICES

APPENDIX A THE SYNTHESIS OF DPP EMITTERS 279
APPENDIX B THE SYNTHESIS OF THERMALLY ACTIVATED DELAYED FLUORESCENCE MATERIALS 281
APPENDIX C THE SYNTHESIS OF TADF DENDRIMERS 285
APPENDIX D THE SYNTHESIS OF AIE EMITTERS 287

CURRICULUM VITAE 291

LIST OF TABLES

Table **Page**

2.1 HOMOs and LUMOs of the DPP dendrimers estimated from the calculation. 27

2.2 Photophysical data of the DPP dendrimers. 29

2.3 CIE, lifetime and quantum yield data of the DPP dendrimers. 30

2.4 Cyclic voltammetry, and theoretically calculated energy levels of DPP dendrimers. 32

2.5 Quantum yield of DPP dendrimers in neat film and doped film. 35

2.6 Device characteristics of OLEDs. 37

3.1 Photophysical properties of TADF emitters. 67

3.2 CIE(x,y) coordinates of TADF emitters. 68

3.3 The lifetimes of prompt and delayed fluorescence of TADF emitters. 70

3.4 The fluorescence quantum yield of the non-degassed solution and degassed solution of G1DPS (**5**), G1-2PhDPS (**8**), and G1-4PhDPS (**10**). 74

3.5 Electrochemical properties of all TADF compounds. 79

3.6 Thermal properties of all TADF compounds. 80

4.1 Photophysical properties of TADF dendrimers. 101

4.2 CIE(x,y) coordinates of TADF dendrimer **14-16**. 102

4.3 The lifetimes of prompt and delayed fluorescence of TADF dendrimers **14-16**. 103

LIST OF TABLES (Continued)

Table **Page**

4.4 Electrochemical properties of all TADF compounds. 108

4.5 Thermal properties of all TADF compounds. 109

5.1 Photophysical properties of DPP dendrimers. 132

5.2 CIE(x,y) coordinates of AIE emitters **17-26**. 133

5.3 Electrochemical properties of AIE emitters **17-26**. 139

5.4 Quantum yield of AIE emitters **17-26** 141

5.5 Device characteristics of OLEDs 142

LIST OF FIGURES

Figure **Page**

1.1 DPP dendrimer compounds (**1-3**). 2

1.2 TADF emitters (**4-13**). 4

1.3 TADF dendrimers (**14-16**). 5

1.4 AIE red emitters (**17-26**). 7

1.5 Hole injection materials (**27**, **28**) and hole-transporting materials (**29-32**). 8

1.6 Aluminum *tris*-8-hydroxy quinoline (**33**) and 9, 10-di (2-napthyl) anthracene (**34**). 9

2.1 Centres of potential chemical reactivity in the molecule of DPP (**35**). 13

2.2 Conjugated polymers (**36-41**) obtained from the Suzuki reaction. 14

2.3 The DPP derivatives (**41-44**). 15

2.4 The synthesis of DPP polymer semiconductor (**45**). 16

2.5 The unsubstituted DPP (**35**), symmetrically *N*-substituted DPP (**48**, **50**, and **52**), and asymmetrically *N*-substituted DPP. 16

2.6 The synthesis of diketopyrrolopyrrole borondifluoride cyanide emitter (**54**). 17

2.7 The diketopyrrolopyrrole based D-π-A-π-D molecules (**55-63**). 18

2.8 The diketopyrrolopyrrole derivatives (**64-70**). 18

2.9 Synthetic approach to the synthesis of DPP dendrimers. 19

2.10 The synthesis of 3,6-diiodo-9-tosyl-carbazole (**72**). 20

LIST OF FIGURES (Continued)

Figure **Page**

2.11 The synthesis of 3,6-di-*tert*-butyl-carbazole (**73**). 20

2.12 The proposed mechanisms of Friedel-Crafts alkylation. 21

2.13 The synthesis of G2 (**74**). 21

2.14 The proposed mechanisms of Ullmann *N*-arylation. 22

2.15 The synthesis of G1hexyl bromide (**75**) and G2hexyl bromide (**76**). 23

2.16 The proposed mechanisms of *N*-alkylation. 23

2.17 The synthesis of GnDPP (**1-3**). 24

2.18 The ^{1}H NMR spectrum of GnDPP (**1-3**). 24

2.19 HOMO and LUMO orbitals of G0DPP (**1**), G1DPP (**2**), and G2DPP (**3**) calculated by the B3LYP/6-31G(d,p) method. 27

2.20 UV-vis absorption and fluorescence spectra of (a) G0DPP (**1**) (b) G1DPP (**2**) and (c) G2DPP (**3**) in dilute toluene solution (10^{-5} M) and in a solid film. 28

2.21 CIE chromaticity diagram (a), Photoluminescence decay spectra of DPP dendrimers in solution (b) and neat film (c). 30

2.22 CV curves of DPP dendrimers in CH_2Cl_2 solution using 0.1 M Bu_4NPF_6 at a scan rate of 50 mV/s. 32

2.23 TGA curves of G0DPP (**1**), G1DPP (**2**), and G2DPP (**3**) with heating rate of 10°C/min under a nitrogen atmosphere. 33

2.24 Schematic energy diagram and electroluminescence spectra of all dendrimers doped in 3% mCP. 34

LIST OF FIGURES (Continued)

Figure **Page**

2.25 Tapping mode AFM images of the spin-coated films. 36

2.26 Plots of EL spectra of the OLEDs, current density–luminance–voltage (*J*–*V*–*L*), and external quantum efficiency (EQE) of the devices 37

3.1 Schematic view of the reverse intersystem crossing mechanism. 41

3.2 Energy alignment of singlet and triplet energy levels to achieve efficient TADF. 42

3.3 The molecular structure of the eosin dye (**78**). 43

3.4 The molecular structure of the *bis* (triphenylphosphine) phenanthroline copper (I) (**79**). 43

3.5 Molecular structures of the six Sn(IV)-porphyrin complexes **80-85**. 44

3.6 Molecular structure of PIC-TRZ (**86**) and its HOMO and LUMO calculated by Gaussian 03. 45

3.7 The molecular structures and formation of exciplex state between *m*-MTDATA (**87**) and 3TPYMB (**89**). 46

3.8 The molecular structures of TADF molecules (**90-103**). 47

3.9 The molecular structures of diphenyl sulfoxide derivatives. 48

3.10 The molecular structures of DTC-DPS (**106**) and DMOC-DPS (**107**), and their HOMO and LUMO distribution. 49

3.11 The molecular structures of the investigated compounds. 50

3.12 The molecular structures of the desired compounds (**114-119**). 51

3.13 The molecular structures of DPS derivatives. 52

LIST OF FIGURES (Continued)

Figure **Page**

3.14 The chemical structures and the schematic energy diagram of DMOC-DPS (**107**) and TMC-DPS (**122**). 53

3.15 The chemical structures of the BPSB derivatives (**123-127**). 53

3.16 The molecular structures of pDTCz-2DPyS (**128**) and pDTCz-3DPyS (**129**). 54

3.17 The molecular structures of the desired TADF molecules **4-13**. 56

3.18 Synthetic approach to the synthesis of the TADF molecules. 57

3.19 The synthesis of dibromo-substituted (**131**) and tetrabromo-substituted (**132**) sulfone. 58

3.20 The synthesis of key intermediates **133** and **134**. 58

3.21 The mechanism of Suzuki reaction. 59

3.22 The synthesis of key intermediates **136** and **138**. 59

3.23 The synthesis of the TADF emitters **4-13**. 60

3.24 UV-vis absorption of TADF emitters in (a) dilute solution in toluene (10^{-5} M) (b) solid film and fluorescence spectra in (c) dilute solution in toluene (10^{-6} M) and (d) solid film. 66

3.25 Chromaticity diagram of all TADF emitters **4-13** in (a) dilute solution in toluene (10^{-5} M) and (b) solid neat film. 69

3.26 The emission decay of all TADF **4-13** in toluene under oxygen (a) and argon (b) atmosphere at room temperature. 71

LIST OF FIGURES (Continued)

Figure **Page**

3.27 Emission spectra of all TADF materials **4-13** in degassed solution (black) and non-degassed solution (red) in toluene (10^{-5} M). 72

3.28 The quantum yield of G1DPS (**5**) in degassed solution (black) and non-degassed solution (red) by using argon bubbles method (a) and freeze-thaw method (b). 73

3.29 Time-resolved emission spectrum (TRES) of the prompt and delayed fluorescence of degassed G1-2Ph-DPS (**8**) solution. 75

3.30 UV-vis absorption and fluorescence spectra of TADF emitters **4-13** in various solvent. 76

3.31 The plots of stokes shift versus solvent polarity parameter (Δf) of all TADF compounds **4-13**. 77

3.32 CV curves of TADF emitters in CH_2Cl_2 solution using 0.1 M Bu_4NPF_6 at a scan rate of 50 mV/s under argon flow. 78

3.33 TGA thermograms of TADF emitters **4-13** measured at a heating rate of 10°C min^{-1} under N_2 flow. 80

3.34 DSC 1st heating (solid line) and 2nd heating (dotted line) scans of TADF emitters **4-13**. 81

4.1 The molecular structure of dendrimers (**140-142**). 85

4.2 Molecular structures of donor-acceptor dendrimers D1 (**143**) and D2 (**144**). 86

4.3 Chemical structures of DMAC-BP, CDE1 (**145**) and CDE2 (**146**). 87

LIST OF FIGURES (Continued)

Figure **Page**

4.4 The molecular structures of dendrimers G1 (**106**), G2 (**147**), and G3 (**148**). 88

4.5 The molecular structures of tBuG2TAZ, (**149**), G3Ph (**150**), and G4Ph (**151**). 89

4.6 Molecular structures of GnCT (**152-155**). 90

4.7 Molecular structures of dendrimers (**156-158**). 91

4.8 Synthetic approach to the synthesis of the TADF dendrimers. 93

4.9 Preparation of the key intermediate sulfone **160**. 93

4.10 Preparation of 2-bromo fluorene **162**. 94

4.11 Preparation of bromo hexyl fluorene **164**. 94

4.12 Preparation of 2-bromo-9,9-*bis*(6-bromohexyl) fluorene **165**. 95

4.13 Preparation of TPAfluorene bromide **167**. 95

4.14 Preparation of fluorene boronates **170** and **172**. 96

4.15 The proposed mechanism for the borylation of aryl halides. 97

4.16 The synthesis of TADF dendrimers **14-16**. 97

4.17 UV-vis absorption and fluorescence spectra of TADF dendrimer **14-16** in dilute solution in toluene (10^{-5} M) and in solid film. 101

4.18 Chromaticity diagram of all TADF dendrimers **14-16** in dilute solution in toluene (10^{-5} M) and in solid neat film. 102

4.19 The emission decay and fit tail of TADF dendrimers **14-16** in toluene under oxygen and argon atmosphere at room temperature. 104

LIST OF FIGURES (Continued)

Figure **Page**

4.20 Emission spectra of all TADF dendrimers **14-16** in degassed solution (black) and non-degassed solution (red) in toluene (10^{-5} M). 105

4.21 UV-vis absorption and fluorescence spectra of TADF dendrimer **14-16** in various solvents. 106

4.22 The plots of stokes shift versus solvent polarity parameter (Δf) of TADF dendrimers **14-16**. 107

4.23 CV curves of TADF dendrimers in CH_2Cl_2 solution using 0.1 M Bu_4NPF_6 at a scan rate of 50 mV/s under argon flow. 108

4.24 TGA thermograms of TADF dendrimers **14-16** measured at a heating rate of 10°C min^{-1} under N_2 flow. 109

4.25 DSC 1st heating (solid line) and 2nd heating (dash line) scans of TADF dendrimers **14-16**. 110

5.1 Molecular structure and conformational rotamers of silole molecule **173**. 113

5.2 Molecular structure of NTD derivatives **174-177**. 113

5.3 Molecular structure of BTPE **178**. 114

5.4 Molecular structure of TPATPE **179** and 2TPATPE **180**. 114

5.5 Molecular structure of VP_0-$(TPE)_3$ (**181**), VP_3-$(TPE)_3$ (**182**), and VP_6-$(TPE)_3$ (**183**). 115

5.6 Molecular structure of BTPE **178**, BTPETTD **184**, and BTPEBTTD **185**. 116

5.7 Molecular structure of near IR materials **186-189**. 117

LIST OF FIGURES (Continued)

Figure **Page**

5.8 Molecular structure of methyl-BTPE **190**, isopro-BTPE **191**, Ph-BTPE **192** and Cz-BTPE **193**. 117

5.9 Molecular structure of PTZ-BZP **194**. 118

5.10 Synthetic routes to tetraphenylpyrazine (TPP) and its derivative. 118

5.11 Synthesis of NZ2TPA (**197**). 119

5.12 Synthetic procedure of TPE-TAC (**198**) and TPE-TADC (**199**). 120

5.13 The synthetic approach to the synthesis of AIE emitters. 121

5.14 Preparation of TPEH-borolane **202** and TPE-borolane **203**. 122

5.15 The proposed mechanism for the borylation to afford TPE-borolane **202**. 123

5.16 The synthesis of AIE emitters **17-26**. 124

5.17 The mechanism of Suzuki reaction. 125

5.18 UV-vis absorption of AIE emitters in (a) dilute solution in toluene (10^{-5} M) (b) solid film and fluorescence spectra in (c) dilute solution in toluene (10^{-6} M) and (d) solid film. 129

5.19 Chromaticity diagram of all AIE emitters **17-26** in (a) dilute solution in toluene (10^{-5} M) and (b) solid neat film. 134

5.20 UV-vis absorption and fluorescence spectra of AIE emitters **17-26** in various solvents. 135

5.21 The plots of stokes shift versus solvent polarity parameter (Δf) AIE emitters **17-26**. 136

LIST OF FIGURES (Continued)

Figure **Page**

5.22 Emission spectra of AIE emitters 17-26 in THF-water mixtures (concentration 10^{-5} M)....137

5.23 Relative PL intensity vs water fraction of AIE emitters **17-26**....138

5.24 CV curves of AIE emitters **17-26** in CH_2Cl_2 solution using 0.1 M Bu_4NPF_6 at a scan rate of 50 mV/s under argon flow....138

5.25 Schematic energy diagram of OLED devices....140

5.26 Normalized electroluminescence spectra at high brightness of OLEDs based on WK series AIE materials 20 wt% in CBP....141

LIST OF ABBREVIATIONS

ACQ	Aggregation-caused quenching
ACRFLCN	Spiro-acridine
ADN	9, 10-Di (2-napthyl)anthracene
AFM	Atomic force microscopy
AIE	Aggregation-induced emission
Alq_3	Aluminum *tris*-8-hydroxy quinoline
BNT	*Bis*- naphthothiadiazole
Bphen	4,7-Diphenyl-1,10-phenanthroline
BT	Benzothiadiazole
mCBP	3,3-di(9*H*-carbazol-9-yl) biphenyl
CDCB	Carbazolyl dicyanobenzene
CIE	Commission Internationale De L'Eclairage
mCP	1,3-*bis*(*N*-carbazolyl) benzene
DPP	Diketopyrrolopyrrole
DPS	Diphenyl sulfone
DSC	Differential scanning calorimetry
EL	Electroluminescence
EML	Emitting layer
ETL	Electron transport layer
EQE	External quantum efficiency

LIST OF ABBREVIATIONS (Continued)

FET	Field-effect transistors
HBL	Hole blocking layer
HIL	Hole injection layer
HOMO	Highest occupied molecular orbital
HRMS	High-resolution mass spectrometry
HTL	Hole transport layer
ITO	Indium tin oxide
LUMO	Lowest unoccupied molecular orbital
m-MTDATA	4,4′,4′′-*Tris*(3-methyl-phenylphenylamino)triphenyl amine
NFOSCs	Non-fullerene organic solar cells
NIR	Near-infrared
NMP	*N*-methyl-2-pyrrolidone
NPB	*N*,*N*′-*bis*(naphthalen-1-yl)-*N*,*N*′-*bis*(phenyl)-benzidine
α-NPD	*N*,*N*′-*bis*(naphthalen-1-yl)-*N*,*N*′-*bis* (phenyl)-2,2′-dimethylbenzidine
NT	Naphthothiadiazole
OLED	Organic light-emitting diode
OPV	Organic photovoltaics
PEDOT: PSS	Poly(3,4-ethylenedioxythiophene): poly(4-styrenesulfonate)
PIC-TRZ	2-biphenyl4,6-bis(12-phenylindolo[2,3-a]carbazole-11-yl - 1,3,5triazine
PSCs	Polymer solar cells

LIST OF ABBREVIATIONS (Continued)

PXZ	Phenoxazine
RISC	Reverse intersystem crossing
RMS	Root mean square roughness
TADF	Thermally activated delayed fluorescence
TAPC	Di-[4-(*N*,*N*-ditolyl-amino)-phenyl] cyclo hexane
TAZ	3-(4-Biphenyl)-4-phenyl-5-*tert*-butylphenyl-1,2,4-triazole
TCTA	4,4',4''-Tris(carbazol-9-yl)triphenylamine
T_g	Glass transition temperature
TGA	Thermo gravimetry
TmPyPB	1,3,5-Tri(m-pyridin-3-ylphenyl)benzene
TPA	Triphenylamine
TPD	*N*,*N*′-*bis*(3-methyl phenyl)-*N*,*N*′-*bis*(phenyl)-benzidine
TPE	Tetraphenylethylene
TX	Thioxanthone
UV-vis	Ultraviolet-visible

CHAPTER I

INTRODUCTION

1.1 The synthesis of organic light-emitting diodes (OLEDs) materials

The application of organic materials in organic light-emitting diodes (OLEDs) have received increasing interest, since the first report by Ching W. Tang and Steven Van Slyke in 1987 (VanSlyke, 1987), due to their high potential applications in solid-state lighting and flat-panel displays (Mitschke and Bäuerle, 2000; So, Kido, and Burrows, 2008). The OLED displays provide high efficiency, low driving voltage, flexibility, transparency, low weight, etc (H. J. Kim, Shin, Kim, Kim, and Kim, 2017), (Udagawa, Sasabe, Cai, and Kido, 2014), (J. G. Kim et al., 2018). In order to achieve the high efficiencies of electroluminescence (EL) devices, the multilayer structures of OLED devices, doped emitting layers, novel materials, and efficient injection contacts are used (Ma et al., 2002), (Aizawa et al., 2014). However, current trends in the development of OLEDs are focusing on the development of new emitting materials by the design, synthesis, and application of high-efficiency and long-life emitters. In this work, we mainly focus on the molecular design and synthesis of the OLED materials based on the D-A-D system, in which the structure of the desired molecules are composed of diketopyrrolopyrrole (DPP), diphenyl sulfone (DPS), and benzothiazole derivatives as an acceptor, and carbazole derivatives or tetraphenylethylene (TPE) as a donor.

The first series is DPP dendrimers, which are red-emitting materials for OLED. Diketopyrrolopyrrole is a strong acceptor, which exhibits a high molar absorption coefficient, as well as high fluorescence quantum yields, and it can undergo several synthetic modifications (Sharma, Marri, Koyyada, Singh, and Malapaka, 2014). The introduction of the dendronized carbazole derivatives as a donor and end-capping groups increase the solubility in common organic solvent of DPP cores, decrease the π-π stacking interactions, and is used to further tune the properties of the emitters, such as the energy gap, HOMO and LUMO levels. The molecular structures of DPP dendrimers (**1-3**) are shown in Figure 1.1.

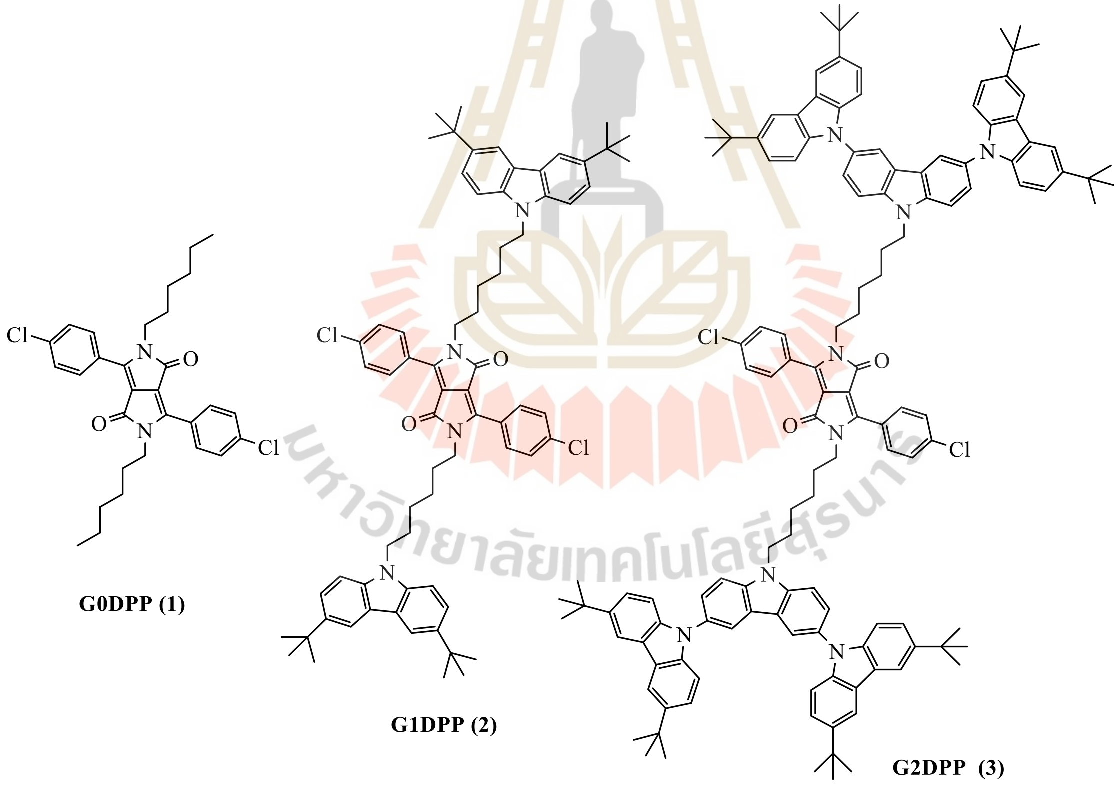

G0DPP (1)

G1DPP (2)

G2DPP (3)

Figure 1.1 DPP dendrimer compounds (**1-3**).

Normally, only the singlet excitons of fluorescent materials can emit light, leading to the low efficiency of the OLED devices. Therefore, new materials for obtaining high efficiency is required. Phosphorescent materials containing heavy metal such as Ir(III), Pt(II), and Os(II), can harvest both singlet and triplet excitons by enhanced spin-orbit coupling (SOC), providing an efficiency close to 100% theoretically (Minaev, Baryshnikov, and Agren, 2014). However, the heavy metals are expensive and non-renewable, resulting in increased cost of the final OLED. Since Adachi and co-workers proposed the mechanisms to harvest both singlet and triplet excitons and avoiding triplet annihilation via the reverse intersystem crossing (ISC) leading to an increase of the fluorescence intensity close to 100%, called thermally activated delayed fluorescence (TADF) (A. Endo et al., 2009). Generally, when the energy gap between HOMO of a donor and the LUMO of an acceptor is small (ΔE_{ST}), reverse intersystem crossing can easily occur. In the second series, we designed the target molecules composed of D-A-D system based on diphenyl sulfone as a core and carbazole derivatives as a donor moiety. The twist angle in the centre of DPS molecules provides a feature for TADF material and the π-linker that inserts between the DPS core and carbazole end groups in order to extend the π-conjugation length and tune the energy gap level. The effect of free rotation of π-linker on TADF property was investigated by varying the number of phenyl substituents in the π-linker. The molecular structures of TADF emitters (**4-13**) are shown in Figure 1.2.

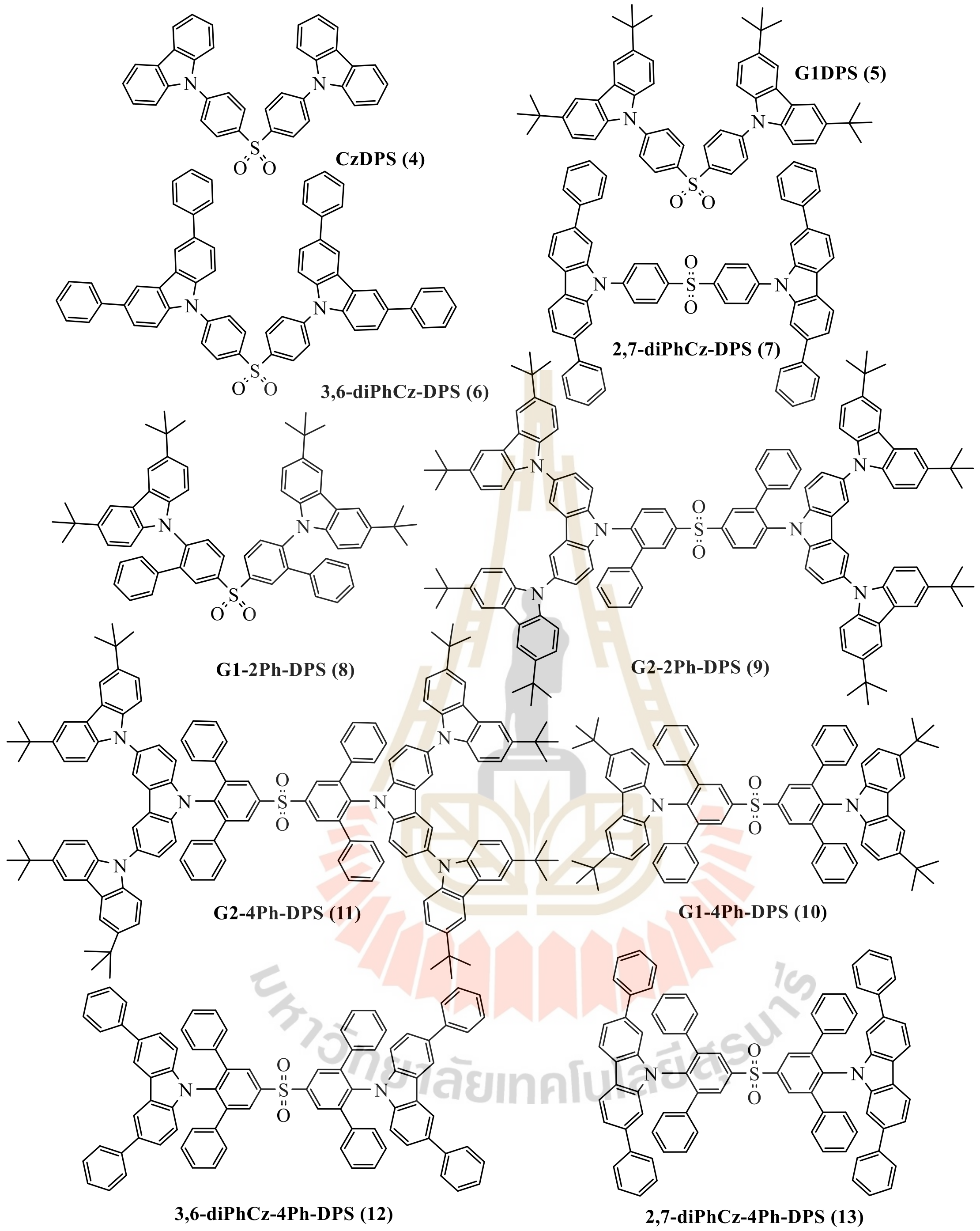

CzDPS (4)

G1DPS (5)

3,6-diPhCz-DPS (6)

2,7-diPhCz-DPS (7)

G1-2Ph-DPS (8)

G2-2Ph-DPS (9)

G2-4Ph-DPS (11)

G1-4Ph-DPS (10)

3,6-diPhCz-4Ph-DPS (12)

2,7-diPhCz-4Ph-DPS (13)

Figure 1.2 TADF emitters (**4-13**).

After that, the third series, the end group of TADF material was designed to the dendronized carbazole, G1fluorene, and G2fluorene. Because the generation of carbazole dendrons leads three-dimensional molecular conformations and the spatial distribution of the HOMO and LUMO of the molecule (J. Li et al., 2017). Thus, the expected results when using the TADF dendrimers as the emitter in the OLED device is increased efficiency of the device. The molecular structure of TADF dendrimers (**14-16**) are shown in Figure 1.3.

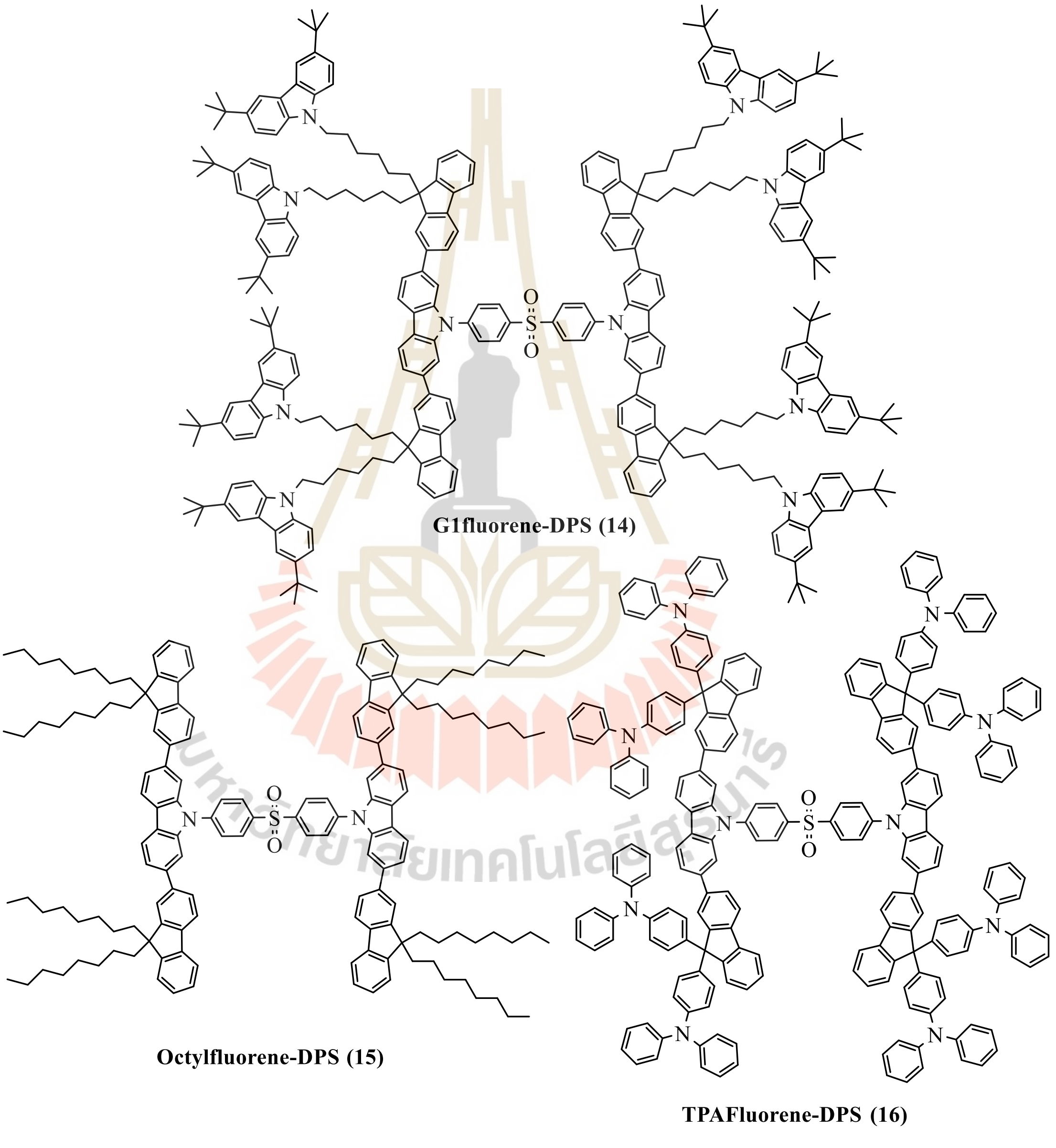

G1fluorene-DPS (14)

Octylfluorene-DPS (15)

TPAFluorene-DPS (16)

Figure 1.3 TADF dendrimers (**14-16**).

From above series, we try to tune the property of fluorescent materials to achieve high efficiency of the OLED devices, such as introduce the π-linker to extend the π-conjugation length, use the twist molecules to decrease the energy gap level between HOMO and LUMO, and reduce the π-π stacking interactions by using the carbazole dendron as the end group. However, some fluorophores reveal high emission in the solution state, but their emission was decreased in solid-state caused by aggregated from strong intermolecular π-π interactions, which is also known as aggregation-caused quenching (ACQ) (Peng et al., 2017). To overcome the strong aggregation-caused quenching effect, the small molecules, which can restrict the intramolecular vibration and rotations have been proposed. The aggregation-induced emission (AIE) characteristics found in some propeller-shaped molecules such as siloles and tetraphenylethenes (TPEs) (Y. Liu et al., 2011; Yu, Hsu, and Weng, 2018). Therefore, we designed and synthesized the AIE molecules containing the TPE linked to a variety of acceptors in order to achieve the different emission colors from yellow to red with the strong emission in solid-state. The desired molecules with the D-A-D system consist of benzothiadiazole derivative as electron acceptor bonded to two TPE as AIE unit. Subsequently, aggregation-induced emission characteristics of the target molecules in the THF/water mixtures have been studied as well as their solvatochromic effects related to their structures. The molecular structures of AIE red emitters (**17-26**) are shown in Figure 1.4.

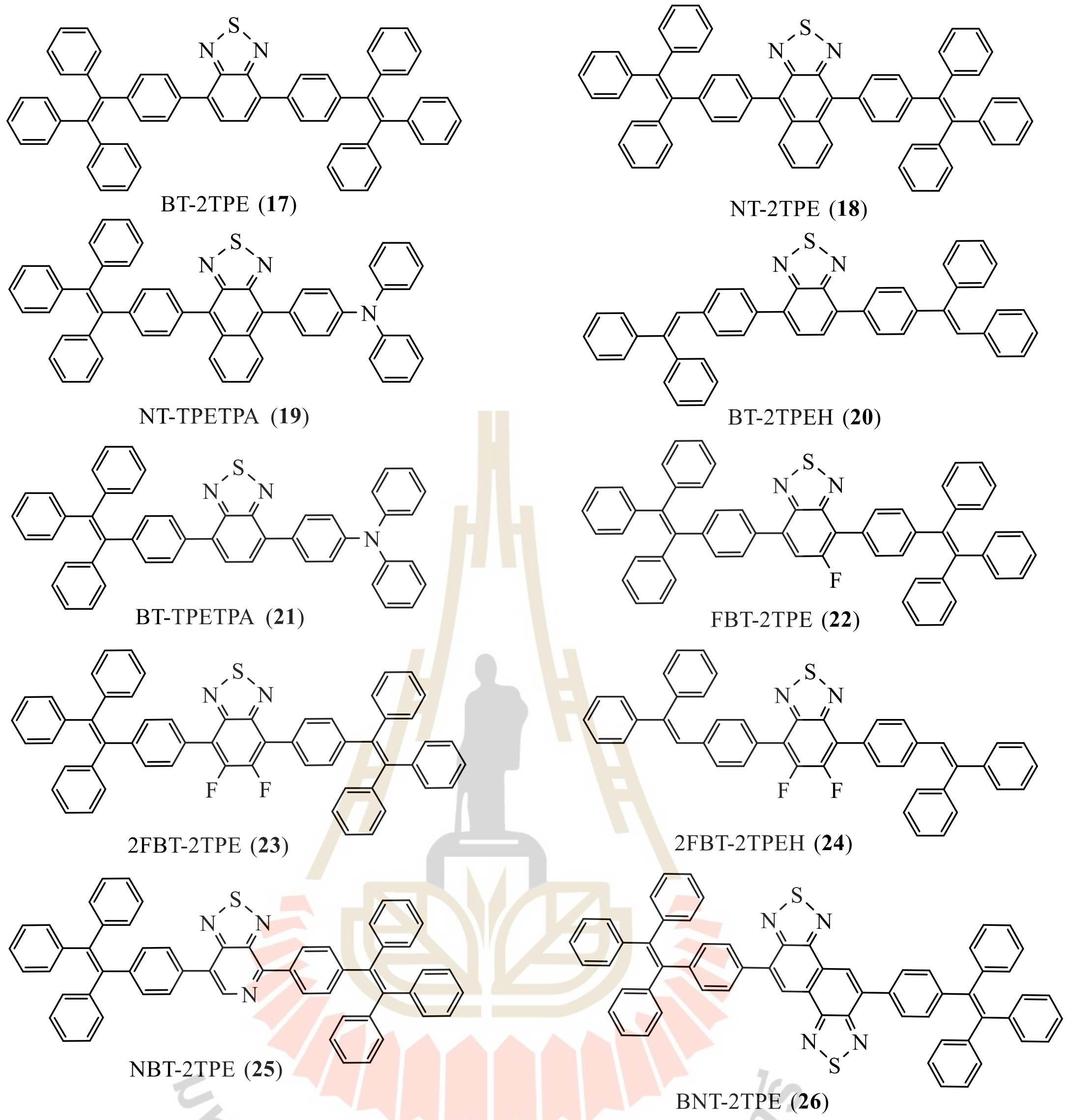

BT-2TPE (**17**)

NT-2TPE (**18**)

NT-TPETPA (**19**)

BT-2TPEH (**20**)

BT-TPETPA (**21**)

FBT-2TPE (**22**)

2FBT-2TPE (**23**)

2FBT-2TPEH (**24**)

NBT-2TPE (**25**)

BNT-2TPE (**26**)

Figure 1.4 AIE red emitters (**17-26**).

1.2 The principle of OLED

The organic light-emitting diode (OLED) can be used to generate the light sources in display devices, which is not require a backlight to function and have a long operation time. The important advantages are pixels directly emit light and the displays boast of higher brightness and resolution at wider viewing angles. OLED is a thin film optoelectronic device, which is consists of a single layer, double layer or multi-layer of organic materials sandwiched between two electrodes, one of which must be transparent. Nowadays, the OLED devices are comprised of Anode, hole injection layer (HIL), hole transport layer (HTL), emitting layer (EML), electron transport layer (ETL), hole blocking layer (HBL), and cathode (Thejo Kalyani and Dhoble, 2015; Thejokalyani and Dhoble, 2014). The materials to be used for each layer in OLEDs require the specific properties. The anode material must be transparent with high work function; such as an indium tin oxide (ITO) glass plate. Hole injection material should have high mobility, high glass transition temperature (T_g) and electron blocking capacity Copper phthalocyanine (CuPc) (**27**) and 4,4′,4′′-*Tris*(3-methylphenylphenylamino)triphenyl amine (*m*-MTDATA) (**28**). Hole transporting material should possess low ionization potential and high hole mobility; such as *N*,*N*′-bis(naphthalen-1-yl)-*N*,*N*′-bis(phenyl)-benzidine (NPB) (**29**), *N*,*N*′-bis(3-methyl phenyl)-*N*,*N*′-bis(phenyl)-benzidine (TPD) (**30**), *N*,*N*′-bis(naphthalen-1-yl)-*N*,*N*′-bis(phenyl)-2,2′-dimethylbenzidine (α-NPD) (**31**) and Di-[4-(*N*,*N*-ditolyl-amino)-phenyl] cyclohexane (TAPC) (**32**). Their structures are shown in Figure 1.5.

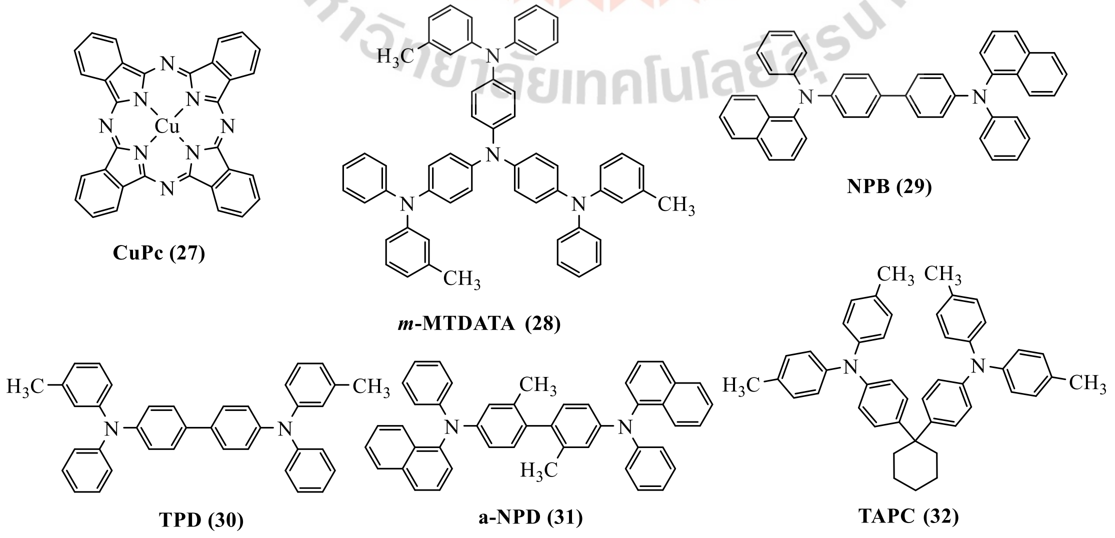

CuPc (27)

***m*-MTDATA (28)**

NPB (29)

TPD (30)

a-NPD (31)

TAPC (32)

Figure 1.5 Hole injection materials (**27, 28**) and hole-transporting materials (**29-32**).

The emissive material must have high-efficiency, long-lifetime, and color purity, which can be classified into three main classes, they are organic small molecules, polymers, and dendrimers. In order to improve the efficiency of the OLED device, the research trend is focused on design and synthesis of the emissive material. Electron transport materials should have high electron affinities with high ionization potentials in order to transport of electrons by accepting negative charges and allowing them to move through the molecules; such as aluminum tris-8-hydroxy quinoline (Alq_3) (**33**) and 9, 10-di (2-napthyl)anthracene (ADN) (**34**) as shown in Figure 1.6. The last components are cathode material, which used to inject electrons into emissive layers, and thus must possess a low work function ($\varphi_w \approx 2.9$–4.0 eV) and low threshold voltage. Mg:Ag (10:1), LiF, Mg:Al, CsF:Al, Al_2O_3:Al are widely used as cathode materials.

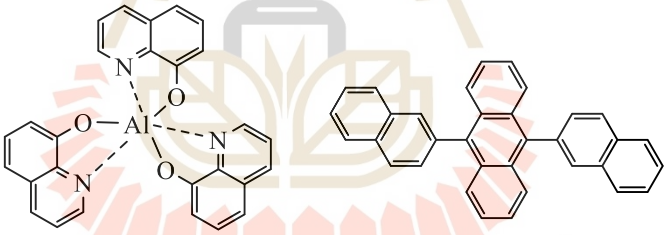

Alq_3 (33) **ADN molecule (34)**

Figure 1.6 Aluminum *tris*-8-hydroxy quinoline (**33**) and 9, 10-di (2-napthyl)anthracene (**34**).

When a voltage is applied across OLED devices, the injected electrons and holes are transferred into the emissive layer. An exciton is formed when electrons and holes are recombined and generates a photon whose wavelength corresponds to the energy gap after completion of its exciton lifetime. The possibility of electron-hole recombination can be increased by the use of multiple material layers, which electron and hole can be dammed by using the different of HOMO/LUMO level of material in each layer, therefore recombination position can be controlled, then the high efficiency of OLED can be achieved. Besides that, the emitting color of the OLED device can be tuned by changing the type of organic molecules in the emissive layer and the energy gap of the emitting material. The intensity or brightness of the light depends on the amount of electrical current applied through the device.

The efficiency of OLED is a function of several factors such as a function of the current density, voltage, efficiency of recombination, luminescence quantum yield and the degree of balance charge carrier injection. Luminescence quantum yield (ϕ) is an important parameter in the emission process. It defined as the ratio of the number of photons emitted to the number of photons absorbed, therefore more photons emitted and fewer photons absorbed lead to the high efficiency of the device. Moreover, the performance of the OLED device can be evaluated by several factors such as current-voltage (*V-I*) characteristics, current density-voltage-luminance (*J-V-L*) characteristics, electroluminescence (EL) spectra, CIE coordinates, and lifetime measurements.

CHAPTER II

THE SYNTHESIS AND CHARACTERIZATION OF DPP DENDRIMERS AS EMITTERS FOR ORGANIC LIGHT-EMITTING DIODES

2.1 Introduction

In this chapter, the structure of 3,6-diphenyl 2,5-dihydro-pyrrolo[3,4-c]pyrrole-1,4 diones, commonly known as DPP, which have been widely used as high-performance pigments such as inks, paints, and plastics has been modified (Figure 2.1) (Iqbal, 1997). DPP derivatives have several advantages such as they are strong acceptors which exhibit a high molar absorption coefficient, as well as high fluorescence quantum yields, and they can undergo several synthetic modifications (Kaur and Choi, 2015). From the above feature, DPP derivatives have been used in polymer solar cells (PSCs) (C. Li et al., 2016), non-fullerene organic solar cells (NFOSCs) (C. Zhao et al., 2019), transistor paint (Nelson et al., 2010), organic photovoltaics (OPV) (S. Qu and Tian, 2012), field-effect transistors (FET) (Malenfant, 2002), sensing fluoride ion and bioimaging (Y. Qu et al., 2014) fluorescent probes (Kaur and Choi, 2015), two-photon absorption (Ftouni, Bolze, de Rocquigny, and Nicoud, 2013), dye sensitizing solar cell (Farré et al., 2016), and organic light-emitting diodes (OLEDs) (Tieke, 2007).

DPP-containing polymers have been used as an emitter for OLED devices, but the small DPP molecule has not been investigated, despite their very high intensity and photoluminescence quantum yield (PLQY) in solution. Owing to DPP has a planar structure induces strong intermolecular H-bonding and π–π stacking with neighboring molecules that may lead to dissipative intermolecular charge transfer and aggravate charge recombination that quenches fluorescence (Data et al., 2016). From our previous work, we reported the red emitter containing carbazole dendrons as the end caps with the oligoarylfluorene cores for OLED, that we are able to reduce the crystallization and retain the high emissive ability of a planar fluorescent core in the solid-state as well as improve the thermal stability of the material.

The light emission can be finely tuned by the selection of the core, solubility can be adjusted by selecting the suitable surface groups and the level of intermolecular interactions can be controlled by the type and generations of the dendrons employed (Sudyoadsuk et al., 2014). The purpose of our current work is, therefore, to report on the new DPP-containing carbazole dendron in order to overcome π–π stacking of DPP molecules and induced to increase the EQE of the OLED device. We synthesized and investigated new solution-processed dendrimer-based red emitters. The DPP dendrimer containing two parts, the first part is 3,6-diphenyl 2,5-dihydro-pyrrolo[3,4-c]pyrrole-1,4 diones (DPP) as a fluorescent core and another part is carbazole dendrimers up to the second generation as end-capping groups. The latter can suppress the aggregation-induced fluorescence quenching of the planar conjugated core as well as increase thermal stability, and solubility of the molecule. With the character of dendron that reduces the π–π stacking interaction of DPP core, the dendrimer molecules will emit in the red region. Previous work, we reported on carbazole dendrimers that are successfully used as efficient solution-processed materials with a simple structure of OLED devices (Moonsin et al., 2012). With this design, a simple solution-processed red emitter can be obtained and can be fabricated. Herein we report a detailed synthesis of a series of DPP end-capped with carbazole dendrons as well as their physical and photophysical properties. The investigation of the device fabrication and performance using these materials as an emissive layer is also reported. The diaryl groups of DPP molecule reveals several centres of reactivity in the molecule as shown in Figure 2.1. The phenyl rings could undergo electrophilic and nucleophilic substitution reactions, while each of three functional groups, namely double bonds, carbonyl and NH moieties of bicyclic lactam enables chemical transformation. Therefore, the reaction of DPP chromophore is focused on electrophilic aromatic substitution, *N*-substitution and nucleophilic transformations of the carbonyl group without ring-opening of the heterocyclic rings. Currently, the most important member of the DPP class of pigments is pigment red 254 which is a very opaque yellow-red pigment of outstanding outdoor durability, brightness, and resistance to heat and chemicals. Pigment red 254 is widely used for exterior coatings in the automotive industry and plastics (Iqbal, 1997).

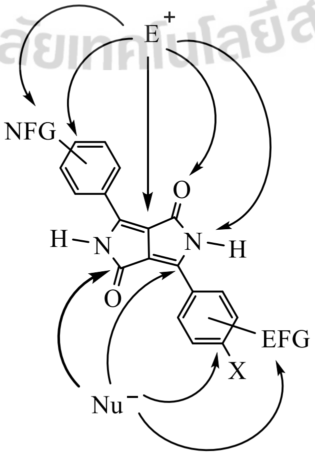

DPP (35)

Figure 2.1 Centres of potential chemical reactivity in the molecule of DPP (**35**).

Some DPP derivatives have been synthesized by a chemical reaction such as Suzuki reaction and alkylation. In 2007, five new soluble conjugated polymers (**36-41**) were prepared upon Suzuki polycondensation reactions, which consist of DPP units and carbazole, triphenylamine, benzo[2,1,3]thiadiazole, anthracene, and fluorene units as shown in Figure 2.2. The polymers are soluble in common organic solvents and exhibit brilliant red colors with the photoluminescence quantum yields up to 86% (Tieke, 2007).

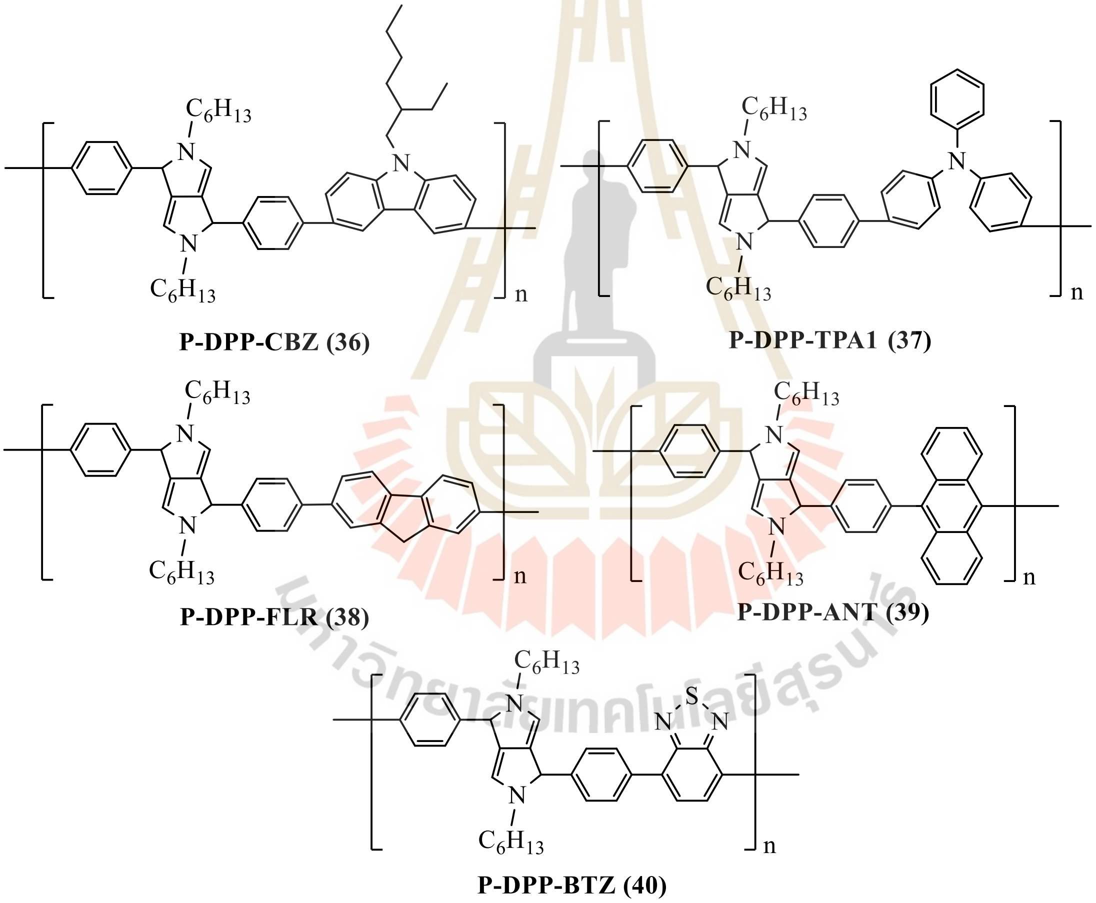

Figure 2.2 Conjugated polymers (**36-41**) obtained from the Suzuki reaction.

The DPP derivatives (**41-44**) with mono-alkyl substituted or di-alkyl substituted at *N*-position of lactam rings via N-alkylation reaction have been reported in 2008

(Figure 2.3). The studies reveal that the electronic properties strongly depend on the planarity of the molecules, which was decreased by the substitution. A larger Stokes shift was observed when a phenyl torsion increased, and the vibrational structure decreased. On the other hand, the fluorescence quantum yield reminds nearly the same, which indicated that the thin film of these DPP compounds can be prepared and use for the construction of efficient electroluminescent devices without loss of fluorescence quantum yields (Vala, Weiter, Vynuchal, Toman, and Lunak, 2008).

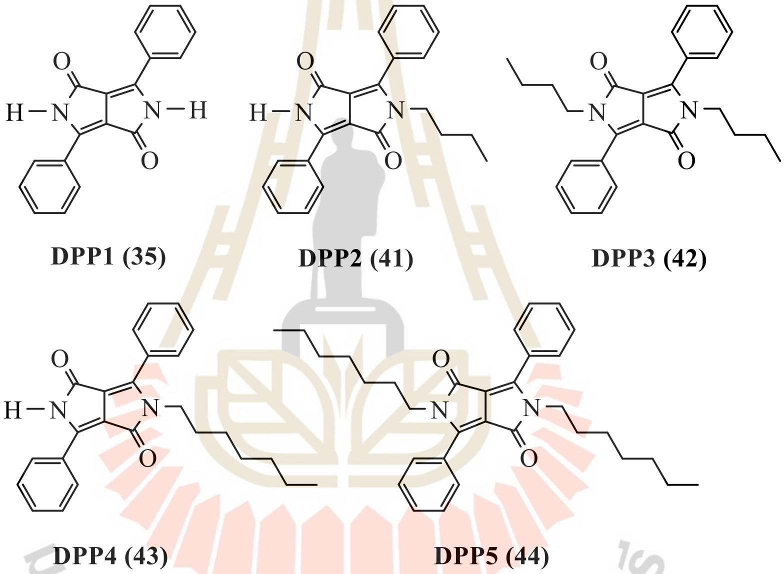
DPP1 (35) **DPP2 (41)** **DPP3 (42)**

DPP4 (43) **DPP5 (44)**

Figure 2.3 The DPP derivatives (**41-44**).

In 2010, Nelson et al. has reported the synthesis of the DPP polymer semiconductor (**45**) with D-A character via the Stille coupling reaction of dibrominated DPP monomer (**46**) with distannylated DTP monomer (**47**) as shown in Figure 2.4. The expected result was to enhance charge mobility and achieved a narrow bandgap by the use of D-A system. The new polymer exhibited hole mobility as high as 0.41 cm^2 /Vs and average mobility of 0.29 cm^2/Vs ± 0.04 for channel lengths of 30–40 µm (Nelson et al., 2010).

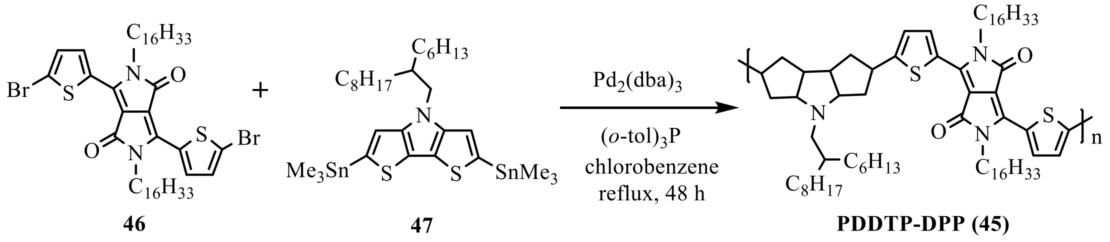
Br
S
C16H33
N
O
+
C6H13
C8H17
Me3Sn
SnMe3
Pd2(dba)3
(o-tol)3P
chlorobenzene
reflux, 48 h
n
46
47
PDDTP-DPP (45)

Figure 2.4 The synthesis of DPP polymer semiconductor (**45**).

The unsubstituted DPP (**35**), symmetrically *N*-substituted DPP (**48**, **50**, and **52**), and asymmetrically *N*-substituted DPP (**49** and **51**) were investigated using thermogravimetry (TGA) and differential scanning calorimetry (DSC) (David, Weiter, Vala, Vyňuchal, and Kučerík, 2011). The results reveal that the different alkyl chains and symmetry of the *N*-substitution effect on physical-chemical properties, which the shorter the alkyl chain and the symmetrical derivatives display less stability. On the other hand, DSC experiments did not reveal the presence of different crystalline structures in DPP.

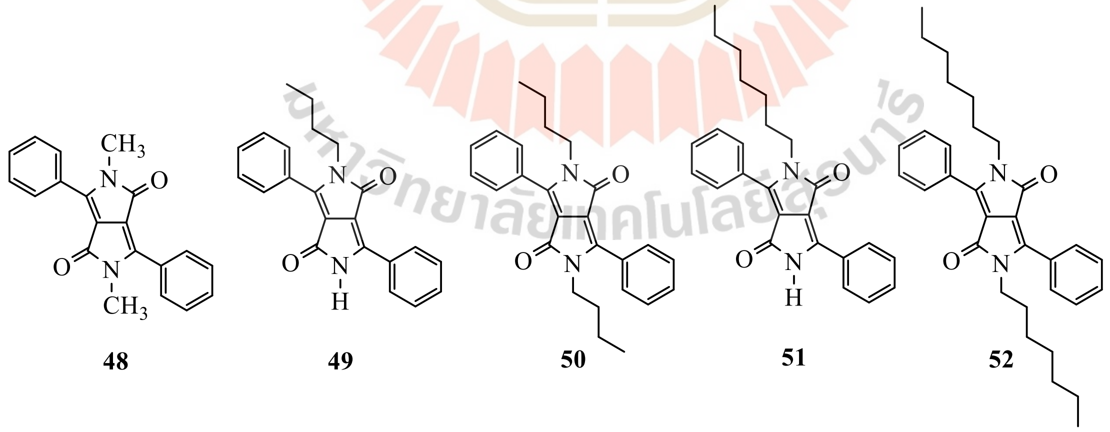
CH3
N
O
H
48
49
50
51
52

Figure 2.5 The unsubstituted DPP (**35**), symmetrically *N*-substituted DPP (**48**, **50**, and **52**), and asymmetrically *N*-substituted DPP.

In 2014 Data et al. was able to improve the efficiency of OLED by creating exciplex emitters from dilution of DPP compounds in TAPC and CBP hosts. The results reveal that the external quantum efficiency of the OLED device with exciplex emitter (12%) is higher than the pure compound (0.2%) (Data et al., 2016).

The near-infrared (NIR) OLED based on NIR emitting diketopyrrolopyrrole borondifluoride cyanine emitter (**54**) has been reported by Sassi et al. in 2016. By incorporating of DPP derivative with NIR chromophores was obtained EQE of 0.55% with no efficiency roll-off and stability for long operation time (Sassi et al., 2016).

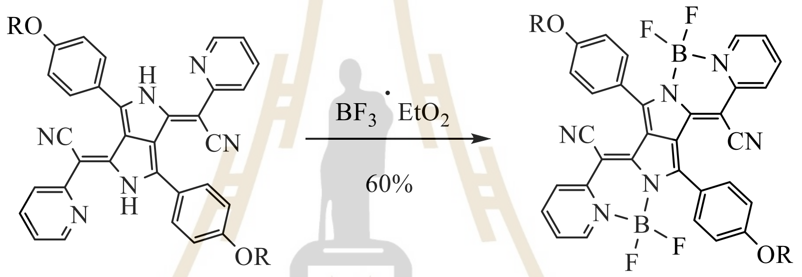

DPP-CN (53)
R = 3,7-dimethylooctyl

DPPcy (54)

Figure 2.6 The synthesis of diketopyrrolopyrrole borondifluoride cyanine emitter (**54**).

Podlesný et al. was designed and prepared the diketopyrrolopyrrole based D-π-A-π-D molecules with quadrupolar chromophores by Suzuki-Miyaura, Migita-Stille, and Sonogashira cross-coupling reactions to afford nine compounds (**55-63**). The properties such as differential scanning calorimetry, electrochemistry, and absorption and emission spectra can be tuned by structural variation of the peripheral substituents (donor) and enlargement of the π-system. The results revealed that the thermal stability is mostly affected by the presence of π-linkers and ferrocene end groups. The variation of donors influences the effect on the HOMO-LUMO gap (Podlesny et al., 2017).

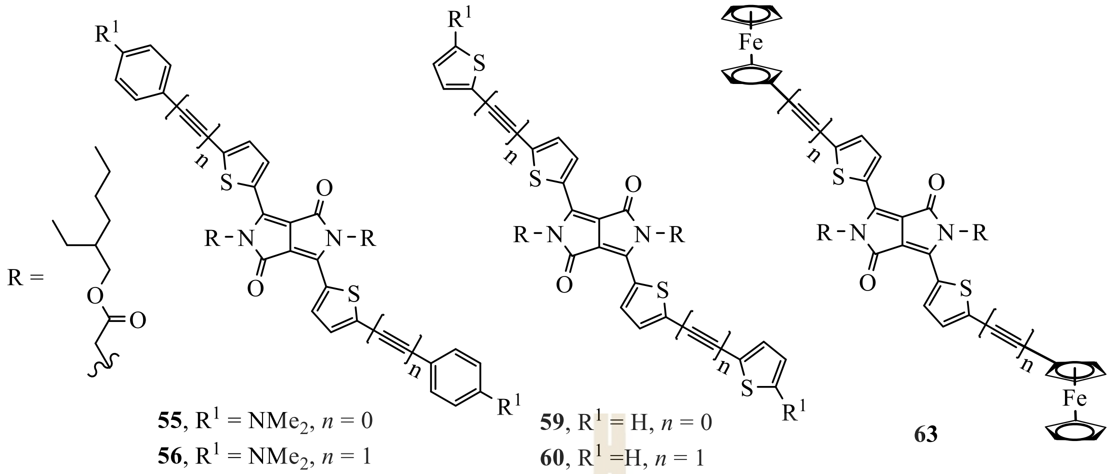

55, R^1 = NMe_2, n = 0
56, R^1 = NMe_2, n = 1
57, R^1 = OMe, n = 0
58, R^1 = OMe, n = 1

59, R^1 = H, n = 0
60, R^1 =H, n = 1
61, R^1 = OMe, n = 0
62, R^1 = OMe, n = 1

63

Figure 2.7 The diketopyrrolopyrrole based D-π-A-π-D molecules (**55-63**).

The optical, electronic, and charge transport properties of a series of donor-acceptor diketopyrrolopyrrole derivatives (**64-70**) have been investigated. The introduction of the various donor end groups of the designed compounds can broaden the absorption spectrum and improve the charge transport property. The results can be concluded that the DPP derivatives were suitable for use as donor materials for OSCs and luminescent materials for OLEDs (Jin, Zhang, Xiao, and Irfan, 2018).

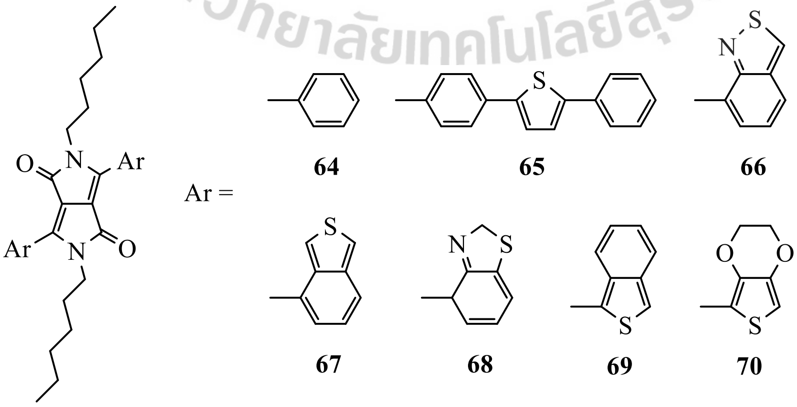

64 **65** **66** **67** **68** **69** **70**

Figure 2.8 The diketopyrrolopyrrole derivatives (**64-70**).

2.2 Research objectives

2.2.1 To design, synthesize and characterize novel fluorescence materials as a non-doped emitter for OLED.

2.2.2 To study the photophysical, electrochemical, and thermal properties by using UV-Visible spectroscopy, fluorescence spectroscopy, cyclic voltammetry, and DSC-TGA techniques.

2.3 Synthesis

2.3.1 Synthetic procedure

Therein we also reported the synthesis of the DPP dendrimer derivatives by Friedel-craft alkylation of carbazole to afford key intermediate followed by Ullmann *N*-arylation to achieve the carbazole dendron. Finally, the *N*-alkylation of DPP with the key intermediate to afford the corresponding compounds (Figure 2.9).

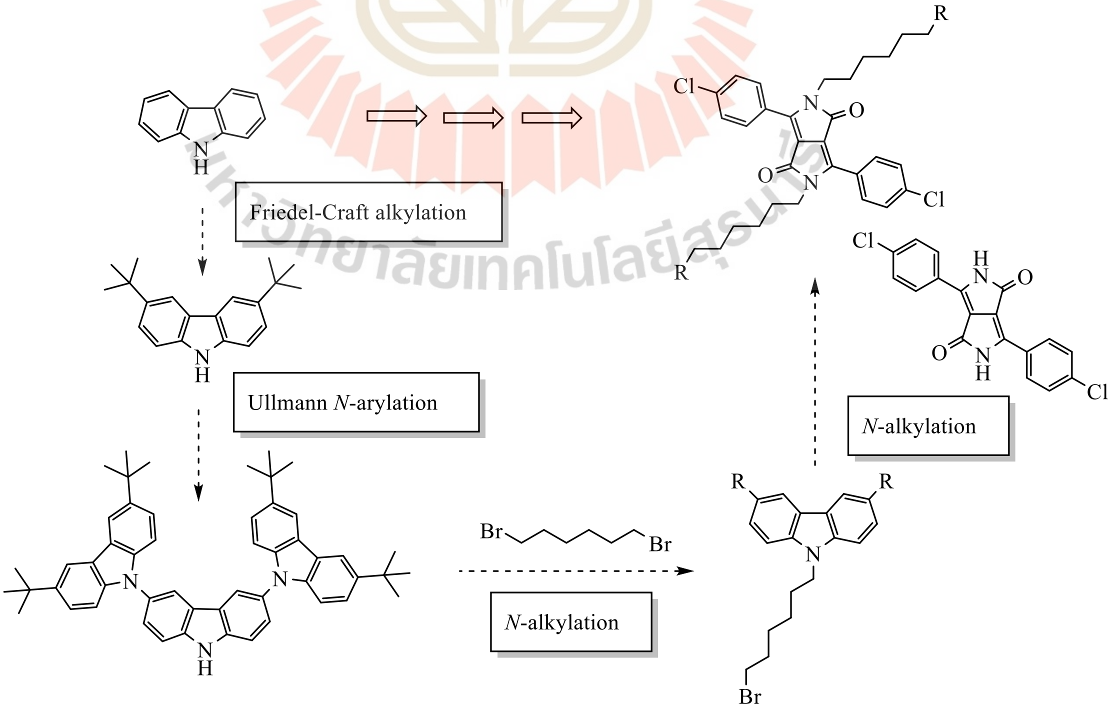
N
H
Friedel-Craft alkylation
Ullmann N-arylation
N-alkylation
Br
Br
N-alkylation
R
R
N
Br
Cl
N
O
O
Cl
R
R
H
N
O
O
N
H
Cl
Cl

Figure 2.9 Synthetic approach to the synthesis of DPP dendrimers.

2.3.2 Preparation of 3,6-diiodo-9-tosyl-carbazole (72)

3,6-diiodo-9-tosyl-carbazole (**72**) could be synthesized on a 10 g scale in two steps starting from the inexpensive carbazole (**71**) according to a simple procedure (Figure 2.10).

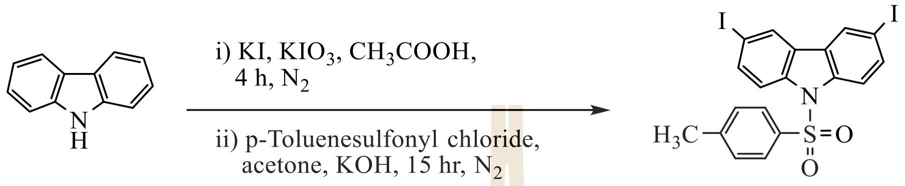
N
H
i) KI, KIO$_3$, CH$_3$COOH,
4 h, N$_2$
ii) p-Toluenesulfonyl chloride,
acetone, KOH, 15 hr, N$_2$
I
I
N
H$_3$C
S=O
O

71 **72**

Figure 2.10 The synthesis of 3,6-diiodo-9-tosyl-carbazole (**72**).

Iodination of carbazole (**71**) with potassium iodide and potassium iodate in acetic acid provided the corresponding 3,6-diiodo carbazole, which protects N atom of carbazole with tosylate group by using *p*-toluenesulfonyl chloride and potassium hydroxide in acetone. After purification by recrystallization from CH_2Cl_2/hexane the desired product was obtained in 64% overall yield.

2.3.3 Preparation of 3,6-di-tert-butyl-carbazole (73)

3,6-di-*tert*-butyl-carbazole (**73**) or G1 could be synthesized on a 10 g scale, which starting from the Friedel-Craft alkylation of inexpensive carbazole (**71**) as shown in Figure 2.11.

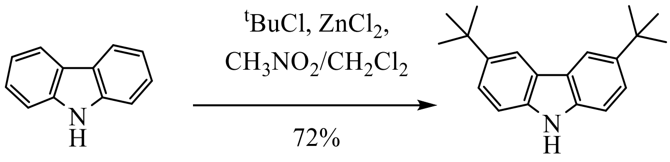
N
H
^{t}BuCl, ZnCl$_2$,
CH$_3$NO$_2$/CH$_2$Cl$_2$
72%
N
H

71 **73, G1**

Figure 2.11 The synthesis of 3,6-di-*tert*-butyl-carbazole (**73**).

Friedel-Crafts alkylation involves C-C bond formation of an aromatic ring with an alkyl halide using a strong Lewis acid, such as aluminium chloride, ferric chloride, as a catalyst. The general mechanism is shown in Figure 2.12.

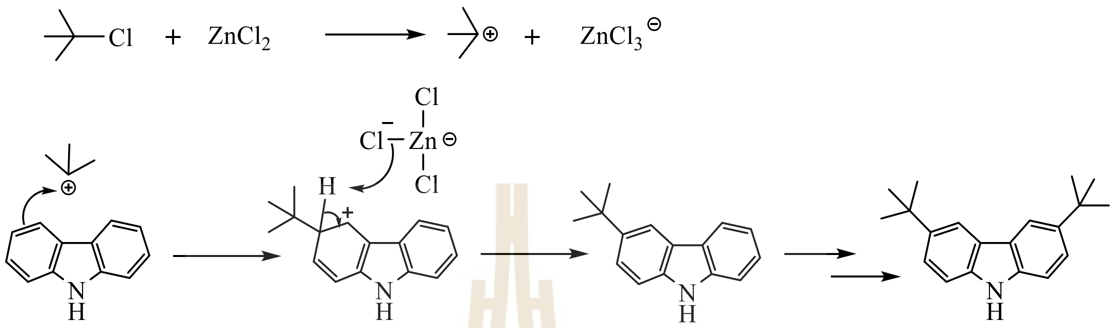
Cl
+
$ZnCl_2$
⊕
+
$ZnCl_3^{\ominus}$
Cl
Cl
Zn ⊖
Cl
H
+
N
H
N
H
N
H
N
H

Figure 2.12 The proposed mechanisms of Friedel-Crafts alkylation.

Friedel-Craft alkylation of carbazole (**71**) with 2-chloro-2-methyl propane and zinc chloride in the mix of CH_2Cl_2 and nitromethane in a ratio of 2:1 provided the corresponding 3,6-di-*tert*-butyl-carbazole (**73**). After purification, by washing with hexane the desired product was obtained in a yield of 72%.

2.3.4 Preparation of G2 (74)

The second generation of dendron (**74**) could be synthesized on a 5 g scale from the Ullmann *N*-arylation of **G1 (73)** as shown in Figure 2.13.

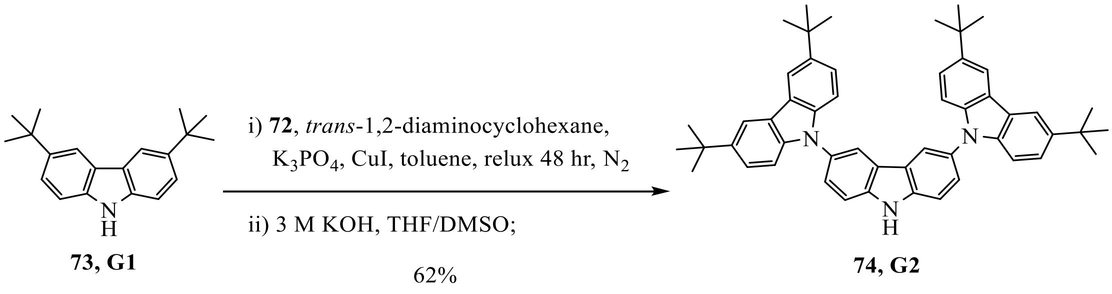
N
H
73, G1
i) **72**, *trans*-1,2-diaminocyclohexane,
K_3PO_4, CuI, toluene, relux 48 hr, N_2
ii) 3 M KOH, THF/DMSO;
62%
N
N
N
H
74, G2

Figure 2.13 The synthesis of G2 (**74**).

Ullmann coupling reaction is a copper-catalyzed cross-coupling reaction in respect of C-C bond formation between two molecules which one of these is aryl halides (Mondal, 2016). Therefore Ullmann *N*-arylation is a coupling reaction of aryl halides with amines by using CuI-catalyzed to create C-N bond (Dawei Ma, 2003; Eric R. Strieter, 2009). The proposed mechanisms of the Cu(I)-catalyzed C-N bond-forming reaction between *N*-nucleophiles and aryl halides involves 2 steps, nucleophile formation and Cu(I)-mediated nucleophilic aromatic substitution (Figure 2.14).

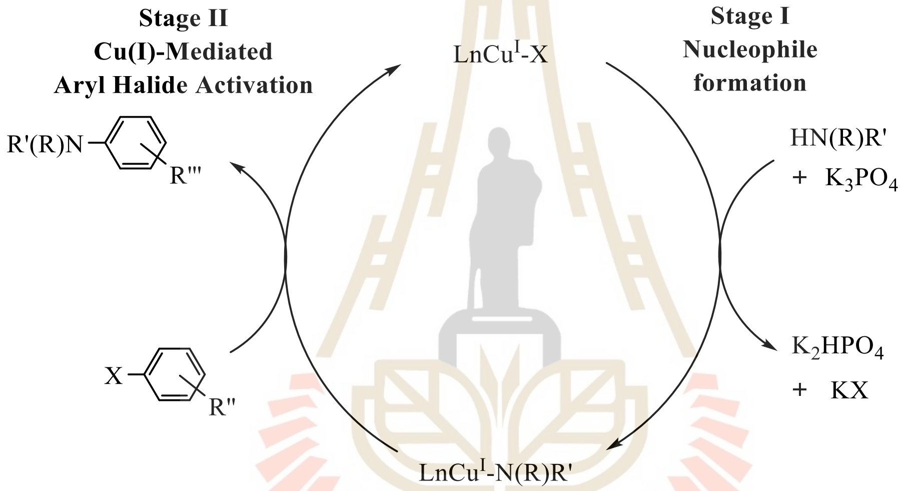

Figure 2.14 The proposed mechanisms of Ullmann *N*-arylation.

A stoichiometric reaction of G1 (**73**) (2.3 equiv) and 3,6-diiodo-tosylcarbazole (**72**) (1 equiv) using CuI as the catalyst, (±)-*trans*-1,2-diaminocyclo hexane as the co-catalyst and K_3PO_4 as base in toluene followed by deprotection of the intermediate compound with 3 M potassium hydroxide in THF/DMSO provided the corresponding G2 (**74**) in a moderate yield of 62%.

2.3.5 Preparation of G1hexyl bromide (75) and G2hexyl bromide (76)

The Gnhexyl bromide (**75** and **76**) could be prepared on a 1 g scale by *N*-alkylation of Gn with 1,6-Dibromohexane in as shown in Figure 2.15.

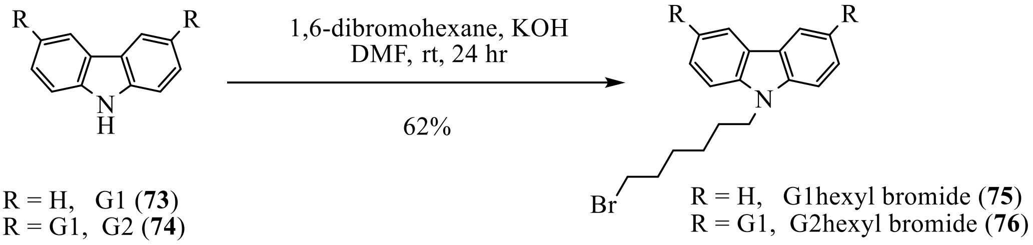

Figure 2.15 The synthesis of G1hexyl bromide (**75**) and G2hexyl bromide (**76**).

N-alkylation or Amine alkylation is a reaction between an alkyl halide and amine to afford the higher substituted amine product. This reaction is called nucleophilic aliphatic substitution and the proposed mechanisms are shown in Figure 2.16.

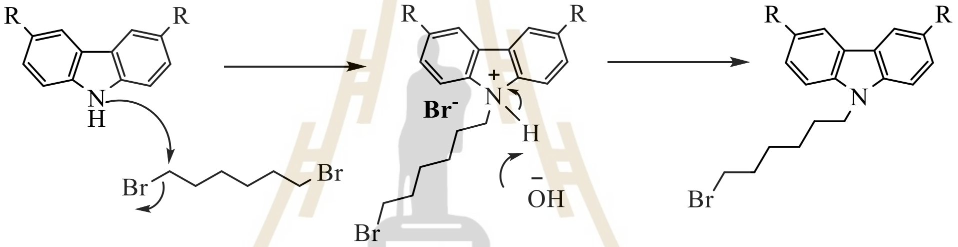

Figure 2.16 The proposed mechanisms of *N*-alkylation.

The alkylation of G1 and G2 with 1,6-dibromohexane in the presence of potassium hydroxide in *N*,*N*-dimethylformamide at room temperature provided the corresponding G1hexyl bromide (**75**) and G2hexyl bromide (**76**). After purification by column chromatography using CH_2Cl_2/hexane as the eluent to afford the products as a white solid in the yields of 77% and 86%, respectively.

2.3.6 Preparation of GnDPP (1-3)

The desired DPP compounds could be synthesized on a milligram scale by using *N*-alkylation of pigment red 254 (**77**) with potassium *tert*-butoxide in *N*-methyl-2-pyrrolidone (NMP) to give corresponding GnDPP (**1-3**) in a low yield as depicted in Figure 2.17.

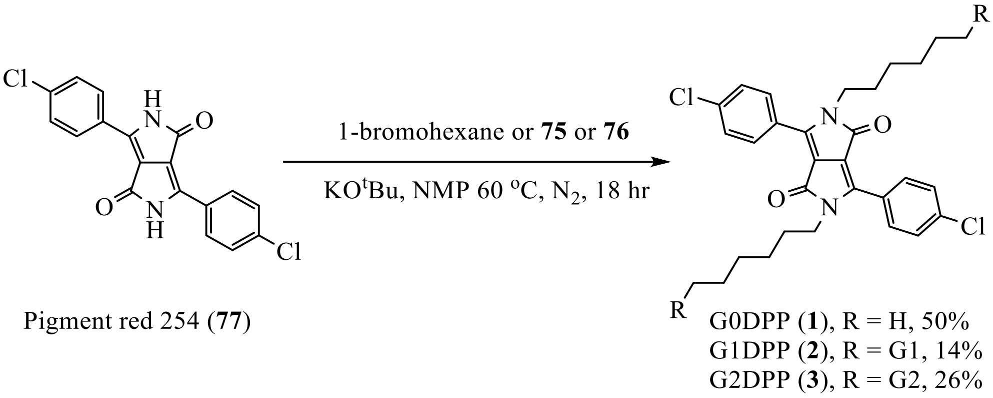
1-bromohexane or **75** or **76**
KO^{t}Bu, NMP 60 °C, N_2, 18 hr
Cl
H
N
O
R

Pigment red 254 (**77**)

G0DPP (**1**), R = H, 50%
G1DPP (**2**), R = G1, 14%
G2DPP (**3**), R = G2, 26%

Figure 2.17 The synthesis of GnDPP (**1-3**).

Nucleophilic substitution of pigment red 254 (**77**) with alkyl bromide in the presence of potassium *tert*-butoxide as base in *N*-methyl-2-pyrrolidone (NMP) at 60°C for 18 hours to afford the desired products. After purification by column chromatography and recrystallization from CH_2Cl_2/MeOH yielded the yellow-orange colored solid of G0DPP (**1**), G1DPP (**2**), and G2DPP (**3**) in the yields of 50%, 14%, and 26%, respectively. All products were soluble in most organic solvents and their structures were confirmed by ^{1}H NMR as shown in Figure 2.18.

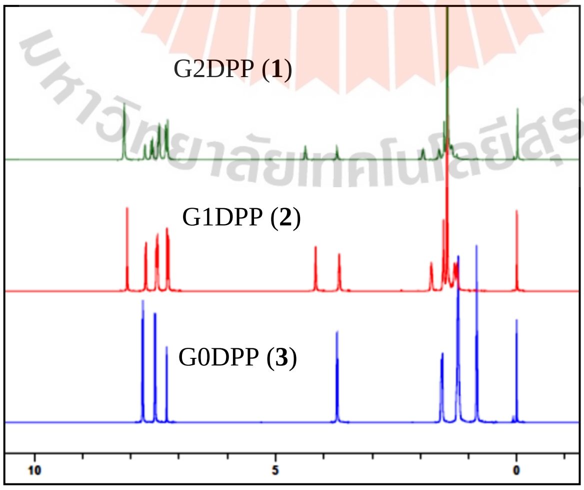

Figure 2.18 The ^{1}H-NMR spectrum of GnDPP (**1-3**).

The structure of G0DPP (**1**) was confirmed by ^{1}H-NMR spectroscopy. The diaryl protons of the DPP core exhibited two doublets peak at δ = 7.76 (4H) and 7.50 (4H) ppm with the coupling constant (*J*) of 8.4 Hz. The alkyl protons at the near position with N-atom of DPP core show the signals at δ = 3.72 (4H, t), while another position displays the signal at δ = 1.56 (4H, m), 1.21 (12H, m), 0.83 (6H, m) ppm. Besides, ^{13}C-NMR reveals the chemical shift of the signals of diaryl carbons was in the range of 162.5- 110.0 ppm and the alkyl carbons were in the range of 41.9-13.9 ppm. Moreover, High resolution mass spectrometry confirmed the identity of the compound with m/z (HRMS) = 524.4251 (required m/z = 524.1997).

The ^{1}H-NMR spectrum of G1DPP (**2**) exhibited the characteristic singlet peak of G_1 protons with the chemical shift at 8.09 (4H) ppm and the chemical shift of another position of G_1 protons was in the range of 7.45-7.23 ppm. The diaryl protons of DPP core exhibited two doublets peak at δ = 7.70 (4H) and 7.49 (4H) ppm with the coupling constant (*J*) of 8.3 Hz. The alkyl protons at the near position with N-atom of DPP core show the triplets signals at δ = 3.72 (4H) and the methylene protons which near the N-atom of G1 show the triplets signals at δ = 3.69 (4H), while another position display the signal at δ = 1.78 (4H), 1.53 (4H) 1.45 (36H), and 1.24-1.30 (8H) ppm. Besides, ^{13}C-NMR reveals the chemical shift of the signals of diaryl carbons was in the range of 162.4-107.9ppm and the alkyl carbons were in the range of 42.9-26.6 ppm. Moreover, High resolution mass spectrometry confirmed the identity of the compound with m/z (HRMS) = 1078.6823 (required m/z = 1078.5658).

The ^{1}H-NMR spectrum of G2DPP (**3**) exhibited the characteristic singlet peak of the second generation of the dendron protons with the chemical shift at 8.17 (8H) ppm, singlet peak of first generation of the dendron protons at 8.15 (4H). The chemical shift of another position of G2 protons and diaryl protons of DPP core was in the range of 7.73-7.30 ppm. The alkyl protons at the near position with N-atom of DPP core show the triplets signals at δ = 4.40 (4H) and the methylene protons which near the N-atom of G1 show the triplets signals at δ = 3.73 (4H), while another position was in the range of 1.61-1.26 ppm. Moreover, High resolution mass spectrometry confirmed the identity of the compound with m/z (HRMS) = 1963.0941 (required m/z = 1963.0476).

2.4 Results and discussion

2.4.1 Quantum chemical calculation

Quantum chemical calculations performed using the B3LYP/631G (d,p) method26 reveal that increasing of the generation of the dendron surrounding the DPP acceptor produced sterically hindering molecular structures increased (Figure 2.19). The distributions of π-electrons in the HOMOs of G_1DPP and G_2DPP are mainly located on the carbazole dendron moieties, while in the LUMOs of two compounds, the excited electrons are localized on the DPP moieties. On the other hand, both HOMOs and LUMOs of G0DPP (**1**) that have only alkyl chain linked to DPP moiety, π-electrons are located on the DPP moiety. The Homos and LUMOs of the DPP dendrimers estimated from the calculation are summarized in Table 2.1. According to the TDDFT, it can be deduced that G0DPP (**1**), G1DPP (**2**), and G2DPP (**3**) would have similar electronic properties with different physical properties.

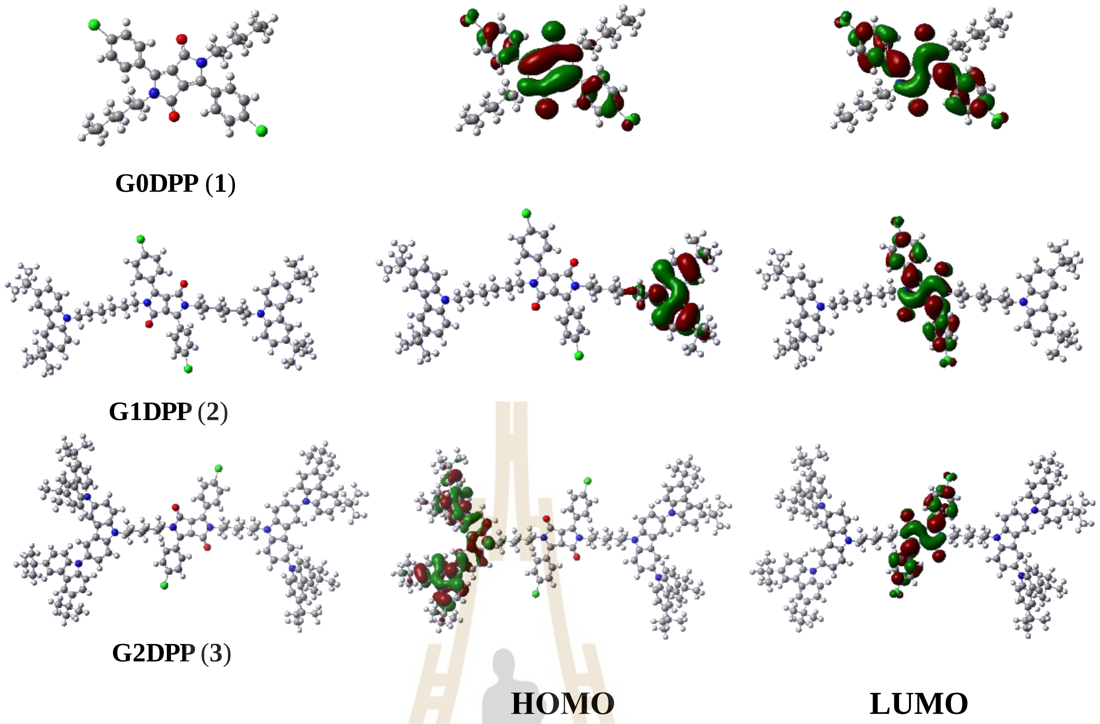

Figure 2.19 HOMO and LUMO orbitals of G0DPP (**1**), G1 DPP (**2**), and G2 DPP (**3**) calculated by the B3LYP/6-31G(d,p) method.

Table 2.1 HOMOs and LUMOs of the DPP dendrimers estimated from the calculation.

Compds	**HOMO (eV)**	**LUMO (eV)**
G0DPP (**1**)	-5.360	-2.561
G1DPP (**2**)	-5.128	-2.690
G2DPP (**3**)	-5.013	-2.757

2.4.2 Optical properties

The UV-vis absorption and fluorescence spectra of the DPP dendrimers were investigated in dilute toluene solution (10^{-5} M) and the neat film by UV-vis and photoluminescence spectroscopies as shown in Figure 2.20. Absorption spectra of G1DPP (**2**) and G2DPP (**3**) exhibit two major absorption bands, a high absorption band around

300 nm assigned to the π–π* transition of the dendrimers and an absorption band at 480 nm corresponding to the π–π* transition of the lactam unit of DPP. Moreover, the UV-vis of G0DPP (**1**) showed the strong absorption band of the π–π* transition of the lactam around 480 nm. Both of GnDPP dendrimers showed similar absorption band in solution and in the neat film. This indicates that the dendron which is substituted on the DPP chromophore does not induce the bathochromic effect on the UV-vis spectra.

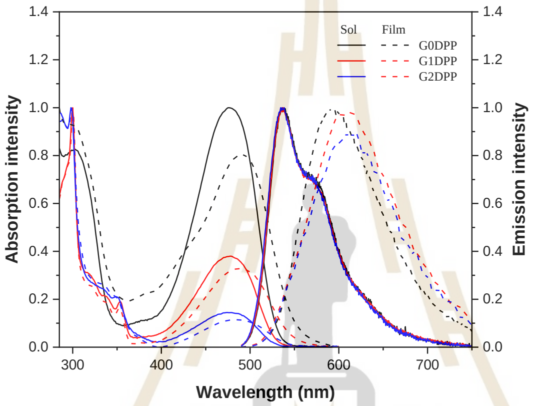

Figure 2.20 UV-vis absorption and fluorescence spectra of (a) G0DPP (**1**) (b) G1DPP (**2**) and (c) G2DPP (**3**) in dilute toluene solution (10^{-5} M) and in a solid film.

The optical band gap of these dendrimers has been calculated from the onset wavelength of absorption. The detailed optical data of all compounds are summarized in Table 2.2. Photoluminescence spectra of G0DPP (**1**), G1DPP (**2**), and G2DPP (**3**) showed an emission band in the toluene solution at 537, 536, and 536 nm, respectively, while in the neat film are 595, 610, and 610 nm. They show the bathochromic shift from the solution to the solid-state (58, 72, and 72 nm for G0DPP (**1**), G1DPP (**2**), and G2DPP (**3**)). Furthermore, they display the large stoke shift with 61, 58, and 58 nm in solution and 104, 118, and 122 nm in the neat film, respectively. Therefore, the introduction of the carbazole dendron with the longer alkyl chain at N-atom of the lactam unit lead to reduce the π- π stacking interaction of the planar molecule in the solid-state and increase their solubility.

Table 2.2 Photophysical Data of the DPP dendrimers**.**

Compds	**λ_{abs}^{sol} (log ε)/ λ_{abs}^{film} (nm/M^{-1}cm^{-1})** ^{a}	**$\lambda_{em}^{sol}/\lambda_{em}^{film}$ (nm)** ^{a}	**$\lambda^{abs}{}_{onset}$ (nm)** ^{b}	**$\lambda^{flu}{}_{onset}$ (nm)** ^{c}	**E_g^{opt} (eV)** ^{d}
G0DPP (**1**)	478 (4.31)/490	536/594	531	506	2.33
G1DPP (**2**)	478 (4.29)/490	536/610	530	505	2.34
G2DPP (**3**)	478 (4.27)/490	536/610	527	503	2.35

[a] Measured in toluene and as thin films.

[b] The onset of the absorption spectra.

[c] The onset of the fluorescence spectra.

[d] Calculate from the absorption spectra threshold, $E_g^{opt} = 1240/\lambda_{onset}$.

The Commission Internationale De L'Eclairage (CIE) Chromaticity diagram describes the color perceived by the human eye in full daylight, which the chromaticity coordinates of samples represented by (x,y). These values can be calculated by x = X/(X + Y + Z), y = Y/(X + Y + Z) where (X,Y,Z) represents a CIE XYZ tristimulus vector. (Sovdat, Kadunc, Batič, and Milčinski, 2019) (Ji, Xue, and Cui, 2015) The CIE coordinates of the emitted orange light in the neat film are (0.56, 0.44), (0.54, 0.45), and (0.57, 0.43) for G0DPP (**1**), G1DPP (**2**), and G2DPP (**3**), respectively as shown in the Figure 2.21 and Table 2.3.

Transient photoluminescence spectra of all dendrimers in solution and neat film are shown in figure 2.20 and the lifetime is summarized in Table 2.2. From the studies, these dendrimer molecules display only prompt fluorescence with the short fluorescence lifetime (nanosecond) either the solution or neat film. Moreover, the G0DPP (**1**) and G1DPP (**2**) have shown a longer lifetime in solution state and a slight decrease when changing to the solid-state. In contrast, G2DPP (**3**) has a longer lifetime in solid-state. The reason could be due to that, the bulky molecule of G2 dendron leads to decrease π-stacked aggregation of the molecules in solid-state. Thus, the planarization of G2DPP (**3**) was decreased, exhibiting the longer fluorescence lifetimes (Ji et al., 2015).

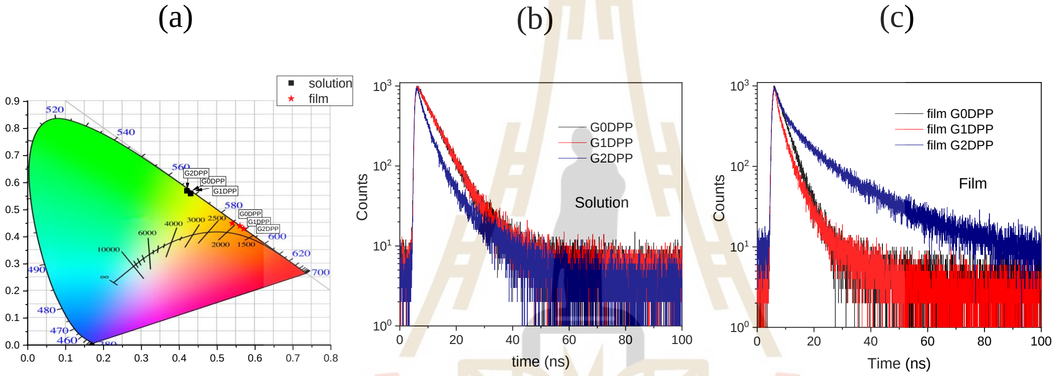
(a) (b) (c)

Figure 2.21 CIE Chromaticity Diagram (a), Photoluminescence decay spectra of DPP dendrimers in solution (b) and neat film (c).

Table 2.3 CIE, lifetime and quantum yield Data of the DPP dendrimers**.**

Compds	**CIE^{sol} (x,y) / CIE^{film} (x,y)**	**τ_{sol} / τ_{film} (ns)** ^{e}	**Φ_F^{sol} / Φ_F^{film}** ^{f}
G0DPP (**1**)	(0.43, 0.56)/(0.56, 0.44)	6.25/4.06	95.93/8.96
G1DPP (**2**)	(0.43, 0.56)/(0.54, 0.45)	6.40/4.39	94.04/4.48
G2DPP (**3**)	(0.42, 0.57)/(0.57, 0.43)	5.70/13.08	47.12/8.86

[e] Measured in toluene.

[f] Measured in toluene and as thin films.

2.4.3 Electrochemical properties

The redox properties of these Dendrimers and their HOMO and LUMO energy levels were investigated by cyclic voltammetry (CV) analysis. The measurements were carried out in CH_2Cl_2 solution containing 0.1 M n-Bu_4NPF_6 as supporting electrolyte using three-electrode systems under an argon atmosphere. The reference electrode was Ag/Ag^+. The results are shown in Figure 2.22 and summarized in Table 2.4. All dendrimers exhibit reversible oxidation processes upon the anodic sweep with a half potential of 1.23 and 1.47 for G0DPP (**1**), 1.15 and 1.52 for G1DPP (**2**), and 1.02, 1.20, and 1.50 for G2DPP (**3**). The HOMO levels of all these molecules calculated from the onsets of the oxidation potentials were -5.80, -5.50 and -5.38 eV, respectively. Moreover, they display two chemically reversible reduction with a half potential of -1.20 and -1.73 for G0DPP (**1**), -1.19 and -1.75 for G1DPP (**2**), and -1.18 and -1.77 for G2DPP (**3**). The LUMO levels of all these molecules calculated from the onsets of the reduction potentials were -3.33, -3.35, and -3.39 eV, respectively. The corresponding optical band gaps (E_g^{ele}) were 2.26, 2.14, and 1.99, respectively. The ratio between the peak current of the first reduction and the first oxidation of G0DPP (**1**) is almost 1, in which the potentials and reversibility of the redox peaks are similar to the reported molecules. We assume that the charge species are high stable lead to form the radical cation and anion during the redox process, and the second oxidation step generates a dicationic species. The two oxidation/reduction potentials assigned to the DPP residues. Furthermore, both of DPP dendrimers exhibit the redox potentials as same as G0DPP (**1**), however they display the third oxidation peak assigned to the dendron residues.

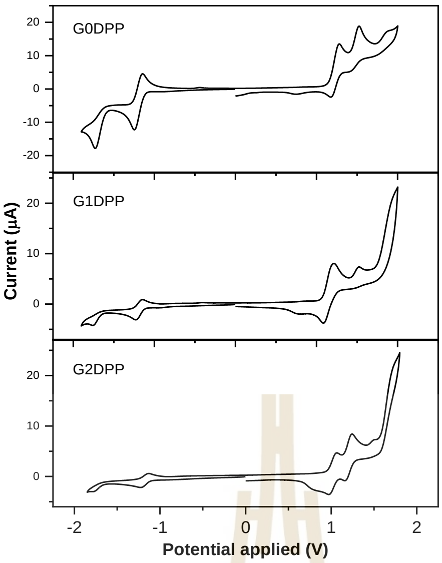

Figure 2.22 CV curves of DPP dendrimers in CH_2Cl_2 solution using 0.1 M Bu_4NPF_6 at a scan rate of 50 mV/s.

Table 2.4 Cyclic voltammetry, and theoretically calculated energy levels of DPP dendrimers.

Compounds	**$E^{ox}_{onset}/E^{red}_{onset}$ ^{g} (eV)**	**E_g^{ele} ^{h} (eV)**	**HOMO / LUMO ^{i} (eV)**
G0DPP (**1**)	1.14/-1.11	2.26	-5.58/-3.33
G1DPP (**2**)	1.06/-1.09	2.14	-5.50/-3.35
G2DPP (**3**)	0.94/-1.05	1.99	-5.38/-3.39

[g] Onset oxidation and reduction potentials versus Ag/Ag^+.

[h] Electrochemical band gaps determined using E^{ox}_{onset} - E^{red}_{onset}.

[i] Estimated from the onset oxidation and reduction potential using HOMO = $-E^{ox}_{onset}$ - 4.44 eV and LUMO = E^{red}_{onset} - 4.44 eV.

2.4.4 Thermal properties

The thermal properties of these dendrimers were determined by thermal gravimetric analysis (TGA) and differential scanning calorimetry (DSC) as shown in Figure 2.23. The results reveal that all molecules exhibit high thermal stability with the decomposition temperatures at 5% weight loss (T_{5d}) of 356, 409, and 432°C, for G0DPP (**1**), G1DPP (**2**), and G2DPP (**3**), respectively.

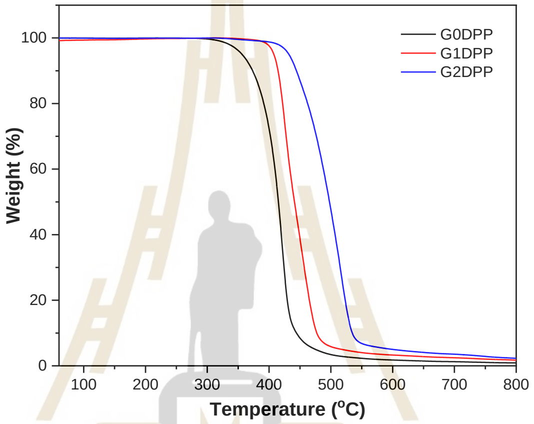

Figure 2.23 TGA curves of G0DPP (**1**), G1DPP (**2**), and G2DPP (**3**) with heating rate of 10◦C/min under a nitrogen atmosphere.

2.4.5 Electroluminescence properties

In order to investigate the electroluminescence properties of G_nDPP dendrimers, OLED devices were fabricated with the following device structure: indium tin oxide (ITO)/PEDOT:PSS/mCP or mCBP (20nm)/EML(20 nm)/Bphen(20 nm)/LiF(0.5 nm):Al(150 nm), where these materials were used as the emitting layer (EML) as shown in Figure 2.24. Conductive polymer poly(3,4-ethylenedioxy thiophene): poly(4-styrenesulfonate) (PEDOT: PSS) as hole injection layer, 1,3-bis(N-carbazolyl) benzene (mCP) or 3,3-di(9H-carbazol-9-yl)biphenyl (mCBP) as hole transporting layer, and 4,7-Diphenyl-1,10-phenanthroline (Bphen) or 3-(4-Biphenyl)-

4-phenyl-5-*tert*-butylphenyl-1,2,4-triazole (TAZ) as hole-blocking layer were also used to enable high-performance devices. The electroluminescence spectra (EL) of all dendrimers doped in 3% mCP showed similar features with their fluorescence spectra without the emission of the host materials as shown in Figure 2.24.

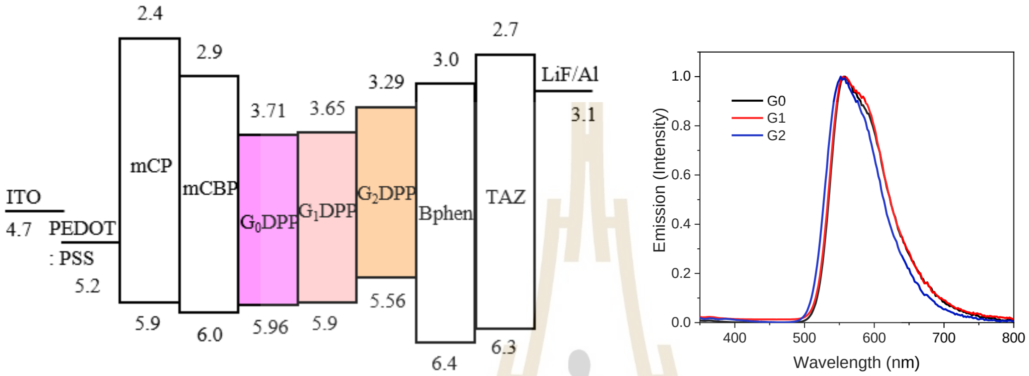

Figure 2.24 Schematic energy diagram and electroluminescence spectra of all dendrimers doped in 3% mCP.

The quantum yield of these dendrimers in neat film and doped mCP and mCBP film with the blending ratio ranging from 1%wt to 2%wt are summarized in Table 2.5. The layers were spin-coated from a $CHCl_3$/toluene (1:1) solution with controlled thickness. The neat film of these molecules either 1 wt% or 2wt% shows a low quantum yield. However, the doped film with mCP and mCBP induce to reach a higher yield. Moreover, the doped film with 1 wt% of mCP of all these compounds shows the highest quantum yield, thus mCP is used as hole transporting layer in the device.

Table 2.5 Quantum yield of DPP dendrimers in neat film and doped film.

QY / Compds	Neat film		Doped with mCP		Doped with mCBP	
	2 wt%	**1 wt%**	**2 wt%**	**1 wt%**	**2 wt%**	**1 wt%**
G0DPP (**1**)	8.96	5.29	21.07	50.09	28.26	46.68
G1DPP (**2**)	4.48	3.44	64.87	57.45	37.75	49.41
G2DPP (**3**)	8.86	5.14	39.43	53.03	47.24	41.31

Normally, the diketopyrrolopyrrole (DPP) core is non-soluble in a most organic solvent, therefore the dendron substituents are introduced to the designed molecules in order to improve the solubility of these molecules. These dendrimers exhibit high solubility in most organic solvents allowing their thin films to be fabricated by a solution casting process, thus overcoming the high cost of the vacuum deposition process. The morphology of the spin-casting films, which is another key factor for the OLED fabrication, was examined by atomic force microscopy (AFM). The AFM images of all thin films spin-coated from the $CHCl_3$/toluene (1 : 1) solution show a smooth surface indicating excellent films forming properties (Figure 2.25). The AFM image of the thin film of G1DPP (**2**) blends with mCP shows a very uniform and smooth surface with the root mean square roughness (RMS) of 0.29 nm, indicating excellent film-forming properties. Furthermore, the surface of the spin-coated film of the G0DPP (**1**) and G2DPP (**3**) blends with mCP have a more surface roughness with RMS of 0.47 and 0.48 nm. This suggests that G1DPP (**2**) form a more homogeneously distributed morphology when mixed with mCP, which provides enhanced exciton dissociation (Más-Montoya and Janssen, 2017).

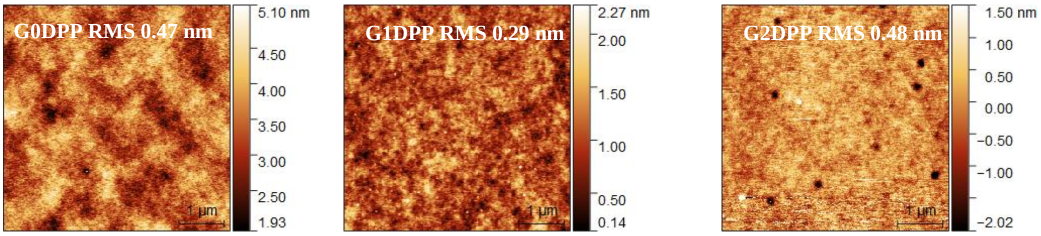
G0DPP RMS 0.47 nm
5.10 nm
4.50
4.00
3.50
3.00
2.50
1.93
1 μm
G1DPP RMS 0.29 nm
2.27 nm
2.00
1.50
1.00
0.50
0.14
1 μm
G2DPP RMS 0.48 nm
1.50 nm
1.00
0.50
0.00
−0.50
−1.00
−2.02
1 μm

Figure 2.25 Tapping mode AFM images of the spin-coated films.

The multi-layer devices using G$_n$DPP dendrimers as EMLs with the structure of ITO/PEDOT:PSS//mCP (20nm)/EML(20 nm)/Bphen or TAZ(20 nm)/LiF(0.5 nm):Al(150 nm) were fabricated. The solution-processed of G0DPP (**1**), G1DPP (**2**), and G2DPP (**3**) OLEDs emit yellow light with the λ_{max}^{EL} around 550 nm. No emission shoulder at a longer wavelength due to excimer and exciplex species formed at the interface of the EML and ETL layers, which often occurs in devices fabricated from EMLs with a planar molecular structure, is detected. The CIE coordinates of the emitted lights are (0.407, 0.485) for the G0DPP (**1**)-based OLED (device IV), (0.415, 0.483) for the G1DPP (**2**)-based OLED (device V) and (0.408, 0.510) for the G2DPP (**3**)-based OLED (device VI). The spin-coated multi-layer OLED using G1DPP (**2**) (device V) as the EML exhibits a massive improvement in the device performance compared to its multi-layer without PVK (device I) with a L_{max} of 1993 cd m^{-2}, V_{max} of 9.4 cd m^{-2}, J_{max} of 96 mA/cm^{2}, and EQE$_{max}$ of 2.90.

Device results with Bphen

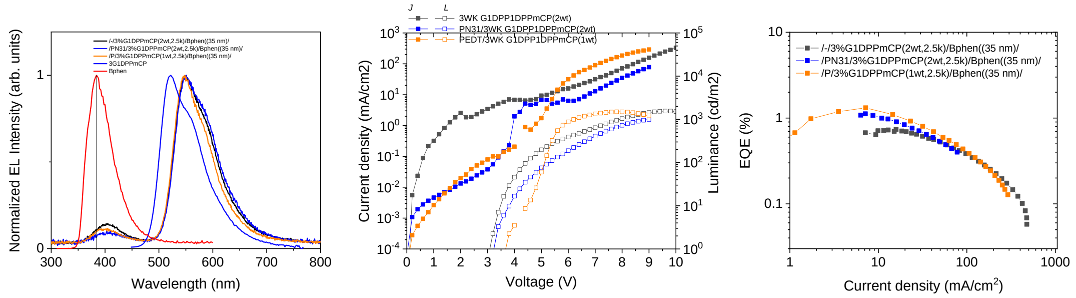

Device results with TAZ

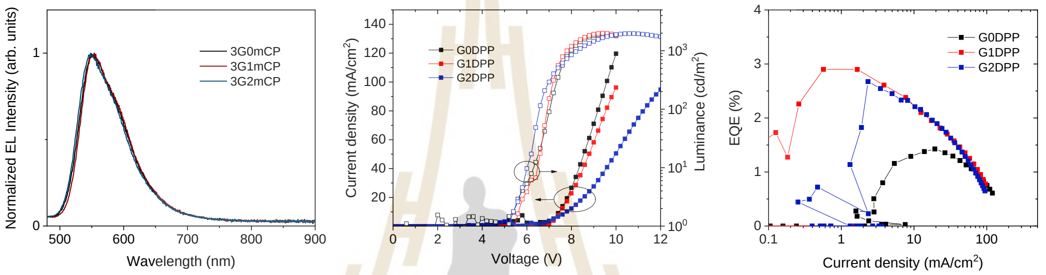

Figure 2.26 Plots of EL spectra of the OLEDs, current density–luminance–voltage (*J*–*V*–*L*), and external quantum efficiency (EQE) of the devices

Table 2.6 Device characteristics of OLEDs.

Device [a]	**HTL**	**EML**	**ETL**	λ^{EL}_{max} **(nm)**	V_{on} [b] **(V**	L_{max} [c] **(cd/m^{2}V)**	V_{max} [d] **(V)**	J_{max} [e] **(mA/cm^2)**	**CE** [f]	**%EQE$_{max}$** [g] **/V**	**CIE$_{xy}$**
I	mCP 2wt	G1DPP	Bphen	550	3.1	1557	9.6	476	-	0.74/6.0	(0.427, 0.529)
II	PN31/mCP 2wt	G1DPP	Bphen	551	3.2	997	9.0	78	-	1.12/6.4	(0.439, 0.529)
III	PVK/mCP 1wt	G1DPP	Bphen	548	3.6	1495	7.8	291	-	1.31/5.4	(0.416, 0.546)
IV	PVK/mCP 1wt	G0DPP	TAZ	554	5.0	1898	9.4	120	4.12	1.43/7.8	(0.407, 0.485)
V	PVK/mCP 1wt	G1DPP	TAZ	554	5.4	1993	9.4	96	9.26	2.90/6.8	(0.415, 0.483)
VI	PVK/mCP 1wt	G2DPP	TAZ	548	5.2	1965	10.6	95	8.92	2.67/6.8	(0.408, 0.510)
VII	PN31/mCP 1wt	G0DPP	TAZ	552	4.7	410	10.4	36	2.3	0.84/8.8	(0.409, 0.474)
VIII	PN31/mCP 1wt	G1DPP	TAZ	552	4.2	1803	10.2	102	4.99	1.61/7.8	(0.413, 0.483)
IX	PN31/mCP 1wt	G2DPP	TAZ	549	3.9	1728	11.0	62	3.86	1.22/9.4	(0.412,0.510)

[a] ITO/PEDOT:PSS/HTL/EML/ETL/LiF:Al. [b] Turn-on voltages at 1 cd m^{-2}. [c] Maximum luminance at applied voltage. [d] Voltage (V) at maximum luminance. [e] Current density at maximum luminance. [f] Current efficiencies. [g] Maximum external quantum efficiency.

2.5 Conclusion

In summary, the synthesis of diketopyrrolopyrrole carbazole dendrimers for OLED has been succeeded. By using the alkyl group linked to the DPP core, we are able to obtain the high solubility of the emitters. Increasing the generation of the carbazole dendrimers (1st and 2nd generations) as a scaffold, we retain the high emissive ability and reduce the π-π stacking interaction of DPP fluorophore as well as improve amorphous glass-forming ability, solution processability and thermal stability of the material. The G1DPP (**2**) exhibit a strong red emission with thermal stability (T_{5d} 411°C). These results revealed that G1DPP (**2**) is promising as red emitter for high-efficiency OLEDs with much simpler device architecture. We believe that our results could provide useful guidance to decorate the highly efficient but planar fluorophore to be suitable for applications in OLEDs devices.

CHAPTER III

THE SYNTHESIS AND CHARACTERIZATION OF NOVEL THERMALLY ACTIVATED DELAYED FLUORESCENCE MATERIALS FOR ORGANIC LIGHT-EMITTING DIODES

3.1 Introduction

Organic light-emitting diodes (OLEDs) are widely used in almost every kind of display such as mobile phones, television, cameras, watch, and wearable devices. Although the OLEDs have a lot of benefits whether it be flexible, thin, and small in size hence are very easy to manufacture OLED displays, but these materials have some weak points such as a shorter lifetime, easily damaged by water, and can be degraded by light. The limited lifetime of the organic materials is the biggest technical problem of OLEDs. The study of the stability of red, green and blue phosphorescent OLED emitters revealed that the photodegradation rate of blue emitters is higher than red and green emitters, thus the lifetime of a blue emitter is shorter than the red and green emitter (Schmidbauer, Hohenleutner, and Konig, 2013). A short lifetime leads to the low efficiency of OLED, red (625 nm), green (530 nm) and blue (430 nm) diodes exhibit an external quantum efficiency value of 20%, 19%, and 4% to 6%, respectively (Bagher, 2014). Therefore, the research for investigating efficient blue emitter as well as deep blue color is required.

Generally, fluorescence materials can harvest only 25 % of singlet exciton under electrical excitation, so the external EL efficiencies (η_{EL}) are intrinsically limited to approximately 5% (A. Endo et al., 2009). On the other hand, OLEDs that use phosphorescent materials such as Ir and Pt complexes can harvest both singlet and triplet exciton and achieved $\eta_{exciton}$ of almost 100% (Kawamura et al., 2005).

However, phosphorescent materials containing heavy metals are rather expensive and unsustainable. Besides that, the toxicity of heavy metal effect the environmental. Therefore, since both fluorescence- and phosphorescence-based OLEDs have both advantages and disadvantages, the use of a novel light-emitting mechanism has been hoped for to avoid the shortcomings.

In 2008, Baleizao and Berberan-Santos reported the second mechanism for fluorescence from fullerenes, which is called thermally activated delayed fluorescence (TADF). The results reveal that the photophysical properties of fullerene C_{70} exhibited the strong TADF characteristic, the small ΔE_{ST} gap, and the long intrinsic phosphorescence lifetime, especially triplet formation (Φ_T) very close to 1 (Baleizao and Berberan-Santos, 2008). After that, Adachi and co-worker proposed a mechanism to enable internal electroluminescence quantum efficiency (η_{int}) 100% without using phosphorescent materials by using reverse intersystem crossing (RISC) from triplet (T_1) to singlet excited states (S_1) as shown in Figure 3.1 (A. Endo et al., 2009).

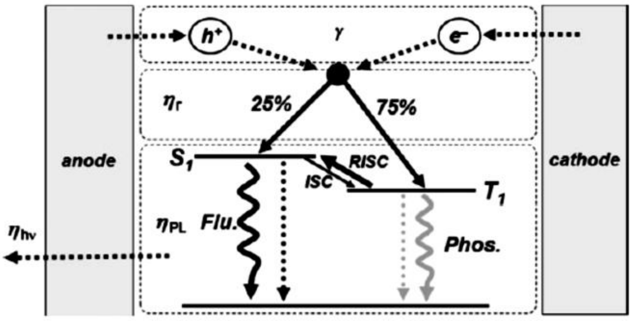

Figure 3.1 Schematic view of the reverse intersystem crossing mechanism.

When applied an electrical across two-electrode of OLED, which consists of cathode and anode. Electrical charge carriers of both polarities were injected into the organic layers originated electrons and holes. The electrons and holes transport and recombination produced light. Because exciton formation under electrical excitation results in 25% singlet excitons and 75% triplet excitons, internal electroluminescence quantum efficiency (η_{int}) 100% was obtained by converse from triplet excitons to singlet excitons via RISC, so small the energy gap of the RISC (ΔE_{ST}) is required as shown in Figure 3.2. Moreover, the lifetime of the triplet excitons has too long enough. Normally, ΔE_{ST} is proportional to the exchange energy between the highest occupied molecular orbital (HOMO) and the lowest unoccupied molecular orbital (LUMO) in the molecules, thus a small ΔE_{ST} can be achieved by separating the HOMO from the LUMO because the exchange energy decreases exponentially with increasing HOMO-LUMO (electron-hole) separation distance (Goushi, Yoshida, Sato, and Adachi, 2012).

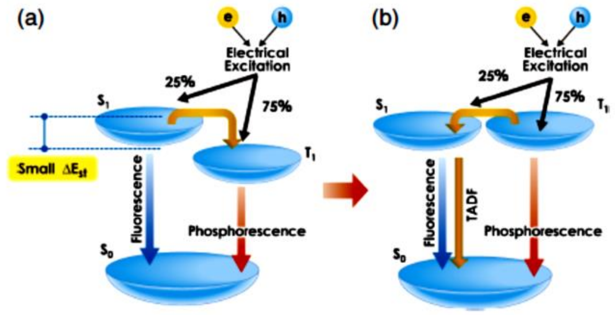
(a)
e
h
Electrical Excitation
25%
75%
S_1
T_1
Small ΔE_{st}
Fluorescence
Phosphorescence
S_0
(b)
e
h
Electrical Excitation
25%
75%
S_1
T_1
Fluorescence
TADF
Phosphorescence
S_0

Figure 3.2 Energy alignment of singlet and triplet energy levels to achieve efficient TADF (Adachi, 2014).

In this chapter, we design the TADF molecules composed of donor-acceptor-donor (D-A-D) systems in order to spatial separated HOMO and LUMO to minimize the exchange integrals between the two orbitals. The best method for separating the spatial distribution of HOMO of donor and LUMO of the acceptor is to use the twisted molecule as the bridge between the donor and the acceptor moieties. Due to, the twist angle between the donor and acceptor planes increased lead to a decrease in the energy gap. However, a large twist angle generally suppresses the intensity of fluorescence decay and leads to a decrease in the internal EL efficiency of the devices (Rajamalli et al., 2016). Therefore, the donor-acceptor-donor (D-A-D) system was designed for reducing the ΔE_{ST} and retain intramolecular space interaction. We expect that the desired molecules with TADF character can be used as emitters in the emitting layer of an OLED to achieve high external EL efficiencies (η_{EL}), high-performance in flexibility over a large area, low-cost fabrication, and high optical and electrical properties.

The thermally activated delayed fluorescence which is previously named as E - type delayed fluorescence was believed to discover from the eosin dye (**78**) in 1961

(Parker and Hatchard, 1961). It is the first purely organic TADF material, the molecular structure is shown in Figure 3.3.

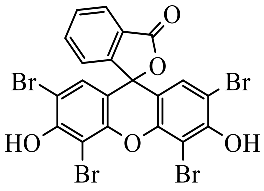

Figure 3.3 The molecular structure of the eosin dye (**78**).

In 1980, the first metal-containing TADF material has been reported. The molecular structure is shown in Figure 3.4. The luminescence spectra and decay tunes of the emission of *bis* (triphenylphosphine) phenanthroline copper (I) ion (**79**) have been measured in liquid helium. The long decay time at low temperatures is interpreted in terms of the triplet level of the charge- transfer state (Blasse and McMillin, 1980).

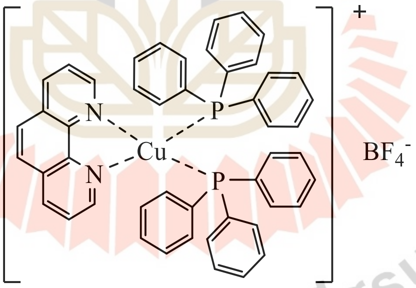

Figure 3.4 The molecular structure of the *bis* (triphenylphosphine) phenanthroline copper (I) (**79**).

In 1996, the delayed thermal fluorescence was founded in fullerenes, owing to this mechanism induced the fluorescence quantum yield of C_{70} increases by one or two orders of magnitude (from $\Phi_F = 5 \times 10^{-4}$ up to $\Phi_F = 0.08$) (Berberan-Santos and Garcia, 1996). After that, in 2008 the fullerene C_{70} was used as the temperature and oxygen sensors (Baleizao and Berberan-Santos, 2008).

In 2009, the new TADF materials were reported as the emitter in OLED devices. Six complexes of tin(IV) fluoride-porphyrin (SnF$_2$-porphyrin) are octaethylporphine (OEP), etioporphyrin I (Etio I), hematoporphyrin IX (Hemato IX), protoporphyrin IX (Proto IX), mesoporphyrin IX (Meso IX), and Copro III as shown in Figure 3.5. These SnF$_2$-porphyrin complexes exhibited a rather strong TADF at room temperature and displayed an increase in fluorescence intensity with increasing temperature (A. Endo et al., 2009).

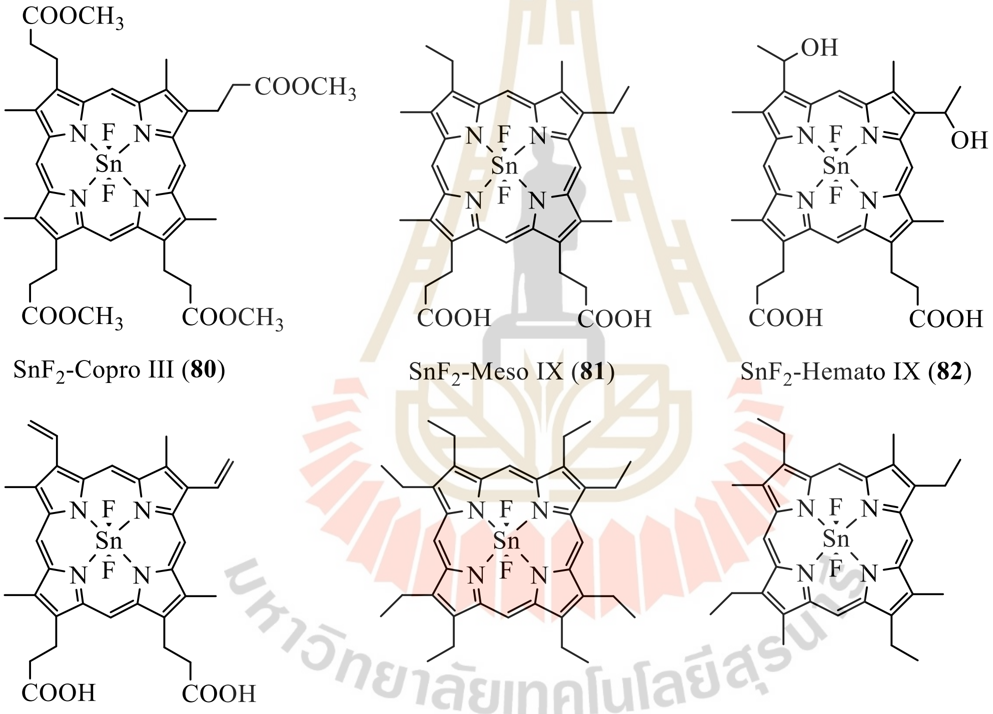

SnF$_2$-Copro III (**80**) SnF$_2$-Meso IX (**81**) SnF$_2$-Hemato IX (**82**)

SnF$_2$-Proto IX (**83**) SnF$_2$-OEP (**84**) SnF$_2$-Etio I (**85**)

Figure 3.5 Molecular structures of the six Sn(IV)-porphyrin complexes **80-85**.

After successfully synthesizing the TADF materials, this approach is a general concept for designed the fluorescence materials to provide OLEDs with high EL efficiency. The variety of TADF molecules can be designed and synthesized rationally, which are discussed as follow;

In 2011, the purely aromatic compounds, 2-biphenyl4,6-bis(12-phenylindolo[2,3-a]carbazole-11-yl -1,3,5triazine (PIC-TRZ) (**86**) that exhibit highly efficient TADF have been reported. The molecules containing an indolocarbazole donor unit and a triazine acceptor unit in which the introduction of bulky groups leads to occur steric hindrance effect that can distort π-conjugation. The highest occupied molecular orbital (HOMO) and lowest unoccupied molecular orbital (LUMO) orbitals can be located around donor and acceptor moieties, respectively, leading to a small ΔE_{ST} (0.11 eV). The molecular structure of PIC-TRZ (**86**) is shown in Figure 3.6 (Ayataka Endo et al., 2011).

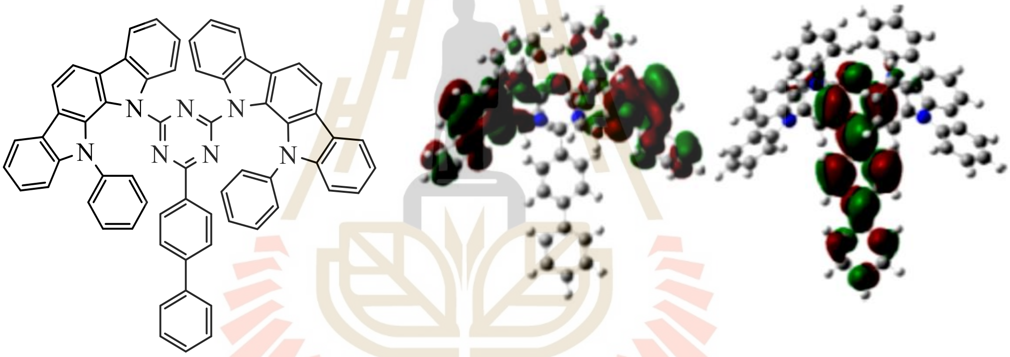

PIC-TRZ (**86**) **HOMO** **LUMO**

Figure 3.6 Molecular structure of PIC-TRZ (**86**) and its HOMO and LUMO calculated by Gaussian 03.

The exciplex between *m*-MTDATA (**87**) and ^{t}Bu-PBD (**88**) was used as an emitter in EML of the OLED device. They show a very high RISC of 86.5% between triplet and singlet excited states. OLEDs device made using *m*-MTDATA as the donor material and 3TPYMB (**89**) as the acceptor material produced the external quantum efficiencies of 5.4% (Goushi et al., 2012). The molecular structures and formation of exciplex state between m-MTDATA and 3TPYMB are depicted in Figure 3.7.

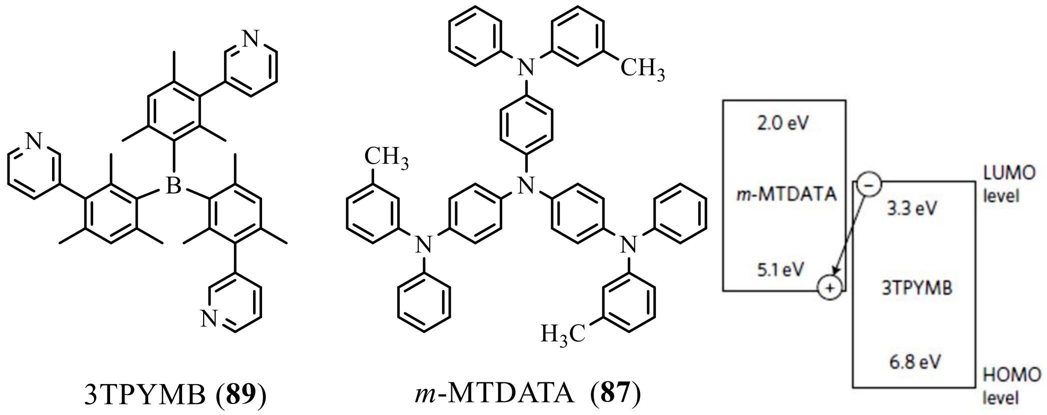

3TPYMB (**89**)

m-MTDATA (**87**)

Figure 3.7 The molecular structures and formation of exciplex state between m-MTDATA (**87**) and 3TPYMB (**89**).

The several TADF materials have been designed and synthesized based on the D-A system such as the spirobifluorene derivatives, spiro-acridine (ACRFLCN) derivatives, phenoxazine (PXZ) derivatives, carbazolyl dicyanobenzene (CDCB) derivatives, thioxanthone (TX) derivatives. The external quantum efficiency of OLED devices made from these TADF materials was in the range of 4-21% (Nakagawa, Ku, Wong, and Adachi, 2012), (Mehes, Nomura, Zhang, Nakagawa, and Adachi, 2012), (Uoyama, Goushi, Shizu, Nomura, and Adachi, 2012; Wang et al., 2014; X. Wei et al., 2017). Their molecular structures are shown in Figure 3.8.

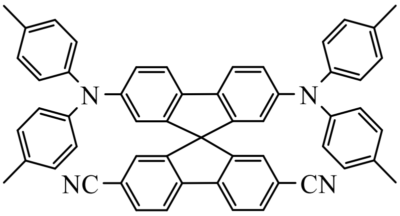

Spirobifluorene derivative (**90**)

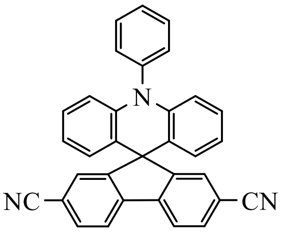

ACRFLCN (**91**)

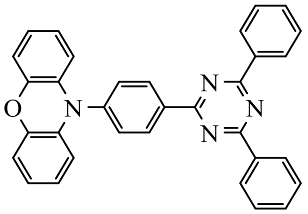

PXZ-TRZ (**92**)

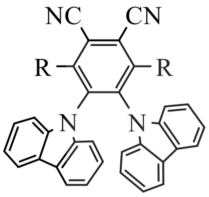

4CzPN (**93**): R = carbazoyl
2CzPN (**94**): R = H

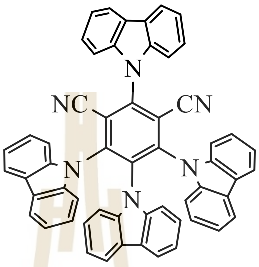

4CzIPN (**95**)

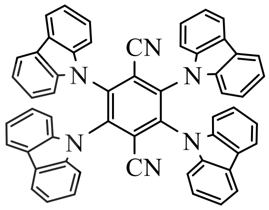

4CzTPN (**96**): R = H
4CzTPN-Me (**97**): R = Me
4CzTPN-Ph (**98**): R = Ph

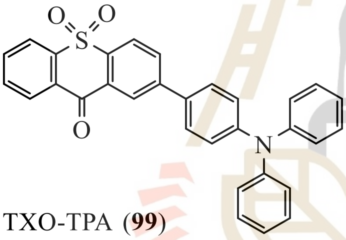

TXO-TPA (**99**)

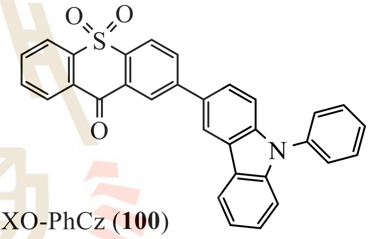

TXO-PhCz (**100**)

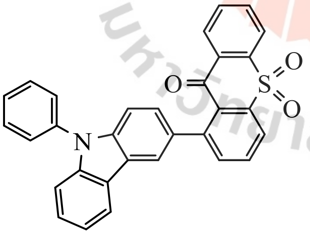

TXO-PhCz1 (**101**)

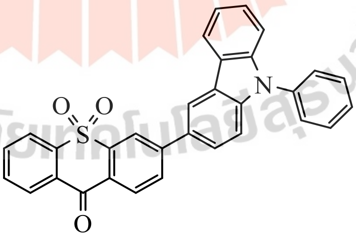

TXO-PhCz3 (**102**)

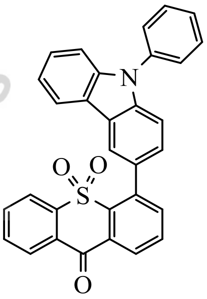

TXO-PhCz4 (**103**)

Figure 3.8 The molecular structures of TADF molecules (**90-103**).

The TADF materials, which containing diphenylsulfone as an acceptor moiety and carbazoyl groups as a donor moiety with the donor-acceptor-donor (D-A-D) system have been reported since 2012 by Adachi et al. Diphenylsulfone (DPS) is widely studied acceptor in the literature because its electron-withdrawing ability and a twist angle in the center with tetrahedral geometry structure, which limits the conjugation of the compounds, provides promising features for TADF material. The first pure blue emission with a diphenylsulfone derivatives was reported. The structure of DPA-DPS (**104**), DTPA-DPS (**105**), and DTC-DPS (**106**) were containing two arylamine derivatives as donor moieties and diphenylsulfone as an acceptor. Their structures are shown in Figure 3.9 (Q. Zhang et al., 2012). The OLED devices based on these compounds exhibited a very high external quantum efficiency (EQE) of nearly 10% at low current density with bright pure blue emission. The studies reveal that (**104**), DTPA-DPS (**105**), and DTC-DPS (**106**) display small ΔE_{ST} values of 0.54, 0.45, and 0.32 eV, respectively. Owing to the *tert*-butyl group on the diphenylamine unit enhances the electron-donating ability leads to lowers the CT energy and the ΔE_{ST}. Moreover, the replacement of a diphenylamine unit with a carbazole unit slightly raises the ^{1}CT state, and raises the $^3\pi\pi^*$ state, resulting in a further decrease in its ΔE_{ST}.

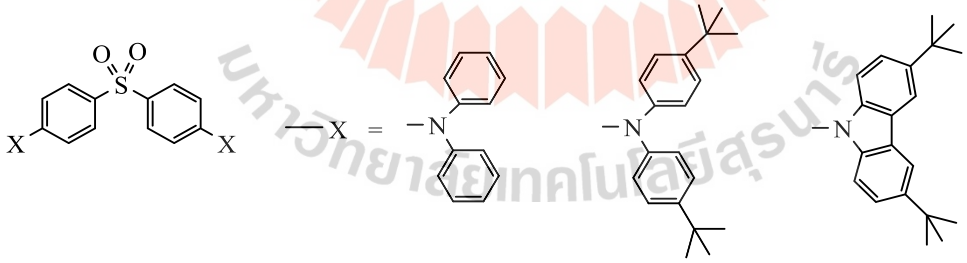

DPA-DPS (**104**) DTPA-DPS (**105**) DTC-DPS (**106**)

Figure 3.9 The molecular structures of diphenyl sulfoxide derivatives.

The concept to reduce the ΔE_{ST} is to enhance the electron-donating ability of the donor moieties by added the *tert*-butyl group into the molecules, so the more electron-rich methoxy groups were used to replace the *tert*-butyl substituents on the carbazole donors. The deep blue TADF material, *bis*[4-(3,6-dimethoxycarbazole)phenyl]sulfone (DMOC-DPS (**107**)) has been synthesized. The results reveal that significantly decreases the ΔE_{ST} from 0.32 eV for DTC-DPS (**105**) to 0.21 eV for DMOC-DPS (**107**) in a doped film. The OLED device exhibited a turn-on voltage at 4.0 V, a maximum EQE of 14.5%, CIE coordinate of (0.16, 0.16). The molecular structures of DTC-DPS (**29**) and DMOC-DPS (**107**), HOMO and LUMO distribution of DMOC-DPS (**107**) is depicted in Figure 3.10 (Wu et al., 2014).

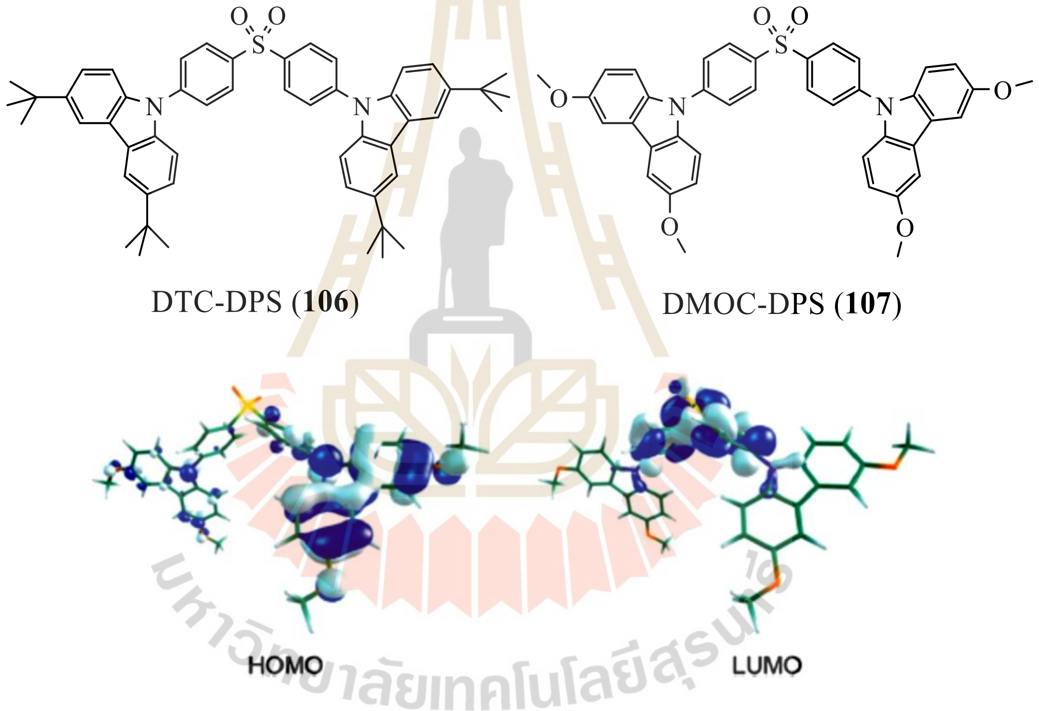

DTC-DPS (**106**) DMOC-DPS (**107**)

Figure 3.10 The molecular structures of DTC-DPS (**106**) and DMOC-DPS (**107**), and their HOMO and LUMO distribution.

After that, the blue OLED containing a 9,10-dihydroacridine/diphenylsulphone derivative have been designed and synthesized. The OLED devices were fabricated and revealed a high external quantum efficiency of 19.5% and reduced efficiency roll-off characteristics at high luminance. The molecules were designed as chare transfer (CT) molecules with the D-A type molecules and D-A-D-type molecules. D-A type molecules consist of 5-phenyl-5,10-dihydrophenazine (PPZ) as a donor unit and different acceptor units of 2,5-diphenyl-1,3,4-oxadiazole (DPO) and 3,4,5-triphenyl-1,2,4-triazole (TPT). Moreover, the D-A-D-type molecules consist of diphenylsulphone (DPS) as an acceptor and different donor units of PPZ, phenoxazine (PXZ) and 9,9-dimethyl-9,10-dihydroacridine (DMAC). The results revealed that the large twisted intramolecular charge transfer molecules can emit an efficient and short lifetime when the emission peak energy is high enough and the lowest locally excited triplet state (^{3}LE) state is higher than the ^{3}CT state. The molecular structures of all compounds are presented in Figure 3.11 (Q. Zhang et al., 2014).

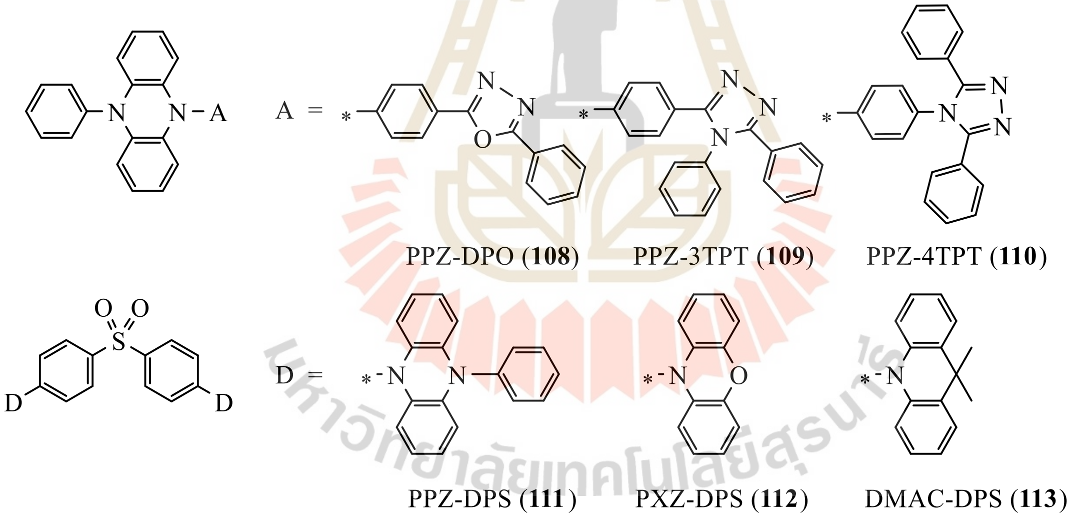

Figure 3.11 The molecular structures of the investigated compounds.

Divinyl sulfides and sulfones derivatives with the D-π-A system have been synthesized by using a Wittig-Horner reaction. The intramolecular charge transfer (ICT) occurs from the combination of the electron from the carbazole moiety (D) and sulfone acceptor (A) which connected by a π-linker leads to obtaining a large Stokes' shift, which behaves like a “push-pull” architecture. Owing to the D-π-A-π-D structure of these materials separated the charge in the ground and excited-state provides them with unique optical and electrical properties. These novel molecules represent an efficient alternative as stable non-heterocyclic π-conjugated compounds for potential applications as photoactive or two-photon absorption chromophores. The molecular structures of all compounds are presented in Figure 3.12 (Monçalves, Rampon, Schneider, Rodembusch, and Silveira, 2014).

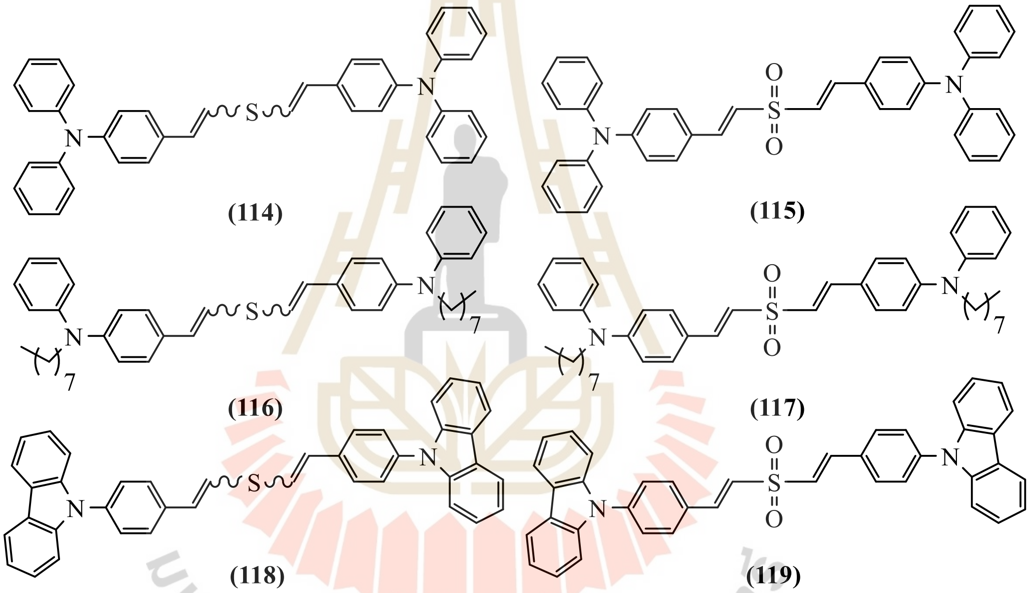

(114) **(115)** **(116)** **(117)** **(118)** **(119)**

Figure 3.12 The molecular structures of the desired compounds (**114-119**).

Novel TADF emitters containing diphenylsulphone (DPS) as an electron acceptor and spiro[acridine-9,90fluorene] (ACFL) and spiro[acridine-9,90-xanthene] (ACXA) as electron donors have been reported. Their electronic and optical properties were investigated theoretically for an OLED. The calculated ΔE_{ST} values of ACFL-DPS and ACXA-DPS of 0.012 and 0.014 eV, respectively. The OLED device based on ACXA-

DPS as emitter showed a small ΔE_{ST} with an emission wavelength of 2.802 eV (442 nm). Their molecular structures are presented in Figure 3.13 (Lee and Kim, 2016a).

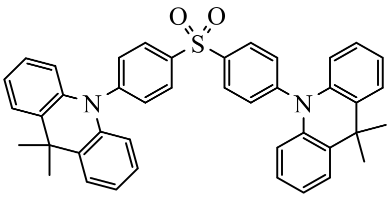
DMAC-DPS (**113**)

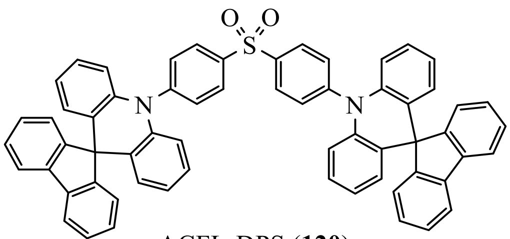
ACFL-DPS (**120**)

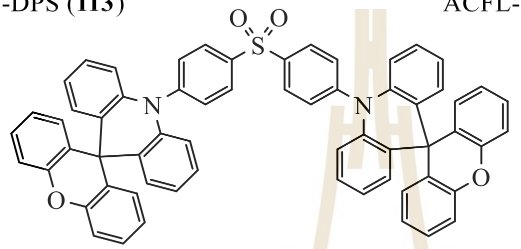
ACXZ-DPS (**121**)

Figure 3.13 The molecular structures of DPS derivatives.

The novel TADF was designed and synthesized by replaced the methoxy group of DMOC-DPS to tetra-methyl in the 1, 3, 6, and 8 positions of carbazolyl group in order to enhance the TADF efficiency. The results revealed that the calculated ΔE_{ST} of TMC-DPS (**122**) (0.094 eV) was smaller than DMOC-DPS (**107**) (0.386 eV) due to the two methyl groups in the 1,8 positions of carbazole ring working to maintain a large dihedral angle through steric repulsion. Both materials showed an emission wavelength of 439.9 nm (2.82 eV), but TMC-DPS (**122**) exhibited the TADF OLED character because of its small ΔE_{ST} and large dihedral angle. The chemical structures and the schematic energy diagram of these materials are shown in Figure 3.14 (Lee and Kim, 2016b).

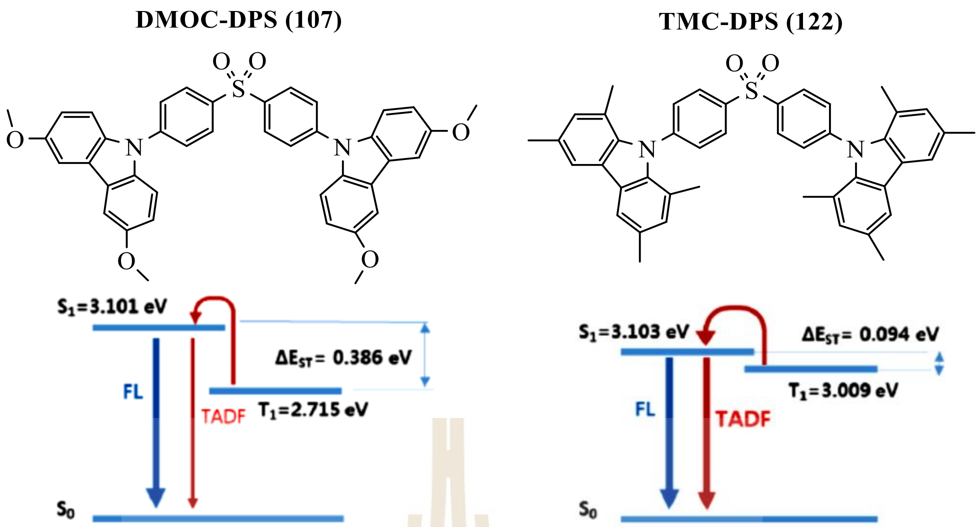
DMOC-DPS (107)
TMC-DPS (122)
S_1=3.101 eV
ΔE_{ST}= 0.386 eV
FL
TADF
T_1=2.715 eV
S_0
S_1=3.103 eV
ΔE_{ST}= 0.094 eV
T_1=3.009 eV
FL
TADF
S_0

Figure 3.14 The chemical structures and the schematic energy diagram of DMOC-DPS (**107**) and TMC-DPS (**122**).

The blue TADF materials for OLED which containing of *bis*(phenylsulfonyl) benzenes (BPSBs) as acceptor core and the different donor were reported. The introduction of alkyl groups or *ortho*-substituted and thus twisted, sterically demanding diphenylamine donors in order to increase the solubility of these compounds. Solution-processed OLEDs were fabricated by using these compounds as an emitter in the EML lead to deep blue emission from 466 to 436 nm with a low CIE_y value of 0.08, reach brightnesses of 10000 cd/ m^2, and also show efficiencies of 1000 cd/m^2. The chemical structures of these materials are shown in Figure 3.15 (Jürgensen et al., 2017).

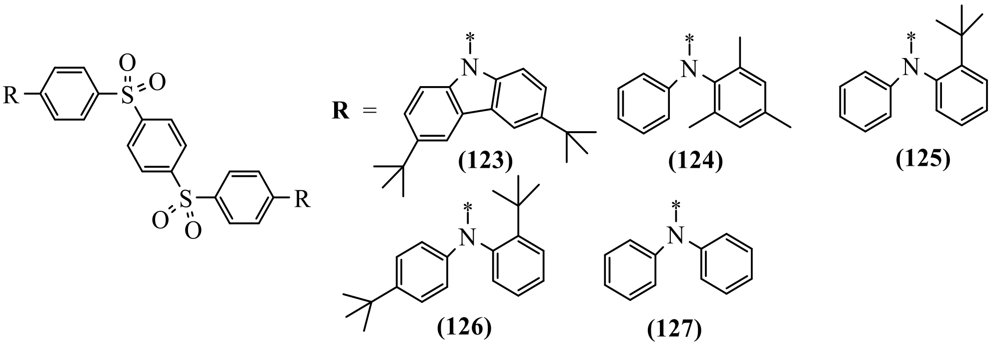
R =
(123)
(124)
(125)
(126)
(127)

Figure 3.15 The chemical structures of the BPSB derivatives (**123-127**).

TADF materials containing dipyridylsulfone core as the electron-accepting unit and di-tert-butyl carbazoles as electron-donating units, *p*DTCz-2DPyS (**128**) and *p*DTCz-3DPyS (**129**) have been reported. Both emitters show blue emission in the range of 450–465 nm with a similar ΔE_{ST} (0.22 eV for *p*DTCz-3DPyS (**129**) and 0.21 eV and *p*DTCz-2DPyS) (**128**). The delayed emission of *p*DTCz-2DPyS (**128**) is higher than *p*DTCz-3DPyS (**129**). In the doped films, *p*DTCz-2DPyS (**128**) exhibited photoluminescence quantum yields of 60%. The EQE of *p*DTCz-2DPyS (**128**) and *p*DTCz-3DPyS (**129**) when doped in *bis*[2-(diphenylphosphino) phenyl]ether oxide (DPEPO) was 13.4% and 11.4%, respectively, which is higher than the reference *p*DTCz-DPS (4.6%). Moreover, *p*DTCz-3DPyS (**129**) shows pure blue electroluminescence with CIE color coordinates of (0.15, 0.12) compared to *p*DTCz-2DPyS (**128**) with coordinates of (0.15, 0.19). The molecular structure of *p*DTCz-2DPyS (**128**) and *p*DTCz-3DPyS (**129**) are shown in Figure 3.16.

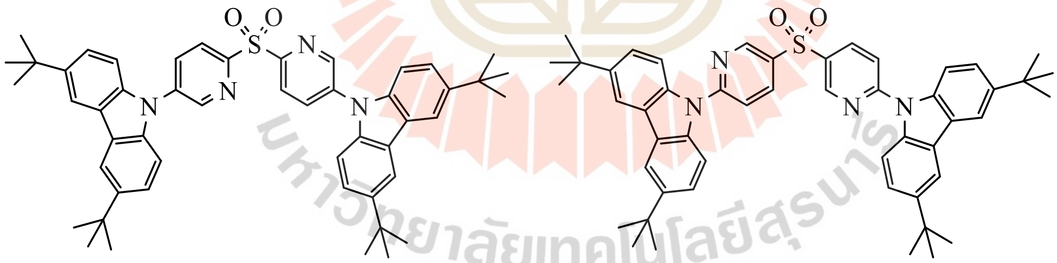

*p*DTCz-2DPyS (**128**) *p*DTCz-3DPyS (**129**)

Figure 3.16 The molecular structures of *p*DTCz-2DPyS (**128**) and *p*DTCz-3DPyS (**129**).

The thermally activated delayed fluorescence (TADF) emitters are extensively developed because of their potential as high-efficiency emitter with near 100% internal quantum efficiency for high performance organic light-emitting diodes. From the above review, there are several strategies to design and synthesized TADF materials to improve the performance and efficiency of OLED devices base on these compounds. The one concept is used D-π-A-π-D system which behaves like a “push-pull” architecture to obtain a small ΔE_{ST} and separated The HOMO and LUMO. In this chapter, novel TADF emitters based on D-π-A-π-D system of *bis*(4-carbazolephenyl) sulfone were designed and synthesized which compose of carbazole derivatives as the donor, benzene as the π-linker, and sulfone as the acceptor. The effect of electron-donating ability on TADF property was investigated by varying the donor moieties which linked on the phenyl π-linker. The effect of free rotation of π-linker on TADF property was investigated by a varying number of phenyl substituents on the π-linker. The photophysical, electrochemical, and delayed fluorescence properties of these materials were characterized by UV-vis, CV, and time-resolved fluorescence spectroscopic analyses.

3.2 Research objectives

3.2.1 To design, synthesize and characterize TADF materials for OLED as shown in Figure 3.17.

3.2.2 To study the photophysical, electrochemical, and thermal properties by using UV-Visible spectroscopy, fluorescence spectroscopy, cyclic voltammetry, and DSC-TGA techniques.

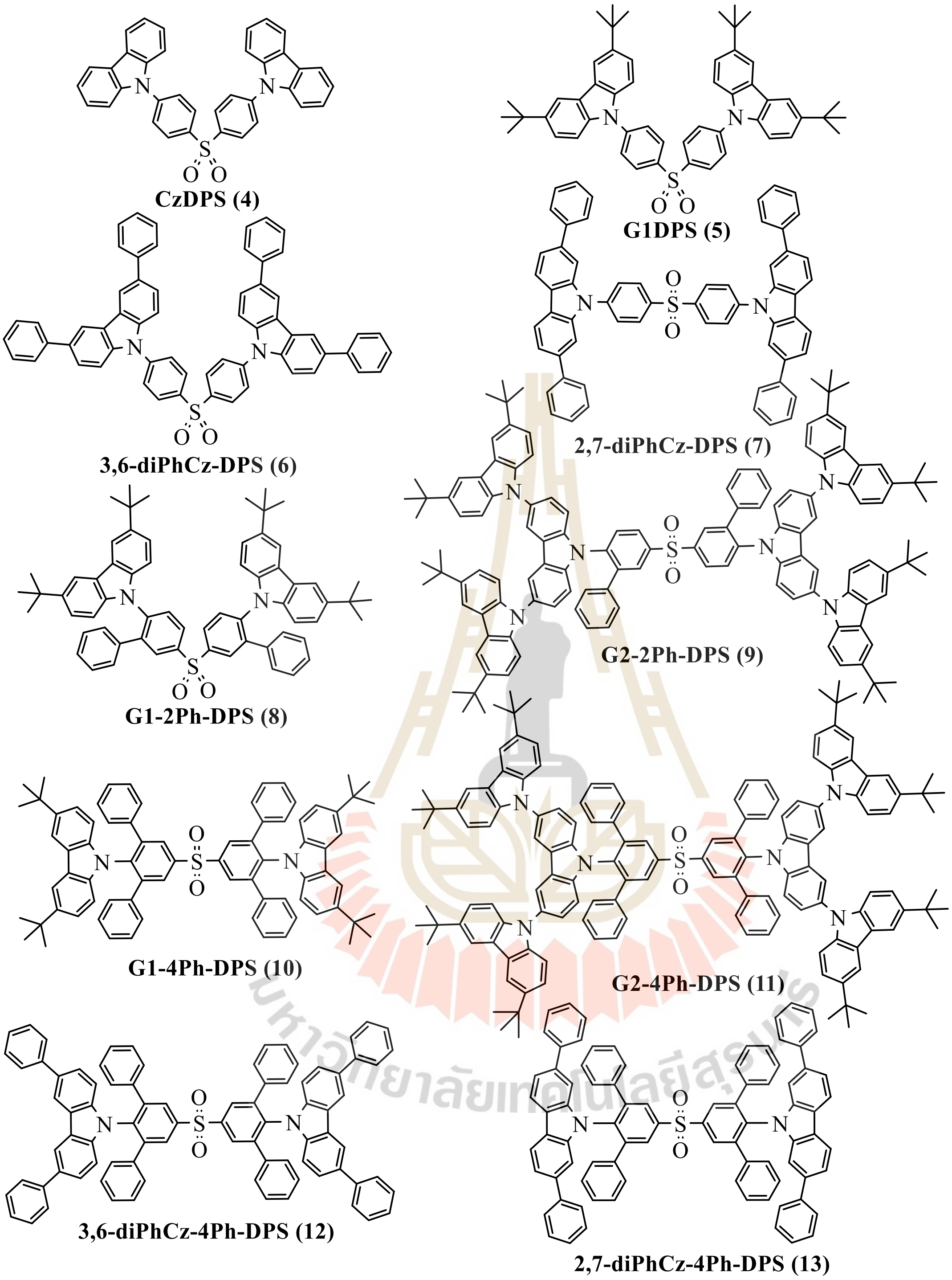

CzDPS (4)

G1DPS (5)

3,6-diPhCz-DPS (6)

2,7-diPhCz-DPS (7)

G1-2Ph-DPS (8)

G2-2Ph-DPS (9)

G1-4Ph-DPS (10)

G2-4Ph-DPS (11)

3,6-diPhCz-4Ph-DPS (12)

2,7-diPhCz-4Ph-DPS (13)

Figure 3.17 The molecular structures of the desired TADF molecules **4-13**.

3.3 Synthesis of TADF emitters

3.3.1 Synthetic approach

The desired TADF emitters should be obtained by bromination of *bis*(4-fluorophenyl) sulfone to afford dibromo- or tetrabromo sulfone followed by Suzuki cross-coupling reaction of dibromo- or tetrabromo sulfone with phenylboronic acid to afford the key intermediate which composed of diphenyl or tetraphenyl substituted on phenyl linker. Finally, the nucleophilic substitution of key intermediate with carbazole donor derivatives and after purification by chromatography and recrystallization, the desired TADF compounds should be obtained as outlined in Figure 3.18.

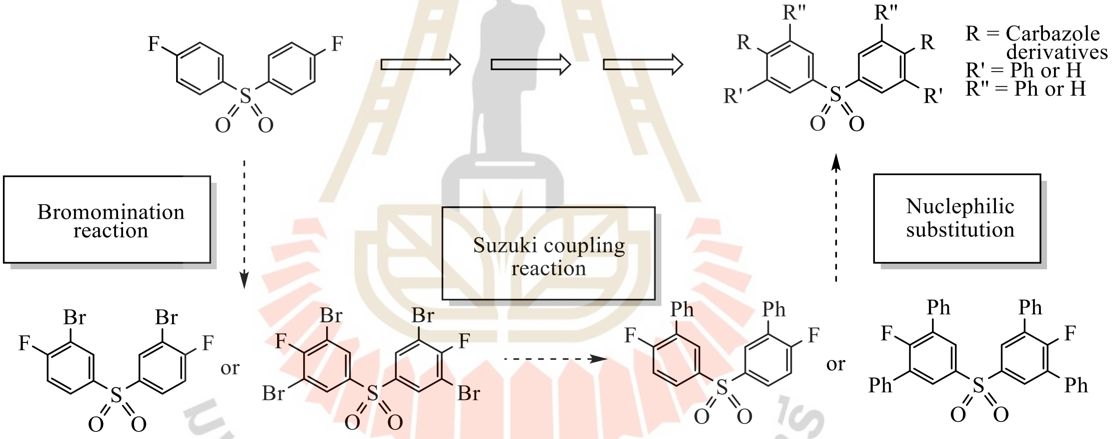
R = Carbazole derivatives
R' = Ph or H
R" = Ph or H
Bromomination reaction
Suzuki coupling reaction
Nuclephilic substitution
or
or

Figure 3.18 Synthetic approach to the synthesis of the TADF molecules.

3.3.2 The synthesis of 131 and 132

The bromo di-substituted and tetra-substituted compounds **131** and **132** was synthesized via bromination of *bis*(4-fluorophenyl) sulfone (**130**) using *N*-bromo succinimide in sulfuric acid at room temperature and heated at 70°C to afford **131** and **132** in a moderate yield of 44% and 46%, respectively, as shown in Figure 3.19.

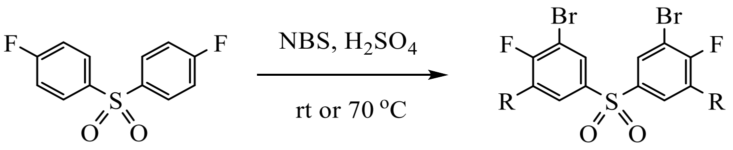

130

131, R = H, 44%
132, R = Br, 46%

Figure 3.19 The synthesis of dibromo-substituted (**131**) and tetrabromo-substituted (**132**) sulfone.

3.3.3 The synthesis of key intermediates 133 and 134

The key intermediates were used as the starting materials for the final step to the synthesis of TADF emitters, which could be synthesized on a milligram scale starting from the dibromo-substituted (**133**) and tetrabromo-substituted (**134**) sulfone using Suzuki cross-coupling reaction as outlined in Figure 3.20.

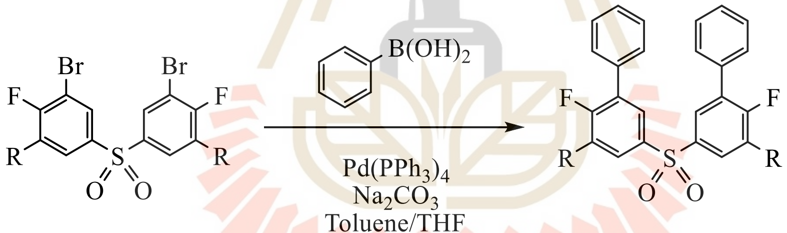

131, R = H
132, R = Br

133, R = H, 82%
134, R = Ph, 58%

Figure 3.20 The synthesis of key intermediates **133** and **134**.

Suzuki coupling is a palladium-catalyzed cross-coupling reaction of organoboranes with organic halides. The first step was the oxidative addition of palladium (0) to the organic halide starting material (**131**) to form the organopalladium species. The second step was metathetic exchange with base gives intermediate, which via transmetalation with the phenylboronic acid forms the oganopalladium species. Finally, reductive elimination of the desired product (**133**) restores the original palladium catalyst (0) as shown in Figure 3.21.

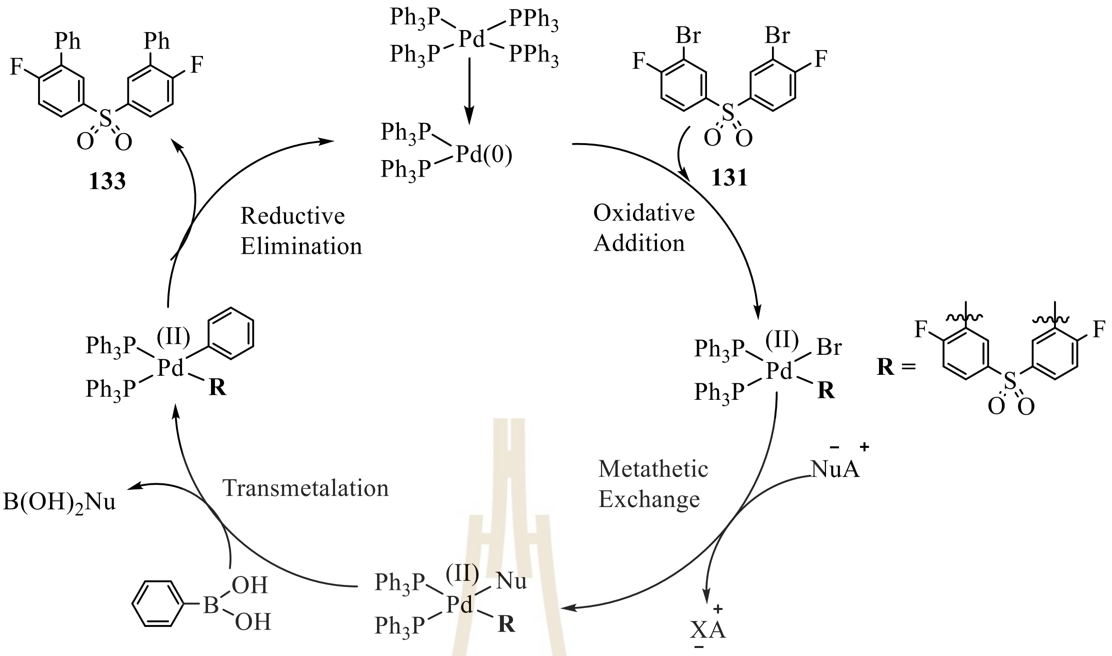
Ph
Ph
F
F
S
O
O
133
Ph3P
PPh3
Pd
Ph3P
PPh3
Ph3P
Pd(0)
Ph3P
Br
Br
F
F
S
O
O
131
Reductive Elimination
Oxidative Addition
Ph3P
(II)
Pd
Ph3P
R
Ph3P
(II)
Br
Pd
Ph3P
R
R =
F
F
S
O
O
Transmetalation
Metathetic Exchange
B(OH)2Nu
NuA
OH
B
OH
Ph3P
(II)
Nu
Pd
Ph3P
R
XA

Figure 3.21 The mechanism of the Suzuki reaction.

The dibromo-DPS (**131**) and tetrabromo-DPS (**132**) were reacted with phenylboronic acid in the presence of sodium carbonate as base via Suzuki reaction to give key intermediates **133** and **134** in a good yield of 82% and 58%, respectively.

3.3.4 The synthesis of carbazole donor 136 and 138

The carbazole donor **136** and **138** could be synthesized on a gram scale starting from the 3,6-diiodo carbazole (**135**) and 2,7-dibromo carbazole (**136**) using the Suzuki cross-coupling reaction as outlined in Figure 3.22.

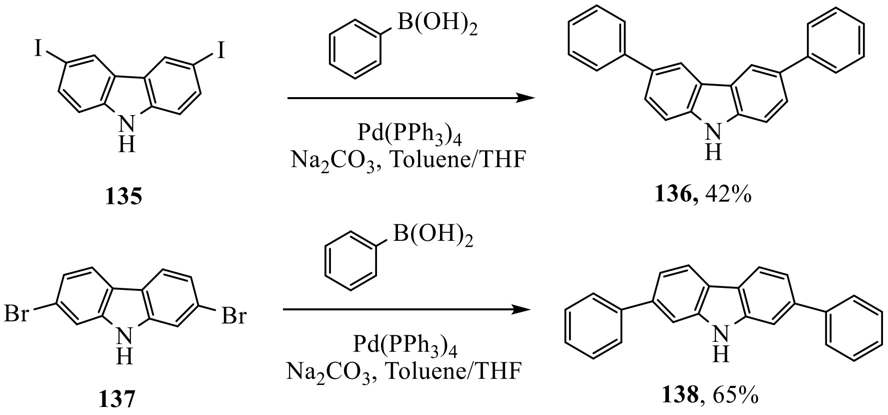
I
I
N
H
135
B(OH)2
Pd(PPh3)4
Na2CO3, Toluene/THF
N
H
136, 42%
Br
Br
N
H
137
B(OH)2
Pd(PPh3)4
Na2CO3, Toluene/THF
N
H
138, 65%

Figure 3.22 The synthesis of key intermediates **136** and **138**.

The 3,6-diiodo carbazole (**135**) and 2,7-dibromo carbazole (**137**) were reacted with phenylboronic acid in the presence of sodium carbonate as base via Suzuki reaction to give 3,6-diphenyl carbazole (**136**) and 2,7-diphenyl carbazole (**138**) in a moderate yield of 42% and 65%, respectively.

3.3.5 The synthesis of TADF emitters (4-13)

Finally, Nucleophilic substitution of key intermediates **133** and **134** with carbazole derivatives (**136**, **138**, Cz (**139**), G1 (**73**), and G2 (**74**)) using sodium hydride in dimethylformamide afforded the desired molecules, DPS1-DPS10 in a yield of 9-94%. Their structures were confirmed by ^{1}H NMR, ^{13}C NMR, and HRMS spectrometric methods. The synthetic procedure of the TADF emitters (**4-13**) is shown in Figure 3.23.

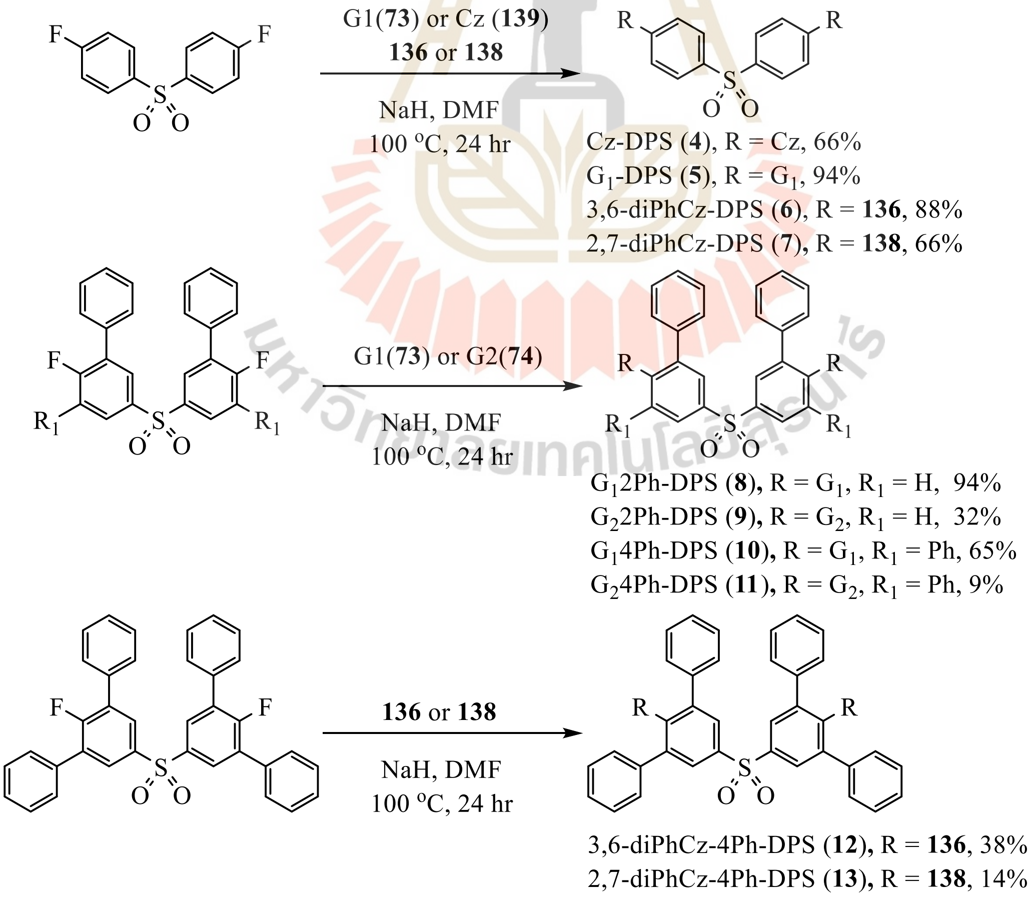
F
F
S
O
O
G1(73) or Cz (139)
136 or 138
NaH, DMF
100 °C, 24 hr
R
R
Cz-DPS (4), R = Cz, 66%
G1-DPS (5), R = G1, 94%
3,6-diPhCz-DPS (6), R = 136, 88%
2,7-diPhCz-DPS (7), R = 138, 66%
R1
R1
G1(73) or G2(74)
NaH, DMF
100 °C, 24 hr
G12Ph-DPS (8), R = G1, R1 = H, 94%
G22Ph-DPS (9), R = G2, R1 = H, 32%
G14Ph-DPS (10), R = G1, R1 = Ph, 65%
G24Ph-DPS (11), R = G2, R1 = Ph, 9%
136 or 138
NaH, DMF
100 °C, 24 hr
3,6-diPhCz-4Ph-DPS (12), R = 136, 38%
2,7-diPhCz-4Ph-DPS (13), R = 138, 14%

Figure 3.23 The synthesis of the TADF emitters **4-13**.

The structure of CzDPS (**4**) was confirmed by ^{1}H-NMR spectroscopy. The ^{1}H-NMR spectrum showed doublet of the para position of phenyl linker at δ = 8.27 (4H) and 7.84 (4H) ppm with the coupling constant (*J*) of 8.4 Hz. The carbazole protons produce doublet signals at 8.14 (4H) and 7.50 (4H) ppm with the *J* of 7.4 Hz, another proton showed signals at δ = 7.43 (4H, t), 7.33 (4H, t) ppm. The ^{13}C-NMR spectrum showed the chemical shift of carbon signals in the range of 142.8-109.6 ppm. Moreover, High resolution mass spectrometry confirmed the identity of the compound with m/z (HRMS) = 548.1002 (required m/z = 548.1558).

The ^{1}H-NMR spectrum of G1DPS (**5**) showed doublet of the para position of phenyl linker at δ = 8.23 (4H) and 7.82 (4H) ppm with the coupling constant (*J*) of 8.4 Hz. The carbazole protons produce singlet signals at 8.13 (4H) and another proton showed multiplet signals at δ = 7.49-7.43 (8H) ppm. The protons of *tert*-butyl group of G_1 showed the singlet signal at 1.46 (36H) ppm. The ^{13}C-NMR spectrum showed the chemical shift of aryl carbon signals in the range of 144.1-109.2 ppm and the alkyl carbon at 34.8 and 31.9 ppm. Moreover, HRMS of the compound with m/z = 772.3282 (required m/z = 772.4062).

The ^{1}H-NMR spectrum of 3,6-diPhCz-DPS (**6**) showed doublet of the para position of phenyl linker at δ = 8.33 (4H) and 7.90 (4H) ppm with the coupling constant (*J*) of 8.4 Hz. The carbazole protons produce singlet signals at 8.39 (4H), while another proton of carbazole and phenyl showed multiplet signals at δ = 7.70 (12H, m), 7.58 (4H, d, J = 8.4 Hz), 7.49 (8H, t), 7.37 (4H, t) ppm. The ^{13}C-NMR spectrum showed the chemical shift of aryl carbon signals in the range of 142.7-108.2 ppm. Moreover, HRMS of the compound with m/z = 853.1968 (required m/z = 853.2844).

The ^{1}H-NMR spectrum of 2,7-diPhCz-DPS (**7**) showed doublet of the para position of phenyl linker at δ = 8.33 (4H) and 7.91 (4H) ppm with the coupling constant (*J*) of 8.4 Hz. The carbazole protons produce singlet signals at 7.66 (4H) ppm, while another proton of carbazole produces doublet signals at δ = 8.19 (4H) and 7.58 (4H). Phenyl protons showed the multiplet signals at δ = 7.63 (8H), 7.42 (8H), and 7.34 (4H) ppm. The ^{13}C-NMR spectrum showed the chemical shift of aryl carbon signals in the range of 142.7-110.1 ppm. Moreover, HRMS of the compound with m/z = 852.7777 (required m/z = 853.2844).

The ^{1}H-NMR spectrum of G1-2Ph-DPS (**8**) showed singlet protons of the phenyl linker at δ = 8.35 (2H) and doublet protons of ortho position at 8.15 (2H) and 7.69 (2H) ppm. The carbazole protons produce singlet signals at 8.02 (4H, s) and another proton showed multiplet signals at δ = 7.30-6.97 (18H) ppm. The protons of *tert*-butyl group of G_1 showed the singlet signal at 1.40 (36H) ppm. The ^{13}C-NMR spectrum showed the chemical shift of aryl carbon signals in the range of 143.2-109.4 ppm and the alkyl carbon at 34.7 and 31.9 ppm. Moreover, HRMS of the compound with m/z = 924.4772 (required m/z = 924.4688).

The ^{1}H-NMR spectrum of G2-2Ph-DPS (**9**) showed singlet protons of the phenyl linker at δ = 8.39 (2H) and doublet protons of ortho position at 8.12 (2H) and 7.69 (2H) ppm. The carbazole protons produce singlet signals at 8.03 (4H, s) and another proton showed multiplet signals at δ = 7.47-7.17 (18H) ppm. The protons of *tert*-butyl group of G_1 showed the singlet signal at 1.44 (72H) ppm. The ^{13}C-NMR spectrum showed the chemical shift of aryl carbon signals in the range of 142.7-109.0 ppm and the alkyl carbon at 34.7 and 32.0 ppm. Moreover, HRMS of the compound with m/z = 1809.1216 (required m/z = 1808.9506).

The ^{1}H-NMR spectrum of G1-4Ph-DPS (**10**) showed singlet protons of the phenyl linker at δ = 8.27 (4H) ppm. The carbazole protons produce singlet signals at 7.85 (4H) and another proton showed multiplet signals at δ = 7.16-6.77 (28H) ppm. The protons of *tert*-butyl group of G_1 showed the singlet signal at 1.34 (36H) ppm. The ^{13}C-NMR spectrum showed the chemical shift of aryl carbon signals in the range of 143.3-108.6 ppm and the alkyl carbon at 34.7 and 32.0 ppm. Moreover, HRMS of the compound with m/z = 1076.5097 (required m/z = 1076.5315).

The ^{1}H-NMR spectrum of G2-4Ph-DPS (**11**) showed singlet protons of the phenyl linker at δ = 8.45 (4H). The carbazole protons produce singlet signals at δ = 7.96 (4H), the second generation of dendron produce singlet signals at δ = 8.11 (8H), and another proton showed multiplet signals at δ = 7.42-7.14 (44H) ppm. The protons of *tert*-butyl group of G_2 showed the singlet signal at 1.40 (72H) ppm. The ^{13}C-NMR spectrum showed the chemical shift of aryl carbon signals in the range of 144.4-109.0 ppm and the alkyl carbon at 34.7 and 32.0 ppm. Moreover, HRMS of the compound with m/z = 1961.3507 (required m/z = 1961.0132).

The ^{1}H-NMR spectrum of 3,6-diPhCz-4Ph-DPS (**12**) showed singlet signals of phenyl linker at δ = 8.36 (4H) ppm. The carbazole protons produce singlet signals at 8.16 (4H), while another proton of carbazole and phenyl showed multiplet signals at δ = 7.64 (8H), 7.44 (12H), 7.30 (4H), 7.03 (24H) ppm. The ^{13}C-NMR spectrum showed the chemical shift of aryl carbon signals in the range of 144.1-108.8 ppm. Moreover, HRMS of the compound with m/z = 1157.2931 (required m/z = 1157.4096).

The ^{1}H-NMR spectrum of 2,7-diPhCz-4Ph-DPS (**13**) showed singlet signals of phenyl linker at δ = 8.22 (4H)ppm. The carbazole protons produce singlet signals at 8.04 (4H), while another proton of carbazole and phenyl showed multiplet signals at δ = 7.92 (4H), 7.58 (8H), 7.51 (16H), 7.47 (16H), 7.42 (16H), 7.31 (16H), 7.01 (20H) ppm. The ^{13}C-NMR spectrum showed the chemical shift of aryl carbon signals in the range of 144.4-110.4 ppm. Moreover, HRMS of the compound with m/z = 1157.2896 (required m/z = 1157.4096).

3.4 Results and discussion

3.4.1 Optical properties

The UV-vis absorption and fluorescence spectra of the TADF emitters were investigated in dilute toluene solution (10^{-5}-10^{-6} M) and the neat film by UV-vis and photoluminescence spectroscopies as shown in Figure 3.24. All TADF (**4-13**) compounds showed two broad and structureless absorption bands, an absorption band around 290 nm corresponding to the π-π* transition of the carbazole moieties and an absorption band with a maximum at 340 nm assigned to the n-π* transition leads to occur intramolecular charge-transfer (ICT). All the TADF emitters showed a similar absorption band in solution and in the neat film. CzDPS (**4**) and G1DPS (**5**) exhibited strong occur ICT bands with a maximum at 340 nm and high molar absorptivity (ε). In addition, G1-2Ph-DPS (**8**), G2-2Ph-DPS (**9**), G1-4Ph-DPS (**10**), G2-4Ph-DPS (**11**), 3,6-diPhCz-DPS (**6**), and 3,6-diPhCz-4Ph-DPS (**12**) revealed the ICT band appears as a shoulder below the π-π* absorption peak with a slightly red-shifted at 344 nm indicating that there are charge transfer from the LUMO of the acceptor moieties to the HOMO of the carbazole donor moieties like a push-pull system and the spatial overlap due to the twist angle between DPS core and the carbazole derivatives. The small bathochromic effect implied that the intermolecular interactions could be effectively prevented due to the bulky carbazole dendrons. In the other hand, the absorption bands of 2,7-diPhCz-DPS (**7**) and 2,7-diPhCz-4Ph-DPS (**13**) showed a slightly blue-shifted with a maximum at 320 nm, which indicates that the C-C bonds of π-linker of these molecules were restricted due to the steric hindrance from the phenyl groups at the 2 and 7 positions of carbazole donor moieties. Besides that, the ICT character of the molecules remained with the increase of the phenyl group. The fluorescence spectra of TADF emitters exhibited emission bands with a maximum of around 370-455 nm in toluene. The fluorescence spectra in neat films are identical to those in toluene. 2,7-diPhCz-DPS (**7**) and 2,7-diPhCz-4Ph-DPS (**13**) revealed a deep blue emission band at around 370 nm, while G2-2Ph-DPS (**9**) and G2-4Ph-DPS (**11**) showed sky blue emission with the longest wavelength at 455 nm because of their donor moieties which containing the second generation of 3,6-di-*tert*-butylcarbazole, G2. The photophysical data of TADF emitters were listed in Table 3.1. The energy gap (E_g^{opt}) of all TADF materials which calculated from the onset wavelength of absorption spectra were in the range of 3.04-3.39 (eV). All TADF emitters exhibited the singlet state (S_1) which calculated from the onset of the fluorescence spectra in the range of 3.03-3.51 (eV). In the case of the dendron group, the singlet state (S_1) of G1DPS (**5**), G1-2Ph-DPS (**8**), G2-2Ph-DPS (**9**), G1-4Ph-DPS (**10**), and G2-4Ph-DPS (**11**) was decreased when the dendron generation increase indicating that by attaching higher generation carbazoles via their *N*-position to the 3,6-positions of the inner carbazole moiety influence on the singlet energy of the whole molecule.

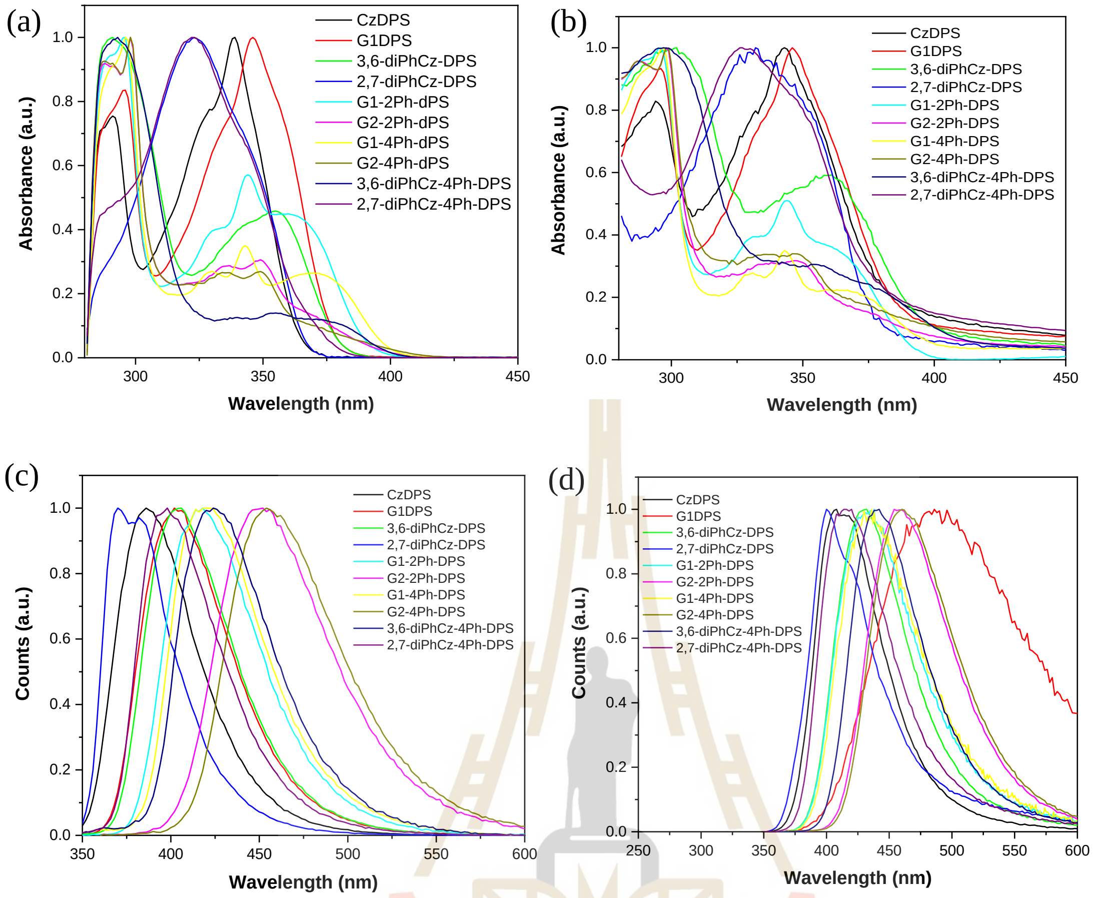

Figure 3.24 UV-vis absorption of TADF emitters in (a) dilute solution in toluene (10^{-5} M) (b) solid film and fluorescence spectra in (c) dilute solution in toluene (10^{-6} M) and (d) solid film.

Table 3.1 Photophysical properties of TADF emitters.

Compds	Solution	Film	$\lambda^{abs}_{onset}{}^{a}$	$E_g^{opt\,b}$	$\lambda^{flu}_{onset}{}^{c}$	$S_1{}^{d}$
	λ_{UV} (log ε) /λ_{em} (nm/M^{-1}cm^{-1})	λ_{UV} /λ_{em} (nm)	(nm)	(eV)	(nm)	(eV)
CzDPS	339 (4.81)/386	342/413	366	3.39	354	3.51
G1DPS	346 (4.53)/406	346/424	382	3.25	368	3.37
3,6-diPhCz-DPS	355 (4.60)/404	359/430	381	3.26	370	3.35
2,7-diPhCz-DPS	323 (4.98)/377	333/401	368	3.37	353	3.51
G1-2Ph-DPS	344 (4.25)/418	344/433	392	3.16	380	3.26
G2-2Ph-DPS	349 (4.50)/451	348/458	399	3.11	402	3.08
G1-4Ph-DPS	343 (4.11)/422	343/436	401	3.10	386	3.21
G2-4Ph-DPS	349 (4.35)/455	347/460	408	3.04	409	3.03
3,6-diPhCz-4Ph-DPS	355 (4.09)/424	357/440	403	3.07	388	3.20
2,7-diPhCz-4Ph-DPS	322 (4.90)/398	329/416	370	3.35	368	3.37

[a] The onset of the absorption spectra.

[b] Calculated from the absorption spectra threshold, $E_g^{opt} = 1240/\lambda_{onset}$.

[c] The onset of the fluorescence spectra.

[d] Calculated from the onset of the fluorescence spectra.

3.4.2 Commission International de l'Eclairage (CIE)

The color perceived by the human eye in full daylight by sensors on the retina, called cones. Cones are divided into three types by the sensitivity from the light of cones, they are short (S, 420-440 nm), middle (M, 530-540 nm), and long (L, 560-580 nm) wavelengths which can be assigned to blue, green, and red, respectively. If the light is not bright enough, the cones do not work resulting in vision without color, so the human eyes perceived colors only in the range of 10^{-2} to 10^{5} cd/m². Therefore, the CIE chromaticity diagram is used to describe the color perceived by eye because color perception differs from person to person. Chromaticity diagram and CIExy values of all TADF emitters in dilute toluene solution and in the neat film are shown in Figure 3.25 and summarized in Table 3.2. The results revealed that G2-2Ph-DPS (**9**) and G24Ph-DPS (**11**) exhibited the high x,y coordinate with blue emission. It might be from the electron move from the second generation of dendron moieties to the center acceptor like a push-pull interaction induce a red-shifted in the emission spectrum. On the other hand, 2,7-diPhCz-DPS (**7**) and 2,7-diPhCz-4Ph-DPS (**13**) showed the deep blue emission with the lowest CIExy values of (0.163, 0.030) and (0.160, 0.038), when compared to the standard blue (0.14, 0.08).

Table 3.2 CIE(x,y) coordinates of TADF emitters.

Compounds	**CIE^{sol} (x,y)**	**CIE^{film} (x,y)**
CzDPS	(0.161, 0.029)	(0.160, 0.061)
G1DPS	(0.159, 0.038)	(0.162, 0.093)
3,6-diPhCz-DPS	(0.159, 0.039)	(0.158, 0.086)
2,7-diPhCz-DPS	(0.163, 0.030)	(0.173, 0.112)
G1-2Ph-DPS	(0.157, 0.052)	(0.160, 0.109)
G2-2Ph-DPS	(0.152, 0.134)	(0.159, 0.173)
G1-4Ph-DPS	(0.153, 0.049)	(0.159, 0.117)
G2-4Ph-DPS	(0.152, 0.155)	(0.160, 0.186)
3,6-diPhCz-4Ph-DPS	(0.155, 0.059)	(0.156, 0.108)
2,7-diPhCz-4Ph-DPS	(0.160, 0.038)	(0.163, 0.088)

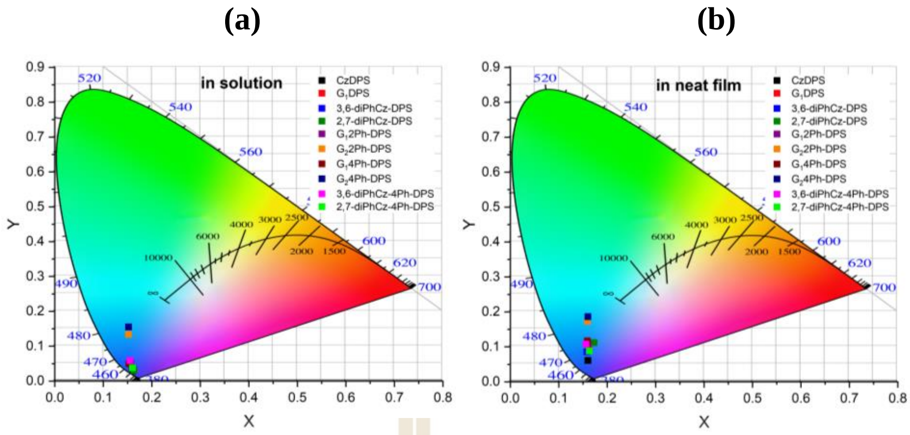

Figure 3.25 Chromaticity diagram of all TADF emitters **4-13** in (a) dilute solution in toluene (10^{-5} M) and (b) solid neat film.

3.4.3 Emission decays

To further demonstrate the character of TADF occurred in the solution state, the emission decays of these TADF compounds were investigated in dilute toluene solution (10^{-6} M) under argon and oxygen atmosphere. In order to prevent the oxygen quenching of triplet state, argon gas has been used to replaced oxygen gas by using a freeze-thaw cycle, which is consists of quickly freezing at -195°C in liquid nitrogen and thawing at room temperature in sequence (the tubes could be thawed quickly at 6-10°C in a water bath for 10 min and kept at room temperature). Then argon gas has been flushed into the tube and repeats freeze-thaw cycles for three times. The transient PL decay of all emitters displayed two components, the first component is a fast decay which can be assigned to prompt fluorescence which arising from $S_1 \rightarrow S_0$ transition and the second component is a slower one which can be assigned to delayed fluorescence which arising from repopulation of the S_1 through RISC from the T_1 followed by $S_1 \rightarrow S_0$ transition. The lifetimes of prompt and delayed fluorescence were summarized in Table 3.3. The lifetimes were estimated to be 4-19 ns for prompt fluorescence and 36-600 ns for delayed fluorescence under the argon atmosphere. The emission decay of all TADF **4-13** in toluene under argon and oxygen atmosphere at room temperature are shown in Figure 3.26.

Table 3.3 The lifetimes of prompt and delayed fluorescence of TADF emitters.

Compds	**τ_P (ns) in solution (τ_{air}/τ_{N2})**	**τ_d (ns) in solution (τ_{air}/τ_{N2})**
CzDPS	4.6/5.6	13.2/139.1
G1DPS	5.2/6.6	206.0/361.6
3,6-diPhCz-DPS	3.8/4.4	13.2/36.2
2,7-diPhCz-DPS	4.2/5.1	7.5/64.7
G1-2Ph-DPS	7.1/9.5	187.3/261.1
G2-2Ph-DPS	10.0/15.0	10.3/605.4
G1-4Ph-DPS	8.1/10.8	192.1/184.5
G2-4Ph-DPS	11.9/19.3	16.0/339.1
3,6-diPhCz-4Ph-DPS	5.8/7.1	215.8/188.3
2,7-diPhCz-4Ph-DPS	6.3/8.0	318.7/238.1

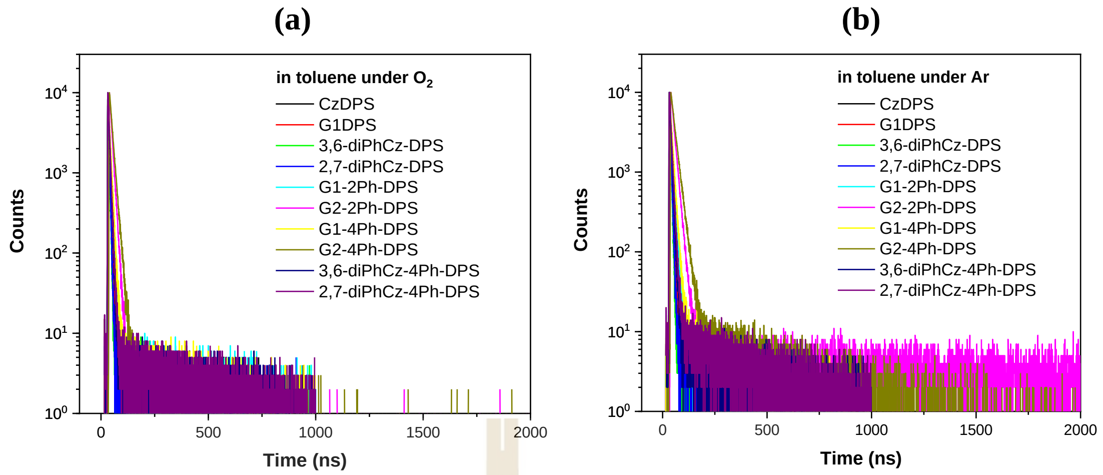

Figure 3.26 The emission decay of all TADF **4-13** in toluene under oxygen (a) and argon (b) atmosphere at room temperature.

3.4.4 Oxygen quenching of the photoluminescence quantum yield

Thermally activated delayed fluorescence involves reverse intersystem crossing (RISC) from triplet state (T_1) to singlet state (S_1) followed by a fluorescent transition from $S_1 \rightarrow S_0$ and emit light. The intensity of the emission depends on the mechanism that removes the excitons from T_1. However, TADF emission has been quenched by oxygen molecule (O_2) because it has a triplet ground state and repopulation of the T_1 state via energy transfer. Therefore, the TADF character can be checked by measurement of the photoluminescence quantum yield in the absence and presence of oxygen. The photoluminescence quantum yields were measured using the direct method with the integrating sphere module. The quantum yield of the non-degassed solution was measured using the integrating sphere module and the degassed solution extrapolated based on the relative intensity of the emission. The change in emission intensity when all TADF solution **4-13** are exposed to oxygen are shown in Figure 3.27. The photoluminescence quantum yield of all TADF emitters **4-13** in the toluene solution exhibited enhancement under Argon atmosphere, suggests that the T_1 state is involved in the emission process and can be concluded that the reduction in quantum yield is the first indicator that the emission could contain TADF.

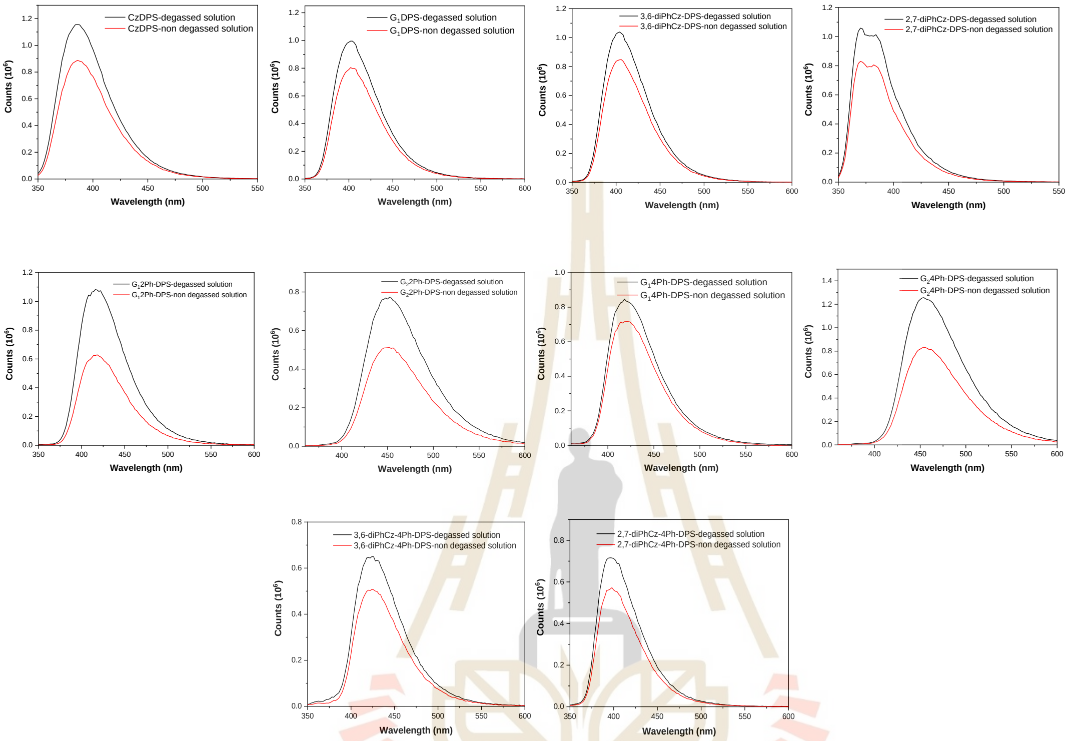

Figure 3.27 Emission spectra of all TADF materials **4-13** in degassed solution (black) and non-degassed solution (red) in toluene (10^{-5} M).

The degassed quantum yield of G1DPS (5) which is calculated based on the relative intensity of the emission and measured by the integrating sphere module has been investigated. In the first attempt, the solution has been degassed by flushed argon gas into the solution for 1 hour. The quantum yield of degassed and non-degassed solutions was measured using FLS-980 fluorescence spectrometer via the integrating sphere module. The quantum yield value of measurement was determined to be 61%. The ratio of the emission decay from the argon bubbles method was calculated to be 1.21 and the quantum yield was estimated to be 66%. In addition, the quantum yield of

G1DPS (**5**) from these two methods shows almost the same value which indicated that quantum yield of degassed can be estimated from the relative intensity of the emission decay as shown in Figure 3.28(a). Moreover, the emission decay of the G1DPS (**5**) solution which using the freeze-thaw method has been measured by using the FLS-980 fluorescence spectrometer. The relative intensity ratio of the emission was calculated to be 1.23, which is near the ratio from the argon bubbles method as shown in Figure 3.28(b). However, the freeze-thaw method is the most effective and acceptable method for degassing of the solution.

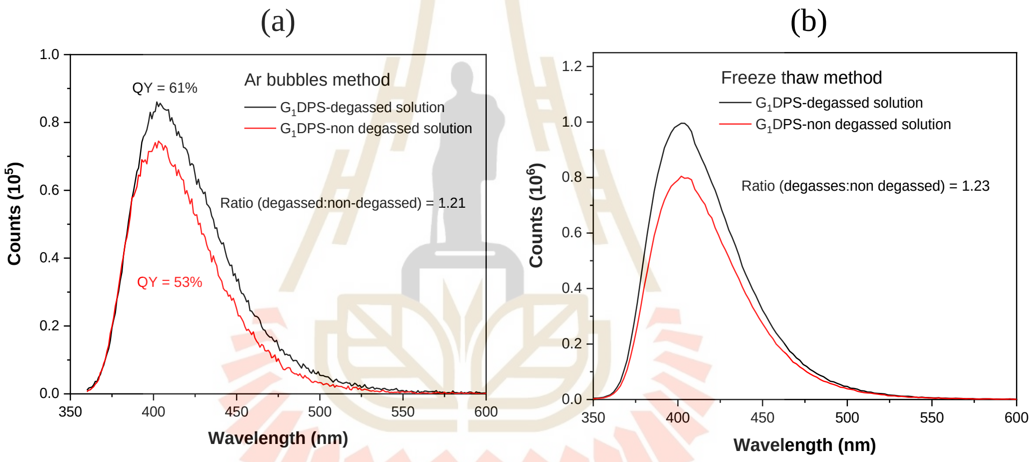

Figure 3.28 The quantum yield of G1DPS (**5**) in degassed solution (black) and non-degassed solution (red) by using argon bubbles method (a) and freeze-thaw method (b).

The fluorescence quantum yield of a non-degassed solution and degassed solution of G1DPS (**5**), G1-2PhDPS (**8**), and G1-4PhDPS (**10**) are summarized in table 3.3. The results revealed that G1DPS (**5**) has the highest yield, while G1-4PhDPS (**10**) shows the lowest yield which might be from the steric hindrance of phenyl groups linked on π-linker restricted free rotation of C-N bond of carbazole donor group. The number of phenyl group increase the quantum yield decrease.

Table 3.4 The fluorescence quantum yield of the non-degassed solution and degassed solution of G1DPS (**5**), G1-2PhDPS (**8**), and G1-4PhDPS (**10**).

Compds	**Quantum yield in non-degassed solution (ϕ_{O2})**	**Quantum yield in degassed solution (ϕ_{Ar})**
G1DPS (**5**)	54	61
G1-2Ph-DPS (**8**)	45	53
G1-4Ph-DPS (**10**)	19	21

3.4.5 Time-Resolved Emission Spectrum (TRES)

The time-resolved emission spectrum (TRES) is a method for approving the origin of the delayed component is delayed fluorescence or phosphorescence by comparing the spectral shape of the prompt and delayed components. In a TRES measurement, a three-dimensional time-resolved spectrum is built up from the emission decay which is measured as a function of emission wavelength. Then the TRES data can be sliced to a snapshot of the emission spectrum at a specified time after the laser flash. The prompt component is a shorter snapshot than the delayed component. If they are identical can be concluded that the delayed component is originated from the fluorescence. As shown in Figure 3.29, the prompt fluorescence of G1-2Ph-DPS (**8**) (red line) and the delayed emission at 30-110 nanoseconds are identical. Therefore, this compound exhibited the TADF characteristic and can be concluded that this strategy for designed TADF molecules is an effective method to achieve efficient TADF.

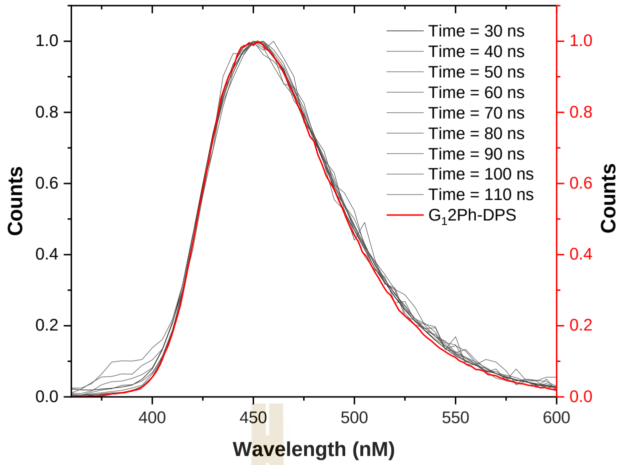

Figure 3.29 Time-resolved emission spectrum (TRES) of the prompt and delayed fluorescence of degassed G1-2Ph-DPS (**8**) solution.

3.4.6 Solvatochromic behaviors

Normally, the D-A molecules which containing π-π* transition presented the solvatochromism in their absorption spectra due to the high polarization of the ground-state molecular structure. The changing in the polarity of the solvent leads to the bathochromic shift or hypsochromic in the absorption spectra. Usually, the more polar solvent species polarizes molecules with a higher static dipole moment more strongly, but in some molecules, with a symmetrical structure the static dipole moment of the whole system is equal to zero due to some group were restrict, so these molecules should not display the solvatochromism in the absorption spectra. However, if the excited state of these molecules corresponds to the CT ππ*-state with the twisted structure and the dipole moment is not equal to zero, the solvatochromic behavior should be observed in the emission spectra rather than in absorption spectra. In order to study the solvatochromic behavior of all TADF compounds **4-13**, various solvents with different polarities such as toluene, chloroform, dichlorobenzene, tetrahydrofuran, and acetonitrile were selected. The UV-vis and emission spectra of all compounds have been measured. The results revealed that only emission spectra could be observed the bathochromic shifted in polar solvent due to their ICT behavior. The absorption spectra and emission spectra of all TADF emitters **4-13** in different solvents are shown in Figure 3.30.

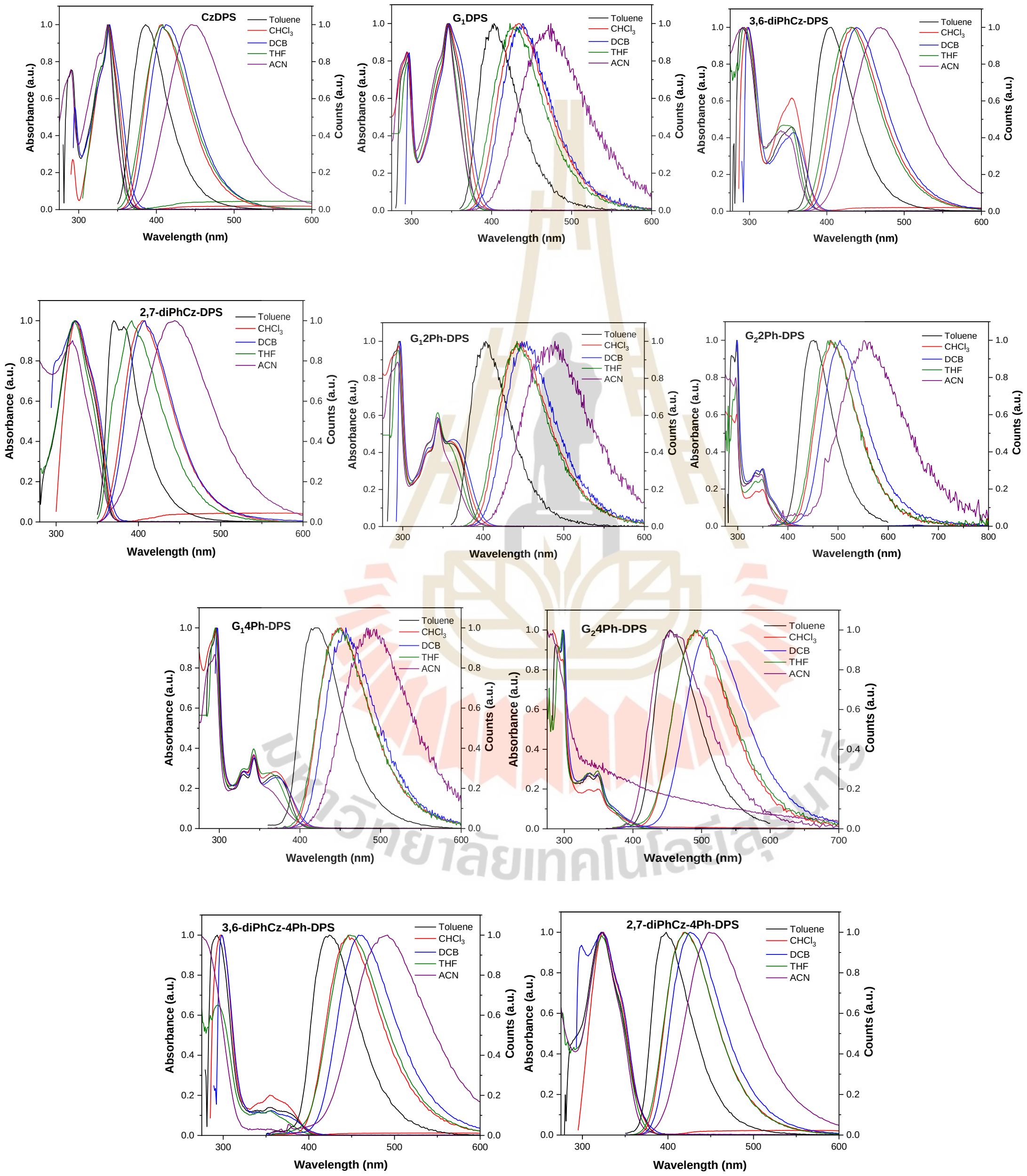

Figure 3.30 UV-vis absorption and fluorescence spectra of TADF emitters **4-13** in various solvent.

Normally, as the solvent polarity parameter (Δ*f*) based on the Lipper-Mataga equation increases, the stokes shift also increases with a linear correlation. The plots of stokes shift versus solvent polarity parameter (Δ*f*) of all compounds **4-13** were shown in Figure 3.31. The results revealed that the fluorescent properties of all compounds are strongly related to the solvent polarity which might be from the formation of large charge separation due to the twisted structure and high dipole moment in the excited state.

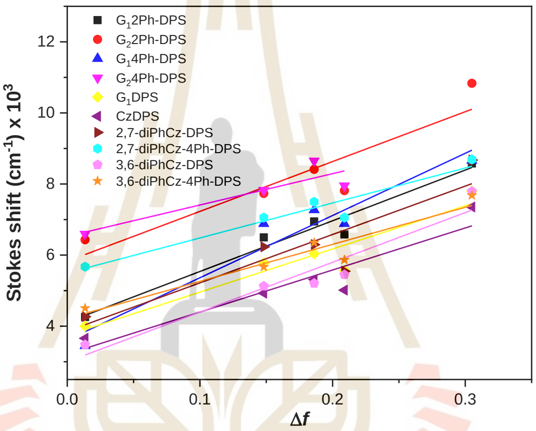

Figure 3.31 The plots of stokes shift versus solvent polarity parameter (Δ*f*) of all TADF compounds **4-13**.

3.4.7 Electrochemical properties

The electrochemical characteristics of the TADF emitters were measured by cyclic voltammetry. All compounds exhibited reversible oxidation processes upon the anodic sweep as shown in Figure 3.32. The first oxidation process assigns to the removal of electrons from the carbazole donor, resulting in radical cations. The HOMO levels of all compounds determined from the onsets of the oxidation potentials were in the range of -5.80 to -5.04 eV, which are similar to the HOMO values from AC2 method and close to the work function of a commonly used indium tin oxide (ITO) anode

(-4.80 eV). The LUMO levels determined from the onsets of the reduction potentials except for G1DPS (**5**), G1-2Ph-DPS (**8**), and G1-4Ph-DPS (**10**) have no reduction signal thus the LUMO levels of these emitters were calculated from the HOMO levels and the corresponding optical bandgaps (E_g^{opt}). The LUMO levels were in the range of -3.81 t0 -2.46 eV. Electrochemical band gaps (E_g^{ele}) determined using the onsets of the oxidation potentials subtracts by the onsets of the reduction potentials were in the range of 1.29-2.13 eV. The electrochemical data are summarized in Table 3.5.

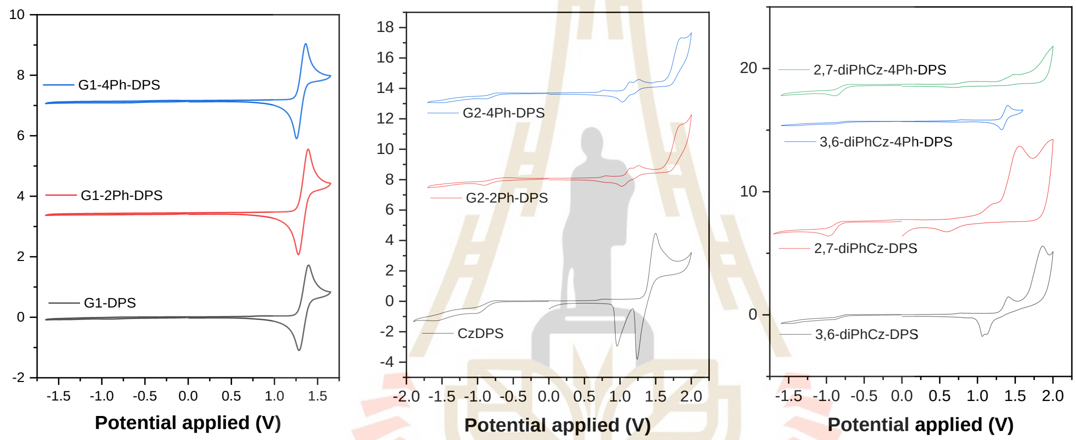

Figure 3.32 CV curves of TADF emitters in CH_2Cl_2 solution using 0.1 M Bu_4NPF_6 at a scan rate of 50 mV/s under argon flow.

Table 3.5 Electrochemical properties of all TADF compounds.

Compounds	**$E^{ox}_{onset}/E^{red}_{onset}$ (eV) ^{e}**	**HOMO/LUMO from CV (eV) ^{f}**	**$E^{Ox}_{1/2}/E^{Re}_{1/2}$ ^{h} vs. Ag/Ag^{+} (eV) ^{g}**	**HOMO from AC2 ^{h}**	**E_g^{ele} ^{e} (eV) ^{i}**
CzDPS	1.36/-0.77	-5.80/-3.67	1.36/-0.90	5.80	2.13
G1DPS	1.27	-5.71/-2.46	1.35/-	5.81	-
3,6-diPhCz-DPS	1.27/-0.69	-5.71/-3.75	1.24/-0.82	5.75	1.96
2,7-diPhCz-DPS	0.87/-0.78	-5.31/-3.66	1.07/-0.90	5.80	1.65
G1-2Ph-DPS	1.26	-5.70/-2.54	1.33/-	5.64	-
G2-2Ph-DPS	1.01/-0.63	-5.45/-3.81	1.33/-0.79	-	1.64
G1-4Ph-DPS	1.25	-5.69/-2.59	1.31/-	5.74	-
G2-4Ph-DPS	1.01/-0.66	-5.45/-3.78	1.14/-0.81	-	1.68
3,6-diPhCz-4Ph-DPS	1.25/-0.64	-5.69/-3.80	1.37/-0.80	5.88	1.89
2,7-diPhCz-4Ph-DPS	0.60/-0.69	-5.04/-3.75	0.82/-0.81	5.83	1.29

[e] Onset oxidation and reduction potentials versus Ag/Ag+.

[f] Estimated from the onset oxidation and reduction potential using HOMO = $-E^{ox}_{onset} - 4.44$ eV and LUMO $= -E^{ox}_{onset} - 4.44$ eV or HOMO + E_g^{opt}.

[g] Obtained from CV measured in CH_2Cl_2–n-Bu_4NPF_6 (0.1 M) at a scan rate of 50 ms^{-1}.

[h] Obtained from AC2 measured in solid neat film.

[i] Electrochemical band gaps determined using $E^{ox}_{onset} - E^{red}_{onset}$

3.4.8 Thermal properties

The thermal properties of TADF emitters **4-13** were determined by differential scanning calorimetry (DSC) and thermogravimetric analysis (TGA). TGAs reveal that their decomposition temperatures at 5 % weight loss (T_{5d}) are above 400°C, indicating the high thermal stability. The thermogram of TADF materials is shown in Figure 3.33 and the data are listed in Table 3.6.

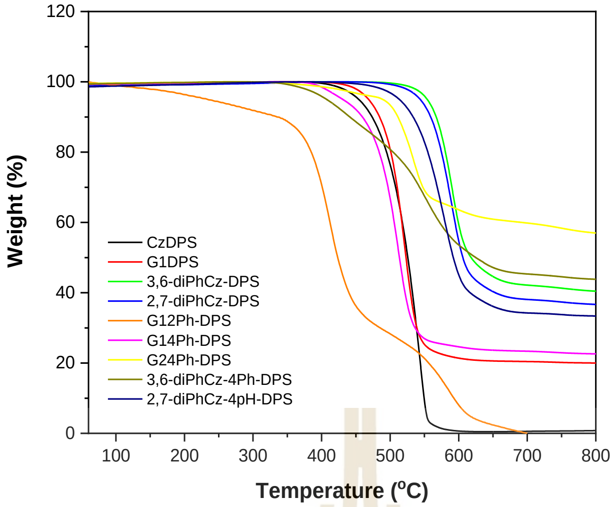

Figure 3.33 TGA thermograms of TADF emitters **4-13** measured at a heating rate of 10°C min^{-1} under N_2 flow.

Table 3.6 Thermal properties of all TADF compounds.

Compounds	T_{5d} (°C)	T_g (°C)	T_m (°C)
CzDPS	454	125	-
G1DPS	468	118	350
3,6-diPhCz-DPS	554	191	294
2,7-diPhCz-DPS	543	237	342
G1-2Ph-DPS	233	253	326
G2-2Ph-DPS	nd	nd	nd
G1-4Ph-DPS	430	238	335
G2-4Ph-DPS	489	nd	nd
3,6-diPhCz-4Ph-DPS	407	148	327
2,7-diPhCz-4Ph-DPS	514	267	317

DSCs (1st and 2nd heating scans) of the TADF emitters reveal a distinct glass transition temperature (Tg) in the range of 175-246°C as shown in Figure 3.34 and listed in table 3.6. The peak of crystallization and melting could not be observed at higher temperatures, indicating an excellent amorphous glass state stability. The high Tg of all compounds may be attributed from the rigid structure due to the phenyl substituent on the π-linker induce increasing of the efficiency of the device because an amorphous thin-film device is made from the materials with high Tg is less vulnerable to heat. Therefore, organic materials with high Tg are therefore highly desirable for applications in long lifetime electroluminescent devices.

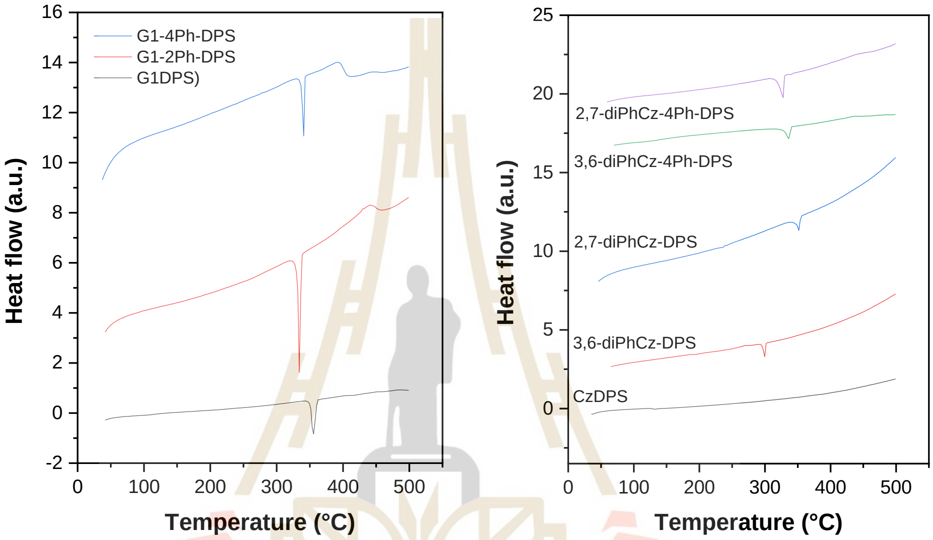

Figure 3.34 DSC 1st heating (solid line) and 2nd heating (dotted line) scans of TADF emitters **4-13**.

3.5 Conclusion

In summary, novel TADF emitters based on D-π-A-π-D system of *bis*(4-carbazolephenyl) sulfone have been successful to synthesized. The molecular structures are composed of carbazole derivatives as the donor, benzene as the π-linker, and sulfone as the acceptor. All TADF emitters exhibited deep blue emission with the strong ICT and showed a slight red shift when changing the donor moieties to a more strongly electron-donating group. Moreover, the twisted molecule with a varying number of phenyl substituents on the π-linker leads to less quantum yield due to the energy loss from the rotation of molecules. Besides that, all compounds revealed the TADF characteristic. We believe that our results could provide a useful guide to design the highly efficient TADF emitter with the twisted molecule to be suitable for applications in OLEDs devices.

CHAPTER IV

THE SYNTHESIS AND CHARACTERIZATION OF THERMALLY ACTIVATED DELAYED FLUORESCENCE DENDRIMERS FOR ORGANIC LIGHT-EMITTING DIODES

4.1 Introduction

As mentioned in Chapter III, an efficient thermally activated delayed fluorescence material has been designed and synthesized by using D-π-A-π-D system leads to a twisted molecule and spatial distribution between the HOMO of donor and LUMO of the acceptor in order to improve the efficiency of OLED devices. The TADF materials are also divided into small molecules, polymers, and dendrimers. The expected results of the dendritic structure of dendrimers are reduced or eliminate strong intermolecular interactions and aggregation that often lead to excimer formation and reduced emission quantum yields due to π-π-stacking interaction of the linear molecules (Kwon, Alam, and Jenekhe, 2004). The light emission of dendrimers can be tuned by changing the core moieties, their solubility can be adjusted by changing the proper surface groups, and their level of intermolecular interactions can be controlled by the type and generation of the dendrons employed. Therefore, in this chapter, we synthesized and investigated new dendrimers based on TADF materials.

In 2004, three new electron-acceptor and light-emitting conjugated dendrimers, (G1-4Q, **140**), (G1-6Q, **141**), and (G2-12Q, **142**), based on a benzene core, poly(phenylene vinylene) dendrons, and diphenylquinoline peripheral groups have been reported by Kwon et al. All dendrimers exhibited blue emission with the high fluorescence quantum yields in the range of 0.69-0.87 and fluorescence lifetimes in the range of 1.4-1.6 ns (Figure 4.1).

Blue TADF dendrimers, which composed of pyrene core, 2-(4-*tert*-butylphenyl)-5-(4-biphenyl)-1,3,4-oxadiazole (PBD) and different carbazole group, 3,6-di-*tert*-butyl-9-phenylcarbazole (CAB) for D1 (**143**) and TPA for D2 (**144**) have been synthesized and characterized (Figure 4.2). The results revealed that D1 (**143**) emit a pure blue emission from the pyrene core without ICT character, while D2 displays ICT in highly polar solvents from both pyrene and PBD core. Besides that, the OLED devices gave a pure blue emission with CIExy of (0.16, 0.12) with a peak current efficiency of 0.21 cd/A and a peak luminance of 2700 cd/m^2 (G. Zhang et al., 2016).

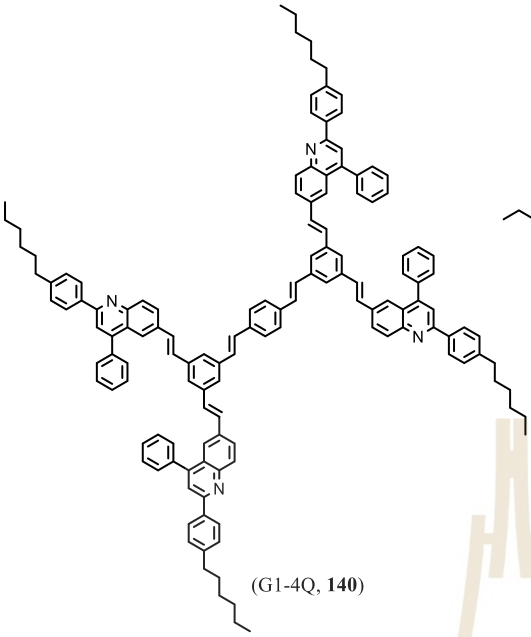

(G1-4Q, **140**)

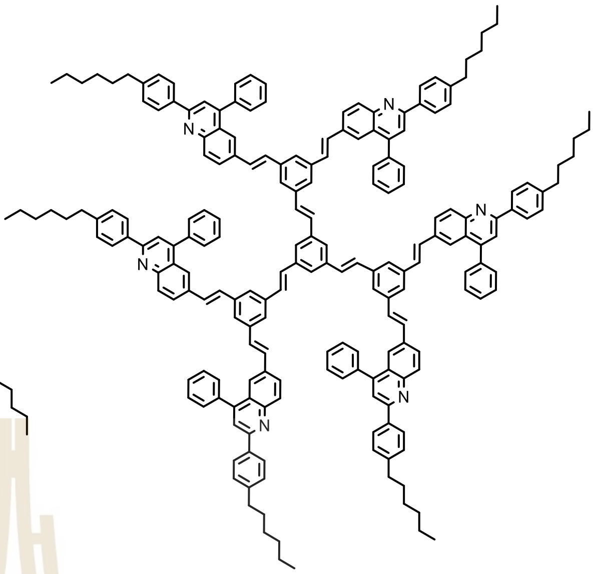

(G1-6Q, **141**)

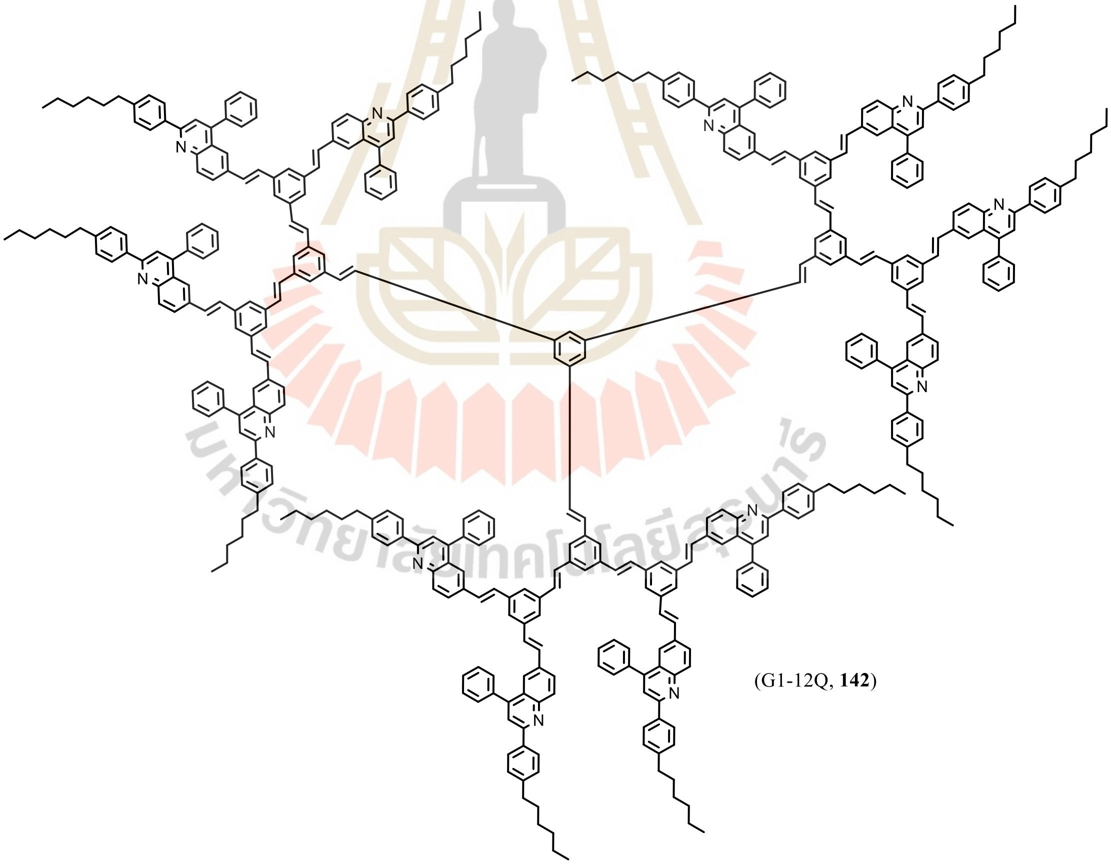

(G1-12Q, **142**)

Figure 4.1 The molecular structure of dendrimers (**140-142**).

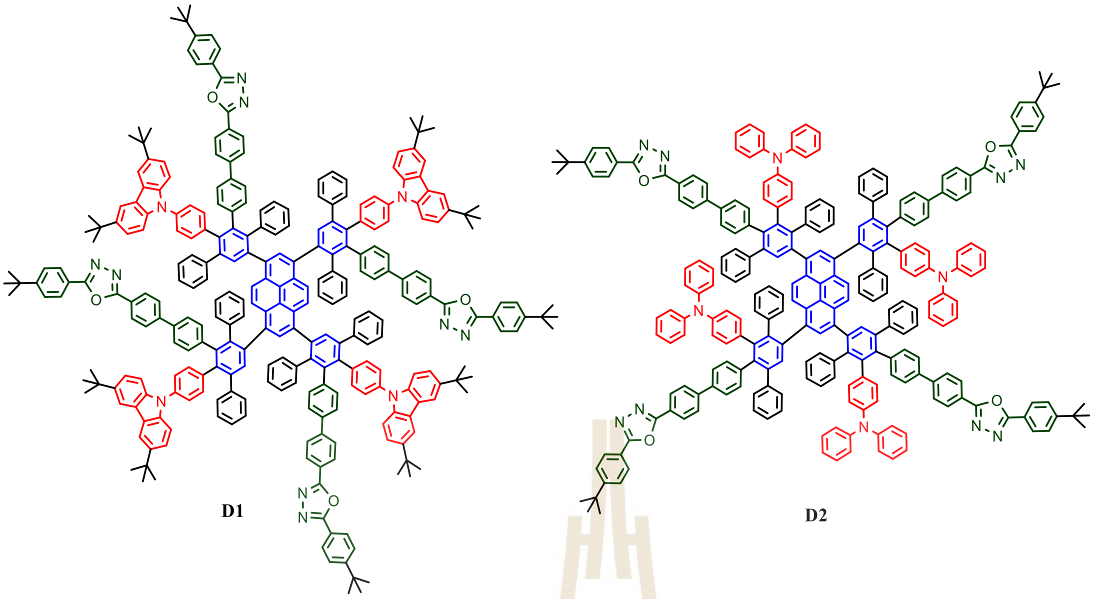

Figure 4.2 Molecular structures of donor-acceptor dendrimers D1 (**143**) and D2 (**144**).

Two new carbazole-dendronized TADF emitters, which consisting of carbazole dendrons and bis(4-(9,9-dimethylacridin-10(9H)-yl)phenyl) methanone (DMAC-BP) as a core, CDE1 (**145**) and CDE2 (**146**) have been synthesized and investigated. They exhibited excellent thermal stability, good solution processability, and an obvious TADF feature. In neat film, their emission peak is blue-shifted with the increasing generation of the carbazole dendrons, indicating that the donor-acceptor feature of CDE2 (**146**) is weaker than that of CDE1 (**145**). The ΔE_{ST} values are 0.11 eV for CDE1 (**145**) and 0.15 eV for CDE2 (**146**), which RISC can easily occur leads to increasing of delayed fluorescence (DF) decay (523 ns for CDE1 (**145**) and 627 ns for CDE2 (**146**)). The non-doped OLED devices were fabricated and exhibited EQE of 13.8%. Their structure is depicted in Figure 4.3 (Y. Li, Xie, Gong, Wu, and Yang, 2016).

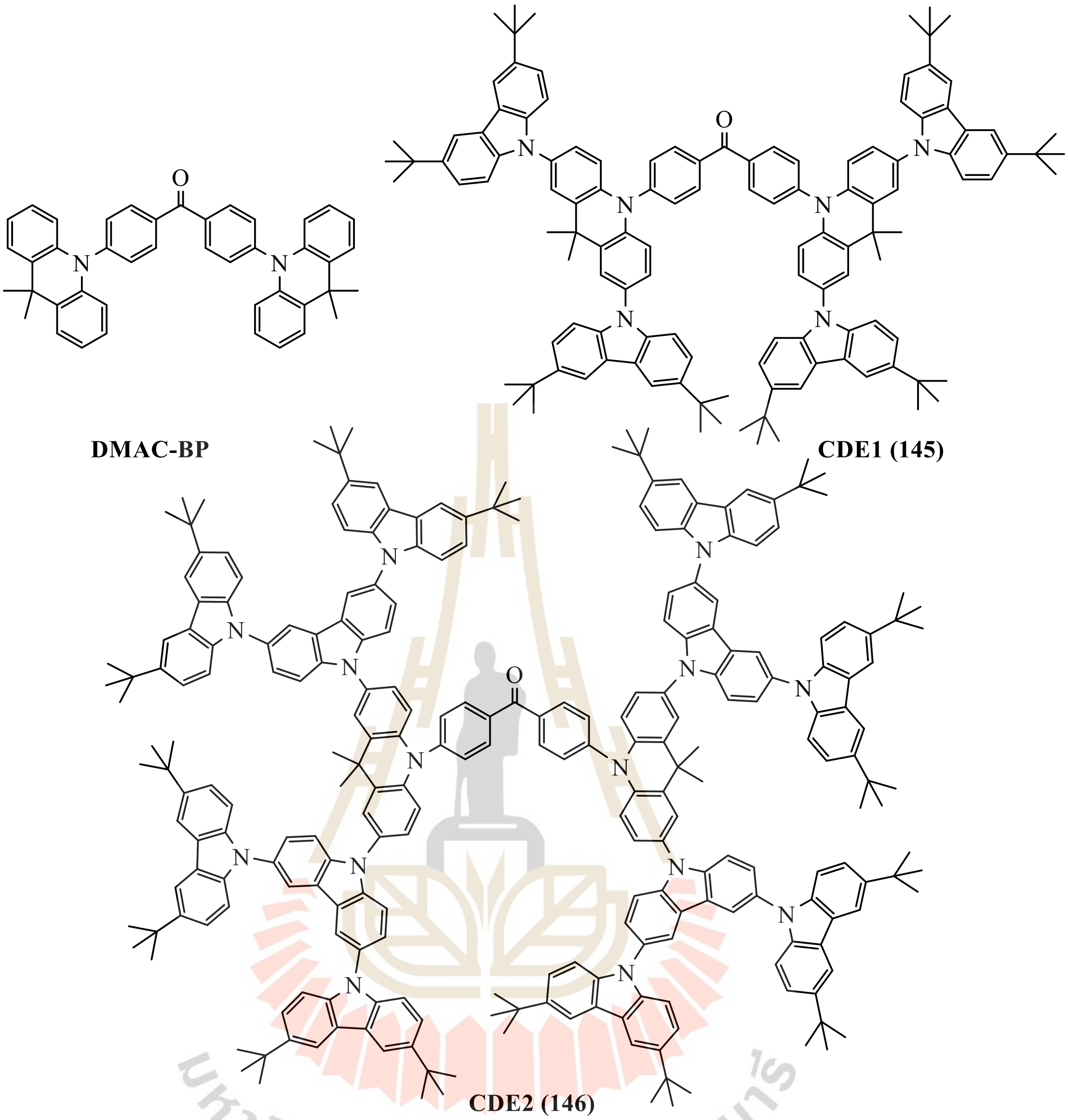

Figure 4.3 Chemical structures of DMAC-BP, CDE1 (**145**) and CDE2 (**146**).

In 2017, two new blue TADF dendrimers G2 (**147**) and G3 (**148**), which composed of a diphenylsulfone core have been reported by Li et al. (Figure 4.4). The results revealed these dendrimers exhibited a reduced singlet-triplet energy gap (ΔE_{ST}) with increasing the dendron generation. The efficient triplet-singlet (T_1-S_1) transition processes, excellent thermal and amorphous stabilities, good solution processability, and appropriate HOMO/LUMO energy levels were suitable for used as non-doped emitting layers for solution-processed OLEDs. The **G2** (**147**) device achieved deep-blue light with an emission peak at 428 nm, a CIE coordinate at (0.15, 0.12) and relatively low-efficiency roll-off at high current density (J. Li et al., 2017).

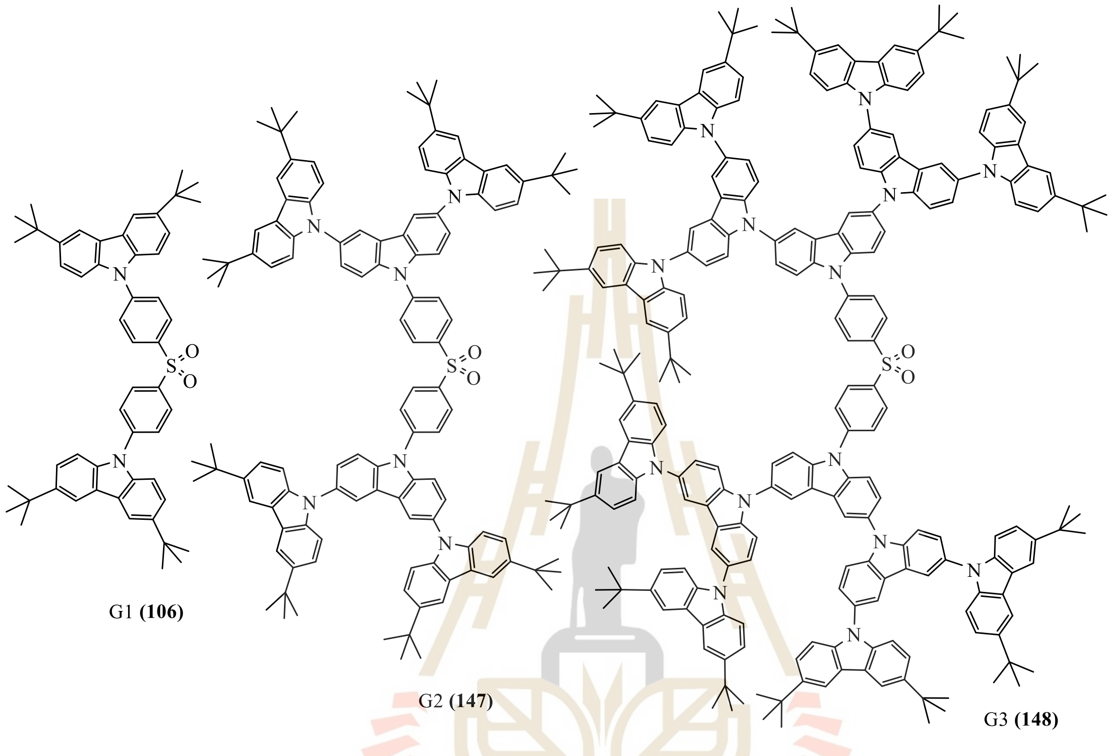

Figure 4.4 The molecular structures of dendrimers G1 (**106**), G2 (**147**), and G3 (**148**).

TADF carbazole dendrimer (^{t}BuG2TAZ, **149**) doped in a carbazole dendrimer host G3Ph **(150**), G4Ph (**151**) has been used as an emissive layer (EML) in a solution-processed OLED device. ^{t}BuG2TAZ doped in G3Ph exhibited green emission (λ_{MAX} = 502 nm) with a maximum external efficiency (EQE_{MAX}) of 16.1% (Albrecht, Matsuoka, Fujita, and Yamamoto, 2018). Their molecular structures are shown in Figure 4.5.

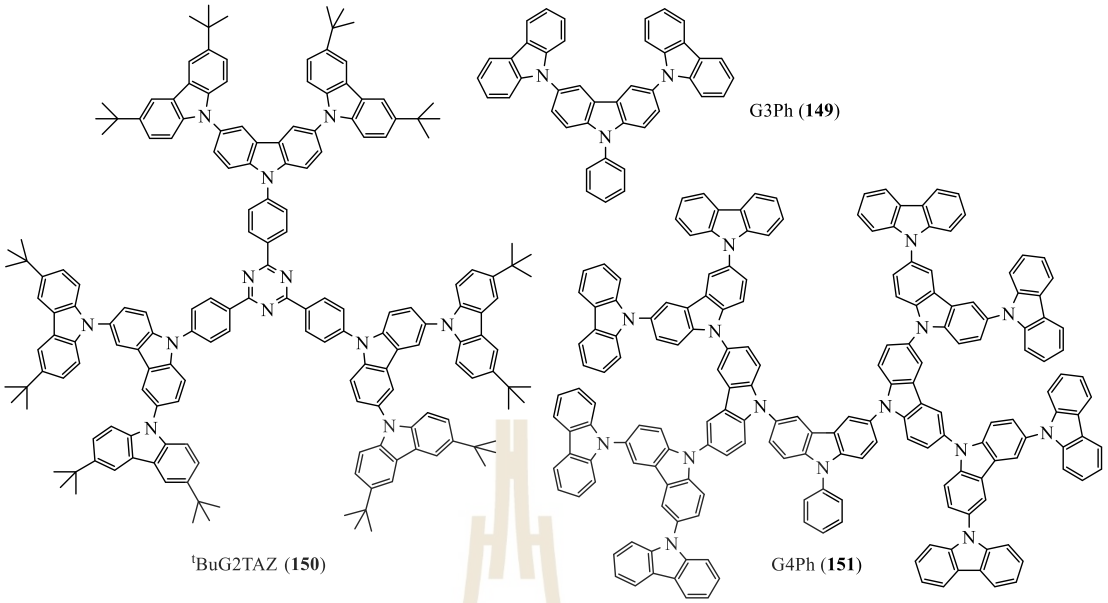

Figure 4.5 The molecular structures of ^{t}BuG$_2$TAZ, (**149**), G$_3$Ph **(150)**, and G$_4$Ph **(151)**.

Besides that, Maasoumi et al. reported the synthesis of poly(dendrimer) containing *fac*-(2-phenylpyridyl)iridium(III) core and fluorenyl-carbazole dendrons, which used as the emitter in the solution-processed OLED device and exhibited an external quantum efficiency of >20% (Maasoumi et al., 2018).

In the same period, the dendrimers with bi-function which are TADF and exciplex-forming, G-TCTA and G-mCP have been synthesized. The introduction of exciplex-forming dendrons into a green TADF emissive core by using a non-conjugated alkyl chain in order to achieve a TADF feature with a reducing the driving voltages by eliminating the injection barrier. The results reveal that a nondoped device of G-mCP achieves an extremely low driving voltage of 2.7 V and high power efficiency of 46.6 lm W^{-1} (Sun et al., 2018).

From the previous work of our group, we success to synthesize the carbazole dendrimers up to the fourth generation and investigate the performance of the OLED devices. Their molecular structure is shown in Figure 4.6. They showed significantly high Tg, amorphous and stable electrochemical properties, and great potential as solution-processed hole-transporting materials for OLEDs. Alq3-based green devices exhibited high luminance efficiency and CIE coordinates of 4.45 cd A^{-1} and (0.29, 0.53), respectively (Moonsin et al., 2012).

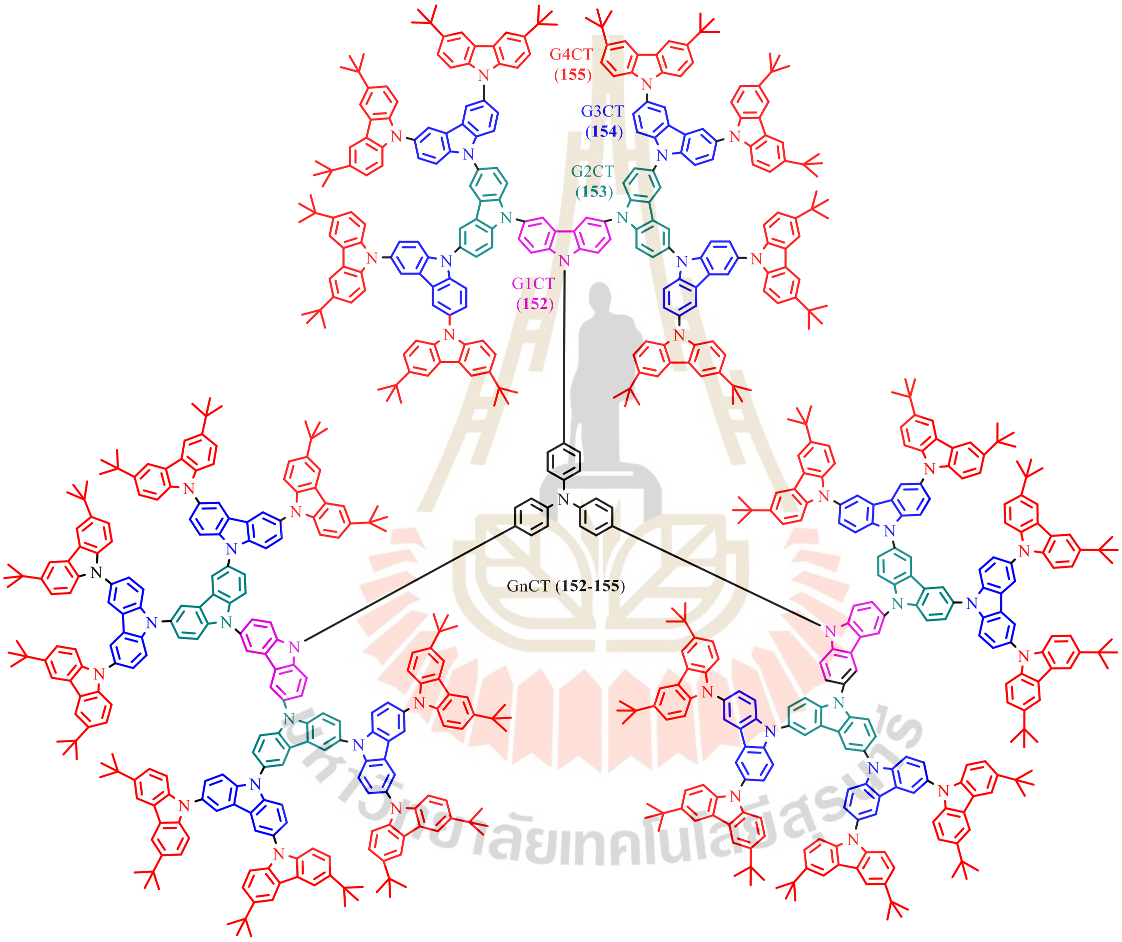

Figure 4.6 Molecular structures of GnCT **(152-155)**.

After that, we reported the synthesis of a series of novel red-emitting bis[5-(fluoren-2-yl)thiophen-2-yl]benzothiadiazole-cored dendrimers **(156-158)** containing carbazole dendrons up to the third generation and the investigation of the solution-processed red OLED device fabrication and performance is also reported. Their molecular structure is shown in Figure 4.7. The end caps carbazole dendrons reduce the crystallization and retain the high emissive ability of a planar fluorescent core in the solid-state as well as improve the thermal stability with high Tg at 283°C. The solution-processed OLEDs was fabricated and exhibited a red emission color with the wavelength in the range of 622−645 nm, with high luminance efficiencies (up to 4.80 cd A^{-1} at 1.2 mA cm^{-2}) and CIE coordinates of (0.65, 0.33), which are close to the pure red color (Prachumrak et al., 2013).

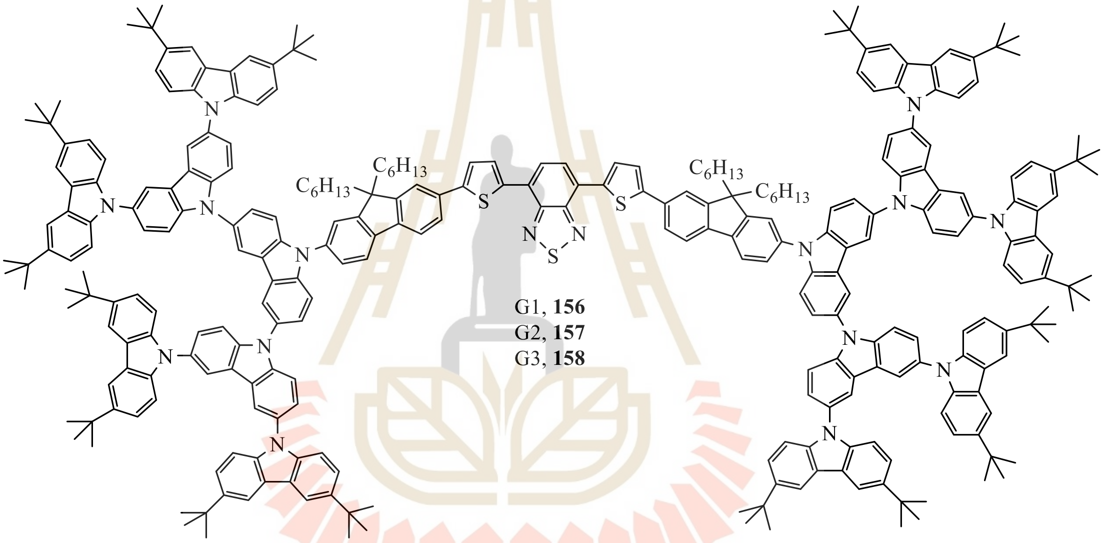

Figure 4.7 Molecular structures of dendrimers **(156-158)**.

Herein, we designed and synthesized the TADF dendrimers by introducing the diphenyl sulfone (DPS) core into the carbazole dendron using a non-conjugated fluorene hexyl as a linker in order to retain the TADF feature and reducing the driving voltages and π-π-stacking interaction of the linear molecules. Their properties were also investigated.

4.2 Research objectives

4.2.1 To design, synthesize and characterize of TADF dendrimers materials as an emitter for OLEDs

4.2.2 To identify the desired molecules by ^{1}H-NMR, ^{13}C-NMR, and Mass spectroscopy

4.2.3 To study the photophysical, electrochemical, and thermal properties by using UV-Visible spectroscopy, fluorescence spectroscopy, cyclic voltammetry, and DSC-TGA techniques

4.3 Synthetic procedure

4.3.1 Synthetic procedure

The desired TADF dendrimers should be obtained by alkylation of *bis*(4-fluorophenyl) sulfone with 2,7-dibromocarbazole to afford key intermediate and followed by Suzuki cross-coupling reaction with fluorene borolane which obtained from borylation of various Bromo fluorene. After purification by chromatography and recrystallization, the desired products should be obtained as outlined in Figure 4.8.

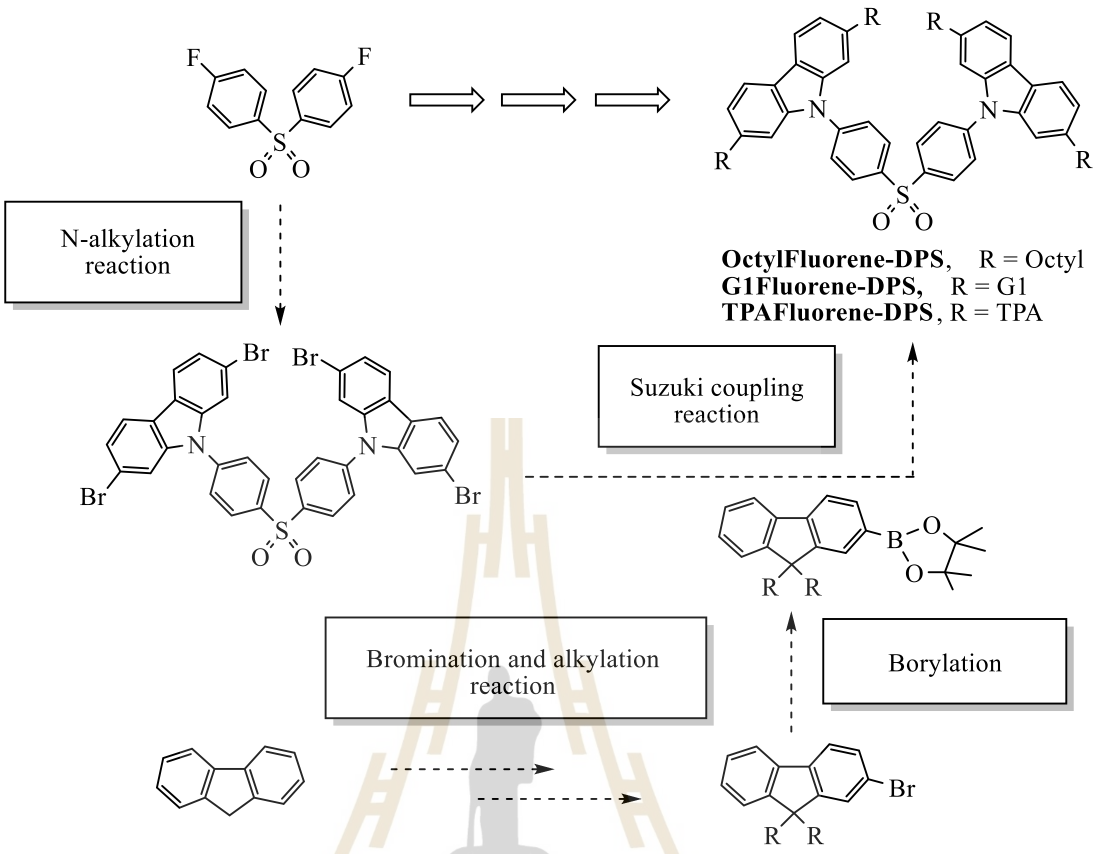
N-alkylation reaction
OctylFluorene-DPS, R = Octyl
G1Fluorene-DPS, R = G1
TPAFluorene-DPS, R = TPA
Suzuki coupling reaction
Bromination and alkylation reaction
Borylation

Figure 4.8 Synthetic approach to the synthesis of the TADF dendrimers.

4.3.2 Preparation of the key intermediate sulfone 160

N-alkylation of **159** with 2,7-dibromocarbazole in the presence of sodium hydride in dimethyl formamide (DMF) at 100°C for 24 hr provided the corresponding sulfone **160**. After purification by recrystallization in CH_2Cl_2/Methanol the desired product **160** was obtained in 35% overall yield as shown in Figure 4.9.

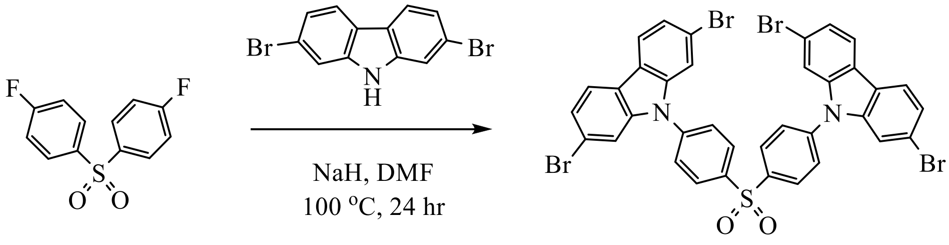
NaH, DMF
100 °C, 24 hr

159

160

Figure 4.9 Preparation of the key intermediate sulfone **160**.

4.3.3 Preparation of 2-bromo fluorene 162

Bromination of **161** with bromine using ferric chloride as Lewis acid in dichloromethane at room temperature to afforded 2-bromo fluorene **162**. After purification by column chromatography and recrystallization in CH_2Cl_2/Methanol the desired product **162** was obtained in 24% overall yield as shown in Figure 4.10.

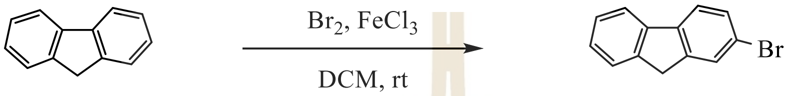

161 **162**

Figure 4.10 Preparation of 2-bromo fluorene **162**.

4.3.4 Preparation of bromo hexyl fluorene 164

Bromo hexyl fluorene **164** was obtained from alkylation of 2-bromo fluorene **163** with 1,6-dibromohexane in the presence of Tetra-*n*-butylammonium bromide (TBAB) in 50 wt% NaOH at room temperature for 24 hr. After purification by column chromatography, the product **164** was obtained in 66% overall yield, respectively (Figure 4.11).

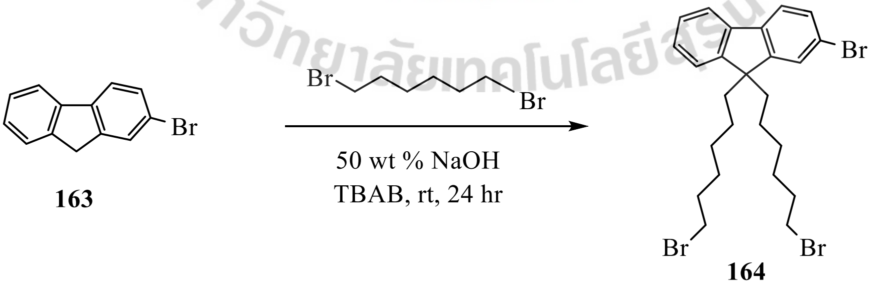

163 **164**

Figure 4.11 Preparation of Bromo hexyl fluorene **164**.

4.3.5 Preparation of G1hexyl fluorene bromide 165

G1hexyl fluorene bromide **165** was obtained from the *N*-alkylation of 2-bromo-9,9-*bis*(6-bromohexyl) fluorene **164** with G1 (**73**) in the presence of potassium hydroxide as a base in DMF at room temperature for 12 hr. After purification by column chromatography and recrystallization in CH_2Cl_2/Methanol the desired product **165** was obtained in 89% overall yield as shown in Figure 4.12.

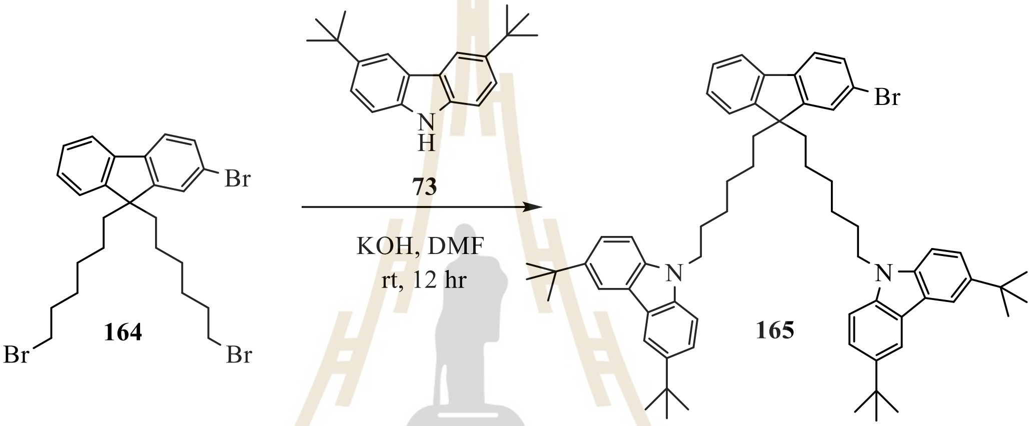

Figure 4.12 Preparation of 2-bromo-9,9-*bis*(6-bromohexyl) fluorene **165**.

4.3.6 Preparation of TPAfluorene bromide 167

TPAfluorene bromide **167** was obtained from 2-bromo-fluorenone **166** reacted with triphenylamine in methanesulfonic acid. After purification by column chromatography and recrystallization in CH_2Cl_2/Methanol the desired product **167** was obtained in 65% overall yield as shown in Figure 4.13.

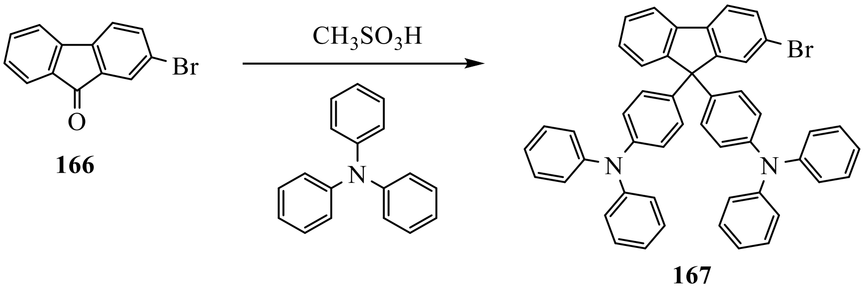

Figure 4.13 Preparation of TPAfluorene bromide **167**.

4.3.7 Preparation of fluorene boronates 170 and 172

The Miyaura borylation reaction enables the synthesis of fluorene borolane **170** and **172** by cross-coupling of bis(pinacolato)diboron (B_2pin_2) with aryl halides (**165** and **167**) using [1,1′-Bis(diphenylphosphino)ferrocene]dichloropalladium(II) palladium as catalyst in the presence of potassium acetate in toluene as shown in Figure 4.14.

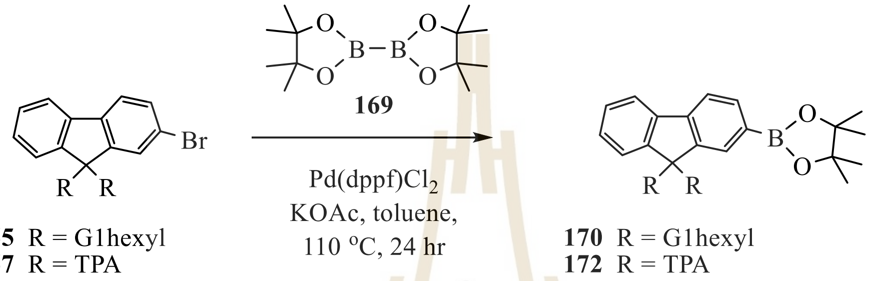

Figure 4.14 Preparation of fluorene boronates **170** and **172**.

The [1,1′-Bis(diphenylphosphino)ferrocene]dichloropalladium(II) was activated to palladium(0) followed by the oxidative addition of the aryl halide. Then the formation of an (acetato)palladium(II) complex was achieved and transmetalation with bis(pinacolato)diboron (B_2pin_2) can be attributed to the high reactivity of Pd–O bond which consists of soft acid and a hard base (HSAB concept). Subsequently, reductive elimination of the fluorene boronates **170** and **172** in the yield of 81 and 86%, respectively and takes place along with the catalyst regeneration. The proposed catalytic cycle for the borylation of aryl halides described by Miyaura is shown in Figure 4.15 (Chow et al., 2013).

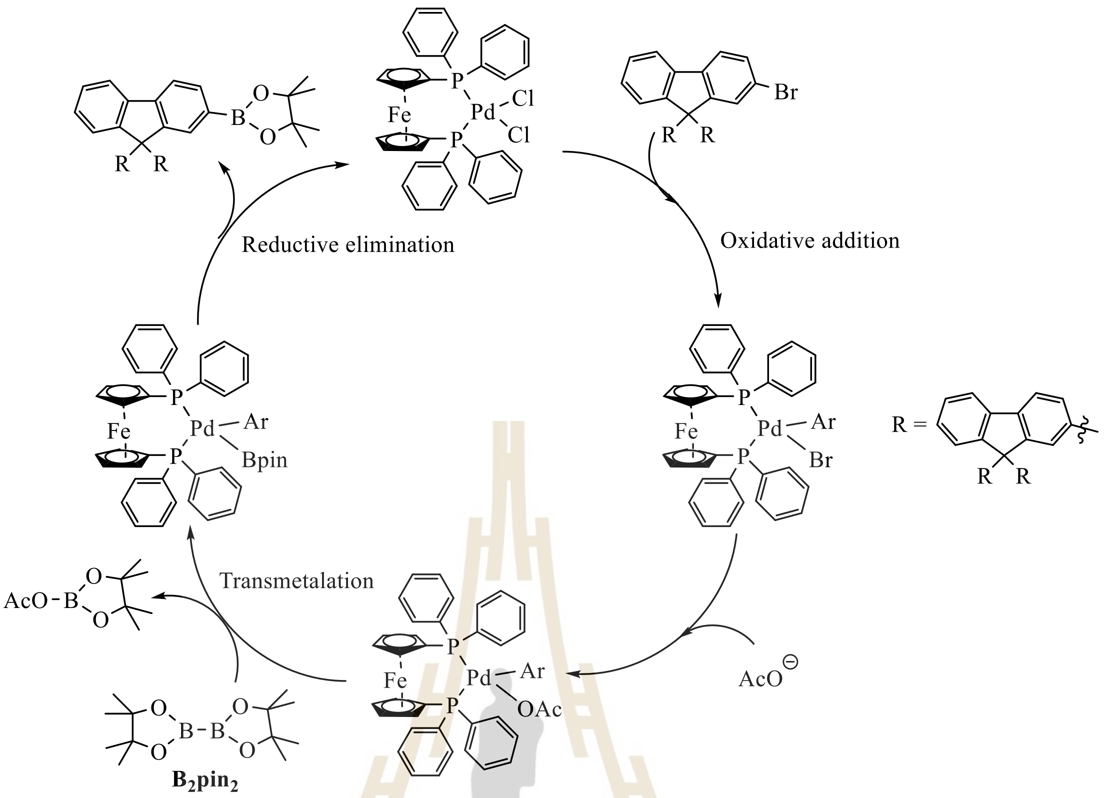
Reductive elimination
Oxidative addition
Transmetalation
Fe
Pd
P
Cl
Br
R R
Ar
Bpin
OAc
AcO⊖
AcO-B
R =
B_2pin_2

Figure 4.15 The proposed mechanism for the borylation of aryl halides.

4.3.8 The synthesis of TADF dendrimers 14-16

The fluorene boronates **170-172** were employed as starting materials for the synthesis of TADF dendrimers **14-16** by reacted with key intermediate sulfone **160** according to the Suzuki coupling reaction as shown in Figure 4.16.

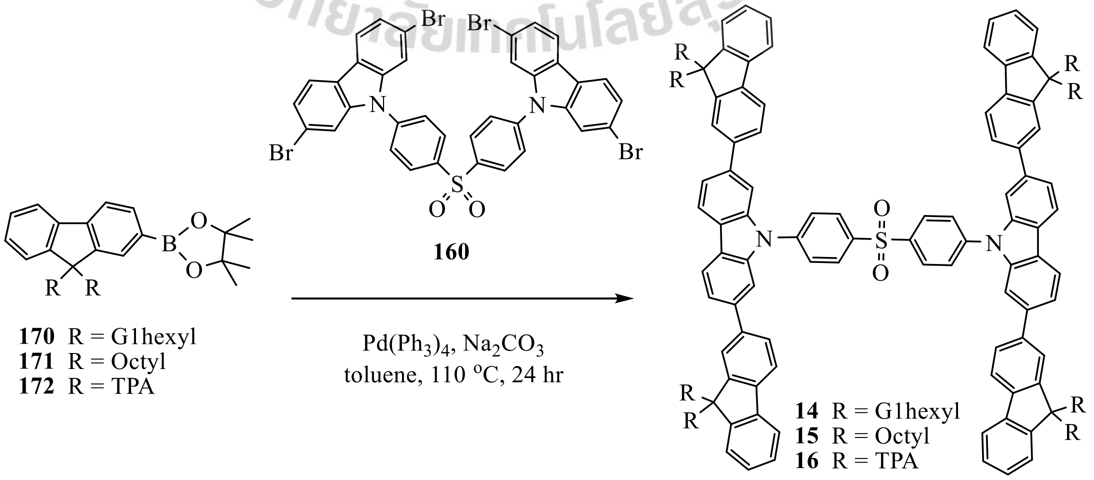
160
170 R = G1hexyl
171 R = Octyl
172 R = TPA
$Pd(Ph_3)_4$, Na_2CO_3
toluene, 110 °C, 24 hr
14 R = G1hexyl
15 R = Octyl
16 R = TPA
Br
N
S
O
B
R

Figure 4.16 The synthesis of TADF dendrimers **14-16**.

The TADF dendrimers could be obtained by the Suzuki coupling reaction which the reaction starts with the oxidative addition of palladium (0) to the organic halide starting material to form the organopalladium species. Subsequently, metathetic exchange with base gives intermediate, which via transmetalation with the phenylboronic acid forms the oganopalladium species. Finally, reductive elimination of the desired products as mentioned in chapter III. The fluorene boronates **170-172** were reacted with intermediate sulfone **160** in the presence of sodium carbonate as base via Suzuki reaction to give the desired products **14, 15** and **16** in a moderate yield of 82%, 49, and 58%, respectively. After purification, their structures were confirmed by ^{1}H NMR, ^{13}C NMR, and HRMS spectrometric methods.

The structure of G1hexylfluorene-DPS (**14**) was confirmed by ^{1}H-NMR spectroscopy. The ^{1}H-NMR spectrum showed doublet of the para position of phenyl linker at δ = 8.17 (4H) and 7.63 (4H) ppm with the coupling constant (*J*) of 8.6 Hz. The carbazole protons produce singlet signals at δ = 8.05 (4H) and multiplet signals at δ = 7.69 (4H) and 7.58 (4H) ppm. The fluorene protons produce multiplet signals at δ = 7.70 (8H), 7.57 (8H) and 7.19 (12H) ppm. The carbazole of the first generation of dendron produces singlet signals at δ = 8.04 (16H) ppm and doublet signal at δ = 7.38 (16H) and 7.11 (16H) ppm. The methylene proton at the near *N*-atom of carbazole position show triplet signal at δ = 4.00 (16H) ppm, the methyl proton of *tert*-butyl group show singlet signal at δ = 1.39 (144H) ppm, and another alkyl proton showed signals at δ = 1.96 (16H), 1.57 (16H), 1.06 (32H), and 0.62 (16H) ppm. The ^{13}C-NMR spectrum showed the chemical shift of carbon signals in the range of δ = 151.3-107.9 ppm can be assigned as aryl carbon and δ = 55.0-23.6 ppm can be assigned as alkyl carbon.

Moreover, High resolution mass spectrometry confirmed the identity of the compound with m/z (HRMS) = 4095.5078 (required m/z = 4094.6219).

The structure of octylfluorene-DPS (**15**) was confirmed by ^{1}H-NMR spectroscopy. The ^{1}H-NMR spectrum showed doublet of the para position of phenyl linker at δ = 8.-7 (4H) and 8.00 (4H) ppm with the coupling constant (*J*) of 9.2 Hz. The carbazole protons produce singlet signals at δ = 7.77 (4H) and doublet signals at δ = 8.23 (4H) and 7.72 (4H) ppm with the coupling constant (*J*) of 8.1 Hz. The fluorene protons produce multiplet signals at δ = 7.27-7.66 (28H) ppm. The methylene proton at the near position of C-fluorene shows signal at δ = 1.99 (16H) ppm, and another alkyl proton showed signals at δ = 1.18-0.66 (136H) ppm. The ^{13}C-NMR spectrum showed the chemical shift of carbon signals in the range of 151.6-108.2 ppm can be assigned as aryl carbon and 55.2-14.0 ppm can be assigned as alkyl carbon. Moreover, High resolution mass spectrometry confirmed the identity of the compound with m/z (HRMS) = 2101.8084 (required m/z = 2101.4079).

The structure of TPAfluorene-DPS (**16**) was confirmed by ^{1}H-NMR spectroscopy. The ^{1}H-NMR spectrum showed doublet of the para position of phenyl linker at δ = 8.21 (4H) and 7.86 (4H) ppm with the coupling constant (*J*) of 8.4 Hz. The carbazole protons produce singlet signals at δ = 7.74 (4H) and doublet signals at δ = 8.14 (4H) and 7.75 (4H) ppm with the coupling constant (*J*) of 8.1 Hz. The fluorene protons produce multiplet signals at δ = 7.70-7.40 (28H) ppm. The proton of the triphenylamine group shows a signal at δ = 7.18-6.88 (112H) ppm. The ^{13}C-NMR spectrum showed the chemical shift of carbon signals in the range of 152.4-108.1 ppm can be assigned as aryl carbon. Moreover, High resolution mass spectrometry confirmed the identity of the compound with m/z (HRMS) = 3149.8115 (required m/z = 3149.2446).

4.4 Results and discussion

4.4.1 Optical properties

The UV-vis absorption and fluorescence spectra of the TADF dendrimer were investigated in dilute toluene solution (10^{-5}-10^{-6} M) and the neat film by UV-vis and photoluminescence spectroscopies as shown in Figure 4.17. All dendrimers **14-16** exhibited absorption bands around 350 nm corresponding to the π-π* transition of the carbazole moieties without ICT character for **14** and **15**, while the dendrimer **16** showed the absorption band around 310 nm corresponding to the π-π* transition with strong ICT character from TPA donor moieties appears as a shoulder below the π-π* absorption peak. The fluorescence spectra of TADF emitters exhibited blue emission in toluene with a maximum wavelength at 353, 354, and 313 nm for **14**, **15**, and **16**, respectively. The fluorescence spectra in neat films are slightly redshift to those in toluene. The photophysical data of TADF dendrimers were listed in Table 4.1. The energy gap (E_g^{opt}) of all materials which calculated from the onset wavelength of absorption spectra were in the range of 3.18-3.21 (eV). All TADF compounds exhibited the singlet state (S_1) which calculated from the onset of the fluorescence spectra in the range of 3.72-3.75 (eV).

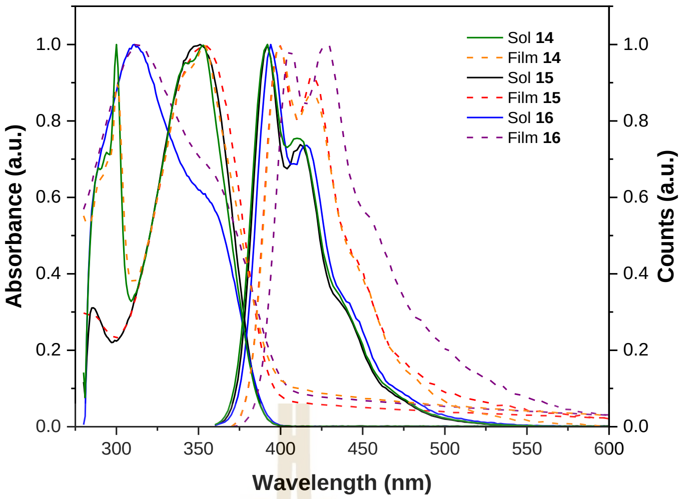

Figure 4.17 UV-vis absorption and fluorescence spectra of TADF dendrimer **14-16** in dilute solution in toluene (10^{-5} M) and in solid film.

Table 4.1 Photophysical properties of TADF dendrimers.

Compds	**Solution**	**Film**	λ^{abs}_{onset} [a] **(nm)**	E_g^{opt} [b] **(eV)**	λ^{flu}_{onset} [c] **(nm)**	S_1 [d] **(eV)**
	λ_{UV} **(log** ε**) /**λ_{em} **(nm/M^{-1}cm^{-1})**	λ_{UV} **/**λ_{em} **(nm)**				
G1hexylfluorene-DPS (**14**)	353(4.87)/410	353/419	386	3.21	372	3.72
Octylfluorene-DPS (**15**)	349 (4.91)/412	354/421	387	3.21	373	3.73
TPAfluorene-DPS (**16**)	310 (4.75)/415	313/428	390	2.18	375	3.75

[a] The onset of the absorption spectra.

[b] Calculated from the absorption spectra threshold, $E_g^{opt} = 1240/\lambda_{onset}$.

[c] The onset of the fluorescence spectra.

[d] Calculated from the onset of the fluorescence spectra.

4.4.2 Commission International de l’Eclairage (CIE)

Chromaticity diagram and CIExy values of all TADF dendrimers in dilute toluene solution and in the neat film are shown in Figure 4.18 and summarized in Table 4.2. The results revealed that all TADF dendrimers **14-16** exhibited the CIExy values in the blue emission region.

Table 4.2 CIE(x,y) coordinates of TADF dendrimer **14-16**.

Compounds	**CIE^{sol} (x,y)**	**CIE^{film} (x,y)**
G1hexylfluorene-DPS (**14**)	(0.160, 0.032)	(0.163, 0.062)
Octylfluorene-DPS (**15**)	(0.160, 0.029)	(0.172, 0.095)
TPAfluorene-DPS (**16**)	(0.160, 0.036)	(0.165, 0.107)

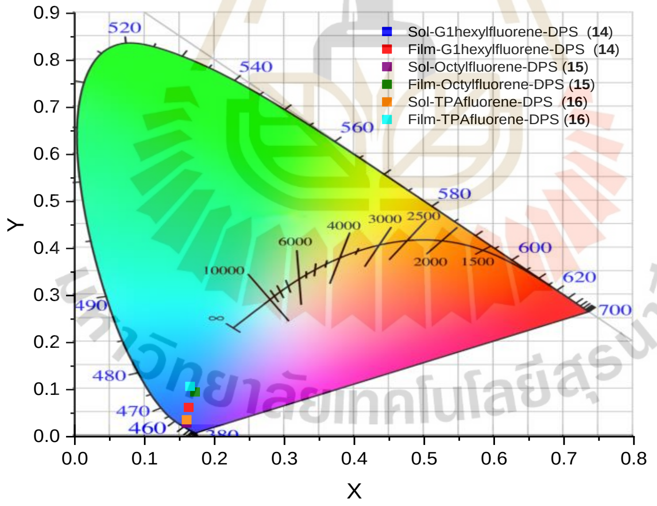

Figure 4.18 Chromaticity diagram of all TADF dendrimers **14-16** in dilute solution in toluene (10^{-5} M) and in solid neat film.

4.4.3 Emission decays

As illustrated in chapter III, the TADF characteristic can be confirmed by the emission decay, which measured in dilute toluene solution (10^{-6} M) under argon and oxygen atmosphere. The results revealed that the transient PL decay of all compounds displayed two components, the first component is a fast decay which can be assigned to prompt fluorescence which arising from $S_1 \rightarrow S_0$ transition and the second component is a slower one which can be assigned to delayed fluorescence which arising from repopulation of the S_1 through RISC from the T_1 followed by $S_1 \rightarrow S_0$ transition. The lifetimes of prompt and delayed fluorescence were summarized in Table 4.3. The lifetimes were estimated to be 20-42 ns for prompt fluorescence and 112-302 ns for delayed fluorescence under the argon atmosphere. The emission decay of all TADF **14-16** in toluene under argon and oxygen atmosphere at room temperature are shown in Figure 4.19.

Table 4.3 The lifetimes of prompt and delayed fluorescence of TADF dendrimers **14-16**.

Compds	**τ_P (ns) in solution (τ_{air}/τ_{Ar})**	**τ_d (ns) in solution (τ_{air}/τ_{Ar})**
G1hexylfluorene-DPS (**14**)	21.5/41.8	310.1/166.1
Octylfluorene-DPS (**15**)	-/20.1	264.8/302.6
TPAfluorene-DPS (**16**)	23.8/24.5	228.0/112.4

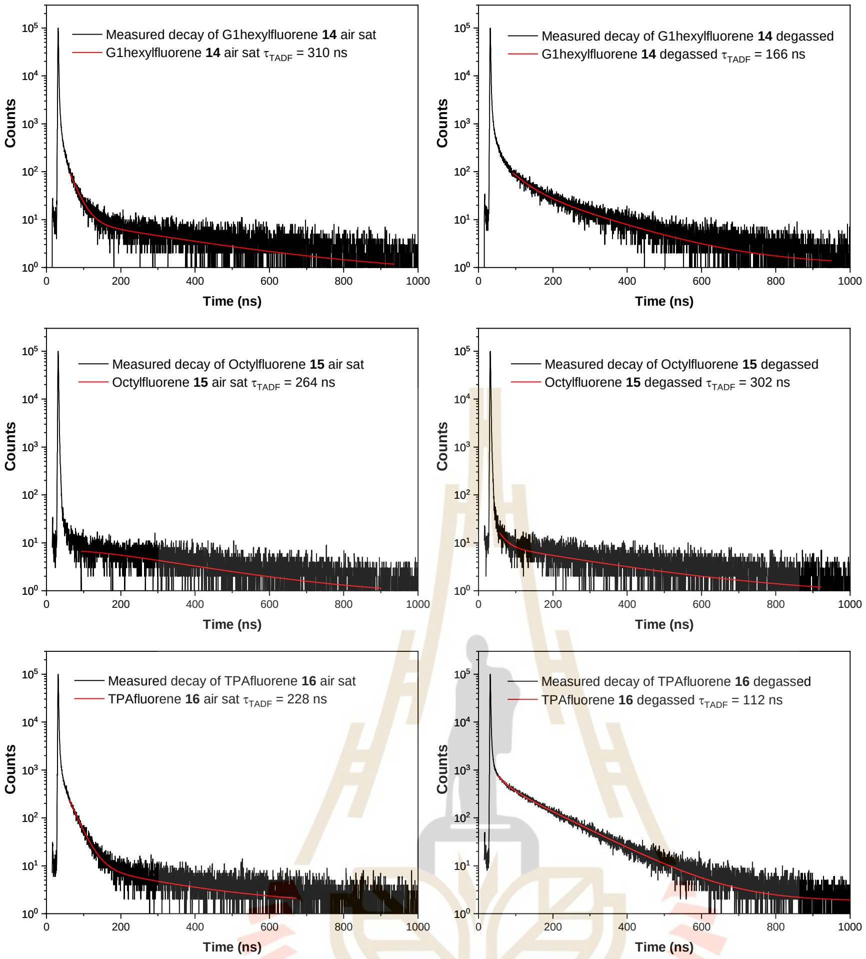

Figure 4.19 The emission decay and fit tail of TADF dendrimers **14-16** in toluene under oxygen and argon atmosphere at room temperature.

4.4.4 Oxygen quenching of the photoluminescence quantum yield

The RISC of TADF emission can be quenched by oxygen molecules (O_2) as mentioned in the previous chapter. Therefore, the TADF character can be check by measurement of the emission decay in the absence and presence of oxygen. The results revealed that TADF dendrimers **14** and **16** can be observed the change in emission intensity when exposed in argon. On the other hand, TADF dendrimers **15** exhibited identical spectra in both oxygen and argon atmosphere, it might be from the molecule of **15** has no intramolecular charge transfer due to the donor-acceptor system. The emission spectra of all compounds are shown in Figure 4.20.

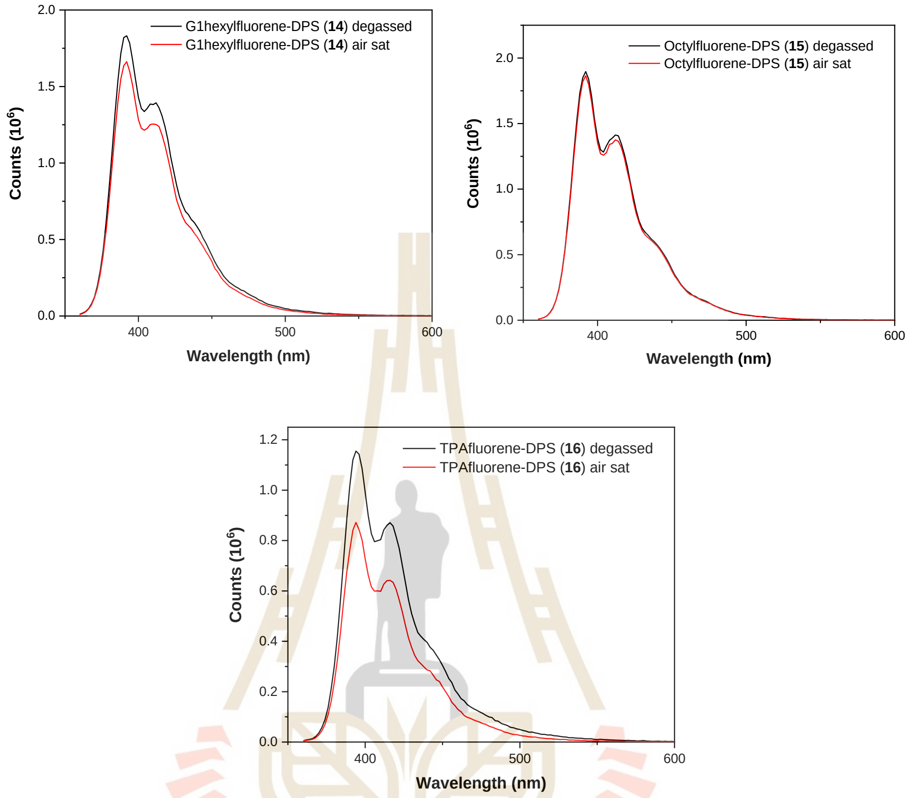

Figure 4.20 Emission spectra of all TADF dendrimers **14-16** in degassed solution (black) and non-degassed solution (red) in toluene (10^{-5} M).

4.4.5 Solvatochromic behaviors

In order to investigate the solvatochromic behavior of all TADF dendrimers **14-16**, toluene, chloroform, dichlorobenzene, tetrahydrofuran, and acetonitrile were selected to dissolve the study compounds in UV-vis and fluorescence measurement. The results revealed that both UV-vis and emission spectra of **14** and **15** could not be observed the bathochromic shifted in polar solvent due to the ICT behavior. It could be suggested that non-conjugated donor and acceptor moieties linker by using alkyl chain resulting in their ICT character. On the other hand, the dendrimer **16** exhibited a slightly bathochromic shifted in polar solvent due to the ICT behavior. The absorption spectra and emission spectra of all TADF **14-16** in different solvents are shown in Figure 4.21.

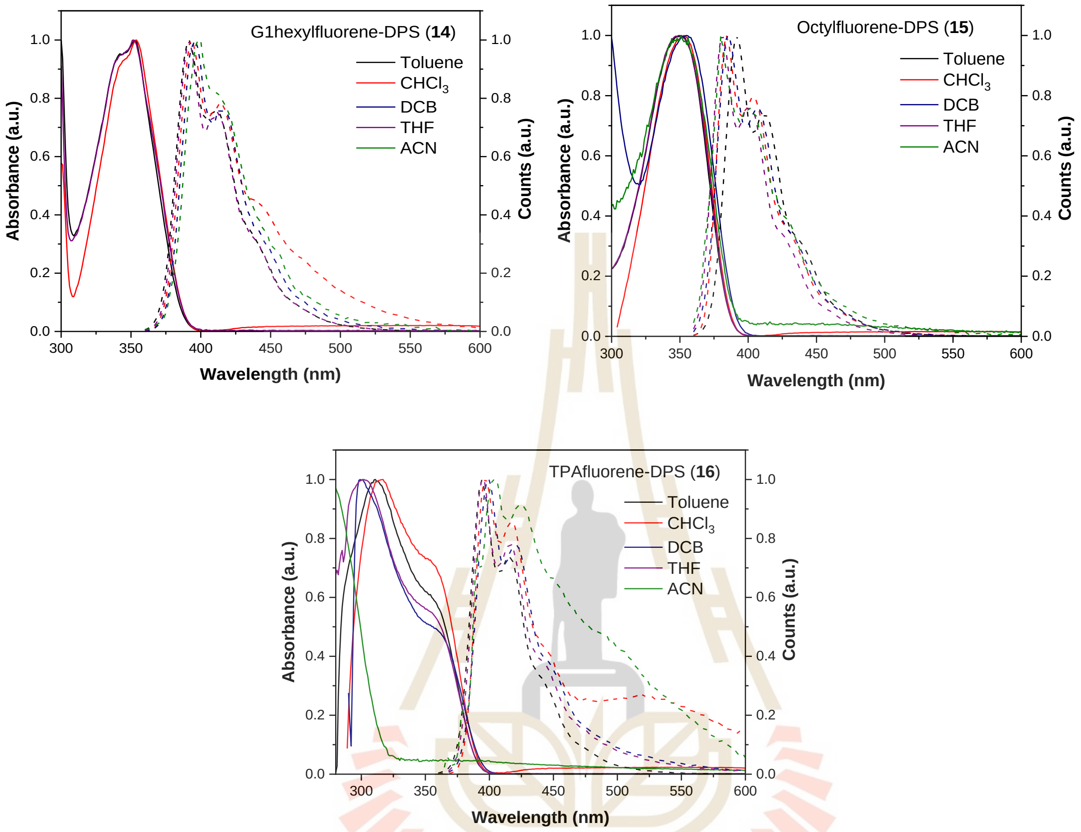

Figure 4.21 UV-vis absorption and fluorescence spectra of TADF dendrimer **14-16** in various solvent.

Besides that, the solvatochromic behavior can be confirmed by using the plots of stokes shift versus solvent polarity parameter (Δ*f*), if Δ*f* increase, the stokes shift also increases with a linear correlation. The results revealed that only dendrimer **16** displays the relation between optical properties and the polarity of solvent which might be from the conjugation of TPA and fluorene moieties lead to the formation of large charge separation. The plots of stokes shift versus solvent polarity parameter (Δ*f*) of all TADF dendrimers **14-16** are shown in Figure 4.22.

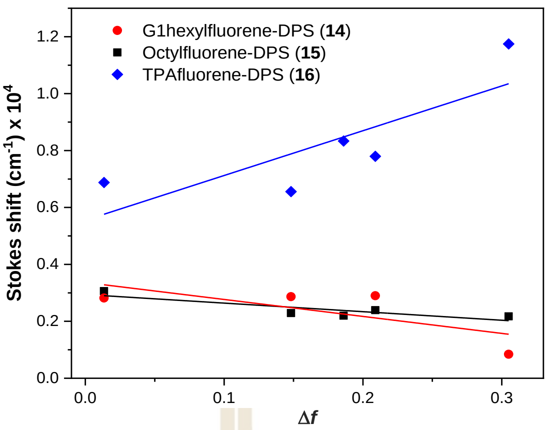

Figure 4.22 The plots of stokes shift versus solvent polarity parameter (Δ*f*) of TADF dendrimers **14-16**.

4.4.6 Electrochemical properties

The electrochemical characteristics of the TADF dendrimers were measured by cyclic voltammetry. All compounds exhibited reversible oxidation processes upon the anodic sweep as shown in Figure 4.23. The first oxidation process assigns to the removal of electrons from the donor, resulting in radical cations. The HOMO levels of all compounds determined from the onsets of the oxidation potentials were in the range of -5.63 to -5.11 eV, which are near to the HOMO values from AC2 method (5.67-5.71 eV). The LUMO levels determined from the onsets of the reduction potentials were in the range of -4.03 t0 -3.73 eV. Electrochemical band gaps (E_g^{ele}) determined using the onsets of the oxidation potentials subtracts by the onsets of the reduction potentials of TADF dendrimers **14**, **15**, and **16** was 1.90, 1.68, and 1.07 eV, respectively. The electrochemical data are summarized in Table 4.4.

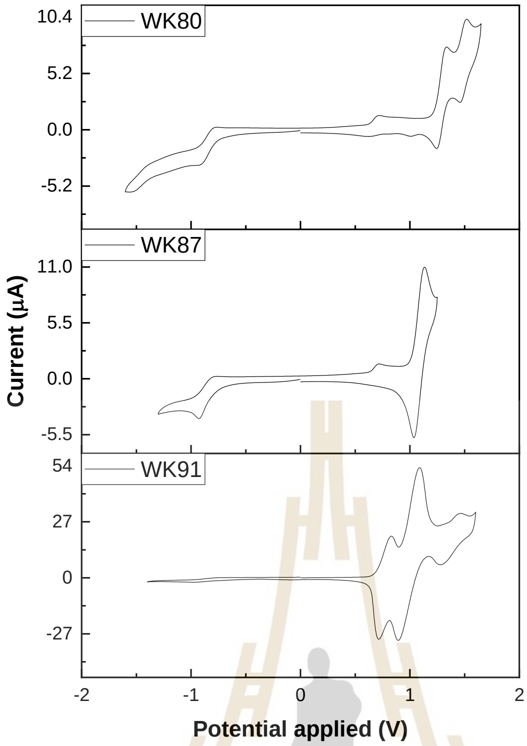

Figure 4.23 CV curves of TADF dendrimers in CH_2Cl_2 solution using 0.1 M Bu_4NPF_6 at a scan rate of 50 mV/s under argon flow.

Table 4.4 Electrochemical properties of all TADF compounds.

Compounds	**HOMO/LUMO from CV (eV)** [e]	$E^{Ox}_{1/2}$ /$E^{Re}_{1/2}$ [h] **vs. Ag/Ag⁺ (eV)** [f]	**HOMO from AC2** [g]	E_g^{ele} [e] **(eV)** [h]
G1hexylfluorene-DPS (**14**)	-5.63/-3.73	1.29/-0.85	5.67	1.90
Octylfluorene-DPS (**15**)	-5.43/-3.75	1.08/-0.86	5.71	1.68
TPAfluorene-DPS (**16**)	-5.11/-4.03	0.78/-0.85	5.68	1.07

[e] Estimated from the onset oxidation and reduction potential using HOMO = $-E^{ox}_{onset}$ - 4.44 eV and LUMO =$-E^{ox}_{onset}$ - 4.44 eV or HOMO + E_g^{opt}.

[f] Obtained from CV measured in CH_2Cl_2–n-Bu_4NPF_6 (0.1 M) at a scan rate of 50 ms^{-1}.

[g] Obtained from AC2 measured in solid neat film.

[h] Electrochemical band gaps determined using E^{ox}_{onset} - E^{red}_{onset}

4.4.7 Thermal properties

The thermal properties of TADF dendrimers **14-16** were determined by differential scanning calorimetry (DSC) and thermogravimetric analysis (TGA). TGAs reveal that their decomposition temperatures (T_{5d}) at 5 wt% weight loss are above 400°C, indicating the high thermal stability. The thermalogram of TADF materials is shown in Figure 4.24 and the data are listed in Table 4.5.

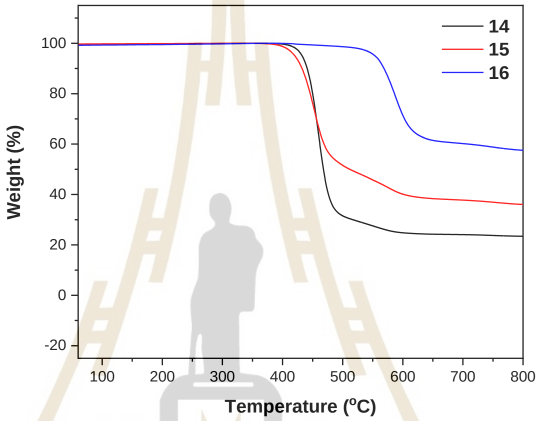

Figure 4.24 TGA thermograms of TADF dendrimers **14-16** measured at a heating rate of 10°C min^{-1} under N_2 flow.

Table 4.5 Thermal properties of all TADF compounds.

Compounds	T_{5d} (°C)	T_g (°C)
G1hexylfluorene-DPS (**14**)	432	162
Octylfluorene-DPS (**15**)	420	77
TPAfluorene-DPS (**16**)	554	250

DSCs (1st and 2nd heating scans) of G1hexylfluorene (**14**) and TPAfluorene (**16**) reveal a distinct glass transition temperature (Tg) of 167 and 260°C, which might be attributed from the rigid structure due to the G1 dendron or TPA end cap moieties at the non-conjugated linker indicating a high thermal stability of amorphous state, while octylfluorene (**15**) exhibited a low Tg at 82°C, which arise from alkyl-substituted on the fluorene moieties. Therefore, the high Tg of G1hexylfluorene (**14**) and TPAfluorene (**16**) resulting in the long lifetime of the electroluminescent devices. The DSC scan is shown in Figure 4.25 and listed in table 4.5.

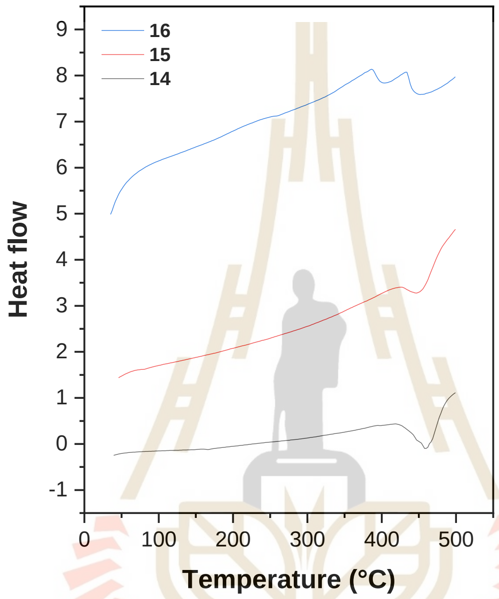

Figure 4.25 DSC 1st heating (solid line) and 2nd heating (dash line) scans of TADF dendrimers **14-16**

4.5 Conclusion

In summary, we have succeeded in synthesizing the TADF dendrimers based on *bis*(4-carbazolephenyl) sulfone as the TADF core. The G1 carbazole and TPA were used as an end-capping group of the fluorene donor moieties and D-π-A-π-D system of the desired molecule was also retaining. All TADF dendrimers can be dissolved in an organic solvent and exhibited blue emission with strong fluorescence intensity, but only TPAfluorene-DPS **16** reveals the ICT characteristic. Their dendritic structure, which arises from G1 and TPA moieties leads to increased Tg resulting in the thermal property of these materials. We believe that our results could provide a useful guide to design the highly efficient TADF dendrimer to be suitable for applications in OLEDs devices.

CHAPTER V

THE SYNTHESIS AND CHARACTERIZATION OF AGGREGATION-INDUCED EMISSION MATERIALS FOR ORGANIC LIGHT-EMITTING DIODES

5.1 Introduction

From the previous chapter, we attempt to designed and synthesized the OLED materials by changing the acceptor core or the donor moieties for adjusting the property of fluorescent materials in order to achieve high efficiency of OLED devices. However, some fluorophores reveal high emission in the solution state, but their emission was decreased in solid-state caused by aggregated from strong intermolecular π-π interactions, which also known as aggregation-caused quenching (ACQ). To overcome the strong aggregation-caused quenching effect, the first new concept of silole molecules **173**, which can restrict the intramolecular vibration and rotations called aggregation-induced emission (AIE) has been reported by Tang et al. in 2001 (Luo et al., 2001). The proposed conformer of silole, when dissolved in a solvent, is twisted conformer of phenyl peripheries and silole core, which is reduced the fluorescence intensity. On the other hand, when added amounts of water into the solution of the silole, its molecule can be aggregated in the solvent mixture with high water content leads to arise coplanar conformer resulting in the increasing fluorescence intensity. It has been proposed that coplanarisation of chromophores can be induced by aggregation.

The molecular structure and conformational rotamers of 1-methyl-1,2,3,4,5-pentaphenylsilole **(173)** are shown in Figure 5.1.

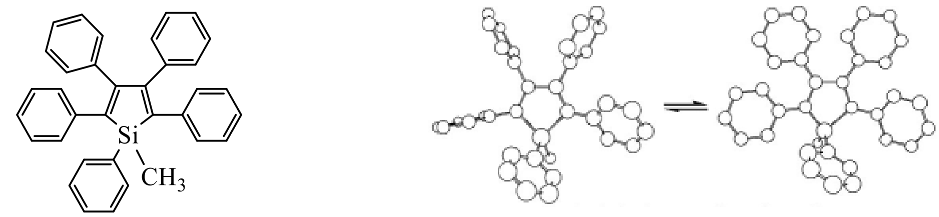

1-methyl-1,2,3,4,5-pentaphenylsilole (**173**) twisted coplanar

Figure 5.1 Molecular structure and conformational rotamers of silole molecules **173**.

After that, AIE research is widely interested and AIEgens have been recognized as an important type of advanced functional material for a wide variety of applications such as in OLED devices (X. Zhang et al., 2019), as a Cell Apoptosis Probe (Hu, Gao, Feng, Chen, and Liu, 2015), photosensitizers (Yang et al., 2019).

The naphtho[2,3-c][1,2,5]thiadiazole derivatives consist of naphthothiadiazole core with different aryl substituents that have been reported by Wei et al. in 2008 as shown in Figure 5.2. The results reveal that these NTD derivatives present both carrier transporting property and high fluorescence quantum yield (P. Wei et al., 2008).

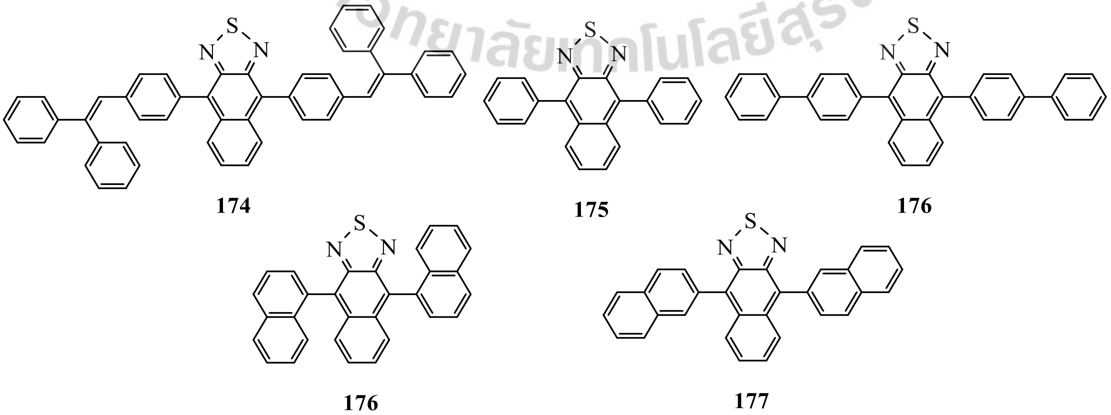

174 **175** **176**

176 **177**

Figure 5.2 Molecular structure of NTD derivatives **174-177**.

In 2010, Tang et al. was reported the luminogen comprised of two units of tetraphenylethene (BTPE), which this compound provides 100% fluorescence efficiency. The electroluminescence devices based on BTPE material **178** exhibited the current efficiency up to B7.3 cd/A (Z. Zhao et al., 2010). The molecular structure is shown in Figure 5.3.

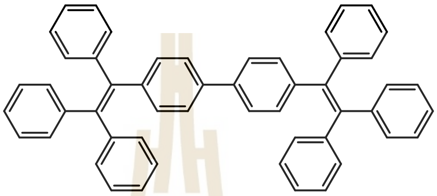

BTPE (**178**)

Figure 5.3 Molecular structure of BTPE **178**.

Triphenylamine (TPA) was introduced into the TPE molecules in order to tun the hole-transporting property and retain the aggregation-induced emission property. The results revealed that the hybrid molecules, TPATPE **179** and 2TPATPE **180** are practically non-luminescent in the solution state, but in the aggregation state, they can be emitted intensely with fluorescence quantum yields up to 100% (Y. Liu et al., 2011). Their molecular structure is shown in Figure 5.4.

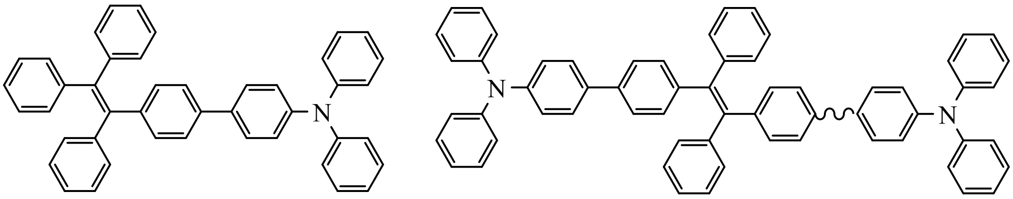

TPATPE (**179**) 2TPATPE (**180**)

Figure 5.4 Molecular structure of TPATPE **179** and 2TPATPE **180**.

Three compounds VP$_0$-(TPE)$_3$ (**181**), VP$_3$-(TPE)$_3$ (**182**), and VP$_6$-(TPE)$_3$ (**183**) containing triphenylethene and tetraphenylethene moieties linked to phenyl-substituted ethylene with different numbers of phenyl rings (Figure 5.5). These compounds exhibited strong fluorescence emission at a maximum wavelength of 469-493 nm in solid states. Their glass transition temperatures were in the range of 138-180°C and the decomposition temperatures were in the range of 495-557°C. The luminescent devices were fabricated and exhibited turns on a voltage at 6 V and the maximum luminance is observed at 1908 cd/m^2. The Commission Internationale de l'Eclairage (CIE) chromaticity coordinate values are (0.18, 0.31) at 10 V.

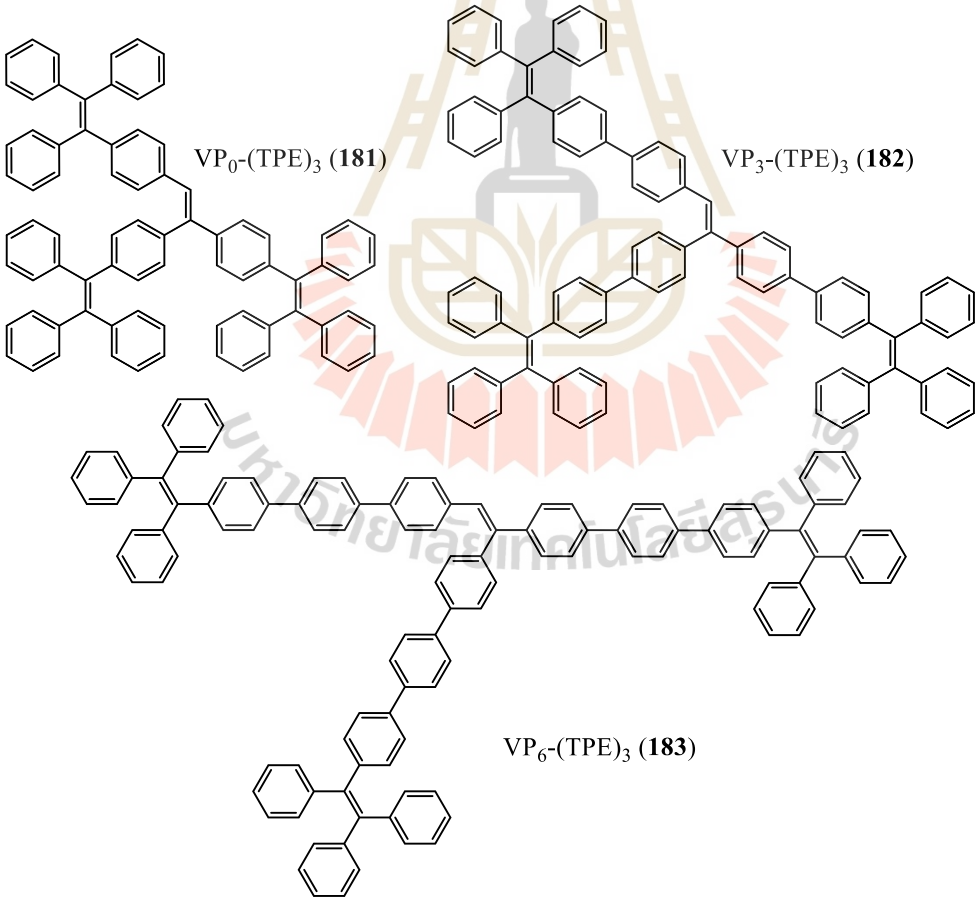
VP$_0$-(TPE)$_3$ (**181**)
VP$_3$-(TPE)$_3$ (**182**)
VP$_6$-(TPE)$_3$ (**183**)

Figure 5.5 Molecular structure of VP$_0$-(TPE)$_3$ (**181**), VP$_3$-(TPE)$_3$ (**182**), and VP$_6$-(TPE)$_3$ (**183**).

The AIEgens containing tetraphenylethene, benzo-2,1,3-thiadiazole and thiophene building blocks, BTPE **178**, BTPETTD **184**, BTPEBTTD **185** have been synthesized and investigated. These molecules emit intense PL in both solution and solid states, which they emitted blue, green, and red emission color in solid states. The OLED device was fabricated and exhibited orange-red color with high luminance and efficiencies of 8330 cd m^{-2}, 6.1 cd A^{-1} and 3.1%, respectively (Z. Zhao et al., 2011). Their molecular structure is shown in Figure 5.6.

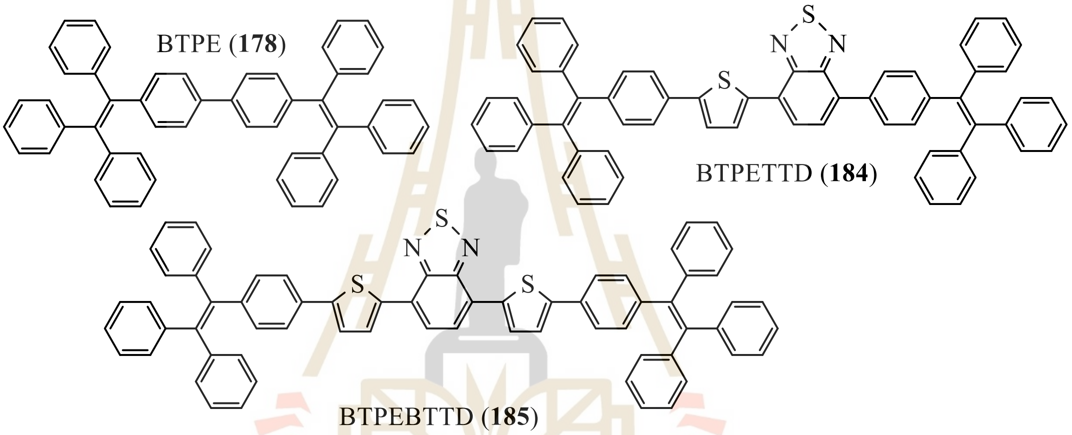

Figure 5.6 Molecular structure of BTPE **178**, BTPETTD **184**, BTPEBTTD **185**.

The near-infrared (NIR) fluorophores with the donor-acceptor-donor (D-A-D) system have been designed and synthesized through Stille coupling reactions. The desired molecules containing tetraphenylethene (TPE) moieties and [1,2,5]thiadiazolo [3,4-g]quinoxaline (QTD) or benzo[1,2-c;4,5c′]bis[1,2,5]thiadiazole (BBTD) as acceptors. These compounds exhibited good aggregation-induced emission enhancement (AIEE) property due to the twisted TPE units, which restrict the intramolecular rotation and reduce the π−π stacking. The OLED devices were fabricated and exhibited EL emission spectra peaking from 706 to 864 nm with the external quantum efficiency (EQE) ranged from 0.89%-0.20% (Du, Qi, Zhang, Ma, and Wang, 2012). Their molecular structure is shown in Figure 5.7.

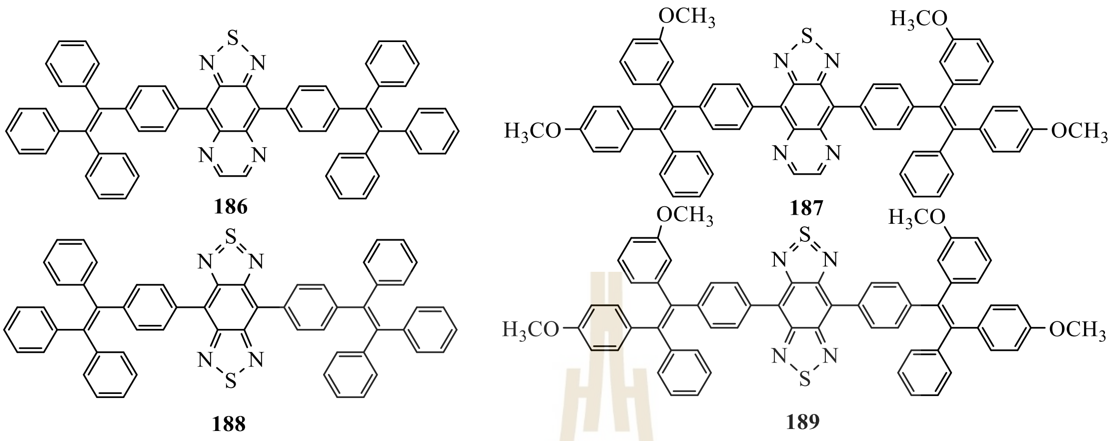
OCH$_3$
H$_3$CO
S
N
N
H$_3$CO
OCH$_3$
186
187
188
189

Figure 5.7 Molecular structures of near IR materials **186-189**.

In 2014, the deep blue AIE emitters have been designed and synthesized. The molecules containing two of TPE groups and the substituents at the 2,2′-positions of BTPE with different sizes, namely methyl-BTPE **190**, isopro-BTPE **191**, Ph-BTPE **192** and Cz-BTPE **193** as shown in Figure 5.8 (Huang et al., 2014).

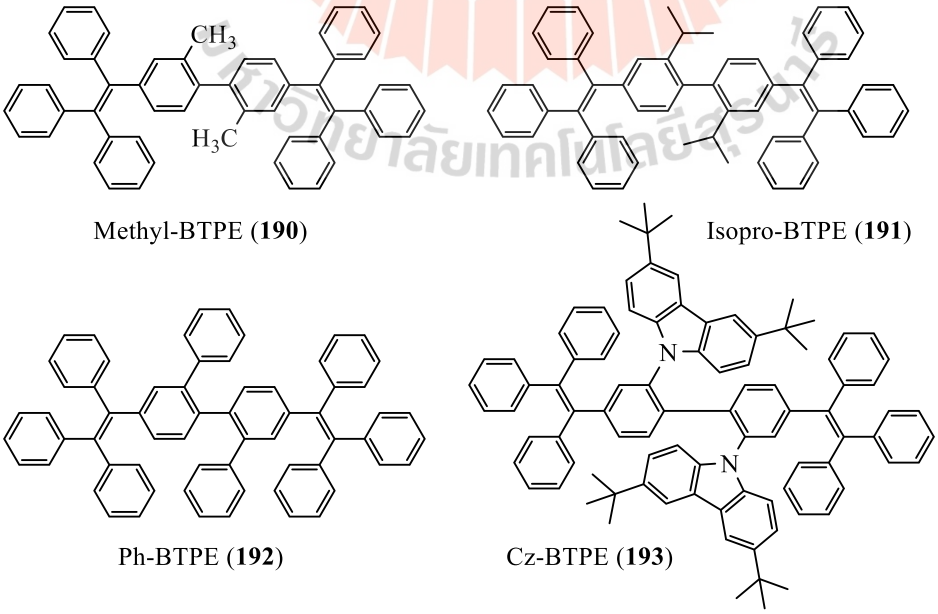
CH$_3$
H$_3$C
Methyl-BTPE (**190**)
Isopro-BTPE (**191**)
N
N
Ph-BTPE (**192**)
Cz-BTPE (**193**)

Figure 5.8 Molecular structures of methyl-BTPE **190**, isopro-BTPE **191**, Ph-BTPE **192** and Cz-BTPE **193**.

The butterfly-shaped NIR chromophore based on the donor-acceptor system, which composed of phenothiazine donor and benzothiadiazole acceptor (PTZ-BZP, **194**) has been investigated. The results revealed that a film of PTZ-BZP **194** displayed strong NIR fluorescence with an emission peak at 700 nm and exhibited quantum efficiency reached to 16% (Yao et al., 2014) The molecular structure of PTZ-BZP **194** is shown in Figure 5.9.

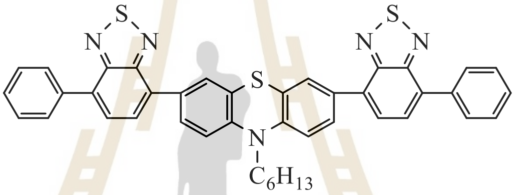

PTZ-BZP **194**

Figure 5.9 Molecular structure of PTZ-BZP **194**.

The AIEgen based on tetraphenylpyrazine (TPP), which could be synthesized using a one-pot procedure under mild reaction conditions as shown in Figure 5.10. The emission color of these compounds can be tuned by varying the substituents on their phenyl rings. The TPP derivatives display good thermal stability and emitted deep-blue to pure blue color due to the various substituents on the phenyl rings (Chen et al., 2015).

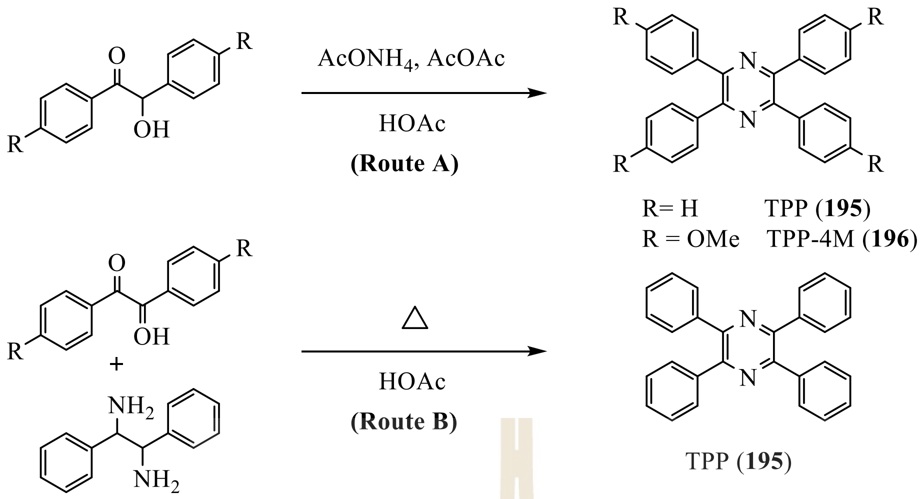
R
O
OH
R
$AcONH_4$, AcOAc
HOAc
(Route A)
R
N
N
R
R
R
R= H TPP (**195**)
R = OMe TPP-4M (**196**)
R
O
OH
R
+
NH_2
NH_2
△
HOAc
(Route B)
N
N
TPP (**195**)

Figure 5.10 Synthetic routes to tetraphenylpyrazine (TPP) and its derivative.

The NIR fluorescent material with a D-π-A-π-D system namely 4,4′-(naphtho [2,3-c][1,2,5]thiadiazole-4,9-diyl)bis(N,Ndiphenylaniline) (**NZ2TPA**, **197**) has been synthesized via Suzuki reaction as shown in Figure 5.11. The desired compound shows aggregation-induced emission (AIE) characteristic with a high photoluminescent quantum yield of 60% in the neat film. Moreover, the OLED device based on NZ2TPA was fabricated and exhibited an external quantum efficiency (EQE) of 3.9% with the emission peak at 696 nm (T. Liu et al., 2017).

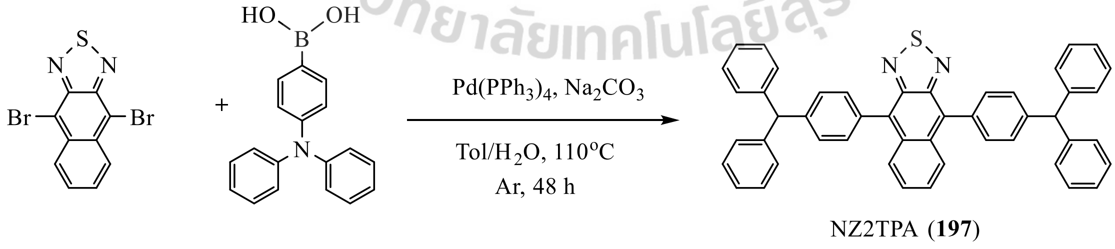
S
N
N
Br
Br
+
HO
OH
B
N
$Pd(PPh_3)_4$, Na_2CO_3
Tol/H_2O, 110°C
Ar, 48 h
S
N
N
NZ2TPA (**197**)

Figure 5.11 Synthesis of NZ2TPA (**197**).

In 2019, the blue luminogens consisting of anthracene, tetraphenylethene, and carbazole groups, TPE-TAC (**198**) and TPE-TADC (**199**) have been synthesized and investigated as shown in Figure 5.12. From the studied, they exhibited aggregation-induced emission property with strong blue fluorescence at 455 nm in neat films. The OLEDs devices were fabricated provided blue electroluminescence (EL) at 451 nm (CIEx,y = 0.165, 0.141) and high EL efficiencies of 5.71% (Y. Li et al., 2019).

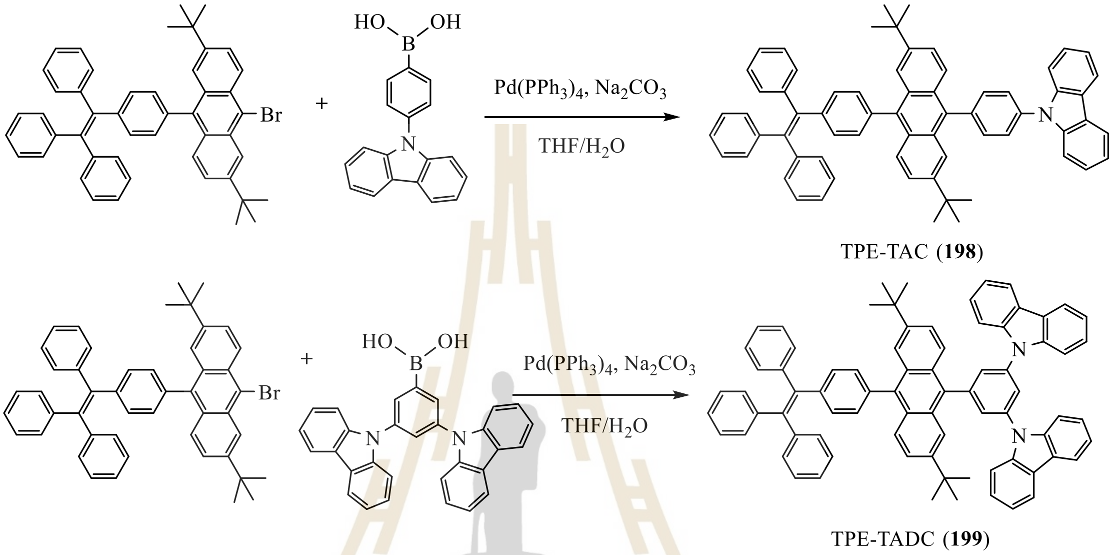

Figure 5.12 Synthetic procedure of TPE-TAC (**198**) and TPE-TADC (**199**).

From the above mentioned, in this chapter, we designed and synthesized the AIE molecules containing the tetraphenylethenes (TPEs) linked to a variety of acceptors in order to achieve the different emission colors from yellow to red with the strong emission in solid-state. The desired molecules with the D-A-D system consist of benzothiadiazole derivative as an electron acceptor bonded to two TPE as the AIE unit. Subsequently, aggregation-induced emission characteristics of the target molecules in the THF/water mixtures have been studied as well as their solvatochromic effects related to their structures.

5.2 Research objectives

5.2.1 To design and synthesize novel AIE materials as an emitter for OLEDs.

5.2.2 To characterize the desired molecules by ^{1}H-NMR, ^{13}C-NMR, and Mass spectroscopy.

5.2.3 To study the photophysical, electrochemical, and thermal properties by using UV-Visible spectroscopy, fluorescence spectroscopy, cyclic voltammetry, and DSC-TGA techniques.

5.3 Synthetic procedure

5.3.1 Synthetic procedure

Herein, the synthesis of the AIE emitters by the Suzuki cross-coupling reaction of benzothiadiazole, naphthothiadiazole, and *bis*- naphthothiadiazole derivatives with the various boronates in the presence of tetrakis(triphenylphosphine) palladium(0) as a catalyst. After purification, the desired AIE emitters should be obtained (Figure 5.13).

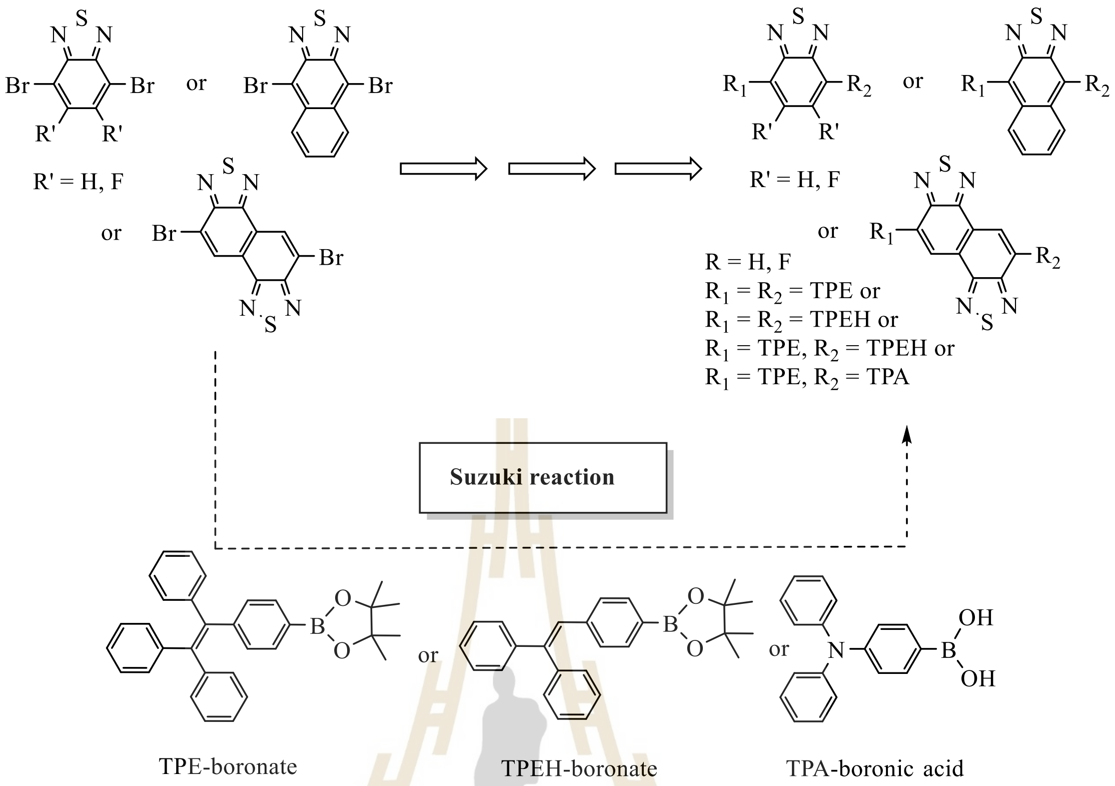
Br
Br
or
R' = H, F
Br
Br
or
Br
Br
R' = H, F
R = H, F
R1 = R2 = TPE or
R1 = R2 = TPEH or
R1 = TPE, R2 = TPEH or
R1 = TPE, R2 = TPA
Suzuki reaction
TPE-boronate
TPEH-boronate
TPA-boronic acid

Figure 5.13 The synthetic approach to the synthesis of AIE emitters.

5.3.2 Preparation of the boronates 202 and 203

The TPE-borolane **202** and TPEH-borolane **203** were achieved from the Miyaura borylation reaction, while TPA-boronic acid **204** was obtained from commercial suppliers and used without further purification. The boronates were obtained from cross-coupling of *bis*(pinacolato)diboron (B_2pin_2) with aryl bromide **200** and **201** using [1,1′-*bis*(diphenylphosphino)ferrocene]dichloropalladium(II) palladium as a catalyst in the presence of potassium acetate in toluene as shown in Figure 5.14.

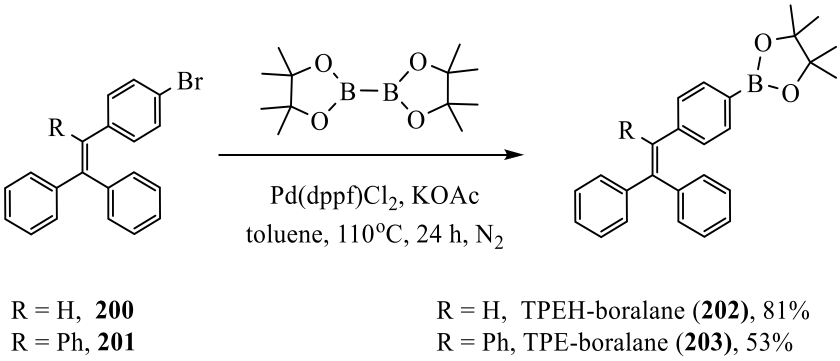
Br
R
Pd(dppf)Cl$_2$, KOAc
toluene, 110^{o}C, 24 h, N$_2$
R
R = H, **200**
R = Ph, **201**
R = H, TPEH-boralane (**202**), 81%
R = Ph, TPE-boralane (**203**), 53%

Figure 5.14 Preparation of TPEH-borolane **202** and TPE-borolane **203**.

The [1,1′-Bis(diphenylphosphino)ferrocene]dichloropalladium(II) was activated to palladium(0) followed by the oxidative addition of the aryl bromide. Then the formation of an (acetato)palladium(II) complex was achieved and transmetalation with bis(pinacolato)diboron (B_2pin_2) can be attributed to the high reactivity of Pd–O bond which consists of soft acid and a hard base (HSAB concept). Subsequently, reductive elimination of the boronates **202** and **203** in the yield of 81% and 53%, respectively and takes place along with the catalyst regeneration. The proposed catalytic cycle for the borylation of aryl halides described by Miyaura is shown in Figure 5.15.

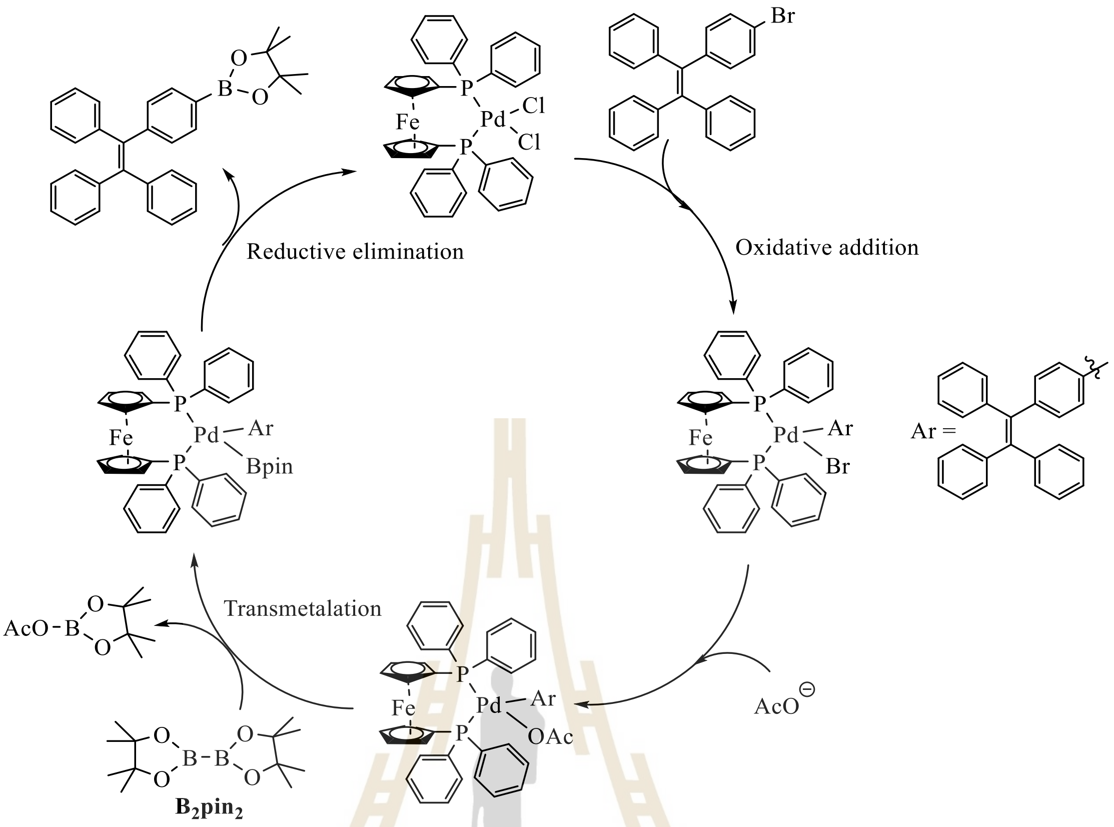
Br
Reductive elimination
Oxidative addition
Fe
Pd
Cl
Cl
P
Ar
Bpin
Br
Ar =
Transmetalation
AcO-B
AcO
OAc
B-B
B2pin2

Figure 5.15 The proposed mechanism for the borylation to afford TPE-borolane **202**.

5.3.3 The synthesis of AIE emitters 17-26

The benzothiadiazole, naphthothiadiazole, and *bis*- naphthothiadiazole derivatives were used as the starting materials in the final step for synthesized AIE emitters via for Suzuki cross-coupling reaction, which could be synthesized on a 100-milligram scale as outlined in Figure 5.16.

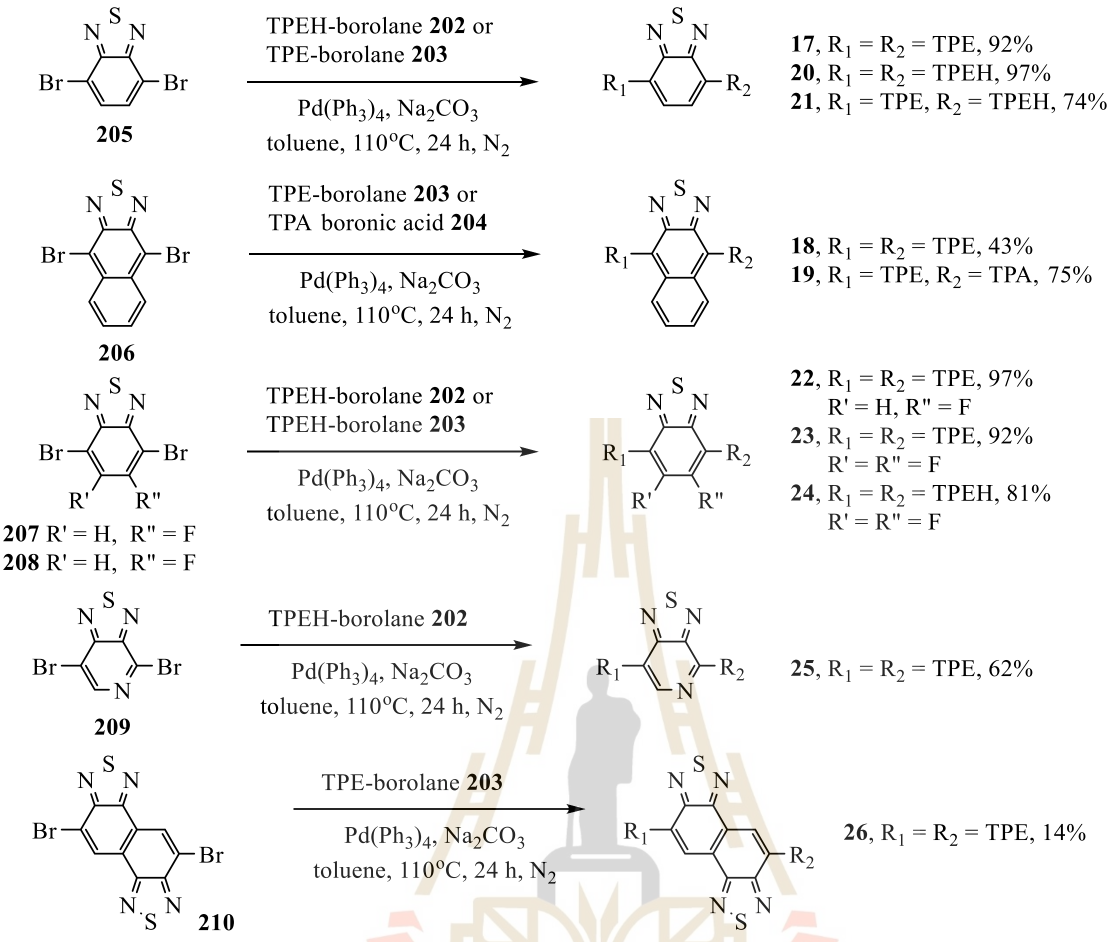
205
TPEH-borolane **202** or
TPE-borolane **203**
Pd(Ph3)4, Na2CO3
toluene, 110°C, 24 h, N2
17, R1 = R2 = TPE, 92%
20, R1 = R2 = TPEH, 97%
21, R1 = TPE, R2 = TPEH, 74%
206
TPE-borolane **203** or
TPA boronic acid **204**
Pd(Ph3)4, Na2CO3
toluene, 110°C, 24 h, N2
18, R1 = R2 = TPE, 43%
19, R1 = TPE, R2 = TPA, 75%
TPEH-borolane **202** or
TPEH-borolane **203**
Pd(Ph3)4, Na2CO3
toluene, 110°C, 24 h, N2
22, R1 = R2 = TPE, 97%
R' = H, R" = F
23, R1 = R2 = TPE, 92%
R' = R" = F
24, R1 = R2 = TPEH, 81%
R' = R" = F
207 R' = H, R" = F
208 R' = H, R" = F
209
TPEH-borolane **202**
Pd(Ph3)4, Na2CO3
toluene, 110°C, 24 h, N2
25, R1 = R2 = TPE, 62%
210
TPE-borolane **203**
Pd(Ph3)4, Na2CO3
toluene, 110°C, 24 h, N2
26, R1 = R2 = TPE, 14%

Figure 5.16 The synthesis of AIE emitters 17-26.

The first step was the oxidative addition of palladium (0) to the organic halide starting material (**205**) to form the organopalladium species. The second step was metathetic exchange with base gives intermediate, which via transmetalation with the phenylboronic acid forms the oganopalladium species. Finally, reductive elimination of the desired product (**17**) restores the original palladium catalyst (0) as shown in Figure 5.17.

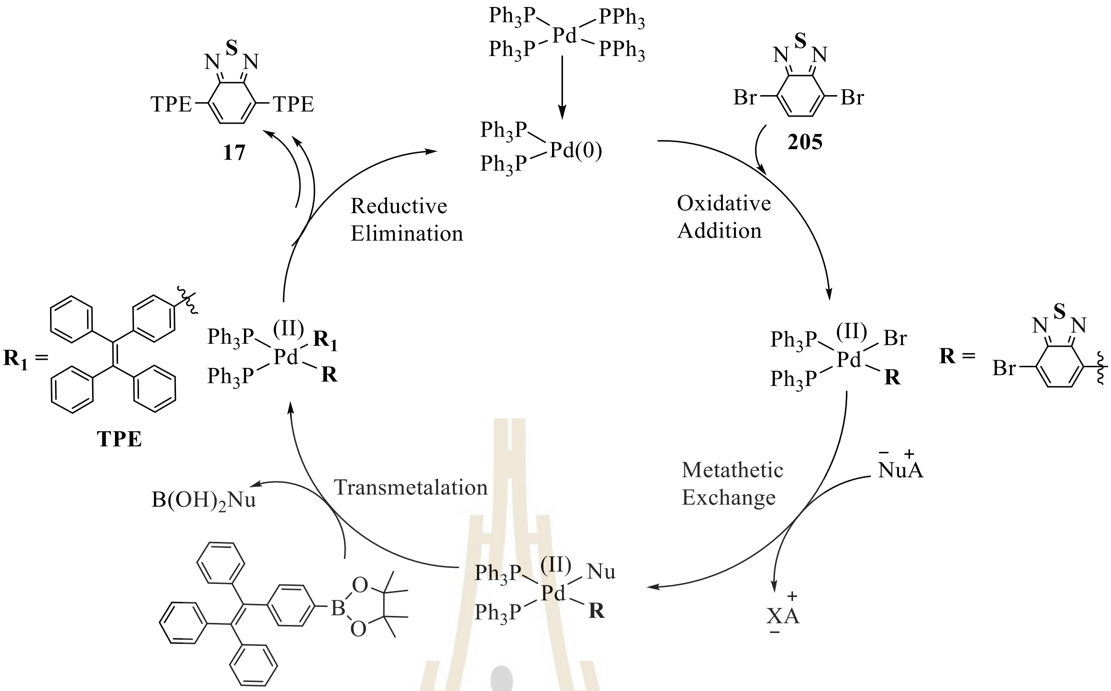
Ph3P
Pd
PPh3
Ph3P
PPh3
Ph3P
Pd(0)
Ph3P
N S N
Br
Br
205
Oxidative Addition
Ph3P
(II)
Br
Pd
Ph3P
R
R =
N S N
Br
Metathetic Exchange
NuA
XA
Ph3P
(II)
Nu
Pd
Ph3P
R
Transmetalation
B(OH)2Nu
B
O
O
Ph3P
(II)
R1
Pd
Ph3P
R
R1 =
TPE
Reductive Elimination
N S N
TPE
TPE
17

Figure 5.17 The mechanism of Suzuki reaction.

The benzothiadiazole, naphthothiadiazole, and *bis*- naphthothiadiazole were reacted with boronates in the presence of sodium carbonate as base via Suzuki reaction to afford the desired product **17-26** in a yield of 14%-97%. After purification, their structures were confirmed by ^{1}H NMR, ^{13}C NMR, and HRMS spectrometric methods.

The ^{1}H-NMR spectrum of BT-2TPE (**17**) showed singlet signals of the two protons of benzothiadiazole core at δ = 7.72 ppm. The TPE units showed the doublet signals at δ = 7.76 (4H) and 7.19 (4H) ppm with the coupling constant (*J*) of 8.7 Hz and other protons were in the range of 7.14-7.05 (30H) ppm. The ^{13}C-NMR spectrum showed the chemical shift of 21 aryl carbon signals in the range of δ = 154.0-126.5 ppm. Moreover, High resolution mass spectrometry confirmed the identity of the compound with m/z (HRMS) = 796.4323 (required m/z = 796.2912).

The ^{1}H-NMR spectrum of NT-2TPE (**18**) showed multiplet signals of the four protons of naphthothiadiazole core at δ = 7.87 and 7.33 ppm. The TPE units showed the doublet signals at δ = 7.39 (4H) and 7.26 (4H) ppm with the coupling constant (*J*) of 8.4 Hz and other protons were in the range of 7.22-7.14 (30H) ppm. The ^{13}C-NMR spectrum showed the chemical shift of 21 symmetrical aryl carbon signals in the range of δ = 151.2-126.1 ppm. Moreover, High resolution mass spectrometry confirmed the identity of the compound with m/z (HRMS) = 846.5767 (required m/z = 846.3069).

The ^{1}H-NMR spectrum of NT-TPETPA (**19**) showed signals of the four protons of naphthothiadiazole core at δ = 8.88, 8.12, 7.37 and 7.35 ppm. The TPA units showed the doublet signals at δ = 7.53 (4H) and 7.40 (4H) ppm and other protons were in the range of 7.32-7.22 (10H) ppm. The TPE units showed the signals were in the range of 7.22-7.11 (15H) ppm. The ^{13}C-NMR spectrum showed the chemical shift of 34 symmetrical aryl carbon signals in the range of δ = 151.5-122.2 ppm. Moreover, High resolution mass spectrometry confirmed the identity of the compound with m/z (HRMS) = 759.5536 (required m/z = 759.2708).

The ^{1}H-NMR spectrum of BT-2TPEH (**20**) showed singlet signals of the two protons of benzothiadiazole core at δ = 7.71 ppm. The TPEH units showed singlet signals of the two alkenyl protons at δ = 7.05 ppm. the doublet signals at δ = 7.78 (4H) and 7.19 (4H) ppm with the coupling constant (*J*) of 8.4 Hz and other protons were in the range of 7.40-7.28 (20H) ppm. The ^{13}C-NMR spectrum showed the chemical shift of 15 aryl carbon signals in the range of δ = 154.0-127.6 ppm. Moreover, High resolution mass spectrometry confirmed the identity of the compound with m/z (HRMS) = 644.4773 (required m/z = 664.2286).

The ^{1}H-NMR spectrum of BT-TPETPA (**21**) showed multiplet signals of the two protons of benzothiadiazole core at δ = 7.74 ppm. The TPA units showed the doublet signals at δ = 7.87 (2H) and 7.78 (2H) ppm with the coupling constant (*J*) of 8.1 Hz. The TPE units showed the multiplet signals at δ = 7.20 (2H) ppm and other protons were in the range of 7.31-7.06 (30H) ppm. The ^{13}C-NMR spectrum showed the chemical shift of 32 aryl carbon signals in the range of δ = 154.1-122.9 ppm. Moreover, High resolution mass spectrometry confirmed the identity of the compound with m/z (HRMS) = 709.5769 (required m/z = 709.2552).

The ^{1}H-NMR spectrum of FBT-2TPE (**22**) showed singlet signals of the benzothiadiazole proton at δ = 7.70 ppm. The doublet signals of TPE proton at the near F-atom position of δ = 7.76 (2H) and 7.60 (2H) ppm with the coupling constant (*J*) of 8.4 Hz and other protons were in the range of 7.21-7.05 (34H) ppm. The ^{13}C-NMR spectrum showed the chemical shift of 44 aryl carbon signals in the range of δ = 155.1-117.0 ppm.

The ^{1}H-NMR spectrum of 2FBT-2TPE (**23**) showed doublet signals of TPE units at δ = 7.60 (4H) and 7.21 (4H) ppm with the coupling constant (*J*) of 8.4 Hz and other protons were in the range of 7.16-7.05 (30H) ppm. The ^{13}C-NMR spectrum showed the chemical shift of 23 symmetrical aryl carbon signals in the range of δ = 151.3-118.3 ppm. Moreover, High resolution mass spectrometry confirmed the identity of the compound with m/z (HRMS) = 832.5317 (required m/z = 832.2724).

The ^{1}H-NMR spectrum of 2FBT-2TPEH (**24**) showed singlet signals of the two alkenyl protons at δ = 7.04 ppm, doublet signals of TPEH units at δ = 7.63 (4H) and 7.21 (4H) ppm with the coupling constant (*J*) of 8.4 Hz and other protons were in the range of 7.40-7.28 (20H) ppm. The ^{13}C-NMR spectrum showed the chemical shift of 23 symmetrical aryl carbon signals in the range of δ = 151.3-118.3 ppm.

The ^{1}H-NMR spectrum of NBT-2TPE (**25**) showed singlet protons of pyridinethiadiazole core at δ = 8.76 ppm. The doublet signals of TPE units at the near N-atom position of δ = 8.42 (2H) and 7.8 (2H) ppm with the coupling constant (*J*) of 8.1 Hz and other protons were in the range of 7.25-7.06 (34H) ppm. The ^{13}C-NMR spectrum showed the chemical shift of 32 symmetrical aryl carbon signals in the range of δ = 156.6-126.4 ppm. Moreover, High resolution mass spectrometry confirmed the identity of the compound with m/z (HRMS) = 1565.6174 (required m/z = 797.2865).

The ^{1}H-NMR spectrum of BNT-2TPE (**26**) showed singlet signals of the two protons of *bis*-naphthothiadiazole core at δ = 8.99 ppm. The doublet signals of TPE units at δ = 7.94 (4H) and 7.26 (4H) ppm with the coupling constant (*J*) of 8.4 Hz and other protons were in the range of 7.26-7.07 (30H) ppm. The ^{13}C-NMR spectrum showed the chemical shift of 23 symmetrical aryl carbon signals in the range of δ = 154.0-125.1 ppm. Moreover, High resolution mass spectrometry confirmed the identity of the compound with m/z (HRMS) = 904.7764 (required m/z = 904.2694).

5.4 Results and discussion

5.4.1 Photophysical properties

The UV-vis absorption and fluorescence spectra of the AIE emitters **17-26** were investigated in dilute toluene solution (10^{-5}-10^{-6} M) and the neat film by UV-vis and photoluminescence spectroscopies as shown in Figure 5.18 and listed in Table 5.1.

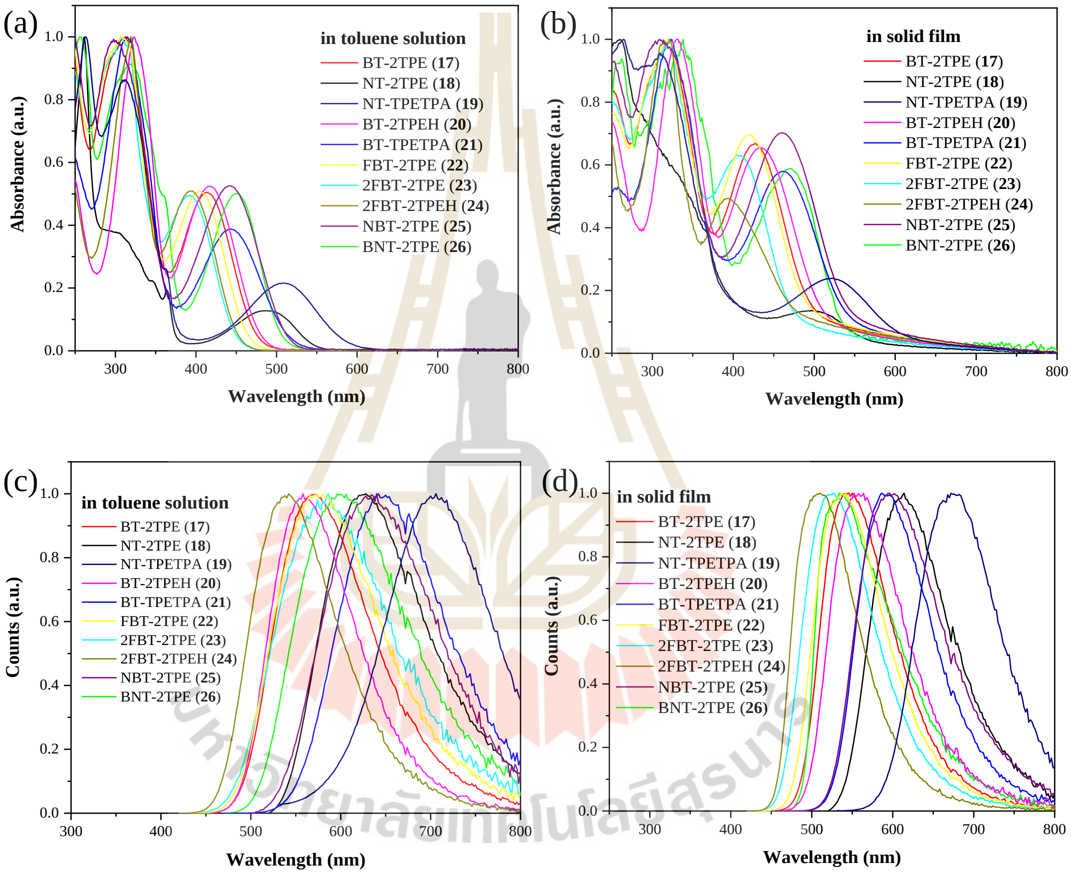

Figure 5.18 UV-vis absorption of AIE emitters in (a) dilute solution in toluene (10^{-5} M) (b) solid film and fluorescence spectra in (c) dilute solution in toluene (10^{-6} M) and (d) solid film.

The results revealed that all AIE compounds **17-26** showed two broad absorption bands, an absorption band around 300 nm corresponding to the π-π* transition of the donor moieties and an absorption band with a maximum at 400-550 nm assigned to the n-π* transition leads to occur intramolecular charge-transfer (ICT) between the donor moieties and the acceptor units. All the AIE emitters showed a similar absorption band in solution and in the neat film. NT-2TPE (**18**) and NT-TPETPA (**19**) exhibited strong red-shifted emission band after change the acceptor core from benzothiadiazole to naphthothiadiazole and showed slightly red-shifted emission band when changing to pyridinethiadiazole NBT-2TPE (**25**) and *bis*-naphthothiadiazole BNT-2TPE (**26**) possibly due to the higher degree of conjugation more electron acceptor ability. In addition, the absorption bands of BT-2TPE (**17**) were blue-shifted after the introduction of the fluorine atom onto the benzothiadiazole core possibly due to a collapsing of the planarity of the molecules as can be seen in FBT-2TPE (**22**), 2FBT-2TPE (**23**) molecules. Moreover, their emission displays a slightly red-shifted when changing the TPE donor to TPEH and TPA moieties as can be seen in BT-2TPEH (**20**) and 2FBT-2TPEH (**24**).

The fluorescence spectra of AIE emitters exhibited emission bands with a maximum around 541-706 nm in the toluene solution and the fluorescence spectra in neat films are identical to those in the toluene solution. The emission bands of BT-2TPE (**17**) were blue-shifted after the introduction of the fluorine atom onto the benzothiadiazole core as can be seen in the molecules of FBT-2TPE (**22**), 2FBT-2TPE (**23**), and 2FBT-2TPEH (**24**). When changing the BT to NT, BNT, and NBT core, the emission bands were red-shifted and extended to the NIR region by using NT core with the TPA donor group. The solid-state absorption maximum of BT-2TPE (**17**), NT-

2TPE (**18**), NT-TPETPA (**19**), BT-2TPEH (**20**), BT-TPETPA (**21**), FBT-2TPE (**22**), 2FBT-2TPE (**23**), 2FBT-2TPEH (**24**), NBT-2TPE (**25**), and BNT-2TPE (**26**) was red-shifted by 15, 14, 14, 16, 17, 15, 15, 0, 19, and 148 nm, respectively compared to that of the solution. This bathochromic shift can be attributed to intermolecular interactions in the solid-state. The solid-state emission maximum wavelength of BT-2TPE (**17**), NT-2TPE (**18**), NT-TPETPA (**19**), BT-2TPEH (**20**), BT-TPETPA (**21**), FBT-2TPE (**22**), 2FBT-2TPE (**23**), 2FBT-2TPEH (**24**), NBT-2TPE (**25**), and BNT-2TPE (**26**) was red-shifted by 116, 110, 150, 123, 138, 118, 116, 115, 147, and 67 nm, respectively compared to that of the solution. The optical bandgap energy calculated by the onset of the absorption edge of NT-2TPE (**18**), NT-TPETPA (**19**), BT-2TPEH (**20**), BT-TPETPA (**21**), NBT-2TPE (**25**), and BNT-2TPE (**26**) were decreased compared to BT-2TPE (**17**). On the other hand, the introduction of the fluorine atom onto the benzothiadiazole increased the optical bandgap energy of FBT-2TPE (**22**), 2FBT-2TPE (**23**), 2FBT-2TPEH (**24**) compared to BT-2TPE (**17**) as listed in table 5.1.

Table 5.1 Photophysical properties of DPP dendrimers.

Compounds	**Solution**	**Film**	λ^{abs}_{onset} [a] **(nm)**	E_g^{opt} [b] **(eV)**	λ^{flu}_{onset} [c] **(nm)**	S_1 [d] **(eV)**
	λ_{UV} (log ε) /λ_{em} (nm/$M^{-1}cm^{-1}$)	λ_{UV} /λ_{em} (nm)				
BT-2TPE (**17**)	312, 414/570	322, 429/545	475	2.61	486	2.55
NT-2TPE (**18**)	260, 487/624	260, 501/611	551	2.25	535	2.32
NT-TPETPA (**19**)	311, 509/706	311, 523/673	588	2.11	590	2.10
BT-2TPEH (**20**)	322, 418/558	332, 434/557	480	2.58	487	2.55
BT-TPETPA (**21**)	316, 444/647	322, 461/599	516	2.40	548	2.26
FBT-2TPE (**22**)	308, 405/578	320, 420/538	464	2.67	483	2.57
2FBT-2TPE (**23**)	306, 393/586	320, 408/524	450	2.76	479	2.59
2FBT-2TPEH (**24**)	317, 394/541	317, 394/509	453	2.74	465	2.67
NBT-2TPE (**25**)	297, 442/644	311, 461/608	511	2.43	530	2.34
BNT-2TPE (**26**)	321, 449/599	337, 469/536	506	2.45	506	2.45

[a] The onset of the absorption spectra.

[b] Calculate from the absorption spectra threshold, $E_g^{opt} = 1240/\lambda_{onset}$.

[c] The onset of the fluorescence spectra.

[d] Calculate from the onset of the fluorescence (for S_1).

5.4.2 Commission International de l'Eclairage (CIE)

Chromaticity diagram and CIExy values of all AIE emitters in dilute toluene solution and in the neat film are shown in Figure 5.19 and summarized in Table 5.2. The results revealed that AIE emitters **17-26** exhibited the high x,y coordinate with yellow-green to orange-red emission color in the solution state, while in solid-state, the emission of FBT-2TPE (**22**), 2FBT-2TPE (**23**), 2FBT-2TPEH (**24**) were blue-shifted, all AIE emitters exhibited green to orange-red emission color. In solid-state, NT-2TPE (**18**), NT-TPETPA (**19**),and NBT-2TPE (**25**) showed the red color in the NIR region with the CIExy values of (0.591, 0.408), (0.686, 0.314) and (0.548, 0.449).

Table 5.2 CIE(x,y) coordinates of AIE emitters **17-26**.

Compounds	**CIE^{sol} (x,y)**	**CIE^{film} (x,y)**
BT-2IE (**17**)	(0.467, 0.514)	(0.404, 0.564)
NT-2TPE (**18**)	(0.599, 0.400)	(0.591, 0.408)
NT-TPETPA (**19**)	(0.666, 0.334)	(0.686, 0.314)
BT-2TPEH (**20**)	(0.442, 0.536)	(0.444, 0.538)
BT-TPETPA (**21**)	(0.625, 0.374)	(0.546, 0.451)
FBT-2TPE (**22**)	(0.471, 0.506)	(0.374, 0.570)
2FVT-2TPE (**23**)	(0.478, 0.495)	(0.327, 0.554)
2FBT-2TPEH (**24**)	(0.376, 0.547)	(0.267, 0.523)
NBT-2TPE (**25**)	(0.592, 0.406)	(0.548, 0.449)
BNT-2TPE (**26**)	(0.531, 0.463)	(0.401, 0.565)

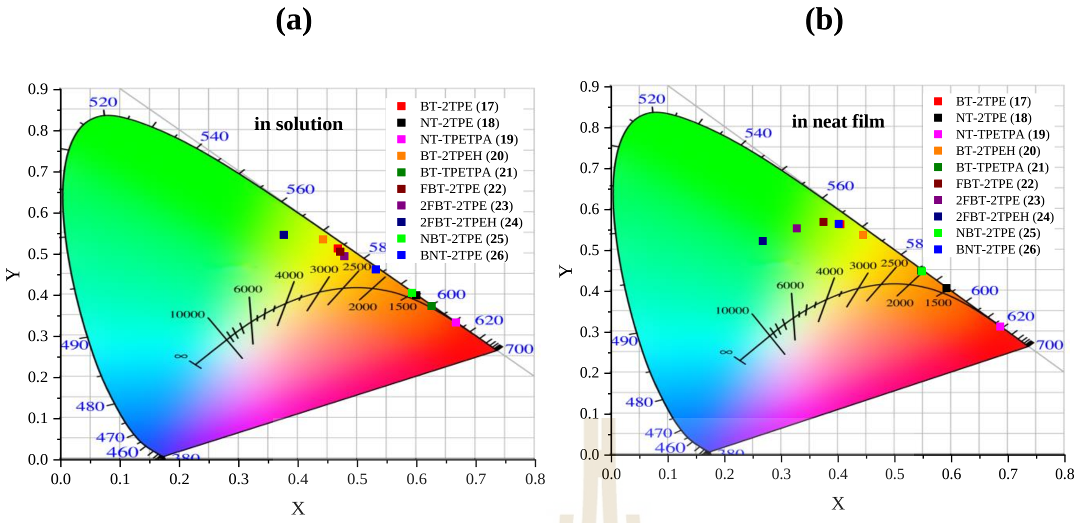

Figure 5.19 Chromaticity diagram of all AIE emitters **17-26** in (a) dilute solution in toluene (10^{-5} M) and (b) solid neat film.

5.4.3 Solvatochromic behaviors

Normally, the D-A molecules which containing π-π* transition presented the solvatochromism in their absorption spectra due to the high polarization of the ground-state molecular structure, while the molecules containing the ICT character, the solvatochromic behavior could be observed in the emission spectra rather than in absorption spectra. In order to study the solvatochromic behavior of all AIE emitters **17-26**, various solvents with different polarities such as hexane, toluene, dichloromethane, tetrahydrofuran, and acetonitrile were selected. The UV-vis and emission spectra of all compounds have been measured. The results revealed that only emission spectra could be observed the bathochromic shifted in polar solvent due to their ICT behavior. The absorption spectra and emission spectra of all AIE emitters **17-26** in different solvents are shown in Figure 5.20.

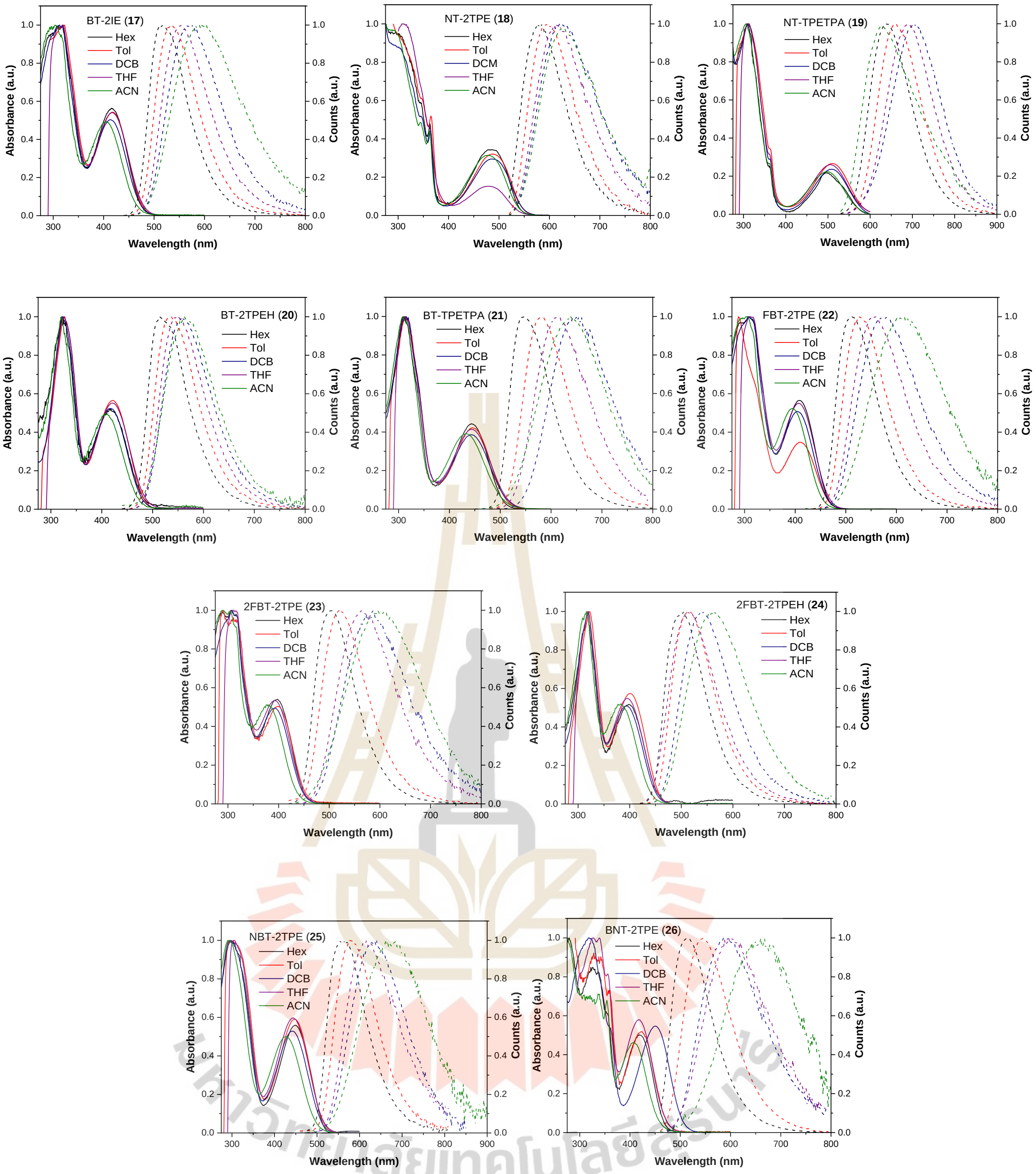

Figure 5.20 UV-vis absorption and fluorescence spectra of AIE emitters **17-26** in various solvent.

The plots of stokes shift versus solvent polarity parameter (Δ*f*) of all AIE emitters **17-26** were shown in Figure 5.21. The results revealed that the fluorescent properties of all compounds are strongly related to the solvent polarity which might be from the formation of large charge separation and high dipole moment in the excited state.

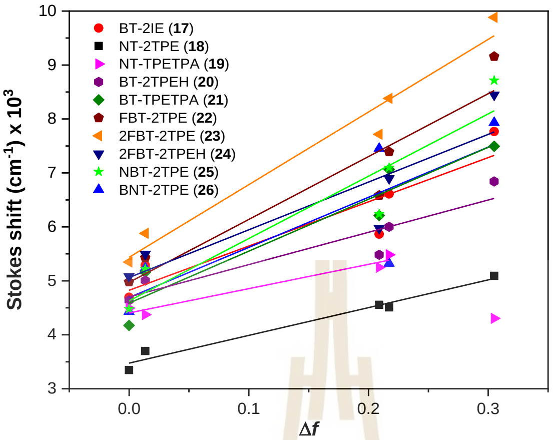

Figure 5.21 The plots of stokes shift versus solvent polarity parameter (Δ*f*) AIE emitters **17-26**.

5.4.4 Aggregation induced emission characteristic

The emission spectra of AIE emitters **17-26** with different water fractions in THF/water mixture are shown in Figure 5.22. The maximum emission wavelength of AIE emitters **17-26** was red-shifted, and the maximum emission intensity gradually decreases upon increasing the water fraction up to 60%. However, upon an increase in the water fraction from 60% to 99%, the maximum emission wavelength was blue-shifted, and the maximum emission intensity gradually increases. Due to their intramolecular charge-transfer state between donor and acceptor moieties could be stabilized upon increasing the polarity of the solvents and upon the higher water fraction, their molecules could be the formation of nanoaggregates that can enhance aggregation-induced emission as shown in Figure 5.23.

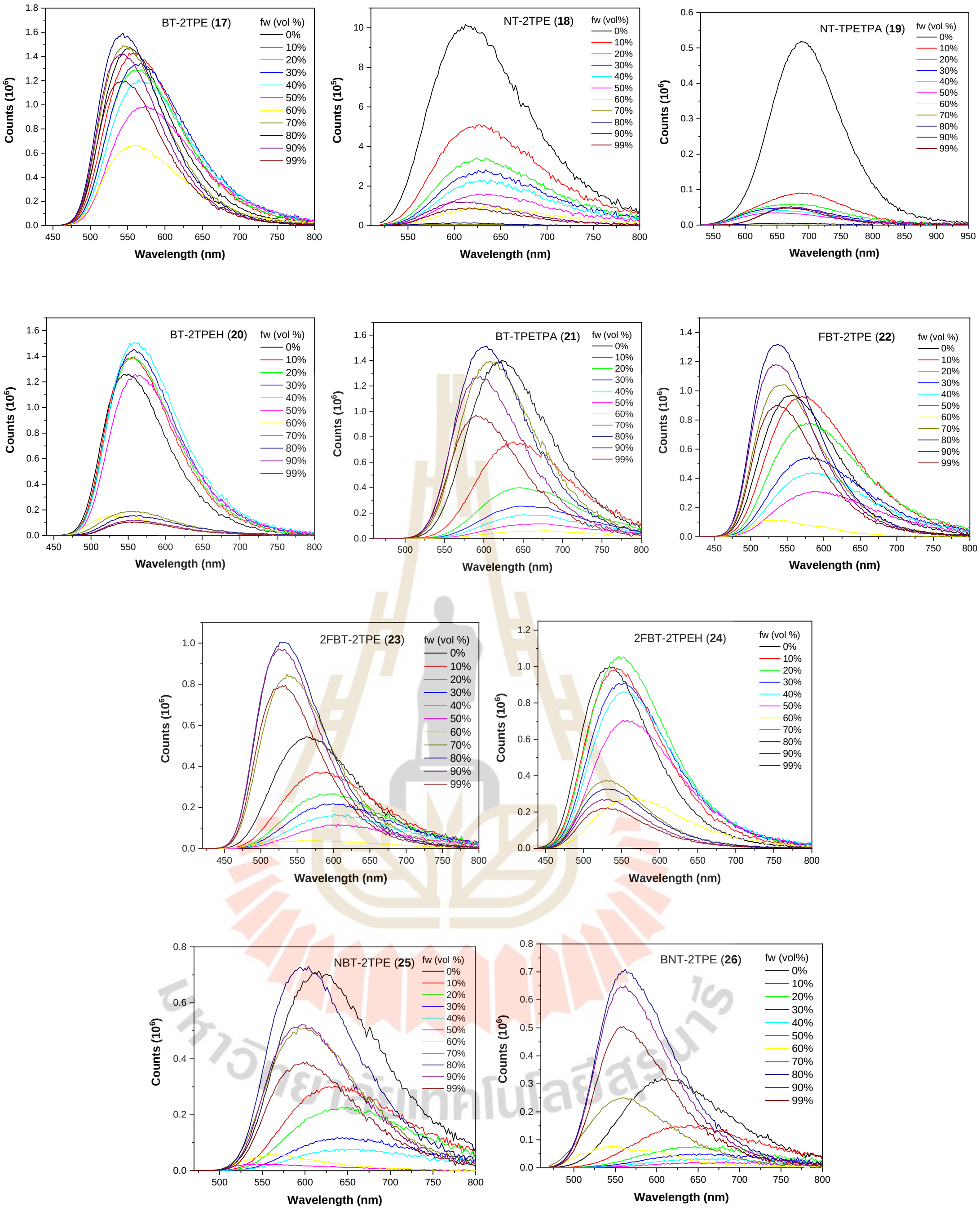

Figure 5.22 Emission spectra of AIE emitters **17-26** in THF-water mixtures (concentration 10^{-5} M).

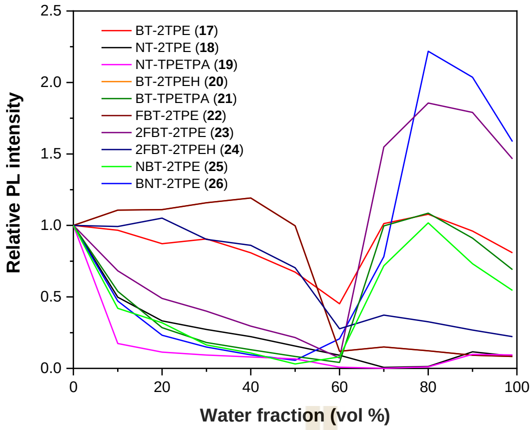

Figure 5.23 Relative PL intensity vs water fraction of AIE emitters **17-26**.

5.4.5 Electrochemical properties

The electrochemical characteristics of the AIE emitters **17-26** were measured by cyclic voltammetry. All compounds exhibited reversible oxidation processes upon the anodic sweep as shown in Figure 5.24.

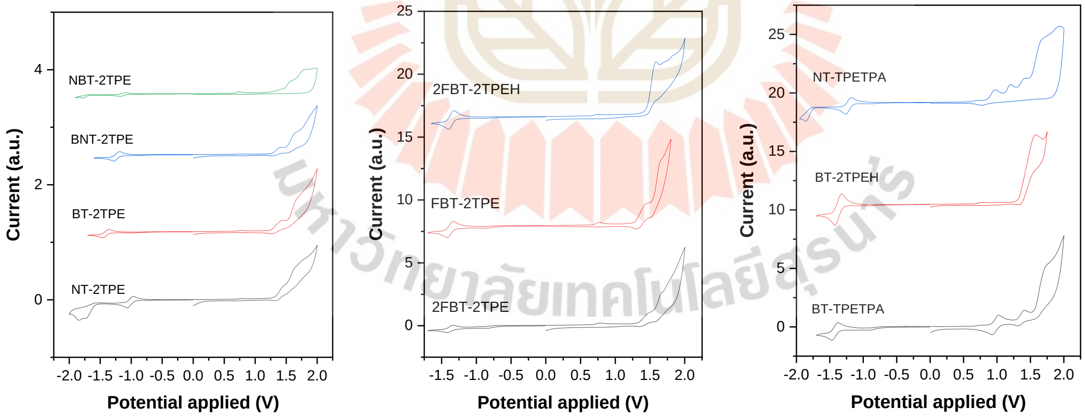

Figure 5.24 CV curves of AIE emitters **17-26** in CH_2Cl_2 solution using 0.1 M Bu_4NPF_6 at a scan rate of 50 mV/s under argon flow.

The first oxidation process assigns to the removal of electrons from the donor moieties, resulting in radical cations. The HOMO levels of all compounds determined from the onsets of the oxidation potentials were in the range of -5.89 to -5.26 eV, which are nearly values from AC2 method. The LUMO levels determined from the onsets of the reduction potentials were in the range of -3.51 t0 -3.13 eV. Electrochemical band gaps (E_g^{ele}) determined using the onsets of the oxidation potentials subtracts by the onsets of the reduction potentials were in the range of 1.97-2.72 eV. The electrochemical data are summarized in Table 5.3.

Table 5.3 Electrochemical properties of AIE emitters **17-26**.

Compounds	**E^{ox}_{onset}/E^{red}_{onset} (eV)** [e]	**HOMO/LUMO from CV (eV)** [f]	**$E^{Ox}_{1/2}$ /$E^{Re}_{1/2}$** [h] **vs. Ag/Ag⁺ (eV)** [g]	**HOMO from AC2** [h]	**E_g^{ele}** [e] **(eV)** [i]
BT-2TPE (**17**)	1.24/-1.31	-5.68/-3.13	1.37/-1.41	5.87	2.55
NT-2TPE (**18**)	1.29/-0.93	-5.73/-3.51	1.34/-1.01	5.91	2.22
NT-TPETPA (**19**)	0.82/-1.15	-5.26/-3.29	0.90/-1.24	5.56	1.97
BT-2TPEH (**20**)	1.33/-1.30	-5.77/-3.14	1.46/-1.38	5.86	2.63
BT-TPETPA (**21**)	0.89/-1.17	-5.33/-3.27	0.98/-1.42	5.63	2.06
FBT-2TPE (**22**)	1.26/-1.29	-5.71/-3.16	1.39/-1.38	5.94	2.55
2FBT-2TPE (**23**)	1.30/-1.19	-5.74/-3.25	1.43/-1.38	6.04	2.49
2FBT-2TPEH (**24**)	1.45/-1.27	-5.89/-3.17	1.52/-1.36	6.03	2.72
NBT-2TPE (**25**)	1.17/-1.04	-5.61/-3.40	1.42/-1.14	5.89	2.21
BNT-2TPE (**26**)	1.26/-1.14	-5.70/-3.30	1.36/-1.24	5.88	2.40

[e] Onset oxidation and reduction potentials versus Ag/Ag⁺.

[f] Estimated from the onset oxidation and reduction potential using HOMO = -(4.44 + E^{ox}_{onset}) and LUMO =-(4.44 + E^{red}_{onset}).

[g] Obtained from CV measured in CH_2Cl_2–n-Bu_4NPF_6 (0.1 M) at a scan rate of 50 ms^{-1}.

[h] Obtained from AC2 measured in solid neat film.

[i] Electrochemical band gaps determined using E^{red}_{onset} - E^{ox}_{onset}

5.4.6 Electroluminescence properties

In order to investigate the electroluminescence properties of AIE emitters, OLED devices were fabricated with the following device structure: indium tin oxide ITO(90nm)/PEDOT:PSS(40nm)/NPB(15nm)/TCTA(5nm)/EL(40nm)/TmPyPB(35nm)/LiF(0.5nm):Al(100nm), where these materials were used as the emitting layer (EML) as shown in Figure 5.25. Conductive polymer poly(3,4-ethylenedioxy thiophene): poly(4-styrenesulfonate) (PEDOT: PSS) as hole injection layer, *N*,*N*′-*bis*(naphthalen-1-yl)-*N*,*N*′-*bis*(phenyl)-benzidine (NPB), 4,4',4''-Tris(carbazol-9-yl)triphenylamine (TCTA), 3,3-di(9H-carbazol-9-yl)biphenyl (mCBP) as a hole-transport layer (HTL), and 1,3,5-Tri(m-pyridin-3-ylphenyl)benzene (TmPyPB) as hole-blocking layer were also used to enable high-performance devices.

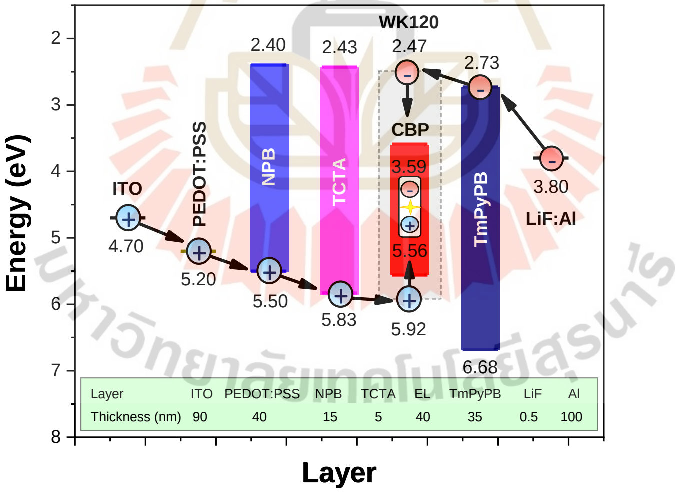
Energy (eV)
2
3
4
5
6
7
8
Layer
ITO
4.70
PEDOT:PSS
5.20
NPB
2.40
5.50
TCTA
2.43
5.83
WK120
2.47
CBP
3.59
5.56
5.92
TmPyPB
2.73
6.68
3.80
LiF:Al
Layer ITO PEDOT:PSS NPB TCTA EL TmPyPB LiF Al
Thickness (nm) 90 40 15 5 40 35 0.5 100

Figure 5.25 Schematic energy diagram of OLED devices.

The electroluminescence spectra (EL) of all AIE emitters doped in 3% CBP showed similar features with their fluorescence spectra without the emission of the host materials as shown in Figure 5.26.

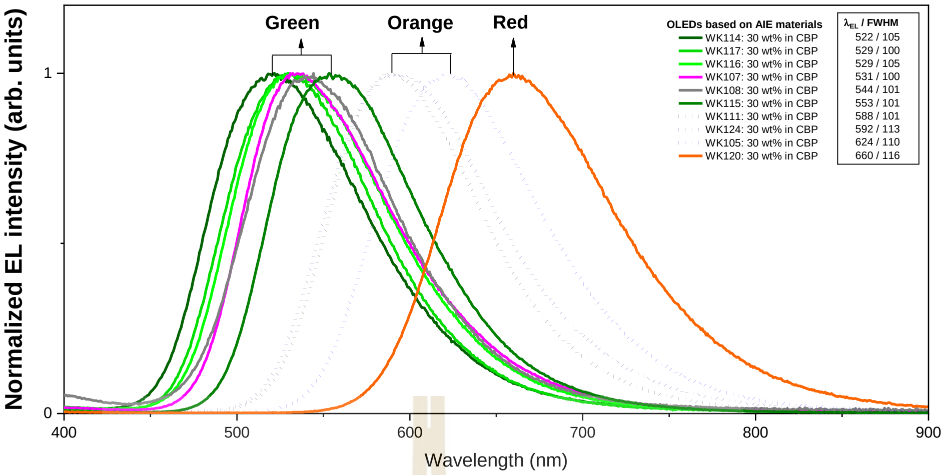

Figure 5.26 Normalized electroluminescence spectra at high brightness of OLEDs based on WK series AIE materials 20 wt% in CBP.

The quantum yield of these AIE emitters in powder are summarized in Table 5.4. All AIE emitters show a moderate quantum yield in the range of 2.41-57.55%.

Table 5.4 Quantum yield of AIE emitters **17-26**.

Compounds	Quantum yield (%)
BT-2TPE (**17**)	43.56
NT-2TPE (**18**)	13.48
NT-TPETPA (**19**)	2.41
BT-2TPEH (**20**)	53.68
BT-TPETPA (**21**)	57.55
FBT-2TPE (**22**)	35.87
2FBT-2TPE (**23**)	45.74
2FBT-2TPEH (**24**)	44.11
NBT-2TPE (**25**)	43.38
BNT-2TPE (**26**)	27.16

The multi-layer devices using AIE emitters as EML were fabricated. The thermal evaporation processed of all AIE emitters emit green, yellow, and red light. No emission shoulder at a longer wavelength due to excimer and exciplex species formed at the interface of the EML and ETL layers, which often occurs in devices fabricated from EMLs with a planar molecular structure, is detected. The devices characteristics based on these materials as an emitter are summerized in Table 5.5. From the results revealed that the external quantum efficiency of OLED devices were in the range of 3.14-4.66%.

Table 5.5 Device characteristics of OLEDs

Emissive layer	%EQE$_{max}$/V	CE$_{max}$/V	PE$_{max}$/V
BT-2TPE (**17**)	3.14/6.0	8.79/7.4	4.63/5.6
NT-2TPE (**18**)	3.47/5.4	4.53/5.0	2.84/5.0
NT-TPETPA (**19**)	3.16/4.4	1.23/4.4	0.91/4.2
BT-2TPEH (**20**)	4.36/4.2	11.85/4.2	8.86/4.2
BT-TPETPA (**21**)	3.64/4.8	8.39/4.8	6.23/4.8
FBT-2TPE (**22**)	3.25/5.4	8.93/5.4	5.20/5.4
2FBT-2TPE (**23**)	4.66/5.0	7.96/5.0	5.00/5.0
2FBT-2TPEH (**24**)	3.41/5.4	8.25/5.2	4.99/5.2
NBT-2TPE (**25**)	3.75/7.2	6.50/7.2	2.84/7.2
BNT-2TPE (**26**)	4.10/4.0	7.81/4.0	6.14/4.0

5.5 Conclusion

In summary, AIE emitters **17-26** were successfully synthesized by a Suzuki-Miyaura cross-coupling reaction using $Pd(PPh_3)_4$ as the catalyst and K_2CO_3 as a base to give the compounds in a high yield. The desired molecules containing the D-A-D system, which comprised of benzothiadiazole, naphthothiadiazole, and *bis*- naphthothia diazole as an acceptor core with the AIE activator such as TPE, TPEH as the donor moieties. All AIE emitters exhibited red emission with the strong ICT in solution and showed a strong PL intensity when the molecules were aggregated. From the studies can be concluded that all compounds exhibited aggregation-induced emission characteristics upon increasing the water fraction. The OLEDs device based on AIE emitters exhibited a high external quantum efficiency of 3.14 - 4.66%. We believe that our results could provide a useful guide to design the highly efficient emitter with a high PL intensity in solid-state to be suitable for applications in OLEDs devices.

CHAPTER VI

EXPERIMENTAL

6.1 General remark

The NMR spectra were measured on a Bruker DRX 600 spectrometer, and chemical shifts were reported in ppm using tetramethylsilane as an internal standard. High-resolution mass spectrometry (HRMS) analysis was performed by a Bruker autoflex MALDI-TOF mass spectrometer. The UV-visible absorption spectra were determined on a Perkin Elmer Lambda-1050 UV/Vis/NIR spectrophotometer. The fluorescence spectra, fluorescence quantum yield, and the transient photoluminescence decay profiles of the target molecules were measured using an Edinburgh Instruments FLS980 spectrometer. Cyclic voltammetry was performed using the Autolab PGSTAT101 with a scan rate of 50 mV/s in CH_2Cl_2 solution at room temperature. A platinum plate as the working electrode, a Pt-wire counter electrode, and a saturated calomel electrode (SCE) as the reference electrode was used. The supporting electrolyte was tetrabutylammonium hexafluorophosphate (0.1 M) and ferrocene was selected as the internal standard. Differential scanning calorimetry (DSC) analysis was performed on a METTLER DSC823e thermal analyzer under N2 atmosphere. Samples were scanned from 25 to 430°C at a heating rate of 10°C/min then rapidly cooled to 25°C and heated at the same heating rate to 430°C. Thermogravimetric analysis (TGA) was carried out on a Seiko EXSTAR 6000 TG/DTA 6300 thermal analyzer at a heating rate of 10°C/min under the N_2 atmosphere.

Tetrahydrofuran (THF) was dried and freshly distilled from sodium/benzaphenone under N_2. Solvents were dried and purified by conventional methods prior to use. CH_2Cl_2 for cyclic voltammetry analysis was washed with conc. H_2SO_4 and freshly distilled twice from calcium hydride under N_2. Reagents of commercial quality were used from freshly opened containers or purified by common methods.

Thin-layer chromatography (TLC) was carried out on Merck silica gel F_{254} TLC alumina sheets. Column chromatography used Merck silica gel 60, particle size 0.063-0.200 mm (70-230 mesh) for column chromatography and particle size 0.40-0.063 mm (230-240 mesh) for flash column chromatography. Preparative chromatography (PLC) was carried out on glass supported silica gel using silica-gel 60 F254 for preparative chromatography from Merck.

All moisture-sensitive reactions were carried out under N_2 in the pre-dried glass apparatus.

6.2 General procedure (GP)

6.2.1 GP 1 : Ullmann coupling reaction

A mixture of Ar-NH (9.2 mmol), 3,6-diiodo-9-tosyl-carbazole (4.0 mmol), CuI (2.0 mmol), K_3PO_4 (1.0 mmol), and (±)-*trans*-1,2-diaminocyclohexane (2.0 mmol) in toluene (120 mL) was degassed with N_2 for 5 min and then stirred at reflux under N_2 atmosphere for 48 h. After the mixture was cooled, water (100 mL) was added, and the mixture was extracted with CH_2Cl_2 (50 mL x 3). The combined organic phase was washed with water (100 mL x 2) and brine solution (100 mL), dried over anhydrous Na_2SO_4 and filtered. The solvent was removed to dryness, and the residue was purified by silica gel column chromatography using a mixture of CH_2Cl_2 and hexane as eluent followed by recrystallization with a mixture of CH_2Cl_2 and methanol to afford the corresponding product.

6.2.2 GP 2 : Alkylation reaction

Pigment red 254 (0.28 mmol), potassium *tert*-butoxide (0.62 mmol) and *N*-Methyl-2-pyrrolidone (NMP) (15 mL) were heated to 60°C. Alkylbromide (0.84 mmol) was added and the mixture was stirred at 60°C for 18 h. After cooling to room temperature then diluted with water (50 mL). The solution was extracted with CH_2Cl_2 (3 x 50 mL), and the combined organic layers, dried over anhydrous Na_2SO_4 and concentrated under reduced pressure. The crude product was purified by column chromatography using a mixture of CH_2Cl_2 and hexane as eluent followed by recrystallization with a mixture of CH_2Cl_2 and methanol to afford the corresponding product.

6.2.3 GP 3 : Suzuki cross-coupling reaction

To a 100 mL flask equipped with an Ar inlet/outlet, a mixture of aryl bromides (1.14 mmol), borolane or boronic acid (1.25 mmol), $Pd(PPh_3)_4$ (0.06 mmol), 10 wt % aqueous sodium carbonate solution (10 mL), and toluene (20 mL) were added under N_2. The reaction mixture was heated at 110°C for 24 h. After the mixture was cooled, CH_2Cl_2 (50 ml) was added. The organic phase was washed with water (50 mL × 2) and brine solution (50 ml), dried over anhydrous Na_2SO_4 and filtered. The solvent was removed to dryness, and the residue was purified by silica gel column chromatography using a mixture of CH_2Cl_2 and hexane as eluent followed by recrystallization with a mixture of CH_2Cl_2 and methanol to afford the corresponding product.

6.2.4 GP 4 : Nucleophilic substitution reaction

A suspension of carbazole derivatives (2.3 mmol) and 60% NaH (3.0 mmol) in DMF (15 mL) was heated at 70°C under nitrogen atmosphere. At this temperature and under vigorous stirring, fluorophenyl sulfone (1.0 mmol) was added. The mixture was stirred at 100°C for 24 h. After cooling to room temperature, the reaction was quenched with water and CH_2Cl_2 (20 ml) was added. The organic phase was washed with water (50 mL × 2) and brine solution (50 ml), dried over anhydrous Na_2SO_4 and filtered. The solvent was removed to dryness, and the residue was purified by silica gel column chromatography using a mixture of CH_2Cl_2 and hexane as eluent followed by recrystallization with a mixture of CH_2Cl_2 and methanol to afford the corresponding sulfone product.

6.2.5 GP 5 : Borylation reaction

Under N_2 atmosphere, aryl bromide (1.0 mmol), bis(pinacolato)diboron (2.0 mmol), KOAc (12 mmol), and Pd(dppf)Cl_2 (0.05 mmol) were dissolved in toluene (20 mL) and heated to 110°C for 24 h. After the reaction solution was cooled to room temperature, the reaction was quenched with water and CH_2Cl_2 (20 ml) was added. The organic phase was washed with water (50 mL × 2) and brine solution (50 ml), dried over anhydrous Na_2SO_4 and filtered. The solvent was removed to dryness, and the residue was purified by silica gel column chromatography using a mixture of CH_2Cl_2 and hexane as eluent followed by recrystallization with a mixture of CH_2Cl_2 and methanol to afford the corresponding borolane product.

6.3 The synthesis

6.3.1 Supplementary data in Chapter 2: the synthesis of DPP dendrimers

3,6-diiodo-9-tosyl-carbazole (72)

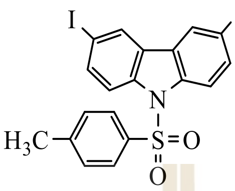

Carbazole (**71**) (5.0g, 0.030 mmol) was dissolved in 30 ml of acetic acid, potassium iodide (6.5 g, 0.038 mmol) and potassium iodate (6.31 g, 0.030 mmol) were added into the solution. The mixture was refluxed for 4 h. After the reaction solution was cooled to room, the brown solid was separated by rapidly filtered off and washed by hexane and methanol, followed by recrystallization with a mixture of CH_2Cl_2 and methanol to afford the diiodo carbazole in the yield of 62%.

After that, diiodo carbazole (5.03g, 0.012 mmol) and potassium hydroxide (0.74 g, 0.013 mmol) were dissolved in 50 ml of acetone, 4-Toluenesulfonyl chloride (2.52 g, 0.013 mmol) was added into the solution. The mixture was refluxed for 5 h. After the reaction solution was cooled to room temperature the reaction was poured into water and CH_2Cl_2 (20 ml) was added. The organic phase was washed with water (50 mL × 2) and brine solution (50 ml), dried over anhydrous Na_2SO_4 and filtered. The solvent was removed to dryness, and the residue was purified by silica gel column chromatography using a mixture of CH_2Cl_2 and hexane as eluent followed by recrystallization with a mixture of CH_2Cl_2 and hexane to afford the 3,6-diiodo-9-tosyl-carbazole (**72**) as a solid (4.44 g, 64%).

3,6-di-*tert*-butyl-carbazole (73)

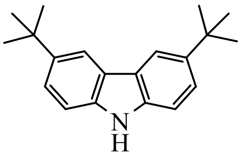

To a solution of carbazole (**71**) (10.0 g, 0.06 mol) in CH_2Cl_2 (80 mL) and CH_3NO_2 (40 mL) were added $ZnCl_2$ (24.5 g, 0.18 mol). Then 2-chloro-2-methyl propane (19.8 mL, 0.18 mol) was added dropwise. Then the mixture was sonicated for 1 h, the mixture was filtered, washed with hexane followed by recrystallization with a mixture of CH_2Cl_2 and hexane to obtain the 3,6-di-*tert*-butyl-carbazole (**73**) (12.0 g, 72%) as white solid; ^{1}H-NMR (600 MHz, $CDCl_3$): δ = 8.09 (s, 2H, -C=C*H*-C), 7.47 (d, *J* = 10.2 Hz, 2H, -HN-C-CH=C*H*-C), 7.33 (d, *J* = 10.2 Hz, 2H, -HN-C-C*H*=CH-C), 1.47 (s, 18H, $-C(CH_3)_3$) ppm; ^{13}C-NMR (150 MHz, $CDCl_3$): δ = 142.2, 138.1, 123.5, 123.4, 116.2, 110.0, 34.7, and 32.0 ppm.

G2 (74)

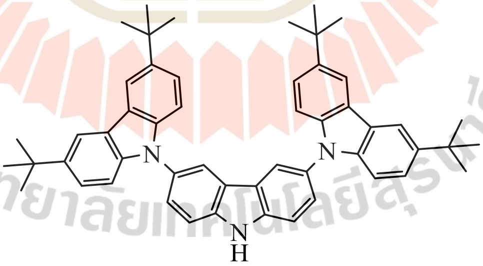

According to GP 1, a mixture of 3,6-di-*tert*-butyl-carbazole (**G1**, **73**) (2.5707 g, 9.2 mmol), 3,6-diiodo-9-tosyl-carbazole (**72**) (2.2928 g, 4.0 mmol), CuI (0.3809 g, 2.0 mmol), K_3PO_4 (2.1227g, 1.0 mmol), and (±)-*trans*-1,2-diaminocyclohexane (0.24 mL, 2.0 mmol) in toluene (120 mL) was refluxed under N_2 atmosphere for 48 h. The crude product was purified by column chromatography (SiO_2, CH_2Cl_2/hexane) and recrystallization by CH_2Cl_2 and methanol to afford the G2 product as white solid (1.8

g, 62%); ^{1}H-NMR (600 MHz, $CDCl_3$): δ = 8.38 (s, 1H, NH), 8.14 (s, 2H, -C=C*H*-C), 8.13 (s, 4H, -C=C*H*-C), 7.64 (d, *J* = 8.4 Hz, 2H, -HN-C-CH=C*H*-C), 7.58 (d, *J* = 8.4 Hz, 2H, -HN-C-C*H*=CH-C), 7.42 (d, *J* = 8.4 Hz, 4H, -HN-C-CH=C*H*-C), 7.28 (d, *J* = 8.4 Hz, 4H, -HN-C-C*H*=CH-C), 1.44 (s, 36H, $-C(CH_3)_3$) ppm; ^{13}C-NMR (150 MHz, $CDCl_3$): δ = 142.5, 140.2, 139.0, 130.5, 126.0, 124.1, 123.5, 123.0, 119.4,116.2, 111.8, 109.11, 34.73, and 32.0 ppm.

G1hexyl bromide (75)

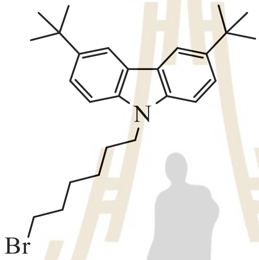

1,6-Dibromohexane (2.8 mL, 18.0 mmol) was added to a mixture of G1 (**73**) (1.0 g, 3.6 mmol), KOH (0.81 g, 14.4 mmol), and *N*,*N*-dimethylformamide (DMF, 50 mL) at 0°C. The mixture was stirred at room temperature for 24 h and then quenched with water and CH_2Cl_2 (20 ml) was added. The organic phase was washed with water (50 mL × 2) and brine solution (50 ml), dried over anhydrous Na_2SO_4, and filtered. The solvent was removed to dryness, and the crude product was purified by column chromatography (SiO_2, CH_2Cl_2/hexane) to afford G1hexyl bromide (**75**) (1.2223 g, 77%) as a white solid; ^{1}H-NMR (600 MHz, $CDCl_3$): δ = 8.10 (s, 2H, -C=C*H*-C), 7.50 (d, *J* = 8.4 Hz, 2H, -HN-C-CH=C*H*-C), 7.30 (d, *J* = 8.4 Hz, 2H, -HN-C-C*H*=CH-C), 4.25 (t, *J* = 7.2 Hz, 2H, $-N-CH_2-CH_2-C$), 3.36 (t, *J* = 6.6 Hz, 2H, $Br-CH_2-CH_2-$), 1.81-1.90 (m, 4H, CH_2-CH_2-), 1.44 (s, 18H, $-C(CH_3)_3$), 1.41-1.39 (m, 4H, CH_2-CH_2-) ppm; ^{13}C-NMR (150 MHz, $CDCl_3$): δ = 141.5, 139.0, 123.3, 122.7, 116.3, 108.0, 43.0, 34.7, 33.7, 32.6, 32.4, 32.1, 29.0, 28.0, and 26.5 ppm; m/z (MALDI-TOF): 441.333 ($C_{26}H_{36}BrN$ required m/z = 441.2031).

G2hexyl bromide (76)

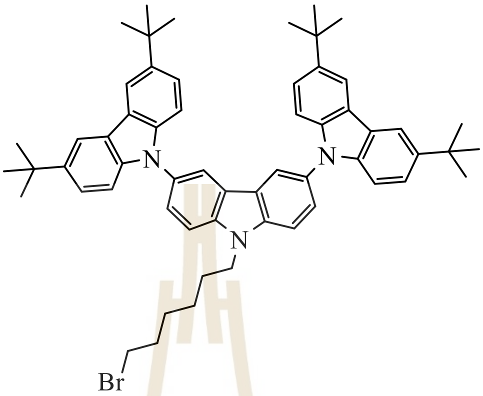

1,6-Dibromohexane (1.1 mL, 6.92 mmol) was added to a mixture of G2 (**74**) (1.0 g, 1.40 mmol), KOH (0.31 g, 5.54 mmol), and *N*,*N*-dimethylformamide (DMF, 50 mL) at 0˚C. The mixture was stirred at room temperature for 24 h and then quenched with water and CH_2Cl_2 (20 ml) was added. The organic phase was washed with water (50 mL × 2) and brine solution (50 ml), dried over anhydrous Na_2SO_4, and filtered. The solvent was removed to dryness, and the crude product was purified by column chromatography (SiO_2, CH_2Cl_2/hexane) to afford G2hexyl bromide (**76**) (1.0605 g, 86%) as a white solid; ^{1}H-NMR (600 MHz, $CDCl_3$): δ = 8.18 (s, 2H, -C=C*H*-C), 8.15 (s, 4H, -C=C*H*-C), 7.64 (m, 4H, -HN-C-C*H*=C*H*-C), 7.44 (m, 4H, -HN-C-C*H*=C*H*-C), 7.31 (m, 4H, -HN-C-C*H*=C*H*-C), 4.49 (t, *J* = 7.2 Hz, 2H, -N-CH_2-CH$_2$-C), 3.43 (m, 2H, Br-CH_2-CH$_2$-), 2.09-1.91 (m, 4H, -CH_2-CH_2-), 1.46 (s, 36H, -C(CH_3)$_3$), 1.44 (m, 4H, CH_2-CH$_2$-) ppm; ^{13}C-NMR (150 MHz, $CDCl_3$): δ = 142.5, 140.3, 139.9, 129.9, 125.7, 123.5, 123.4, 123.0, 119.5, 116.2, 109.9, 109.1, 43.5, 34.7, 33.7, 32.6, 31.9, 29.1, 28.0, 27.3, 26.6 ppm; m/z (MALDI-TOF): 883.605 ($C_{58}H_{66}BrN_3$ required m/z = 883.4440).

G0DPP (1)

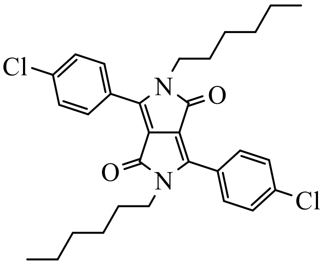

According to GP 2, pigment red 254 (**77**) (0.1000 g, 0.28 mmol), potassium *tert*-butoxide (0.0691 g, 0.62 mmol) and *N*-Methyl-2-pyrrolidone (NMP) (15 mL) were heated to 60°C. 1-bromohexane (0.12 mL, 0.84 mmol) was added and the mixture was stirred at 60°C for 18 h. The crude product was purified by column chromatography (SiO_2, CH_2Cl_2/hexane) and recrystallization by CH_2Cl_2 and methanol to afford the product as orange solid (0.0734 g, 50%); ^{1}H-NMR (600 MHz, $CDCl_3$): $\delta = 7.76$ (d, 4H, $J = 8.4$ Hz, ArH-C(Cl)), 7.50 (d, 4H, $J = 8.4$ Hz, ArH), 3.72 (t, 4H, $J = 7.5$ Hz, NCH_2), 1.56 (m, 4H, NCH_2CH_2), 1.21 (m, 12H, $CH_2CH_2CH_2$), 0.83 (t, 6H, -CH_2CH_3) ppm; ^{13}C-NMR (150 MHz, $CDCl_3$): $\delta = 162.5$, 147.4, 137.4, 130.0, 129.3, 136.6, 110.0, 41.9, 31.2, 29.7, 29.4, 26.4, 22.5, and 13.9 ppm; m/z (MALDI-TOF): 524.4251 ($C_{30}H_{34}Cl_2N_2O_2$ required m/z = 524.1997); . IR (ATR):ν_{max} = 2936, 2847, 1686, 1612,1483, 1374, 1076, 831, 695 cm^{-1}.

G1DPP (2)

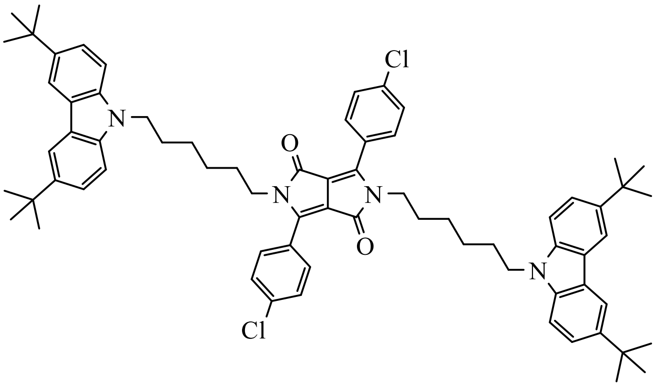

According to GP 2, pigment red 254 (**77**) (0.1000 g, 0.28 mmol), potassium *tert*-butoxide (0.0691 g, 0.62 mmol) and NMP (15 mL) were heated to 60°C. G_1hexylbromide (**75**) (0.3720 g, 0.84 mmol) was added and the mixture was stirred at 60°C for 18 h. The crude product was purified by column chromatography (SiO_2, CH_2Cl_2/hexane) and recrystallization by CH_2Cl_2 and methanol to afford the product as orange solid (0.0418 g, 14%); ^{1}H-NMR (600 MHz, $CDCl_3$): δ = 8.09 (s, 4H, Cz*H*), 7.70 (d, 4H, *J* = 8.4 Hz, Ar*H*-C(Cl)), 7.45-7.49 (m, 8H, Ar*H* and -HN-C-CH=C*H*-C), 7.23 (d, *J* = 8.4 Hz, 4H, -HN-C-C*H*=CH-C), 4.18 (t, 4H, *J* = 6.8 Hz, (G1)NCH_2), 3.69 (t, 4H, *J* = 7.3 Hz, (DPP)NCH_2), 1.78 (m, 4H, m), 1.53 (4H, m, NCH_2CH_2) 1.45 (m, 36H, -$C(CH_3)_3$), 1.24-1.30 (m, 8H, $CH_2CH_2CH_2CH_2$) ppm; ^{13}C-NMR (150 MHz, $CDCl_3$): δ = 162.4, 147.3, 141.5, 138.9, 137.4, 129.9, 129.3, 126.4, 123.2, 122.7, 116.3, 109.9, 107.9, 42.9, 41.8, 34.7, 32.1, 29.3, 29.0, 26.8, 26.6 ppm; m/z (MALDI-TOF): 1078.6823 ($C_{70}H_{80}Cl_2N_4O_2$ required m/z = 1078.5658); . IR (ATR):ν_{max} = 2950, 2868, 2311, 1673, 1605,1475, 1353, 1082, 797, 716 cm^{-1}.

G2DPP (3)

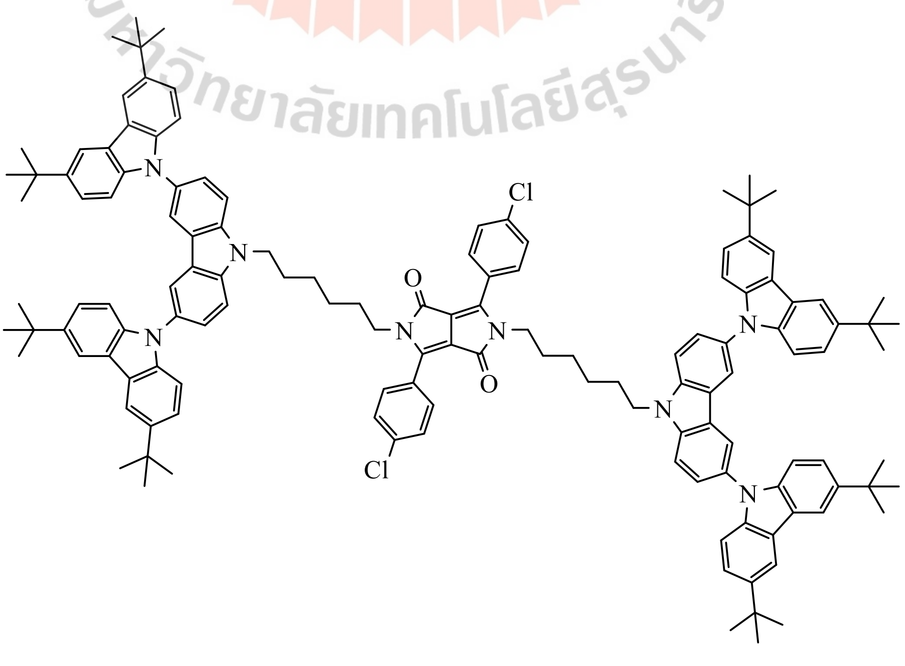

According to GP 2, pigment red 254 (**77**) (0.0500 g, 0.14 mmol), potassium *tert*-butoxide (0.0350 g, 0.31 mmol) and NMP (10 mL) were heated to 60°C. G_2hexylbromide (**7**) (0.3720 g, 0.42 mmol) was added and the mixture was stirred at 60°C for 18 h. The crude product was purified by column chromatography (SiO_2, CH_2Cl_2/hexane) and recrystallization by CH_2Cl_2 and methanol to afford the product as orange solid (0.0418 g, 26%); ^{1}H-NMR (600 MHz, $CDCl_3$): δ = 8.17 (s, 4H, Cz*H*), 8.15 (s, 8H, Cz*H*), 7.73 (d, 4H, *J* = 8.4 Hz, Ar*H*-C(Cl)), 7.55-7.61 (m, 8H, -HN-C-C*H*=CH-C and -HN-C-CH=C*H*-C), 7.42-7.46 (d, 12H, Ar*H* and -HN-C-C*H*=CH-C), 7.30 (d, 8H, *J* = 8.4 Hz, -HN-C-CH=C*H*-C), 4.40 (t, 4H, *J* = 7.2 Hz, (G1)NCH_2), 3.76 (m, 4H, (DPP)NCH_2), 1.94-1.99 (m, 4H, NCH_2CH_2), 1.61-1.65 (m, 4H, NCH_2 CH_2CH_2), 1.26-1.46 (m, 80H, CH_2CH_2 and -C(CH_3)$_3$) ppm; ^{13}C-NMR (150 MHz, $CDCl_3$): δ = 162.4, 147.3, 142.5, 140.3, 139.9, 137.5, 129.9, 129.4, 126.4, 125.7, 123.5, 123.1, 119.5, 116.2, 110.0, 109.8, 109.1, 43.4, 41.8, 34.7, 32.1, 29.4, 29.0, 26.8, and 26.6 ppm; m/z (MALDI-TOF): 1963.0941 ($C_{134}H_{140}Cl_2N_8O_2$ required m/z = 1963.0476); . IR (ATR): ν_{max} = 2963, 2854, 2359, 1673, 1503,1258, 811, 606 cm^{-1}.

6.3.2 Supplementary data in Chapter 3: the synthesis of TADF emitters

3,3′-Dibromo-4,4′-difluorodiphenyl sulfone (131)

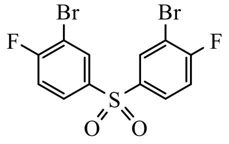

According to a published procedure (N. Li, Shin, Hwang, Lee, and Guiver, 2010), *Bis*(4-fluorophenyl) sulfone (1.0 g, 03.94 mmol) was dissolved in concentrated H_2SO_4 (15mL) at room temperature. To this was added NBS (1.54 g, 2.2 mmol, 2.2 equiv), divided into three portions and added at 15 min intervals. The mixture was stirred vigorously at room temperature for a further 6h and then poured into crushed ice (~500 g) to precipitate the solids. The precipitated solids were filtered, washed with water (600 mL) and then with 100 mL of n-hexane, and purified by recrystallization from toluene to obtain the product as white solid (0.71 g, 44%); ^{1}H-NMR (600 MHz, $CDCl_3$): $\delta = 8.15$ (m, 2H, SO_2Ar*H*), 7.88 (m, 2H, (Br)Ar*H*), 7.27 (m, 2H, (F)Ar*H*) ppm; ^{13}C-NMR (150 MHz, $CDCl_3$): $\delta = 163.1$, 138.3, 133.6, 129.1, 117.8, and 110.9 ppm.

3,3′,5,5′-Tetrabromo-4,4′-difluorodiphenyl sulfone (132)

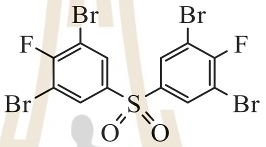

According to a published procedure (N. Li et al., 2010), *Bis*(4-fluorophenyl) sulfone (1.0 g, 3.94 mmol) was dissolved in concentrated H_2SO_4 (25 mL) at room temperature. To this was added NBS (2.95 g, 16.5 mmol, 4.2 equiv) divided into six portions over a period of 1 h. The mixture was stirred vigorously at room temperature for 2 h, and then the temperature was increased to 60°C and maintained at that temperature for 12 h. The mixture was poured into crushed ice (~500 g) to precipitate the solids. The precipitated solids were filtered, washed with water several times, followed by 100 mL of n-hexane, and finally dried to obtain the product as white solid (1.01 g, 46%); ^{1}H-NMR (600 MHz, $CDCl_3$): $\delta = 8.07$ (m, 4H, SO_2Ar*H*) ppm.

3,3′-Diphenyl-4,40-difluorodiphenyl Sulfone (DBDFDPS, 133)

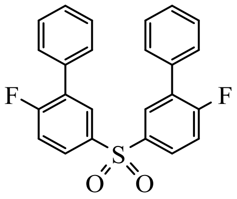

According to GP 3, a mixture of 3,3′,5,5′-Tetrabromo-4,4′-difluorodiphenyl sulfone (**132**) (206 mg, 0.5 mmol), phenyl boronic acid (153 mg, 1.25 mmol, 2.5 equiv), $Pd(PPh_3)_4$ (24 mg, 0.02 mmol), 10 wt % aqueous sodium carbonate solution (7.5 mL), and mixed toluene/THF in the ration of 2:1 (15 mL) were added under N_2. The reaction mixture was heated at 110°C for 24 h. The crude product was purified by column chromatography (SiO_2, CH_2Cl_2/hexane) and recrystallization by CH_2Cl_2 and methanol to afford the product as white solid (166 mg, 82%); ^{1}H-NMR (600 MHz, $CDCl_3$): $\delta = 8.06$ (m, 2H, SO_2Ar*H*), 7.92 (m, 2H, (Ph)Ar*H*), 7.53-7.42 (m, 10H, Ph*H* and (F)Ar*H*), 7.27 (t, 2H, *J* = 9.3 Hz, Ph*H*) ppm; ^{13}C-NMR (150 MHz, $CDCl_3$): δ = 163.3, 161.6, 137.9, 133.7, 130.7, 129.0, 128.9, 128.7, 117.6, and 117.5 ppm.

3,3′,5,5′-Tetraphenyl-4,4′-difluorodiphenyl Sulfone (TBDFDPS, 134)

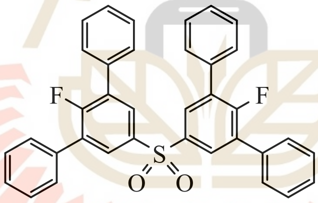

According to GP 3, a mixture of 3,3′-dibromo-4,4′-difluorodiphenyl sulfone (**131**) (302 mg, 0.53 mmol), phenyl boronic acid (324 mg, 2.65 mmol, 5.0 equiv), $Pd(PPh_3)_4$ (25 mg, 0.02 mmol), 10 wt % aqueous sodium carbonate solution (7.5 mL), and mixed toluene/THF in the ration of 2:1 (15 mL) were added under N_2. The reaction mixture was heated at 110°C for 24 h. The crude product was purified by column chromatography (SiO_2, CH_2Cl_2/hexane) and recrystallization by CH_2Cl_2 and methanol to afford the product as white solid (172 mg, 58%); ^{1}H-NMR (600 MHz, $CDCl_3$): $\delta = 8.02$ (d, 2H, SO_2Ar*H*), 7.56-7.41 (m, 10H, Ph*H*) ppm; ^{13}C-NMR (150 MHz, $CDCl_3$): δ = 163.3, 161.6, 137.9, 133.7, 130.7, 129.0, 128.9, 128.7, 117.6, and 117.5 ppm; ^{13}C-NMR

(150 MHz, $CDCl_3$): δ = 137.8, 134.0, 131.6, 131.5, 129.4, 129.3, 129.2, 129.1, and 128.7 ppm.

3,6-diphenyl-9H-carbazole (136)

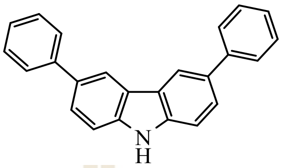

According to GP 3, a mixture of 3,6-diiodo carbazole (**135**) (1.0 g, 2.4 mmol), phenyl boronic acid (729 mg, 6.0 mmol, 2.5 equiv), $Pd(PPh_3)_4$ (111 mg, 0.1 mmol), 10 wt % aqueous sodium carbonate solution (10 mL), and mixed toluene/THF in the ration of 2:1 (20 mL) were added under N_2. The reaction mixture was heated at 110°C for 24 h. The crude product was purified by column chromatography (SiO_2, CH_2Cl_2/hexane) and recrystallization by CH_2Cl_2 and methanol to afford the product as a solid (321 mg, 42%); ^{1}H-NMR (600 MHz, $CDCl_3$): δ = 8.34 (s, 2H, Cz*H*), 8.12 (s, 1H, N*H*), 7.72 (d, 4H, *J* = 7.7 Hz, Ph*H*), 7.69 (d, 2H, *J* = 8.3 Hz, Cz*H*), 7.51 (d, 2H, *J* = 8.3 Hz, Cz*H*), 7.48 (t, 4H, *J* = 8.0 Hz, Ph*H*), 7.34 (t, 2H, *J* = 7.3 Hz, Ph*H*) ppm; m/z (Q-TOF): 319.1292 ($C_{24}H_{17}N$ required m/z = 319.1361).

2,7-diphenyl-9H-carbazole (138)

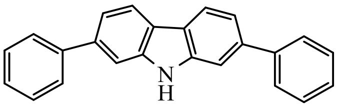

According to GP 3, a mixture of 2,7-dibromo carbazole (**137**) (1.0 g, 3.1 mmol), phenyl boronic acid (939 mg, 7.7 mmol, 2.5 equiv), $Pd(PPh_3)_4$ (150 mg, 0.04 mmol), 10 wt% aqueous sodium carbonate solution (10 mL), and mixed toluene/THF in the ration of 2:1 (20 mL) were added under N_2. The reaction mixture was heated at

110°C for 24 h. The crude product was purified by column chromatography (SiO_2, CH_2Cl_2/hexane) and recrystallization by CH_2Cl_2 and methanol to afford the product as a solid (663 mg, 65%); ^{1}H-NMR (600 MHz, $CDCl_3$): δ = 8.18 (s, 1H, N*H*), 8.13 (d, 2H, *J* = 7.8 Hz, Cz*H*), 7.71 (d, 2H, *J* = 8.1 Hz, Ph*H*), 7.65 (s, 2H, Cz*H*), 7.51 (m, 2H, Cz*H*), 7.48 (t, 4H, *J* = 7.4 Hz, Ph*H*), 7.37 (t, 2H, *J* = 7.1 Hz, Ph*H*) ppm; m/z (Q-TOF): 319.1299 ($C_{24}H_{17}N$ required m/z = 319.1361).

Cz-DPS (4)

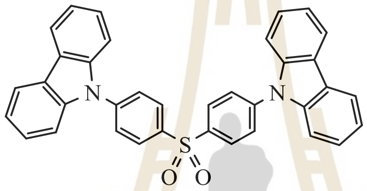

According to GP 4, a suspension of carbazole (**139**) (193 mg, 1.15 mmol, 2.3 equiv) and 60 % sodium hydride (60 g, 2.5 mol) in dry dimethylformamide (DMF) (10 mL) was stirred at 70°C under N_2 atmosphere for 30 minutes. After that, (*Bis*(4-fluorophenyl) sulfone (127 mg, 0.5 mmol) was added into a solution. The mixture was stirred at 100°C for 24 h. The crude product was purified by column chromatography (SiO_2, CH_2Cl_2/hexane) and recrystallization by CH_2Cl_2 and methanol to afford the product as a white crystal (180 mg, 66%); ^{1}H-NMR (600 MHz, $CDCl_3$): δ = 8.29 (d, 4H, *J* = 8.4 Hz, O_2SPh*H*), 8.14 (d, 4H, *J* = 7.9 Hz, Cz*H*), 7.84 (d, 4H, *J* = 8.4 Hz, CzN-Ph*H*), 7.50 (d, 4H, *J* = 8.4 Hz, Cz*H*), 7.44 (t, 4H, *J* = 7.5 Hz, Cz*H*), 7.34 (t, 4H, *J* = 7.5 Hz, Cz*H*) ppm; ^{13}C-NMR (150 MHz, $CDCl_3$): δ = 142.8, 140.0, 139.4, 129.4, 127.2, 126.4, 124.0, 121.0, 120.6, and 109.6 ppm; m/z (Q-TOF): 548.1002 ($C_{36}H_{24}N_2O_2S$ required m/z = 548.1558); . IR (ATR): ν_{max} = 1591, 1510, 1455, 1320, 143, 729, 681, and 600 cm^{-1}.

G1-DPS (5)

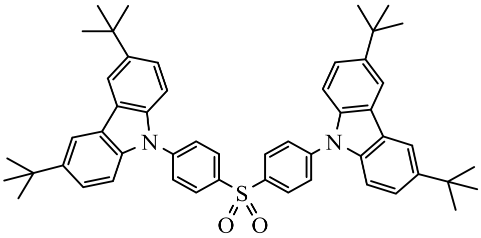

According to GP 4, a suspension of 3,6-di-*tert*-butyl-carbazole (G1, **73**) (322 mg, 1.15 mol, 2.3 equiv) and 60 % sodium hydride (60 g, 2.5 mol) in dry dimethylformamide (DMF) (10 mL) was stirred at 70°C under N_2 atmosphere for 30 minutes. After that, (*Bis*(4-fluorophenyl) sulfone (127 mg, 0.5 mmol) was added into a solution. The mixture was stirred at 100°C for 24 h. The crude product was purified by column chromatography (SiO_2, CH_2Cl_2/hexane) and recrystallization by CH_2Cl_2 and methanol to afford the product as a white crystal (364 mg, 94%); ^{1}H-NMR (600 MHz, $CDCl_3$): δ =8.24 (d, 4H, J = 8.6 Hz, O_2SPhH), 7.82 (d, 4H, J = 8.7 Hz, CzN-Ph*H*), 7.49-7.43 (m, 8H, Cz*H*), 1.46 (m, 36H, -C(CH_3)$_3$) ppm; ^{13}C-NMR (150 MHz, $CDCl_3$): δ = 144.1, 143.2, 138.8, 138.3, 129.6, 126.6, 124.1, 124.0, 116.5 109.2, 34.8, and 31.9 ppm; m/z (MALDI-TOF): 772.4062 ($C_{52}H_{56}N_2O_2S$ required m/z = 773.0782); . IR (ATR): ν_{max} = 2963, 2895, 1591, 1496, 1455, 1302, 1150, 824, and 634 cm^{-1}.

3,6-diPhCz-DPS (6)

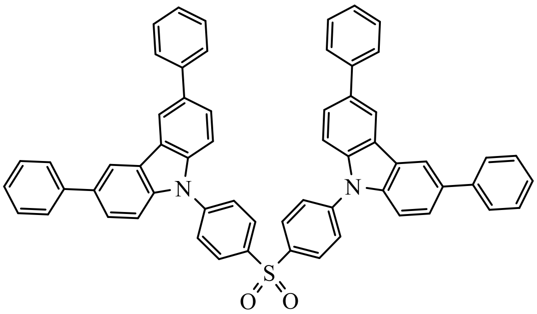

According to GP 4, a suspension of 3,6-diphenyl-9H-carbazole (**136**) (148 mg, 0.5 mmol, 2.3 equiv) and 60% sodium hydride (40 mg, 1.0 mmol) in dry dimethylformamide (DMF) (10 mL) was stirred at 70°C under N_2 atmosphere for 30 minutes. After that, (*Bis*(4-fluorophenyl) sulfone (52 mg, 0.2 mmol) was added into a solution. The mixture was stirred at 100°C for 24 h. The crude product was purified by column chromatography (SiO_2, CH_2Cl_2/hexane) and recrystallization by CH_2Cl_2 and methanol to afford the product as a white crystal (153 mg, 88%); ^{1}H-NMR (600 MHz, $CDCl_3$): δ = 8.40 (s, 4H, Cz*H*), 8.32 (d, 4H, *J* = 8.6 Hz, O_2SPh*H*), 7.89 (d, 4H, *J* = 8.3 Hz, CzN-Ph*H*), 7.72 (d, 8H, *J* = 7.4 Hz, Ph*H*), 7.70 (d, 4H, *J* = 8.7 Hz, Cz*H*), 7.57 (d, 4H, *J* = 8.5 Hz, Cz*H*), 7.50 (t, 4H, *J* = 7.5 Hz, Ph*H*), 7.37 (t, 4H, *J* = 7.5 Hz, Ph*H*) ppm; ^{13}C-NMR (150 MHz, $CDCl_3$): δ = 142.7, 141.5, 139.8, 139.5, 134.8, 129.9, 128.9, 127.3, 127.1, 126.9, 126.1, 124.8, 119.1, and 110.1 ppm; m/z (Q-TOF): 853.1968 ($C_{60}H_{40}N_2O_2S$ required m/z = 853.2844); IR (ATR): ν_{max} = 1578, 1499, 1475, 1326, 1163 1109, 763 and 606 cm^{-1}.

2,7-diPhCz-DPS (7)

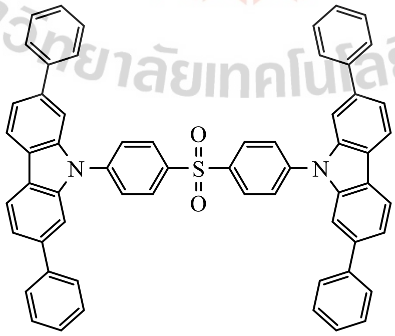

According to GP 4, a suspension of 2,7-diphenyl-9H-carbazole (**138**) (294 mg, 0.92 mmol) and 60 % sodium hydride (80 mg, 2.0 mol, 2.3 equiv) in dry dimethylformamide (DMF) (15 mL) was stirred at 70°C under N_2 atmosphere for 30 minutes. After that, (*Bis*(4-fluorophenyl) sulfone (102 mg, 0.4 mol) was added into a solution. The mixture was stirred at 100°C for 24 h. The crude product was purified by column chromatography (SiO_2, CH_2Cl_2/hexane) and recrystallization by CH_2Cl_2 and methanol to afford the product as a white crystal (226 mg, 66%); ^{1}H-NMR (600 MHz, $CDCl_3$): δ = 8.33 (d, 4H, J = 8.6 Hz, O_2SPh*H*), 8.20 (d, 4H, J = 8.2 Hz, Cz*H*), 7.91 (d, 4H, J = 8.6 Hz, CzN-Ph*H*), 7.66 (s, 4H, Cz*H*), 7.62 (d, 8H, J = 7.4 Hz, Ph*H*), 7.58 (d, 4H, J = 8.2 Hz, Cz*H*), 7.42 (t, 4H, J = 7.7 Hz, Ph*H*), 7.34 (t, 4H, J = 7.7 Hz, Ph*H*) ppm; ^{13}C-NMR (150 MHz, $CDCl_3$): δ = 142.7, 142.6, 141.1, 140.0, 139.5, 130.0, 129.9, 129.9, 128.8, 127.5, 127.4, 127.3, 120.9, 120.8, and 108.2 ppm; m/z (Q-TOF): 852.7777 ($C_{60}H_{40}N_2O_2S$ required m/z = 853.2844); IR (ATR): ν_{max} = 1598, 1489, 1428, 1299, 1136, 1106, 749, and 709 cm^{-1}.

G1-2Ph-DPS (8)

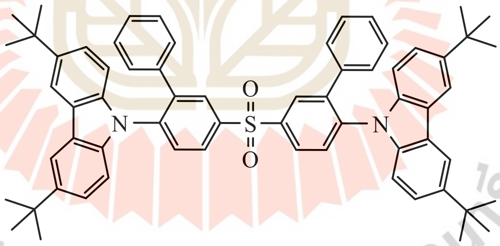

According to GP 4, a suspension of 3,6-di-*tert*-butyl-carbazole (G1, **73**) (161 mg, 0.58 mmol) and 60% sodium hydride (60 mg, 2.5 mmol) in dry dimethylformamide (DMF) (10 mL) was stirred at 70°C under N_2 atmosphere for 30 minutes. After that, DBDFDPS (**133**) (100 mg, 0.25 mmol) was added into a solution. The mixture was stirred at 100°C for 24 h. The crude product was purified by column chromatography (SiO_2, CH_2Cl_2/hexane) and recrystallization by CH_2Cl_2 and methanol to afford the product as a white crystal (173 mg, 74%); ^{1}H-NMR (600 MHz, $CDCl_3$): δ

=8.36 (d, 2H, J = 2.0 Hz, O_2SPhH(Ph)), 8.15 (dd, 2H, J = 2.0 and 8.4 Hz, O_2SPhH(Ph)), 8.02 (s, 4H, CzH), 7.70 (d, 4H, J = 8.4 Hz, G1N-PhH), 7.30-7.28 (m, 4H, G1H), 7.15-7.13 (m, 4H, G1H), 7.08-7.07 (m, 6H, PhH), 6.97 (d, 4H, J = 8.5 Hz, PhH), 1.40 (s, 36H, -C(CH_3)$_3$) ppm; ^{13}C-NMR (150 MHz, $CDCl_3$): δ = 143.2, 141.6, 140.7, 140.6, 138.8, 137.2, 131.2, 130.7, 128.6, 128.1, 127.9, 127.8, 123.6, 123.6, 116.1, 109.4, 34.7, and 31.91 ppm; m/z (MALDI-TOF): 924.4772 ($C_{64}H_{64}N_2O_2S$ required m/z = 924.4688); . IR (ATR): ν_{max} = 2949,2895, 1483, 1326, 1286, 1157, 797, 702, and 648 cm^{-1}.

G2-2Ph-DPS (9)

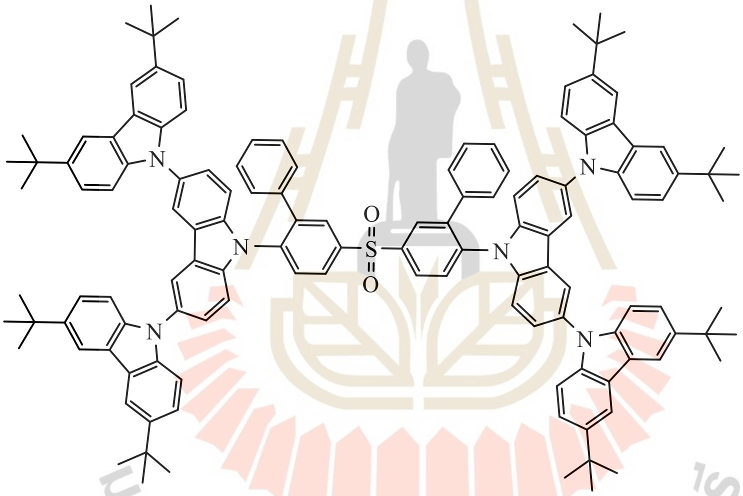

According to GP 4, a suspension of G2, **74** (614 mg, 0.85 mmol) and 60 % sodium hydride (45 mg, 1.85 mmol) in mixed DMF/THF in the ration of 2:1 (20 mL) was stirred at 70°C under N_2 atmosphere for 30 minutes. After that, DBDFDPS (**133**) (150 mg, 0.4 mmol) was added into a solution. The mixture was stirred at 100°C for 24 h. The crude product was purified by column chromatography (SiO_2, CH_2Cl_2/hexane) and recrystallization by CH_2Cl_2 and methanol to afford the product as a white crystal (211 mg, 32%); ^{1}H-NMR (600 MHz, $CDCl_3$): δ = 8.50 (s, 2H, J = 2.0 Hz, O_2SPhH(Ph)), 8.39 (d, 2H, J = 8.4 Hz, O_2SPhH(Ph)), 8.13 (s, 12H, G2H), 8.02 (d, 4H, J = 8.6 Hz, G2N-

Ph*H*), 7.47-7.42 (m, 12H, G2*H*), 7.31 (d, 4H, *J* = 8.4 Hz, G2*H*), 7.25-7.17 (m, 18H, G2*H*, Ph*H*), 1.45 (s, 72H, -C(CH_3)$_3$) ppm; ^{13}C-NMR (150 MHz, $CDCl_3$): δ = 142.7, 142.0, 141.6, 140.0, 139.7, 139.6, 136.8, 131.5, 131.4, 130.9, 128.9, 128.7, 128.4, 127.8, 125.9, 124.2, 123.5, 123.2, 119.2, 116.2, 111.3, 109.0, 34.7, 32.0, and 29.7 ppm; m/z (MALDI-TOF): 1809.1216 ($C_{128}H_{124}N_6O_2S$ required m/z = 1808.9506); IR (ATR): ν_{max} = 2969, 2882, 1489, 1266, 1154, 804, 695, and 606 cm^{-1}.

G1-4Ph-DPS (10)

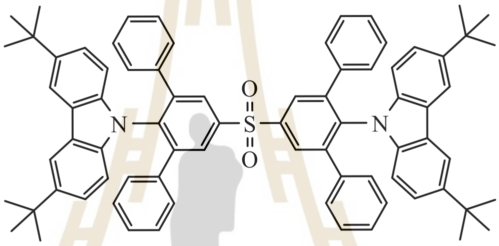

According to GP 4, a suspension of 3,6-di-*tert*-butyl-carbazole (G1, **73**) (47 mg, 0.17 mmol) and 60 % sodium hydride (10.0 mg, 0.04 mmol) in dry dimethylformamide (DMF) (10 mL) was stirred at 70°C under N_2 atmosphere for 30 minutes. After that, TBDFDPS (**134**) (40 mg, 0.07 mmol) was added into a solution. The mixture was stirred at 100°C for 24 h. The crude product was purified by column chromatography (SiO_2, CH_2Cl_2/hexane) and recrystallization by CH_2Cl_2 and methanol to afford the product as a white crystal (50 mg, 94%); ^{1}H-NMR (600 MHz, $CDCl_3$): δ = 8.36 (s, 4H, O_2SPh*H*), 7.85 (s, 4H, G1*H*), 7.16 (d, 4H, *J* = 8.8 Hz, G1*H*), 7.20-6.90 (m, 20H, Ph*H*), 6.76 (d, 4H, *J* = 8.8 Hz, G1*H*), 1.34 (m, 36H, -C(CH_3)$_3$) ppm; ^{13}C-NMR (150 MHz, $CDCl_3$): δ = 143.3, 142.5, 140.1, 137.8, 136.9, 136.4, 128.7, 127.1, 126.8, 126.7, 122.2, 122.1, 114.7, 108.5, 33.5, 30.9, and 30.8 ppm; m/z (MALDI-TOF): 1076.5097

($C_{76}H_{72}N_2O_2S$ required m/z = 1076.5315); IR (ATR): ν_{max} = 2963, 2882, 1483, 1340, 1266, 1150, and 695 cm^{-1}.

G2-4Ph-DPS (11)

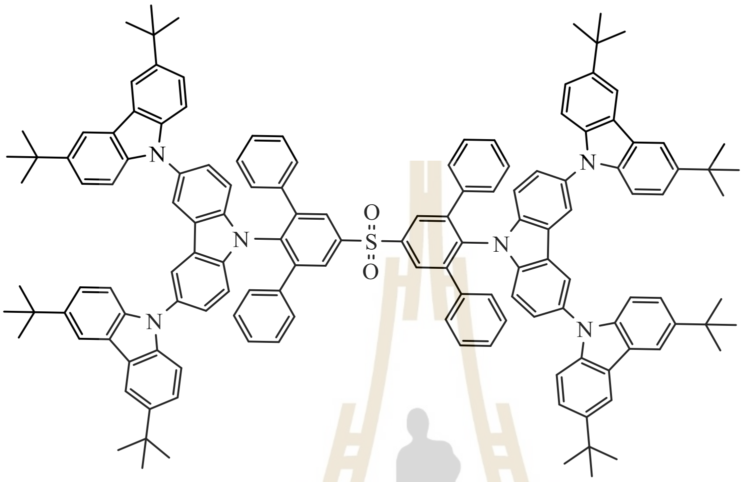

According to GP 4, a suspension of G2, **74** (299 mg, 0.41 mmol) and 60 % sodium hydride (22 mg, 0.9 mmol) in mixed DMF/THF in the ration of 2:1 (15 mL) was stirred at 70°C under N_2 atmosphere for 30 minutes. After that, TBDFDPS (**134**) (100 mg, 0.18 mmol) was added into a solution. The mixture was stirred at 100°C for 24 h. The crude product was purified by column chromatography (SiO_2, CH_2Cl_2/hexane) and recrystallization by CH_2Cl_2 and methanol to afford the product as a white crystal (32 mg, 9%); ^{1}H-NMR (600 MHz, $CDCl_3$): δ = 8.44 (s, 4H, O_2SPh*H*), 8.11 (s, 8H, G2*H*), 7.96 (s, 4H, G2*H*), 7.42 (d, 8H, *J* = 8.6 Hz, G2*H*), 7.34 (d, 4H, *J* = 9.1 Hz, G2*H*), 7.22-7.21 (m, 4H, G2*H*), 7.18-7.13 (m, 28H, G2*H*, Ph*H*), 1.44 (s, 72H, -C(CH_3)$_3$) ppm; ^{13}C-NMR (150 MHz, $CDCl_3$): δ = 144.3, 142.6, 140.0, 139.8, 137.1, 130.8, 130.0, 128.6, 128.5, 127.9, 125.6, 123.8, 123.5, 123.1, 119.0, 116.2, 111.5, 109.0, 34.7, and 32.0 ppm; m/z (MALDI-TOF): 1961.3507 ($C_{140}H_{132}N_6O_2S$ required m/z = 1961.0132); IR (ATR): ν_{max} = 2960, 2901, 1483, 1272, 1157, 797, 716, and 614 cm^{-1}.

3,6-diPhCz-4Ph-DPS (12)

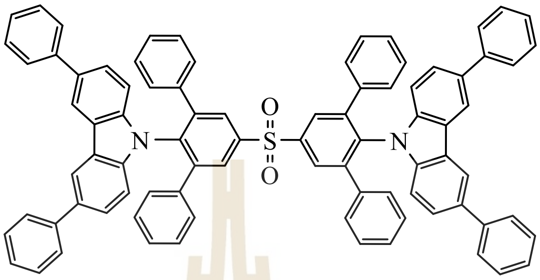

According to GP 4, a suspension of 3,6-diphenyl-9H-carbazole (**136**) (110 mg, 0.35 mmol) and 60% sodium hydride (30 mg, 0.75 mmol) in dry dimethylformamide (DMF) (10 mL) was stirred at 70°C under N_2 atmosphere for 30 minutes. After that, TBDFDPS (**134**) (84 mg, 0.15 mol) was added into a solution. The mixture was stirred at 100°C for 24 h. The crude product was purified by column chromatography (SiO_2, CH_2Cl_2/hexane) and recrystallization by CH_2Cl_2 and methanol to afford the product as a white crystal (131 mg, 38%); ^{1}H-NMR (600 MHz, $CDCl_3$): δ = 8.36 (s, 4H, O_2SPh*H*), 8.17 (s, 4H, Cz*H*), 7.63 (d, 8H, *J* = 8.0 Hz, CzPh*H*), 7.46-7.42 (m, 12H, Cz*H* and CzPh*H*), 7.30 (t, 4H, *J* = 7.5 Hz, CzPh*H*), 7.07-6.98 (m, 24H, Cz*H* and O_2SPh-Ph*H*) ppm; ^{13}C-NMR (150 MHz, $CDCl_3$): δ = 144.4, 141.6, 141.5, 140.3, 137.2, 137.1, 133.3, 129.9, 128.8, 128.7, 128.4, 128.3, 127.7, 127.2, 127.1, 126.6, 125.3, 123.8, 118.5, and 110.4 ppm; m/z (MALDI-TOF): 1157.2931 ($C_{84}H_{56}N_2O_2S$ required m/z = 1157.4096); IR (ATR): ν_{max} = 1598, 1475, 1258, 1143, 1089, 1014, 756, and 695 cm^{-1}.

2,7-diPhCz-4Ph-DPS (13)

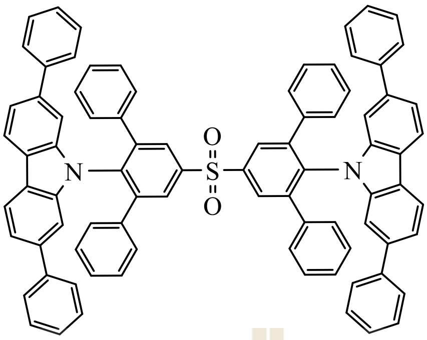

According to GP 4, a suspension of 2,7-diphenyl-9H-carbazole (**138**) (221 mg, 0.69 mmol) and 60% sodium hydride (60 mg, 1.5 mol) in dry dimethylformamide (DMF) (10 mL) was stirred at 70°C under N_2 atmosphere for 30 minutes. After that, TBDFDPS (**134**) (161 mg, 0.30 mmol) was added into a solution. The mixture was stirred at 100°C for 24 h. The crude product was purified by column chromatography (SiO_2, CH_2Cl_2/hexane) and recrystallization by CH_2Cl_2 and methanol to afford the product as a white crystal (47 mg, 14%); ^{1}H-NMR (600 MHz, $CDCl_3$): δ = 8.37 (s, 4H, O_2SPh*H*), 7.92 (d, 4H, *J* = 8.1 Hz, Cz*H*), 7.46 (d, 8H, *J* = 7.3 Hz, CzPh*H*), 7.38 (t, 8H, *J* = 7.3 Hz, CzPh*H*), 7.33 (d, 4H, *J* = 8.2 Hz, Cz*H*), 7.29 (t, 64H, *J* = 7.2 Hz, CzPh*H*), 7.08-7.07 (m, 8H, O_2SPh-Ph*H*), 7.05 (s, 4H, Cz*H*), 7.04-7.00 (m, 12H, O_2SPh-Ph*H*) ppm; ^{13}C-NMR (150 MHz, $CDCl_3$): δ = 144.1, 141.7, 141.6, 140.9, 139.1, 137.4, 137.1, 130.0, 128.7, 128.4, 128.3, 127.8, 127.4, 127.3, 127.1, 122.2, 120.2, 119.8, and 108.8 ppm; m/z (MALDI-TOF): 1157.2896 ($C_{84}H_{56}N_2O_2S$ required m/z = 1157.4096); IR (ATR): ν_{max} = 1591, 1462, 1421, 1333, 1143, 756, and 681 cm^{-1}.

6.3.3 Supplementary data in Chapter 4: the synthesis of TADF dendrimers

Bis(4-(2,7-dibromocarbazole)phenyl) sulfone (160)

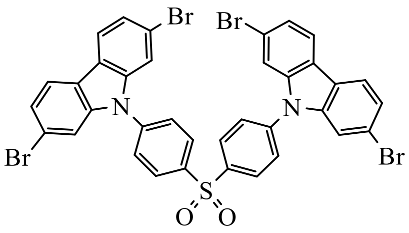

According to GP 4, a suspension of 2,7-dibromocarbazole (**159**) (1.47 g, 4.5 mmol) and 60 % sodium hydride (394 mg, 9.85 mmol) in dry dimethylformamide (DMF) (10 mL) was stirred at 70°C under N_2 atmosphere for 30 minutes. After that, *Bis*(4-fluorophenyl) sulfone (0.5 g, 2.0 mmol) was added into a solution. The mixture was stirred at 100°C for 24 h. The crude product was purified by column chromatography (SiO_2, CH_2Cl_2/hexane) and recrystallization by CH_2Cl_2 and methanol to afford the product as a white crystal (0.59 g, 35%); ^{1}H-NMR (600 MHz, $CDCl_3$): δ = 8.34 (d, 4H, J = 8.7 Hz, O_2SPhH), 7.95 (d, 4H, J = 8.7 Hz, Cz*H*), 7.78 (d, 4H, J = 8.6 Hz, Ph*H*N), 7.57 (s, 4H, Cz*H*), and 7.45 (d, 4H, J = 8.4 Hz, Cz*H*) ppm; m/z (Q-TOF): 859.7586 ($C_{36}H_{20}Br_4N_2O_2S$ required m/z = 859.7979)

2-bromo fluorene (162)

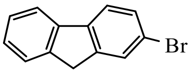

Fluorene (10.0 g, 60 mmol) was dissolved in acetone (100 mL) and NBS (11.8 g, 66 mmol) was added. The solution was refluxed for 3 h. The mixture was extracted with dichloromethane (50 mL x 3). The combined organic phase was washed with brine and dried over sodium sulfate. Then filtered and the solvent was removed to dryness. The crude product was recrystallization by hexane to afford the product as a

white crystal (3.5 g, 24%); ^{1}H-NMR (600 MHz, $CDCl_3$): δ = 7.75 (d, 1H, *J* = 7.5 Hz, Ph*H*), 7.68 (s, 1H, BrPh*H*), 7.64 (d, 1H, *J* = 7.4 Hz, BrPh*H*), 7.53 (d, 1H, *J* = 7.0 Hz, Ph*H*), 7.50 (d, 1H, *J* = 7.0 Hz, BrPh*H*), 7.38 (t, 1H, *J* = 7.0 Hz, Ph*H*), 7.32 (t, 1H, *J* = 7.0 Hz, Ph*H*), and 3.89 (s, 2H, C*H*$_2$) ppm; ^{13}C-NMR (150 MHz, $CDCl_3$): δ = 145.4, 143.0, 140.9, 140.8, 130.0, 128.4, 127.3, 127.1, 125.2, 121.3, 120.6, 120.1, and 36.9 ppm; m/z (Q-TOF): 243.9702 ($C_{13}H_9Br$ required m/z = 243.9888).

Dibromohexyl-2-bromo fluorene (164)

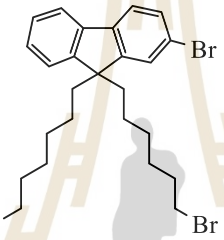

1,6-Dibromohexane (19.50 mL, 0.12 mol) was added to a mixture of 2-bromo fluorene **163** (3.50 g, 0.014 mol) and tetrabutylammonium bromide (TBAB) (0.09 g, 0.3 mmol). Subsequently, 50 wt % sodium hydroxide aqueous solution (30 mL) was added to the mixture. The mixture was stirred at room temperature for 24 h and then quenched with water and CH_2Cl_2 (20 ml) was added. The organic phase was washed with water (50 mL × 2) and brine solution (50 ml), dried over anhydrous Na_2SO_4, and filtered. The solvent was removed to dryness under vacuum, and the crude product was purified by column chromatography (SiO_2, CH_2Cl_2/hexane) to afford Dibromo hexyl-2-bromo fluorene (**164**) as a colorless liquid(1.9331 g, 66%); ^{1}H-NMR (600 MHz, $CDCl_3$): δ = 7.66 (m, 1H, BrPh*H*), 7.55 (m, 1H, BrPh*H*), 7.46-7.45 (m, 2H, BrPh*H* and Ph*H*), 7.33-7.31 (m, 3H, Ph*H*), 3.28 (t, 2H, C*H*$_2$), 1.99-1.90 (m, 4H, fluoreneC*H*$_2$CH$_2$), 1.68-1.63 (m, 4H, G1C*H*$_2$), 1.21-1.16 (m, 4H, fluoreneCH$_2$C*H*$_2$), 1.21-1.16 (m, 4H, G1CH$_2$C*H*$_2$), 1.09-1.05 (m, 4H, CH$_2$C*H*$_2$), and 0.64-0.57 (m, 4H, C*H*$_2$CH$_2$) ppm; ^{13}C-NMR (150 MHz,

$CDCl_3$): δ = 152.7, 150.1, 140.3, 140.2, 130.2, 127.7, 127.2, 126.2, 122.9, 121.2, 121.1, 119.9, 55.4, 40.2, 33.9, 32.7, 29.1, 27.8, and 23.6 ppm; m/z (Q-TOF): 568.8058 ($C_{25}H_{31}Br_3$ required m/z = 567.9976).

G1hexyl-2-bromo fluorene (165)

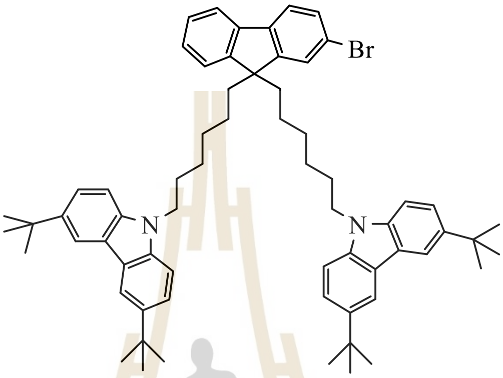

A suspension of 3,6-di-*tert*-butyl-carbazole (G1, **73**) (1.97 g, 7.04 mmol, 2.3 equiv) and potassium hydride (858 mg, 15.3 mmol) in dry dimethylformamide (DMF) (10 mL) was stirred at 70°C under N_2 atmosphere for 30 minutes. After that, G1hexyl fluorene bromide **165** (1.74 g, 3.06 mmol) was added into a solution. The mixture was stirred at room temperature for 24 h. The crude product was purified by column chromatography (SiO_2, CH_2Cl_2/hexane) and recrystallization by CH_2Cl_2 and methanol to afford the product as a white crystal (2.64 g, 89%); ^{1}H-NMR (600 MHz, $CDCl_3$): δ = 8.07 (s, 4H, Cz*H*), 7.63 (m, 1H, BrPh*H*), 7.52 (m, 1H, BrPh*H*), 7.45 (d, 4H, *J* = 8.7 Hz, Cz*H*), 7.43-7.38 (m, 2H, BrPh*H* and Ph*H*), 7.29 (m, 1H, Ph*H*), 7.20-7.18 (m, 2H, Cz*H* and Ph*H*), 4.09 (t, 4H, CH_2), 1.82-1.89 (m, 4H, fluoreneC$H_2$$CH_2$), 1.65-1.60 (m, 4H, G1C$H_2$), 1.44 (s, 36H, C(C$H_3$)$_3$), 1.15-1.06 (m, 8H, CH_2CH_2), and 0.59-0.50 (m, 4H, C$H_2$$CH_2$) ppm; m/z (MALDI-TOF): 966.5436 ($C_{65}H_{79}BrN_2$ required m/z = 966.5427).

TPA-2-bromo fluorene (167)

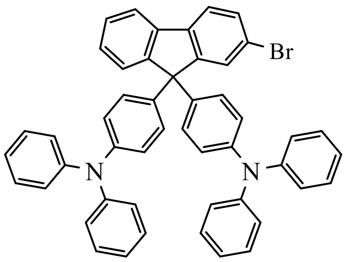

A mixture of 2-bromofluorenone **166**, triphenylamine in methanesulfonic acid was heated at 160°C with constant stirring under N_2 atmosphere for 24 h. The cooled mixture was extracted with CH_2Cl_2 (20 ml). The organic phase was washed with Na_2CO_3, dried over anhydrous Na_2SO_4, and filtered. The solvent was removed to dryness under vacuum, and the crude product was purified by column chromatography (SiO_2, CH_2Cl_2/hexane) to afford the corresponding product **167** as a white solid (3.63 g, 65%); ^{1}H-NMR (600 MHz, $CDCl_3$): δ = 7.71 (d, 1H, *J* = 7.2 Hz, BrPh*H*), 7.61 (d, 1H, *J* = 8.4 Hz, BrPh*H*), 7.55 (s, 1H, BrPh*H*), 7.47 (d, 1H, *J* = 7.8 Hz, Ph*H*), 7.40 (d, 1H, *J* = 7.8 Hz, Ph*H*), 7.35 (t, 1H, *J* = 7.0 Hz, Ph*H*), 7.30 (t, 1H, *J* = 7.0 Hz, Ph*H*), 7.22 (t, 8H, *J* = 7.8 Hz, TPA*H*), 7.05 (d, 8H, *J* = 7.8 Hz, TPA*H*), 7.03 (d, 4H, *J* = 8.4 Hz, TPA*H*), 6.99 (t, 4H, *J* = 8.4 Hz, TPA*H*), and 6.90 (d, 4H, *J* = 8.4 Hz, TPA*H*) ppm; ^{13}C-NMR (150 MHz, $CDCl_3$): δ = 153.8, 151.6, 147.6, 146.6, 139.2, 139.0, 138.8, 130.7, 129.5, 129.3, 129.9, 128.1, 127.7, 126.4, 124.7, 123.0, 121.6, 121.4, 120.3, and 64.7 ppm; m/z (Q-TOF): 730.7290 ($C_{49}H_{35}BrN_2$ required m/z = 730.1984).

G1hexyl fluorene boronate (170)

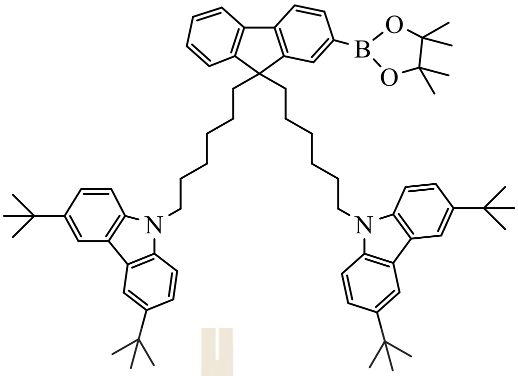

According to GP 5, G1hexyl fluorene bromide (**165**) (1.0 g, 1.03 mmol), bis (pinacolato)diboron (0.53 g, 2.07 mmol), KOAc (1.22 g, 12.42 mmol), and Pd(dppf)Cl_2 (38 mg, 0.05 mmol) were dissolved in dry toluene (30 mL) and heated to 110°C under N_2 atmosphere for 24 h. The crude product was purified by column chromatography (SiO_2, CH_2Cl_2/hexane) and recrystallization by CH_2Cl_2 and methanol to afford the product as white solid (0.85 g, 81%); ^{1}H-NMR (600 MHz, $CDCl_3$): δ = 8.05 (s, 4H, Cz*H*), 7.80 (m, 1H, BrPh*H*), 7.72 (s, 1H, BrPh*H*), 7.68 (t, 2H, Ph*H*),7.45 (d, 4H, *J* = 8.7 Hz, Cz*H*), 7.30-7.22 (m, 3H, Ph*H*), 7.17 (d, 4H, *J* = 8.7 Hz, Cz*H*), 4.07 (t, 4H, CH_2), 1.97-1.86 (m, 4H, fluoreneC$\mathit{H}_2$$CH_2$), 1.63-1.60 (m, 4H, G1C$\mathit{H}_2$), 1.44 (s, 36H, C(C$\mathit{H}_3$)$_3$), 1.36 (s, 12H, $BO_2C(CH_3)_3$), 1.13-1.04 (m, 8H, CH_2CH_2), and 0.57-0.52 (m, 4H, C$\mathit{H}_2$$CH_2$) ppm; ^{13}C-NMR (150 MHz, $CDCl_3$): δ = 144.3, 138.9,133.8, 128.7, 127.6, 126.7, 123.2, 122.8, 122.6, 120.2, 119.0, 116.2, 107.9, 83.7, 54.9, 42.9, 40.2, 34.6, 32.1, 31.9, 31.8, 29.6, 28.8, 26.8, 24.9, and 23.4 ppm; m/z (MALDI-TOF): 1014.5417 ($C_{71}H_{91}BN_2O_2$ required m/z = 1014.7174).

TPA fluorene boronate (172)

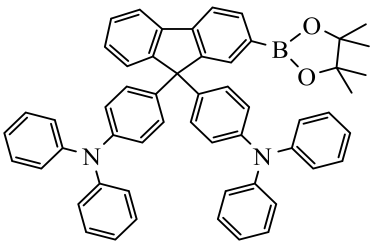

According to GP 5, TPA-2-bromo fluorene (**169**) (1.0 g, 1.40 mmol), bis (pinacolato)diboron (0.70 g, 2.74 mmol), KOAc (1.60 g, 16.4 mmol), and Pd(dppf)Cl_2 (50 mg, 0.06 mmol) were dissolved in toluene (30 mL) and heated to 110°C under N_2 atmosphere for 24 h. The crude product was purified by column chromatography (SiO_2, CH_2Cl_2/hexane) and recrystallization by CH_2Cl_2 and methanol to afford the product as white solid (0.92 g, 86%); ^{1}H-NMR (600 MHz, $CDCl_3$): δ = 7.84-7.83 (m, 2H, BrPh*H*), 7.78-7.48 (m, 2H, BrPh*H* and Ph*H*), 7.42 (d, 1H, *J* = 7.8 Hz, Ph*H*), 7.35 (t, 1H, *J* = 7.0 Hz, Ph*H*), 7.29 (t, 1H, *J* = 7.0 Hz, Ph*H*), 7.20 (t, 8H, *J* = 7.8 Hz, TPA*H*), 7.08-7.05 (m, 12H, TPA*H*), 6.97 (t, 4H, *J* = 8.4 Hz, TPA*H*), 6.90 (d, 4H, *J* = 8.4 Hz, TPA*H*) and 1.36 (s, 12H, $BO_2C(CH_3)_3$) ppm; ^{13}C-NMR (150 MHz, $CDCl_3$): δ = 152.3, 150.9, 147.7, 146.1, 143.1, 139.8, 139.6, 134.4, 132.2, 129.1, 129.0, 128.1, 127.3, 126.3, 124.3, 123.2, 122.7, 120.5, 119.4, 83.8, 64.6, and 24.9 ppm; m/z (Q-TOF): 778.7762 ($C_{55}H_{47}BN_2O_2$ required m/z = 778.3731).

TADF dendrimers (14)

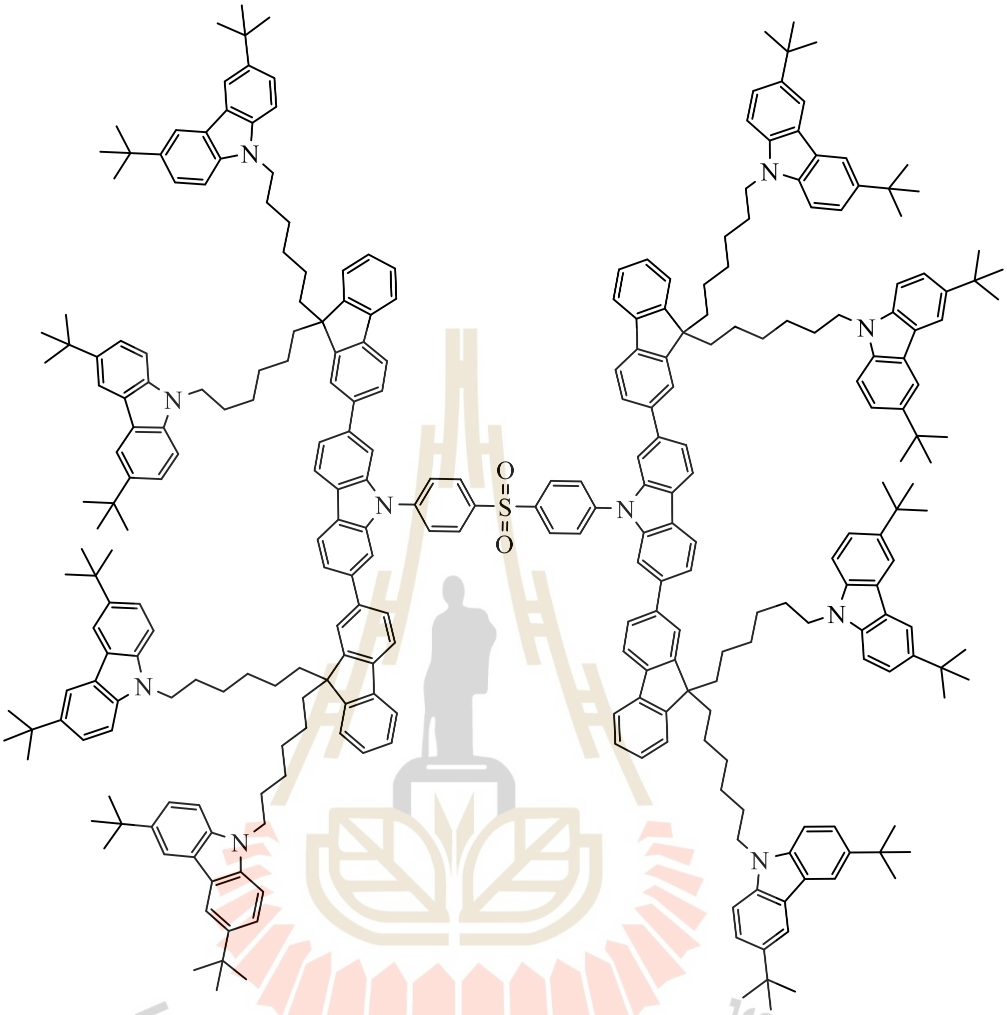

According to GP 3, a mixture of *Bis*(4-(2,7-dibromocarbazole)phenyl) sulfone (**160**) (175 mg, 0.2 mmol), G1hexyl fluorene borolane (**170**) (1.0 g, 1.0 mmol, 5.0 equiv), $Pd(PPh_3)_4$ (12 mg, 0.01 mmol), 10 wt % aqueous sodium carbonate solution (10 mL), and mixed toluene/THF in the ration of 2:1 (20 mL) were added under N_2. The reaction mixture was heated at 110°C for 24 h. The crude product was purified by column chromatography (SiO_2, CH_2Cl_2/hexane) and recrystallization by CH_2Cl_2 and methanol to afford the product as a solid (0.213 g, 25%); ^{1}H-NMR (600 MHz, $CDCl_3$): δ = 8.17 (d, 4H, J = 8.1 Hz, O_2SPh*H*), 8.03 (m, 20H, G1*H* and Cz*H*), 7.70-7.66 (m, 12H, fluorene*H* and CzNPh*H*), 7.62 (d, 4H, *J* = 8.2 Hz, CzNPh*H*), 7.59-7.57 (m, 12H, fluorene*H* and CzNPh*H*), 7.37 (dd, 4H, G1*H*), 7.19 (m, 12H, fluorene*H*), 7.10 (d, 16H, *J* = 8.2 Hz, G1*H*), 4.00 (t, 16H, , fluoreneCH_2), 1.94 (m, 16H, G1CH_2), 1.38 (s, 144H, C(CH_3)$_3$), 1.07-1.03 (m, 32H, CH_2CH_2), and 0.57-0.52 (m, 4H, C$H_2$$CH_2$) ppm; ^{13}C-NMR (150 MHz, $CDCl_3$): δ = 151.3, 150.5, 141.3, 141.0, 140.6, 140.5, 140.4, 140.3, 139.5, 138.9, 129.9, 127.2, 126.9, 126.4, 123.1, 122.9, 122.7, 122.6, 121.7, 121.1, 120.8, 120.1, 119.9, 116.2, 108.1, 107.9, 55.0, 42.8, 40.4, 34.6, 32.0, 29.6, 28.8, 26.7, and 23.6 ppm; m/z (MALDI-TOF): 1014.5417 ($C_{296}H_{336}N_{10}O_2S$ required m/z = 4094.6219). IR (ATR): ν_{max} = 2956, 2854, 1475, 1448,1318, 1265, 792, and 732 cm^{-1}.

TADF dendrimers (15)

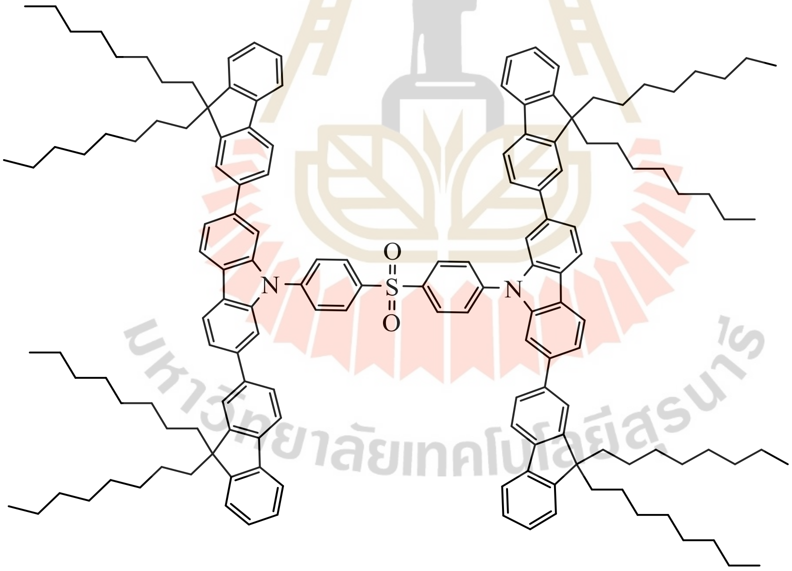

According to GP 3, a mixture of *Bis*(4-(2,7-dibromocarbazole)phenyl) sulfone (**160**) (150 mg, 0.12 mmol), octyl fluorene boronate (**171**) (465 mg 0.60 mmol, 5.0 equiv), Pd(PPh_3)$_4$ (10.5 mg, 0.006 mmol), 10 wt% aqueous sodium carbonate solution (10 mL), and mixed toluene/THF in the ration of 2:1 (30 mL) were added under N_2. The reaction mixture was heated at 110°C for 24 h. The crude product was purified by column chromatography (SiO_2, CH_2Cl_2/hexane) and recrystallization by CH_2Cl_2 and methanol to afford the product as a solid (0.120 g, 49%); ^1H-NMR (600 MHz, $CDCl_3$): δ = 8.37 (d, 4H, *J* = 8.2 Hz, $O_2SPh\mathit{H}$), 8.22 (d, 4H, *J* = 8.2 Hz, CzNPh*H*), 7.99 (d, 4H, *J* = 8.5 Hz, Cz*H*), 7.78 (s, 4H, Cz*H*), 7.72 (d, 4H, *J* = 7.6 Hz, Cz*H*), 7.66-7.64 (m, 8H, Ph*H*), 7.61-7.59 (m, 8H, Ph*H*), 7.33-7.27 (m, 12H, Ph*H*), 2.00-1.97 (m, 16H, fluorene$C\mathit{H}_2$), 1.18-1.13 (m, 16H, fluorene $CH_2C\mathit{H}_2$), 1.10-1.03 (m, 64H, fluorene $CH_2CH_2C\mathit{H}_2$), 0.77 (t, 24H, $CH_2C\mathit{H}_3$), and 0.67-0.65 (m, 16H, $C\mathit{H}_2CH_3$) ppm; ^{13}C-NMR (150 MHz, $CDCl_3$): δ = 151.6, 150.9, 142.8, 141.1, 140.6, 140.5, 140.5, 140.3, 139.5, 130.0, 127.2, 127.1, 126.7, 126.2, 123.0, 122.8, 121.9, 121.1, 120.7, 119.9, 119.7, 108.1, 55.2, 40.3, 31.7, 29.9, 29.2, 23.8, 22.6, and 14.0 ppm; m/z (Q-TOF): 2101.8084 ($C_{152}H_{184}N_2O_2S$ required m/z = 2101.4079); IR (ATR): ν_{max} = 2945, 2849, 1598, 1449, 1332, 1159, 1105, 825,and 748 cm^{-1}.

TADF dendrimers (16)

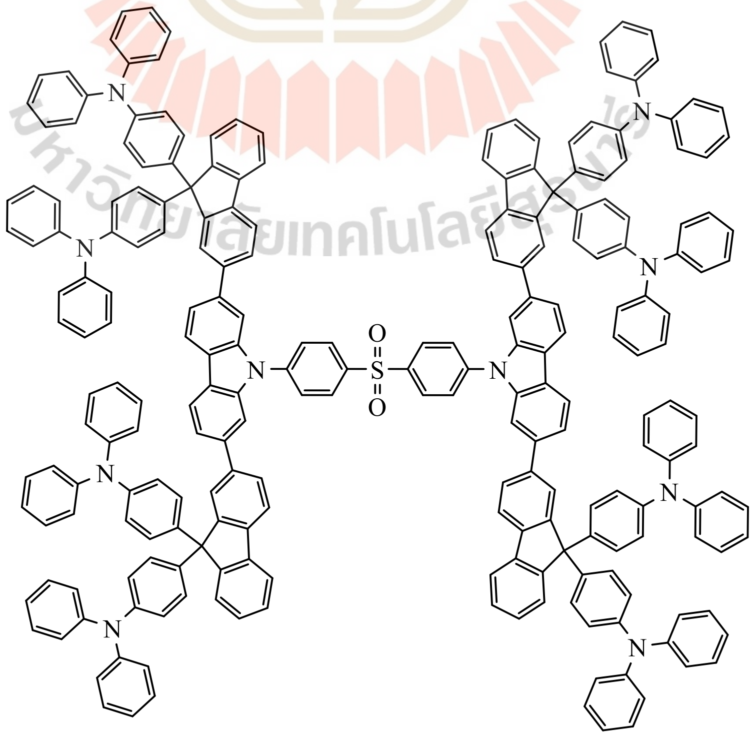

According to GP 3, a mixture of *Bis*(4-(2,7-dibromocarbazole)phenyl) sulfone (**160**) (200 mg, 0.23 mmol), TPA fluorene boronate (**172**) (910 mg, 1.17 mmol, 5.0 equiv), $Pd(PPh_3)_4$ (14 mg, 0.05 mmol), 10 wt% aqueous sodium carbonate solution (10 mL), and mixed toluene/THF in the ration of 2:1 (20 mL) were added under N_2. The reaction mixture was heated at 110°C for 24 h. The crude product was purified by column chromatography (SiO_2, CH_2Cl_2/hexane) and recrystallization by CH_2Cl_2 and methanol to afford the product as a solid (0.35 g, 48%); ^{1}H-NMR (600 MHz, $CDCl_3$): δ = 8.19 (d, 4H, *J* = 8.6 Hz, O_2SPh*H*), 8.14 (d, 4H, *J* = 8.0 Hz, fluorene*H*), 7.85 (d, 4H, *J* = 8.4 Hz, CzNPh*H*), 7.74 (d, 4H, *J* = 8.1 Hz, fluorene*H*), 7.70 (d, 8H, *J* = 12.0 Hz, fluorene*H*), 7.62-7.58 (m, 12H, fluorene*H* and CzN), 7.53 (d, 4H, *J* = 8.4 Hz, fluorene*H*), 7.42-7.40 (m, 4H, fluorene*H*), 7.22-7.21 (m, 8H, fluorene*H*), 7.16 (t, 32H, *J* = 8.1 Hz, TPA*H*), 7.10 (t, 16H, *J* = 8.4Hz, TPA*H*), 7.02 (d, 32H, *J* = 7.4 Hz, TPA*H*), and 6.94-6.88 (m, 32H, TPA*H*) ppm; ^{13}C-NMR (150 MHz, $CDCl_3$): δ =152.4, 151.8, 147.6, 146.3, 142.6, 140.9, 140.8, 140.1, 139.6, 139.5, 129.9, 129.1, 128.9, 127.7, 127.5, 127.0, 126.8, 126.2, 125.3, 124.4, 123.2, 123.0, 122.7, 121.0, 120.8, 120.5, 120.2, 108.1, and 64.6 ppm; m/z (Q-TOF): 3149.8115 ($C_{232}H_{160}N_{10}O_2S$ required m/z = 3149.2446); IR (ATR): ν_{max} = 1585, 1489, 1325, 1268, 1148, 759, and 689 cm^{-1}.

6.3.4 Supplementary data in Chapter 5: the synthesis of AIE emitters

TPEH dioxaborolane (202)

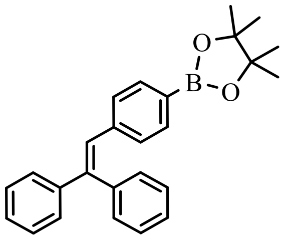

According to GP 5, 2-(4-Bromophenyl)-1,1-diphenylethene (**200**) (1.0 g, 2.98 mmol), bis (pinacolato)diboron (1.52 g, 5.96 mmol), KOAc (3.50 g, 35.8 mmol), and Pd(dppf)Cl_2 (122 mg, 0.15 mmol) were dissolved in dry toluene (30 mL) and heated to 110°C under N_2 atmosphere for 24 h. The crude product was purified by column chromatography (SiO_2, CH_2Cl_2/hexane) and recrystallization by CH_2Cl_2 and methanol to afford the product as white solid (1.20 g, 53%); ^{1}H-NMR (600 MHz, $CDCl_3$): δ = 7.57 (d, 2H, J = 7.9 Hz, Ph*H*BO$_2$), 7.34-7.28 (m, 8H, Ph*H*), 7.20-7.18 (m, 2H, Ph*H*), 7.01 (d, 2H, J = 7.9 Hz, =CHPh*H*), and 6.98 (s, 1H, =C*H*) ppm; ^{13}C-NMR (150 MHz, $CDCl_3$): δ = 143.5, 143.3, 140.2, 140.2, 134.4, 130.4, 128.8, 128.6, 128.2, 128.1, 127.7, 127.6, 127.5, 83.7, 24.7 ppm; m/z (Q-TOF): 382.2226 ($C_{32}H_{31}BO_2$ required m/z = 382.2104).

TPE dioxaborolane (203)

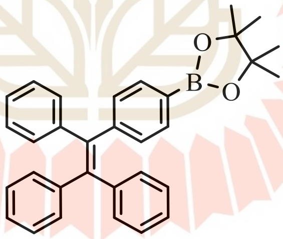

According to GP 5, 1-(4-Bromophenyl)-1,2,2-triphenylethylene (**201**) (500 mg, 1.22 mmol), bis (pinacolato)diboron (620 mg, 2.44 mmol), KOAc (1.44 g, 14.6 mmol), and Pd(dppf)Cl_2 (50 mg, 0.06 mmol) were dissolved in toluene (20 mL) and heated to 110°C under N_2 atmosphere for 24 h. The crude product was purified by column chromatography (SiO_2, CH_2Cl_2/hexane) and recrystallization by CH_2Cl_2 and methanol to afford the product as white solid (448 mg, 81%); ^{1}H-NMR (600 MHz, $CDCl_3$): δ = 7.53 (d, 2H, J = 7.6 Hz, Ph*H*BO$_2$) and 7.09-6.99 (m, 15H, =CHPh*H* and Ph*H*) ppm; ^{13}C-NMR (150 MHz, $CDCl_3$): δ = 146.8, 143.7, 143.6, 143.6, 141.4, 140.9, 134.1, 131.4, 131.3, 131.3, 130.7, 127.7, 127.6, 126.5, 126.4, 126.4, 83.7, and 24.9 ppm; m/z (MALDI-TOF): 458.3458 ($C_{32}H_{31}BO_2$ required m/z = 458.2417).

BT-2TPE (17)

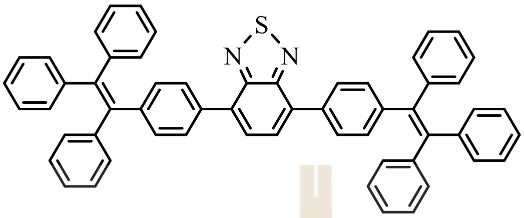

According to GP 3, a mixture of 4,7-dibromobenzo[*c*][1,2,5]thiadiazole (**205**) (100 mg, 0.34 mmol), TPE dioxaborolane (**203**) (467 mg, 1.02 mmol, 3.0 equiv), $Pd(PPh_3)_4$ (20 mg, 0.02 mmol), 10 wt% aqueous sodium carbonate solution (10 mL), and mixed toluene/THF in the ration of 2:1 (20 mL) were added under N_2. The reaction mixture was heated at 110°C for 24 h. The crude product was purified by column chromatography (SiO_2, CH_2Cl_2/hexane) and recrystallization by CH_2Cl_2 and methanol to afford the product as a solid (250 mg, 92%): mp 260°C; ^{1}H-NMR (600 MHz, $CDCl_3$): δ = 7.76 (d, 4H, *J* = 8.3 Hz, BTPh*H*), 7.72 (s, 2H, BT*H*), 7.18 (d, 4H, *J* = 8.2 Hz, TPEPh*H*), and 7.14-7.05 (m, 30H, TPEPh*H*) ppm; ^{13}C-NMR (150 MHz, $CDCl_3$): δ = 154.0, 143.8, 143.7, 143.6, 143.6, 141.5, 140.5, 135.3, 132.6, 131.6, 131.5, 131.4, 131.3, 128.4, 127.9, 127.8, 127.7, 127.6, 126.6, 126.5, and 126.4 ppm; m/z (Q-TOF): 796.4323 ($C_{58}H_{40}N_2S$ required m/z = 796.2912).

NT-2TPE (18)

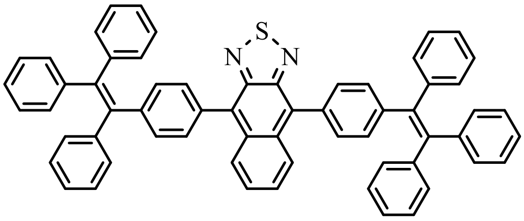

According to GP 3, a mixture of 4,9-dibromonaphtho[2,3-*c*][1,2,5]thiadiazole (**206**) (100 mg, 0.29 mmol), TPE dioxaborolane (**203**) (332 mg, 0.725 mmol, 2.5 equiv), $Pd(PPh_3)_4$ (17 mg, 0.015 mmol), 10 wt% aqueous sodium carbonate solution (10 mL), and mixed toluene/THF in the ration of 2:1 (20 mL) were added under N_2. The reaction mixture was heated at 110°C for 24 h. The crude product was purified by column chromatography (SiO_2, CH_2Cl_2/hexane) and recrystallization by CH_2Cl_2 and methanol to afford the product as a solid (105 mg, 43%): mp 230°C; ^{1}H-NMR (600 MHz, $CDCl_3$): δ = 7.87 (dd, 2H, *J* = 3.4 and 6.9 Hz, NTPh*H*), 7.38 (d, 4H, *J* = 8.1 Hz, TPEPh*H*), 7.34 (dd, 2H, *J* = 3.1 and 7.1 Hz, NTPh*H*), 7.26 (d, 4H, *J* = 8.1 Hz, TPEPh*H*), 7.22-7.10 (m, 30H, TPEPh*H*) ppm; ^{13}C-NMR (150 MHz, $CDCl_3$): δ = 151.2, 143.8, 143.6, 143.5, 143.4, 141.7, 140.8, 134.6, 132.0, 131.5, 131.4, 131.3, 130.6, 130.0, 128.2, 127.8, 127.7, 127.0, 126.6, 126.5, and 126.1 ppm; m/z (Q-TOF): 846.5767 ($C_{62}H_{42}N_2S$ required m/z = 846.3069).

NT-TPETPA (19)

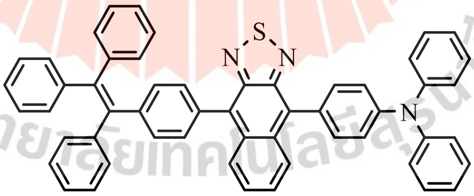

According to GP 3, a mixture of 4,9-dibromonaphtho[2,3-*c*][1,2,5]thiadiazole (**206**) (100 mg, 0.29 mmol), TPE dioxaborolane (**203**) (332 mg, 0.725 mmol, 2.5 equiv), $Pd(PPh_3)_4$ (17 mg, 0.015 mmol), 10 wt% aqueous sodium carbonate solution (10 mL), and mixed toluene/THF in the ration of 2:1 (20 mL) were added under N_2. The reaction mixture was heated at 110°C for 24 h. The crude product was purified by column chromatography (SiO_2, CH_2Cl_2/hexane) and recrystallization by CH_2Cl_2 and methanol to afford the corresponding intermediate as a solid. After that, the Suzuki reaction of a mixture of the intermediate (100 mg, 0.17 mmol), triphenyl boronic acid (**204**) (75 mg, 0.255 mmol), $Pd(PPh_3)_4$ (10 mg, 0.0085 mmol), 10 wt% aqueous sodium carbonate solution (10 mL), and mixed toluene/THF in the ration of 2:1 (20 mL) were refluxed under N_2. The crude product was purified by column chromatography (SiO_2, CH_2Cl_2/hexane) and recrystallization by CH_2Cl_2 and methanol to afford the product as red solid (96 mg, 75%): mp 300°C; ^{1}H-NMR (600 MHz, $CDCl_3$): δ = 8.12 (dd, 2H, NTPh*H*), 7.88 (dd, 2H, NTPh*H*), 7.38 (d, 4H, *J* = 8.1 Hz, TPEPh*H*), 7.34 (dd, 2H, *J* = 3.1 and 7.1 Hz, NTPh*H*), 7.53 (d, 2H, *J* = 8.4 Hz, TPAPh*H*), 7.39 (d, 2H, *J* = 8.3 Hz, NTPh*H*), 7.37-7.31 (m, 6H, NT*H* and TPA*H*), 7.28-7.26 (m, 8H, TPA*H*), and 7.22-7.07 (m, 19H, TPE*H*) ppm; ^{13}C-NMR (150 MHz, $CDCl_3$): δ = 151.5, 151.3, 147.8, 147.6, 143.8, 143.6, 143.5, 143.4, 141.7, 140.8, 134.7, 132.2, 132.1, 131.9, 131.5, 131.5, 131.4, 131.3, 130.7, 130.0, 129.8, 129.7, 129.4, 127.8, 127.7, 127.2, 127.0, 126.6, 126.5, 126.2, 126.1, 125.2, 123.4, and 122.2 ppm; m/z (Q-TOF): 759.5536 ($C_{54}H_{37}N_3S$ required m/z = 759.2708).

BT-2TPEH (20)

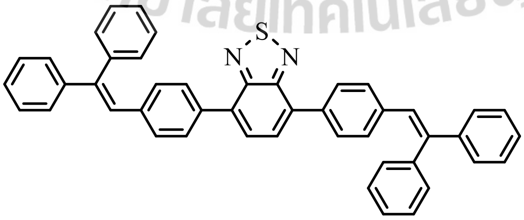

According to GP 3, a mixture of 4,7-dibromobenzo[*c*][1,2,5]thiadiazole (**205**) (150 mg, 0.51 mmol), TPEH dioxaborolane (**202**) (585 mg, 1.53 mmol, 3.0 equiv), $Pd(PPh_3)_4$ (30 mg, 0.025 mmol), 10 wt% aqueous sodium carbonate solution (10 mL), and mixed toluene/THF in the ration of 2:1 (20 mL) were added under N_2.

The reaction mixture was heated at 110°C for 24 h. The crude product was purified by column chromatography (SiO_2, CH_2Cl_2/hexane) and recrystallization by CH_2Cl_2 and methanol to afford the product as a solid (319 mg, 97%): mp 250°C; ^{1}H-NMR (600 MHz, $CDCl_3$): $\delta = 7.77$ (d, 4H, $J = 8.4$ Hz, TPEHPh*H*), 7.71 (s, 2H, BT*H*), 7.39-7.28 (m, 20H, TPE*H*) 7.18 (d, 4H, $J = 8.3$ Hz, TPEHPh*H*), and 7.05 (s, 2H, TPE*H*) ppm; ^{13}C-NMR (150 MHz, $CDCl_3$): $\delta = 154.0$, 143.3, 143.2, 140.4, 137.5, 135.6, 132.7, 130.4, 129.8, 128.8, 128.8, 128.2, 127.8, 127.6, and 127.5 ppm; m/z (Q-TOF): 644.4773 ($C_{46}H_{32}N_2S$ required m/z = 664.2286).

BT-TPETPA (21)

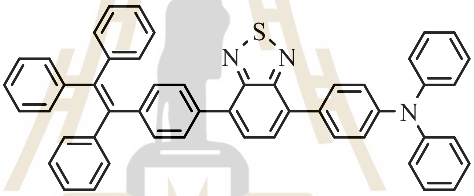

According to GP 3, a mixture of 4,7-dibromobenzo[*c*][1,2,5]thiadiazole (**205**) (100 mg, 0.34 mmol), TPEH dioxaborolane (**202**) (467 mg, 1.02), $Pd(PPh_3)_4$ (20 mg, 0.017 mmol), 10 wt% aqueous sodium carbonate solution (10 mL), and mixed toluene/THF in the ration of 2:1 (20 mL) were added under N_2. The reaction mixture was heated at 110°C for 24 h. The crude product was purified by column chromatography (SiO_2, CH_2Cl_2/hexane) and recrystallization by CH_2Cl_2 and methanol to afford the corresponding intermediate. After that, the Suzuki reaction of a mixture of the intermediate (50 mg, 0.09 mmol), triphenyl boronic acid (**204**) (75 mg, 0.255 mmol), $Pd(PPh_3)_4$ (10 mg, 0.0085 mmol), 10 wt% aqueous sodium carbonate solution (10 mL), and mixed toluene/THF in the ration of 2:1 (20 mL) were refluxed under N_2. The crude product was purified by column chromatography (SiO_2, CH_2Cl_2/hexane) and recrystallization by CH_2Cl_2 and methanol to afford the product as red solid (48 g, 74%): mp 175°C; ^{1}H-NMR (600 MHz, $CDCl_3$): $\delta = 7.87$ (d, 2H, $J = 8.4$ Hz, TPAPh*H*), 7.78 (d, 2H, $J = 8.1$ Hz, TPAPh*H*), 7.73 (m, 2H, BT*H*), 7.30-7.18 (m, 12H, TPA*H* and TPEPh*H*), and 7.13-7.05 (m, 15H, TPE*H*) ppm; ^{13}C-NMR (150 MHz, $CDCl_3$): $\delta = 154.1$, 154.0, 148.1, 147.5, 143.8, 143.7, 143.6, 143.6, 141,5, 140.6, 135.3, 132.6, 132.1, 131.6, 131.5, 131.4, 131.4, 130.9, 129.9, 129.3, 128.3, 128.0, 127.8, 127.7,127.6, 127.3, 126.6, 126.5, 126.5, 124.9, 123.3, and 122.9 ppm; m/z (Q-TOF): 709.5769 ($C_{50}H_{35}N_3S$ required m/z = 709.2552).

FBT-2TPE (22)

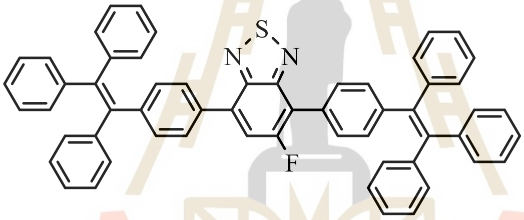

According to GP 3, a mixture of 4,7-dibromo-5-fluorobenzo[c][1,2,5] thiadiazole (**207**) (100 mg, 0.32 mmol), TPE dioxaborolane (**203**) (440 mg, 0.96 mmol, 3.0 equiv), $Pd(PPh_3)_4$ (20 mg,0.016 mmol), 10 wt % aqueous sodium carbonate solution (10 mL), and mixed toluene/THF in the ration of 2:1 (20 mL) were added under N_2. The reaction mixture was heated at 110°C for 24 h. The crude product was purified by column chromatography (SiO_2, CH_2Cl_2/hexane) and recrystallization by CH_2Cl_2 and methanol to afford the product as a solid (252 mg, 97%): mp 195°C; ^{1}H-NMR (600 MHz, $CDCl_3$): $\delta = 7.77$ (d, 2H, $J = 8.0$ Hz, BTFPh*H*), 7.60-7.58 (m, 3H, BT*H* and TPEPh*H*), 7.20-7.18 (m, 4H, TPEPh*H*), and 7.14-7.05 (m, 30H, TPEPh*H*) ppm; ^{13}C-NMR (150 MHz, $CDCl_3$): $\delta = 158.8$, 155.1, 151.0, 144.6, 143.8, 143.7, 143.6, 143.6, 143.5, 143.5, 141.8, 141.6, 140.5, 140.3, 133.9, 133.4, 133.3, 131.7, 131.5, 131.4, 131.4, 131.3, 131.3, 131.2, 129.8, 129.8, 129.2, 128.4, 127.8, 127.8, 127.7, 127.7, 127.6, 127.6, 126.6, 126.6, 126.5, 125.5, 126.5, 126.4, 119.5, 119.3, 117.1, and 117.0 ppm; m/z (MALDI-TOF): 814.2445 ($C_{58}H_{38}F_2N_2S$ required m/z = 814.2818).

2FBT-2TPE (23)

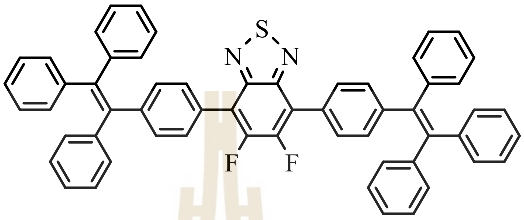

According to GP 3, a mixture of 4,7-dibromo-5,6-difluorobenzo[*c*][1,2,5] thiadiazole (**208**) (100 mg, 0.3 mmol), TPE dioxaborolane (**203**) (413 mg, 0.9 mmol, 3.0 equiv), $Pd(PPh_3)_4$ (20 mg, 0.015 mmol), 10 wt% aqueous sodium carbonate solution (10 mL), and mixed toluene/THF in the ration of 2:1 (20 mL) were added under N_2. The reaction mixture was heated at 110°C for 24 h. The crude product was purified by column chromatography (SiO_2, CH_2Cl_2/hexane) and recrystallization by CH_2Cl_2 and methanol to afford the product as a solid (230 mg, 92%): mp 280°C; ^{1}H-NMR (600 MHz, $CDCl_3$): δ = 7.60 (d, 4H, *J* = 8.1 Hz, 2FBTPh*H*), 7.20 (d, 4H, *J* = 8.1 Hz, TPEPh*H*), and 7.16-7.05 (m, 30H, TPEPh*H*) ppm; ^{13}C-NMR (150 MHz, $CDCl_3$): δ = 151.3, 150.4, 149.6, 149.4, 144.5, 143.6, 143.5, 143.5, 141.9, 140.3, 131.5, 131.4, 131.3, 129.8, 128.3, 127.8, 127.7, 127.6, 126.7, 126.5, 126.5, 118.4, and 118.3 ppm; m/z (Q-TOF): 832.5317 ($C_{58}H_{38}F_2N_2S$ required m/z = 832.2724).

2FBT-2TPEH (24)

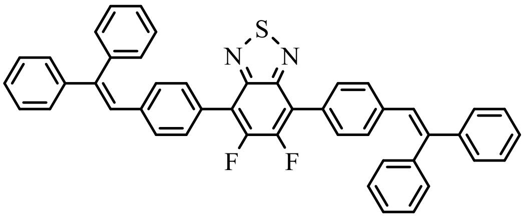

According to GP 3, a mixture of 4,7-dibromo-5,6-difluorobenzo[*c*][1,2,5] thiadiazole (**208**) (100 mg, 0.30 mmol), TPEH dioxaborolane (**202**) (344 mg, 0.90 mmol, 3.0 equiv), $Pd(PPh_3)_4$ (20 mg, 0.015 mmol), 10 wt% aqueous sodium carbonate solution (10 mL), and mixed toluene/THF in the ration of 2:1 (20 mL) were added under N_2. The reaction mixture was heated at 110°C for 24 h. The crude product was purified by column chromatography (SiO_2, CH_2Cl_2/hexane) and recrystallization by CH_2Cl_2 and methanol to afford the product as a solid (166 mg, 81%): mp 270°C; ^{1}H-NMR (600 MHz, $CDCl_3$): δ = 7.62 (d, 4H, *J* = 8.3 Hz, 2FBTPh*H*), 7.39-7.27 (m, 20H, TPE*H*), 7.20 (d, 4H, *J* = 8.3 Hz, TPEHPh*H*), and 7.04 (s, 2H, TPE*H*) ppm; ^{13}C-NMR (150 MHz, $CDCl_3$): δ = 151.2, 151.2, 150.4, 149.5, 149.4, 143.8, 143.3, 140.2, 138.3, 130.3, 130.2, 129.6, 128.8, 128.5, 128.3, 127.8, 127.6, 127.4, 118.3, 113.3, 118.3, and 118.2 ppm; m/z (Q-TOF): 680.1294 ($C_{58}H_{38}F_2N_2S$ required m/z = 680.2098).

NBT-2TPE (25)

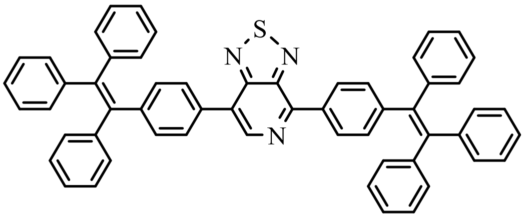

According to GP 3, a mixture of 4,7-dibromo-[1,2,5]thiadiazolo[3,4-*c*]pyridine (**209**) (100 mg, 0.34 mmol), TPE dioxaborolane (**203**) (467 mg, 1.02 mmol, 3.0 equiv), $Pd(PPh_3)_4$ (20 mg, 0.017 mmol), 10 wt% aqueous sodium carbonate solution (10 mL), and mixed toluene/THF in the ration of 2:1 (20 mL) were added under N_2. The reaction mixture was heated at 110°C for 24 h. The crude product was purified by column chromatography (SiO_2, CH_2Cl_2/hexane) and recrystallization by CH_2Cl_2 and methanol to afford the product as a solid (167 mg, 62%): mp 240°C; ^{1}H-NMR (600 MHz, $CDCl_3$): δ = 8.76 (a, 1H, NBT*H*), 8.42 (d, 2H, *J* = 8.1 Hz, NBTPh*H*), 7.80 (d, 2H, *J* = 8.1 Hz, NBTPh*H*), 7.25-7.21 (m, 4H, NBTPh*H*TPE), and 7.14-7.05 (m, 30H, TPEPh*H*); ^{13}C-NMR (150 MHz, $CDCl_3$): δ = 156.6, 151.7, 149.8, 146.2, 144.4, 143.6, 143.6, 143.5, 143.5, 142.5, 142.0, 141.8, 140.4, 140.4, 134.8, 132.5, 131.9, 131.7, 131.4, 131.4, 131.3, 131.3, 129.2, 128.2, 127.9, 127.8, 127.7, 126.7, 126.7, 126.6, 126.5, and 126.4 ppm; m/z (Q-TOF): 797.5906 ($C_{57}H_{39}N_3S$ required m/z = 797.2865).

BNT-2TPE (26)

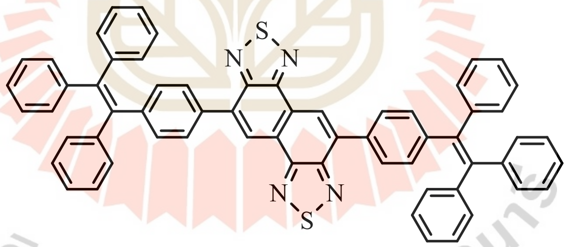

According to GP 3, a mixture of 5,10-dibromonaphtho[1,2-*c*:5,6-*c*']bis ([1,2,5]thiadiazole) (**210**) (120 mg, 0.30 mmol), TPE dioxaborolane (**203**) (344 mg, 0.75 mmol, 3.0 equiv), $Pd(PPh_3)_4$ (15 mg, 0.0125 mmol), 10 wt% aqueous sodium carbonate solution (10 mL), and mixed toluene/THF in the ration of 2:1 (20 mL) were added under N_2. The reaction mixture was heated at 110°C for 24 h. The crude product was purified by column chromatography (SiO_2, CH_2Cl_2/hexane) and recrystallization by CH_2Cl_2 and methanol to afford the product as a solid (37 mg, 14%): mp > 350°C;

^{1}H-NMR (600 MHz, CDCl$_3$): δ = 8.99 (s, 2H, BNT*H*), 7.94 (d, 4H, *J* = 8.3 Hz, NBTPh*H*), 7.24 (m, 4H, NBTPh*H*), and 7.14-7.05 (m, 30H, TPEPh*H*); ^{13}C-NMR (150 MHz, CDCl$_3$): δ = 153.9, 153.8, 144.4, 143.7, 143.6, 141.7, 140.4, 134.8, 133.3, 131.7, 131.4, 131.4, 131.3, 128.6, 127.9, 127.8, 127.7, 126.7, 126.6, 126.5, 125.2, and 125.1 ppm; m/z (Q-TOF): 904.0083 ($C_{57}H_{39}N_3S$ required m/z = 904.2694).

6.4 Spectrum supplementary data

6.4.1 The synthesis of DPP dendrimers

3,6-di-*tert*-butyl-carbazole (73)

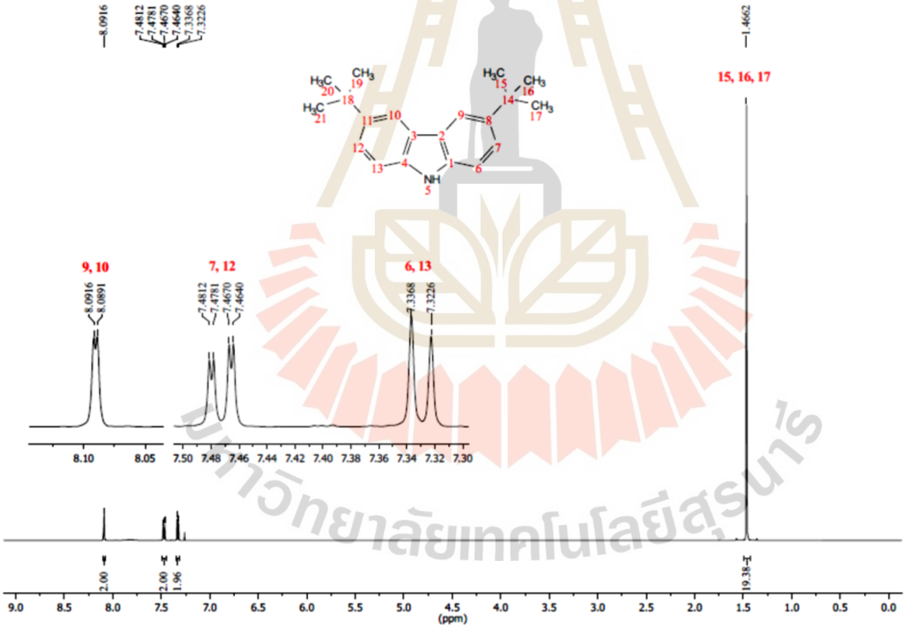

^{1}H-NMR (600 MHz, CDCl$_3$)

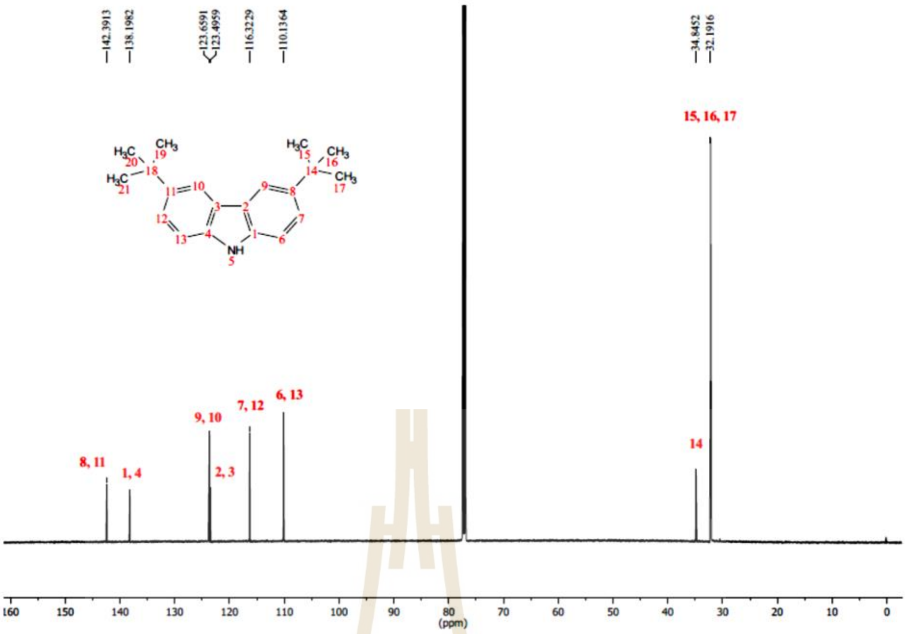

^{13}C-NMR (150 MHz, CDCl$_3$)

G2 (74)

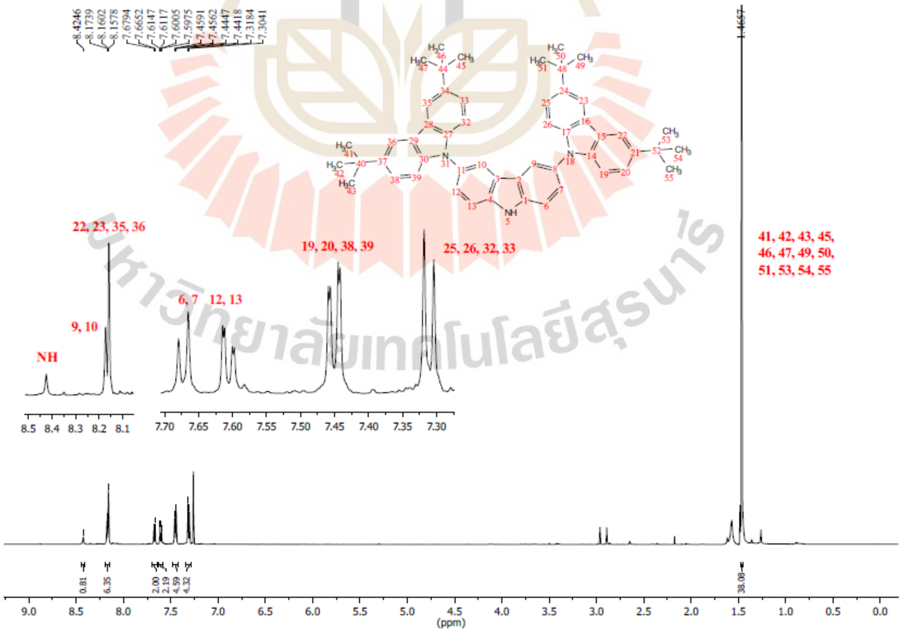

^{1}H-NMR (600 MHz, CDCl$_3$)

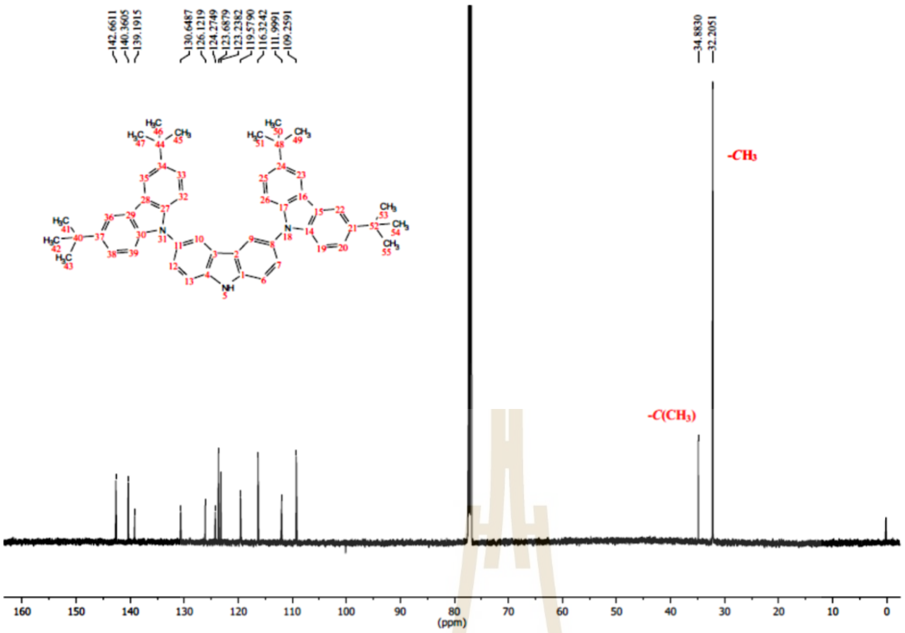

^{13}C-NMR (150 MHz, $CDCl_3$)

G1hexyl bromide (75)

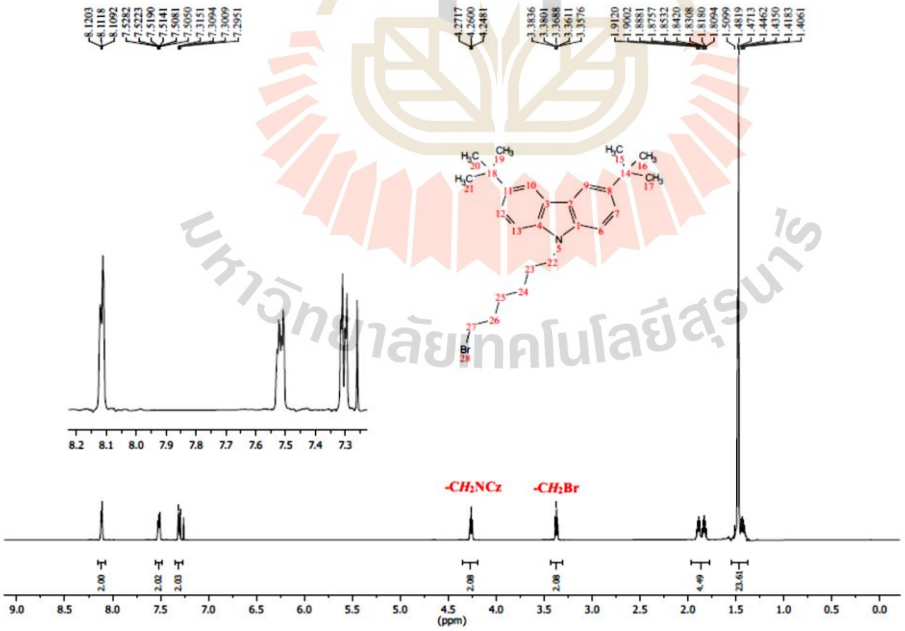

^{1}H-NMR (600 MHz, $CDCl_3$)

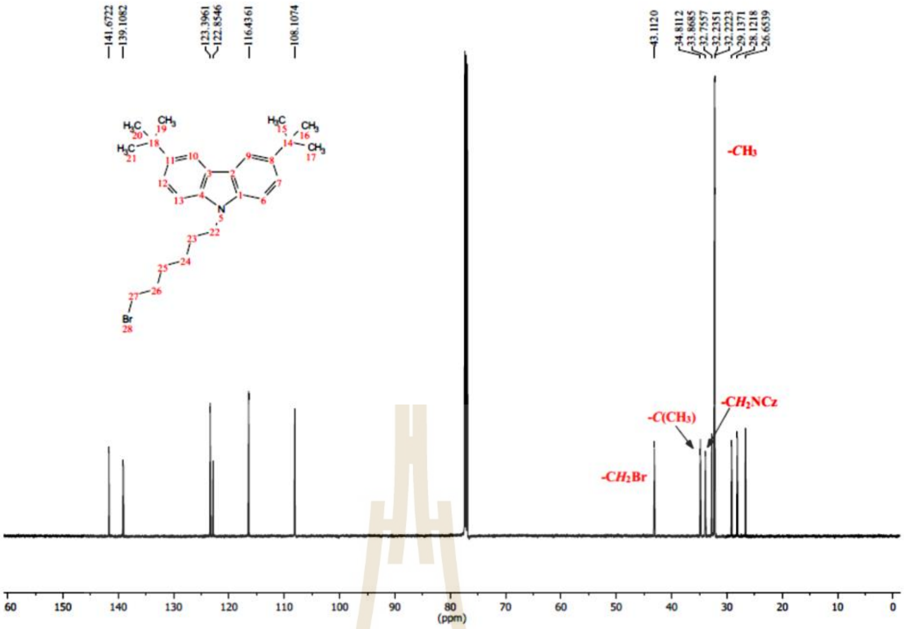

^{13}C-NMR (150 MHz, CDCl$_3$)

G2hexyl bromide (76)

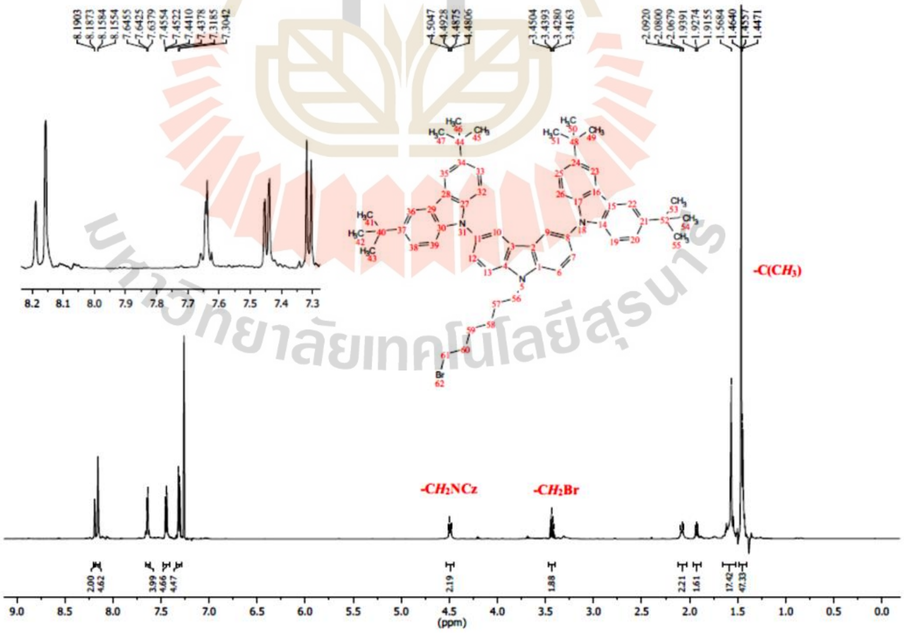

^{1}H-NMR (600 MHz, CDCl$_3$)

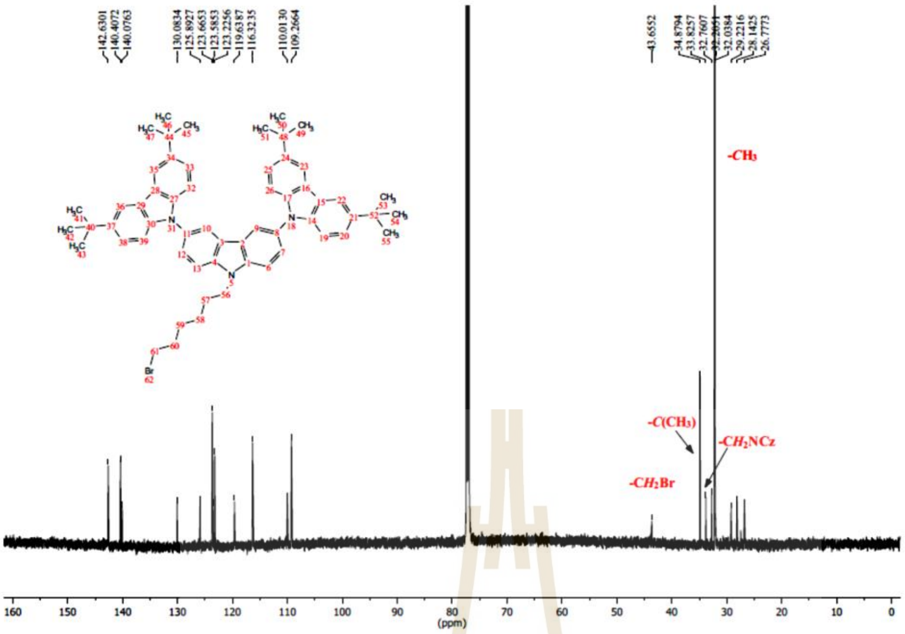

^{13}C-NMR (150 MHz, CDCl$_3$)

G0DPP (1)

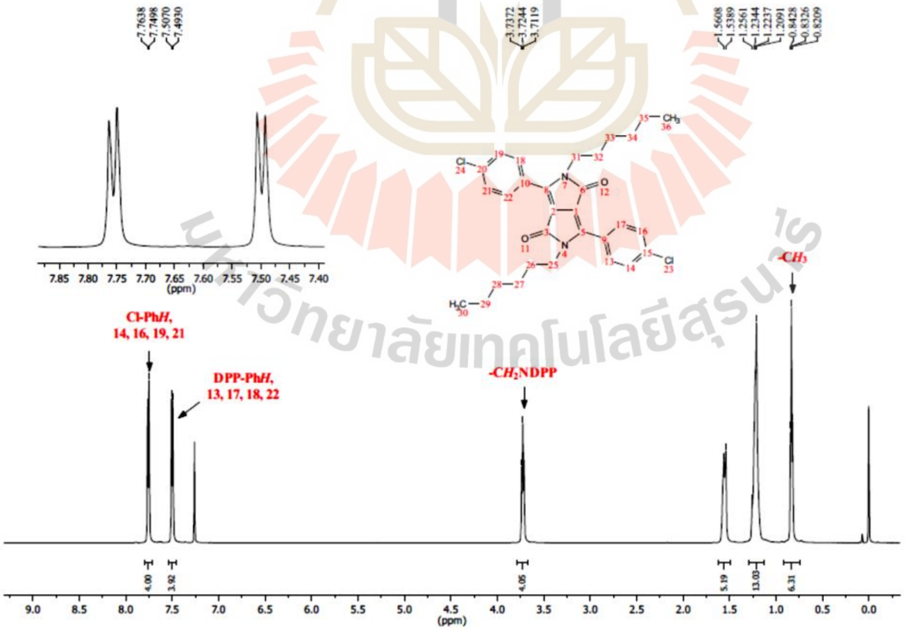

^{1}H-NMR (600 MHz, CDCl$_3$)

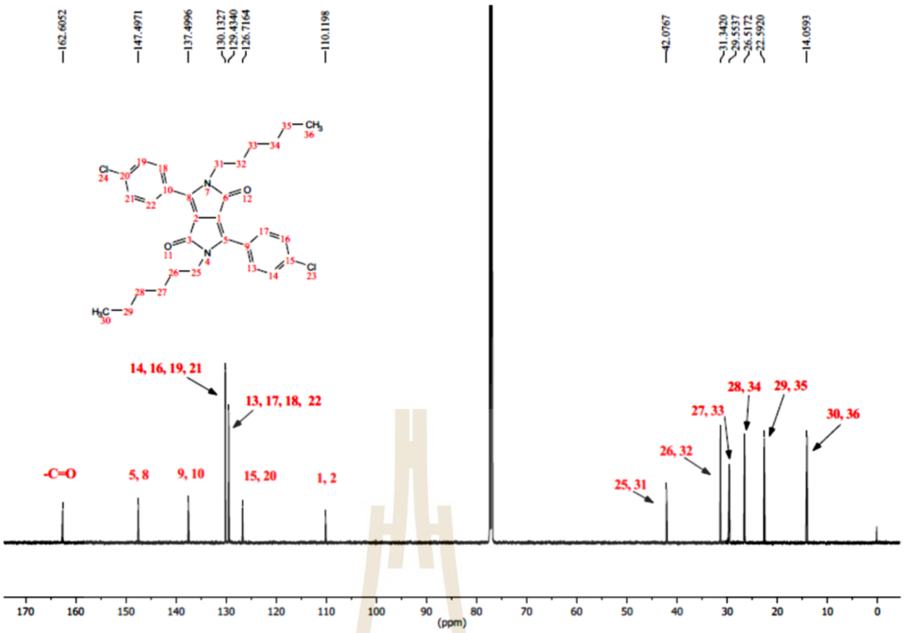

^{13}C-NMR (150 MHz, CDCl$_3$)

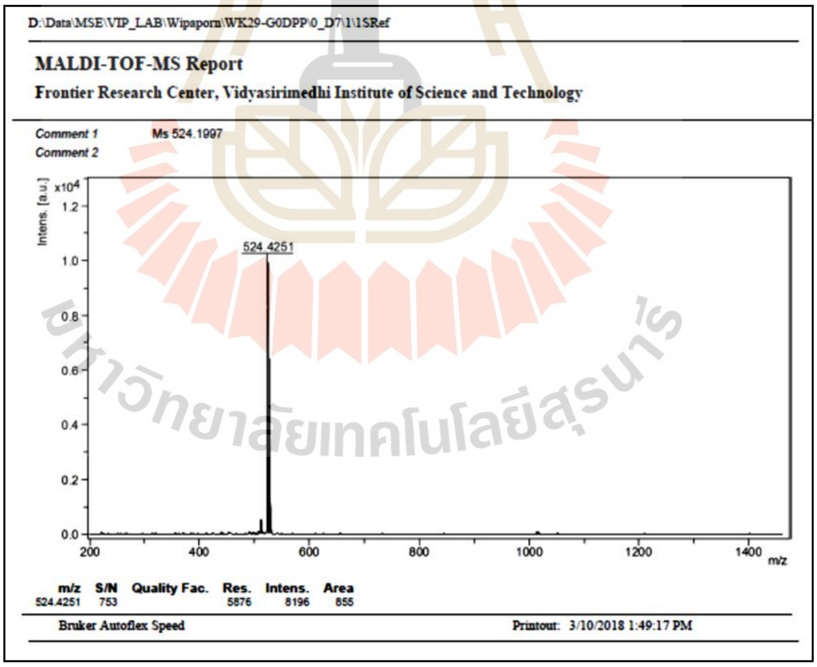

D:\Data\MSE\VIP_LAB\Wipaporn\WK29-G0DPP\0_D7\1\1SRef

MALDI-TOF-MS Report

Frontier Research Center, Vidyasirimedhi Institute of Science and Technology

Comment 1 Ms 524.1997

Comment 2

m/z	S/N	Quality Fac.	Res.	Intens.	Area
524.4251	753		5876	8196	855

Bruker Autoflex Speed   Printout: 3/10/2018 1:49:17 PM

HRMS

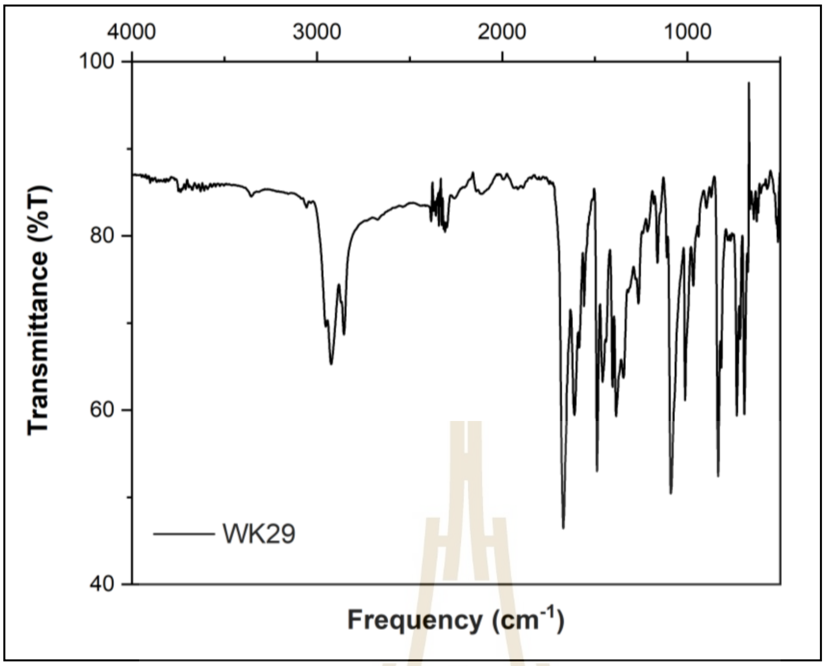

FT-IR

G1DPP (2)

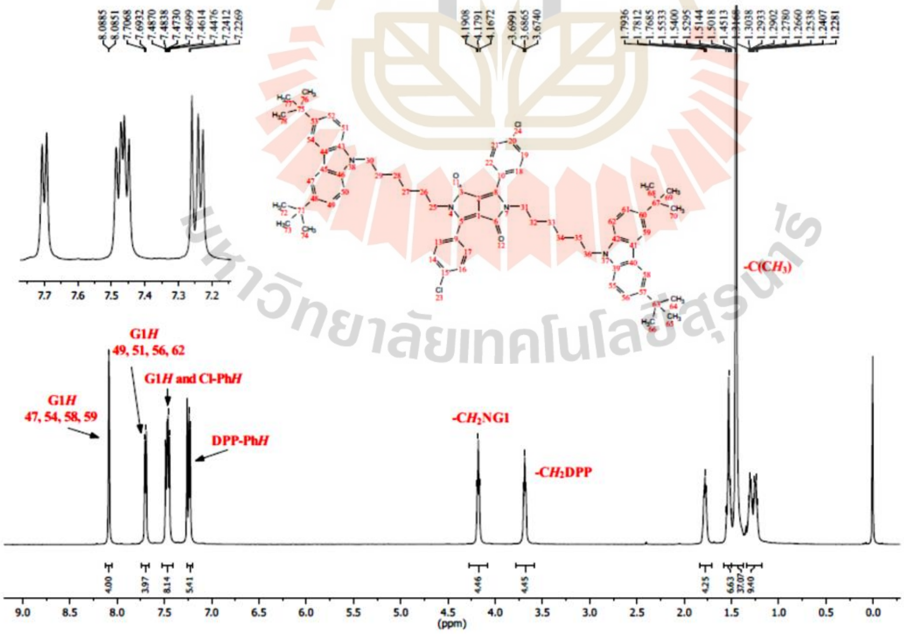

^{1}H-NMR (600 MHz, $CDCl_3$)

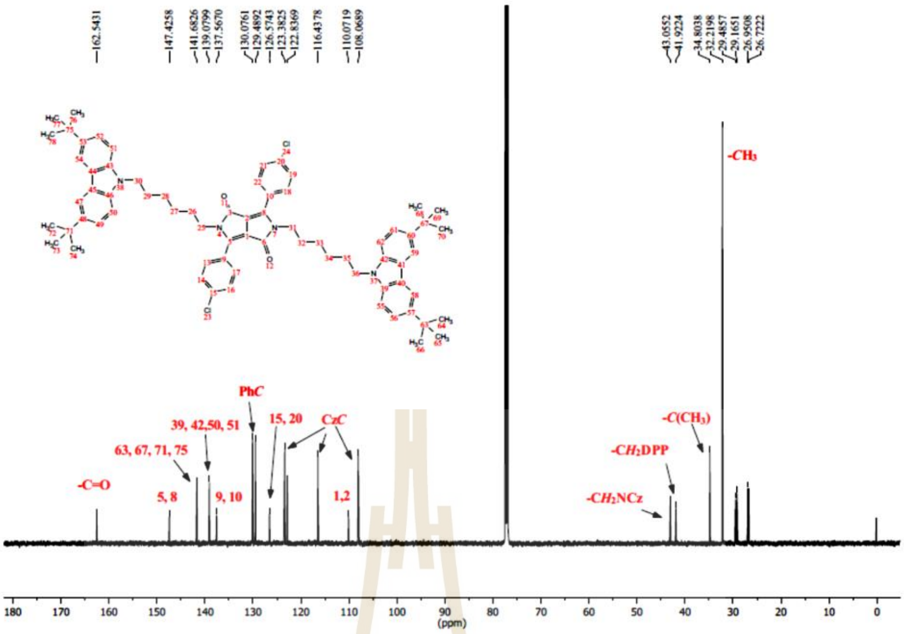

^{13}C-NMR (150 MHz, $CDCl_3$)

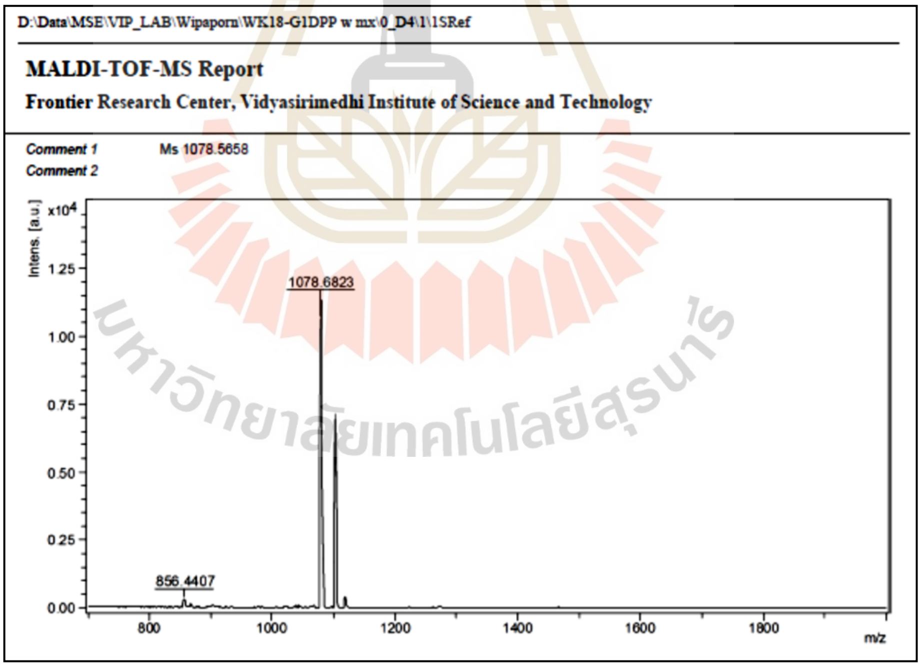
D:\Data\MSE\VIP_LAB\Wipaporn\WK18-G1DPP w mx\0_D4\1\1SRef

MALDI-TOF-MS Report

Frontier Research Center, Vidyasirimedhi Institute of Science and Technology

Comment 1 Ms 1078.5658

Comment 2

HRMS

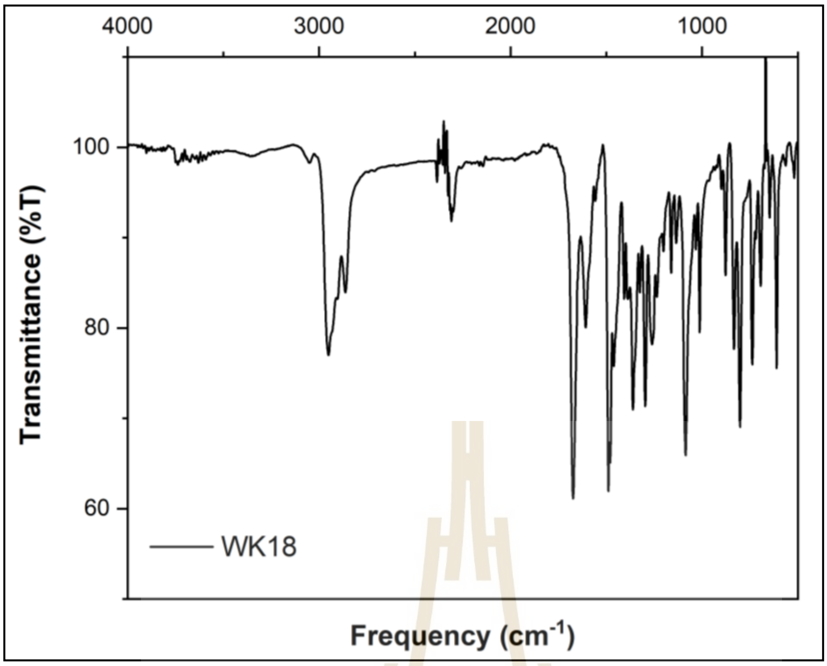

FT-IR

G2DPP (3)

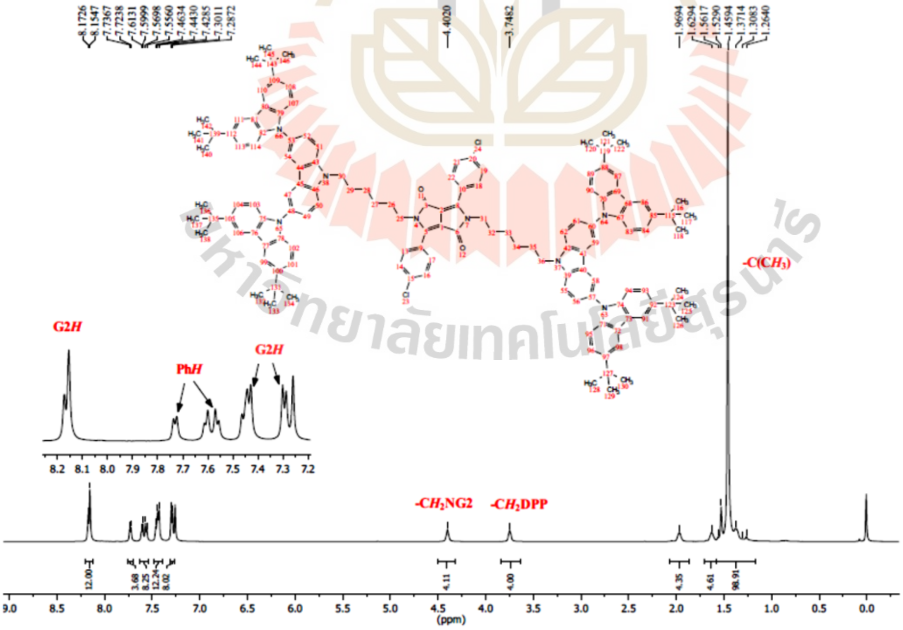

^{1}**H-NMR (600 MHz, CDCl$_3$)**

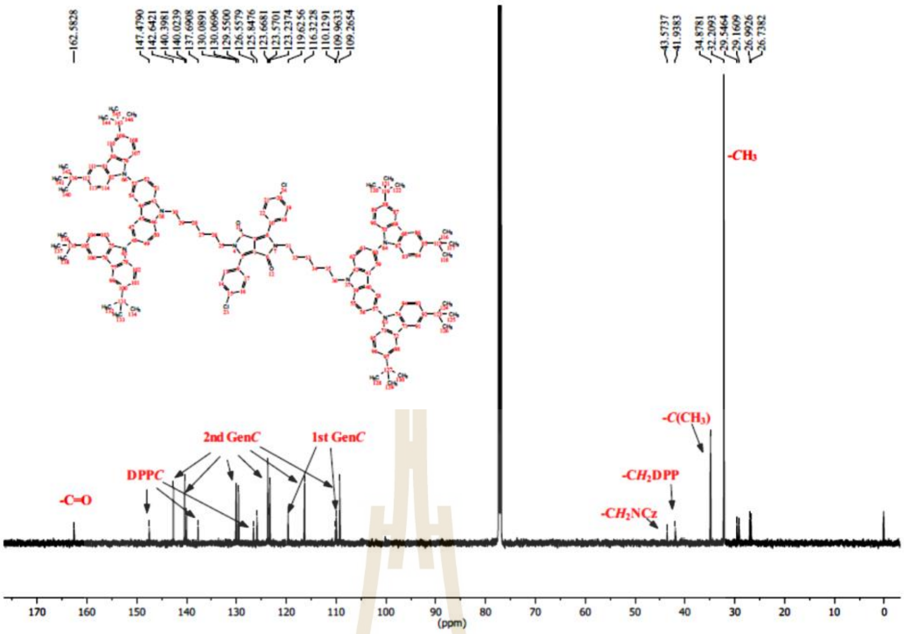

^{13}C-NMR (150 MHz, CDCl$_3$)

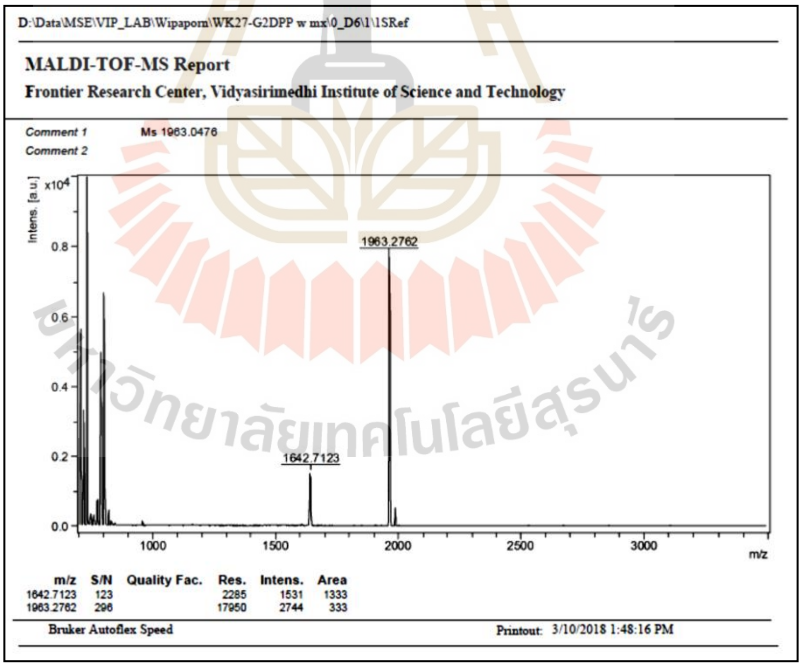

D:\Data\MSE\VIP_LAB\Wipaporn\WK27-G2DPP w mx\0_D6\1\1SRef

MALDI-TOF-MS Report

Frontier Research Center, Vidyasirimedhi Institute of Science and Technology

Comment 1 Ms 1963.0476

Comment 2

m/z	S/N	Quality Fac.	Res.	Intens.	Area
1642.7123	123		2285	1531	1333
1963.2762	296		17950	2744	333

Bruker Autoflex Speed

Printout: 3/10/2018 1:48:16 PM

HRMS

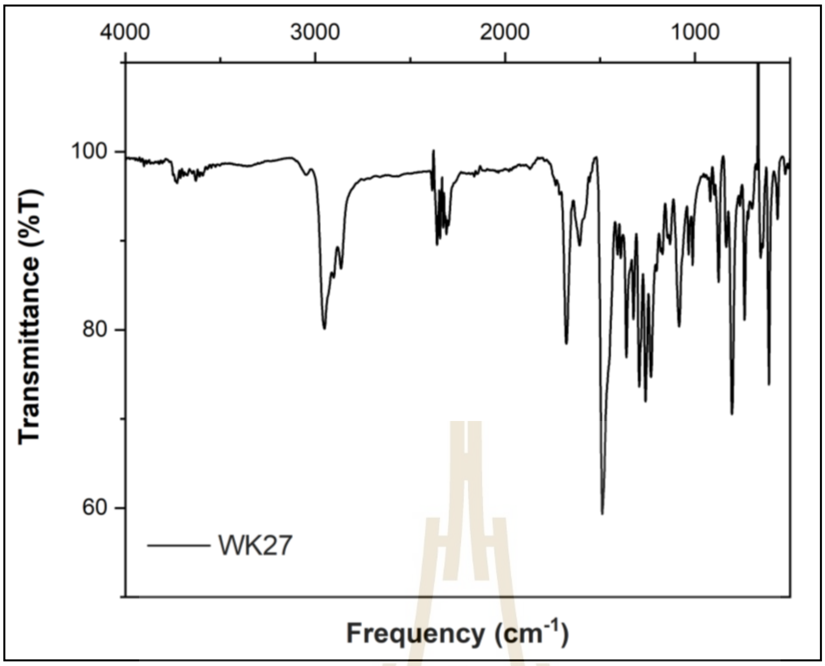

FT-IR

6.4.2 The synthesis of TADF emitters

3,3′-dibromo-4,4′-difluorodiphenyl sulfone (131)

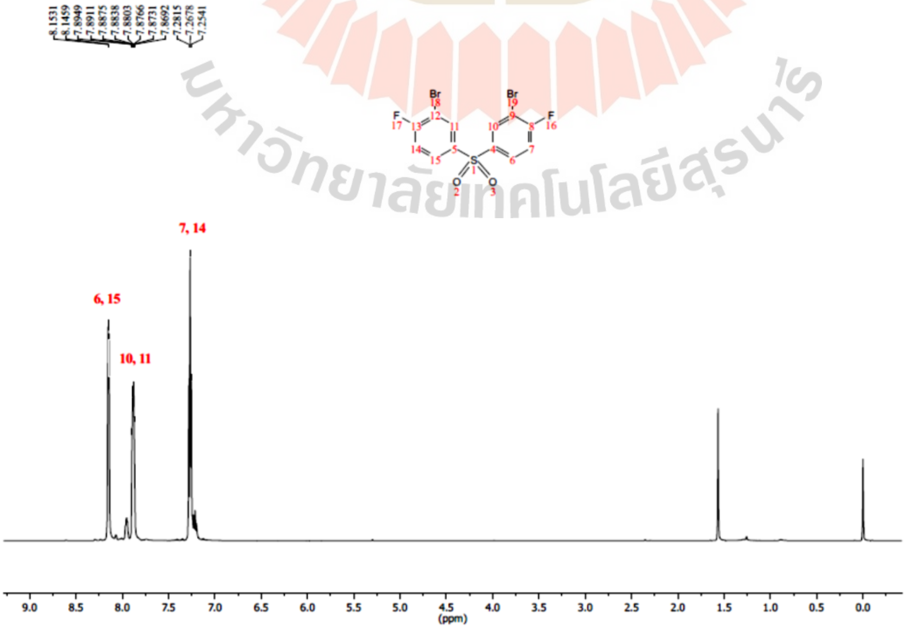

^{1}H-NMR (600 MHz, $CDCl_3$)

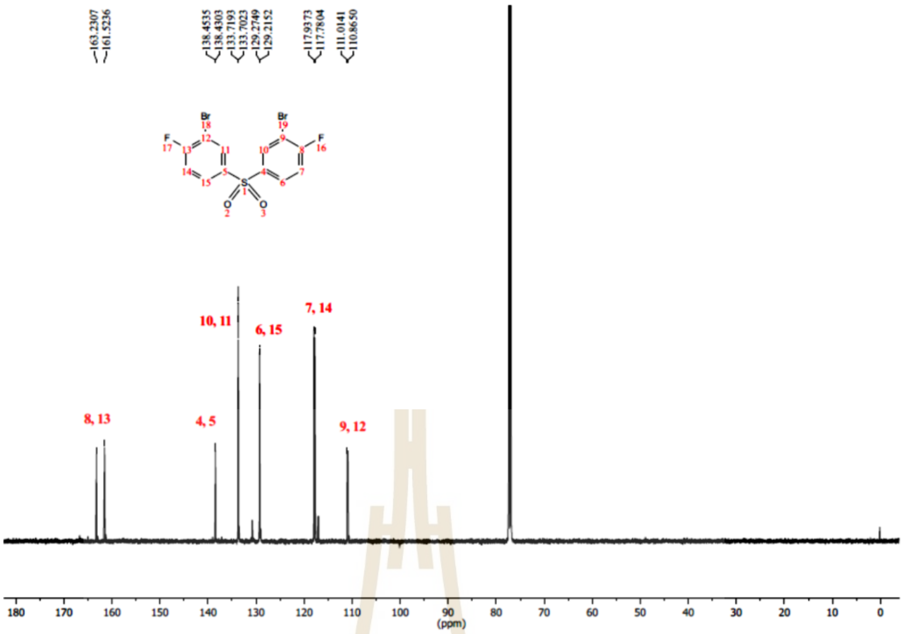

^{13}C-NMR (150 MHz, $CDCl_3$)

3,3′,5,5′-tetrabromo-4,4′-difluorodiphenyl sulfone (132)

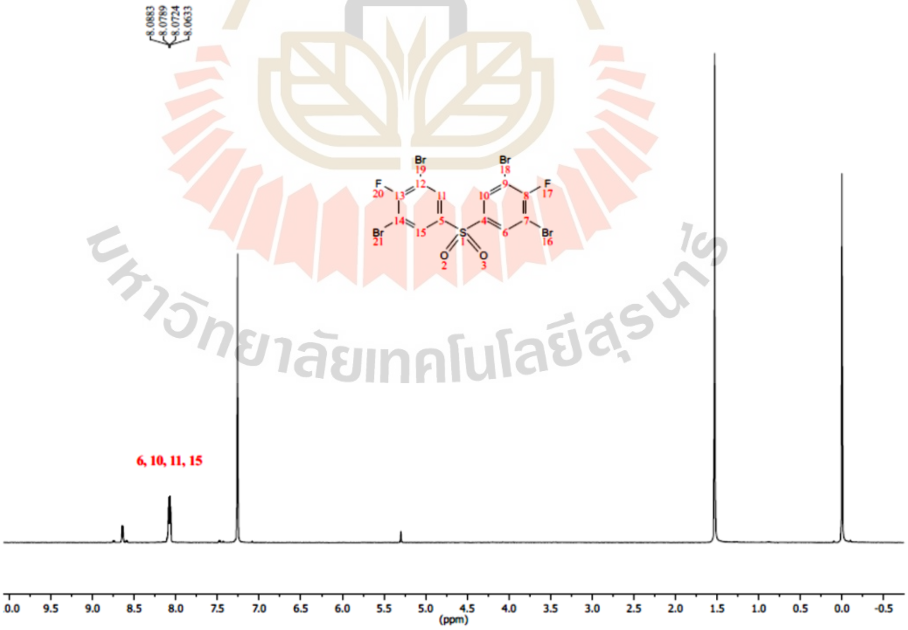

^{1}H-NMR (600 MHz, $CDCl_3$)

3,3′-Diphenyl-4,40-difluorodiphenyl Sulfone (133)

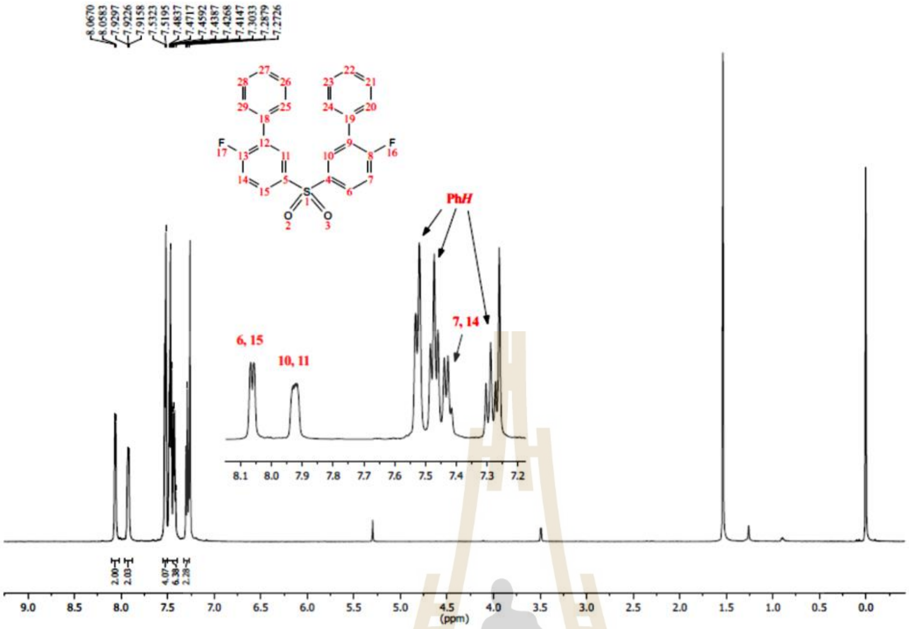

^{1}H-NMR (600 MHz, $CDCl_3$)

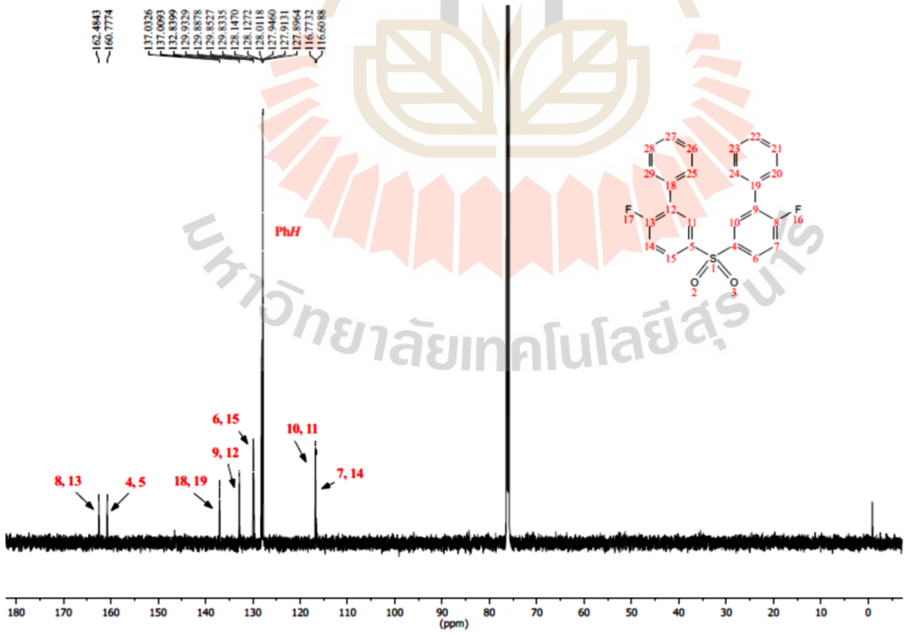

^{13}C-NMR (150 MHz, $CDCl_3$)

3,3′,5,5′-Tetraphenyl-4,4′-difluorodiphenyl Sulfone (134)

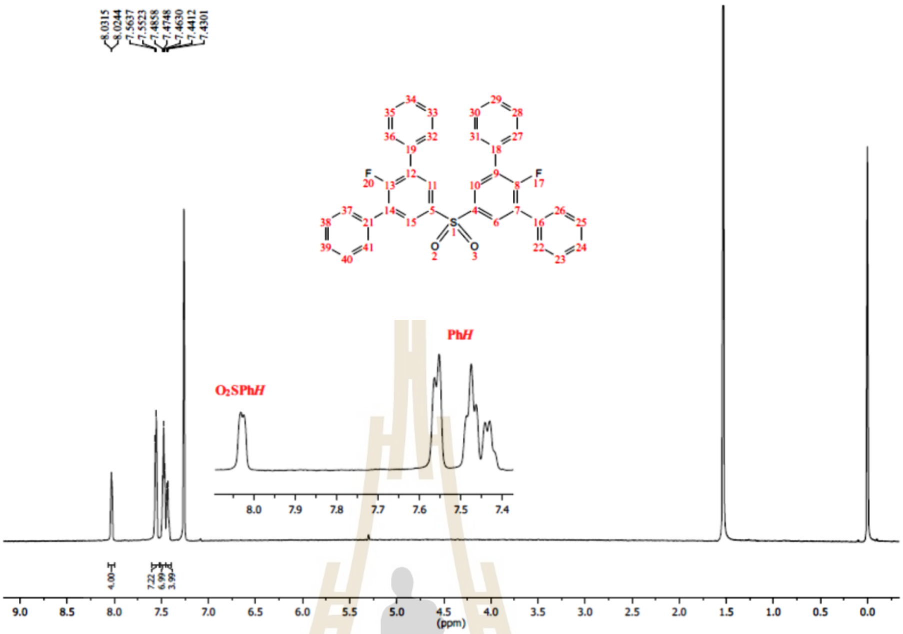

^{1}H-NMR (600 MHz, CDCl$_3$)

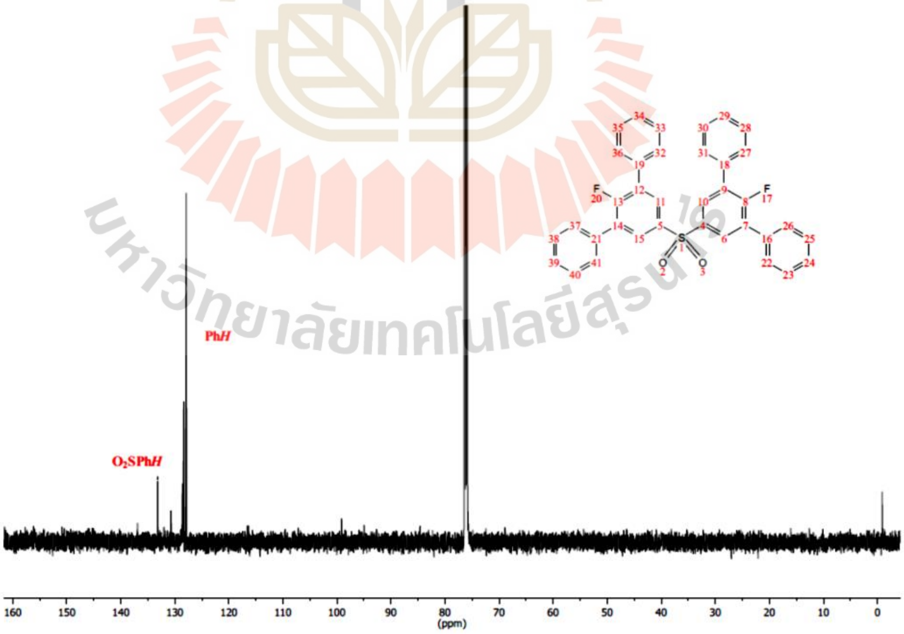

^{13}C-NMR (150 MHz, CDCl$_3$)

3,6-diphenyl-9H-carbazole (136)

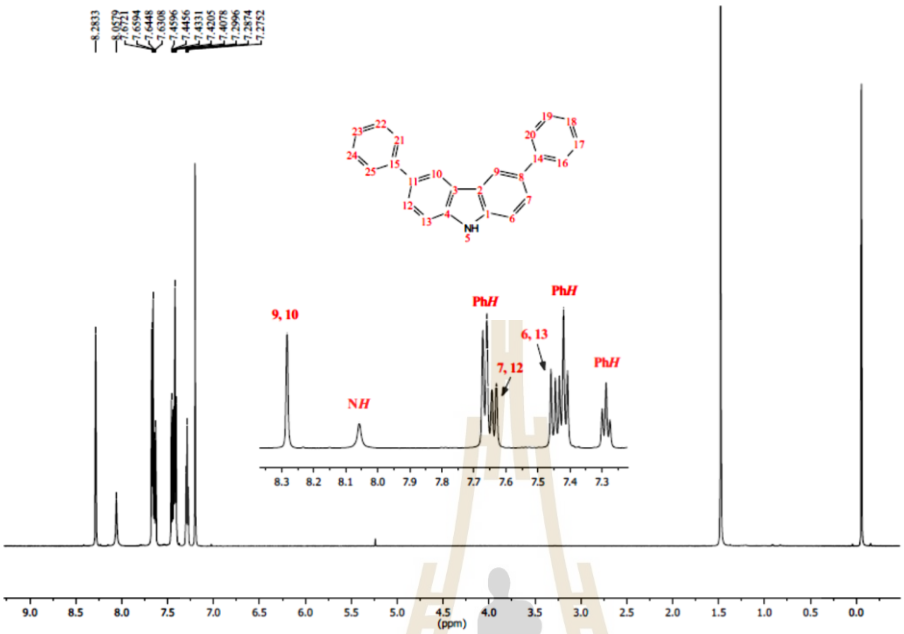

^{1}H-NMR (600 MHz, CDCl$_3$)

2,7-diphenyl-9H-carbazole (138)

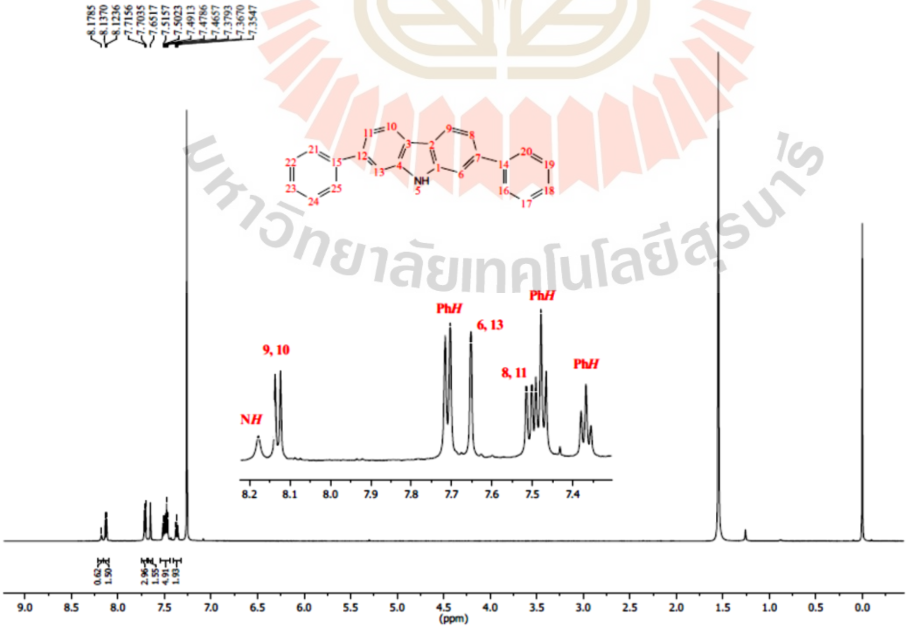

^{1}H-NMR (600 MHz, CDCl$_3$)

Cz-DPS (4)

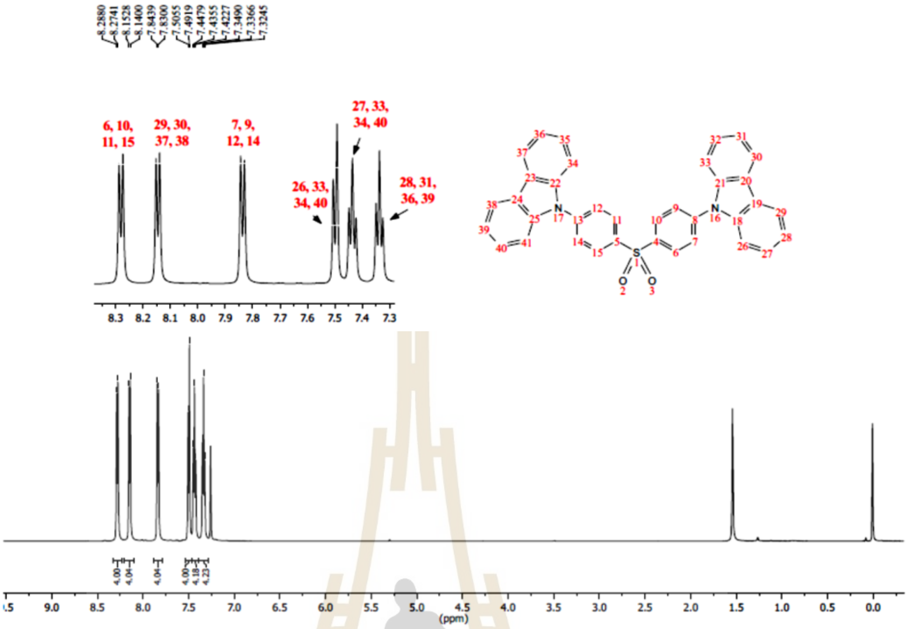

^{1}H-NMR (600 MHz, $CDCl_3$)

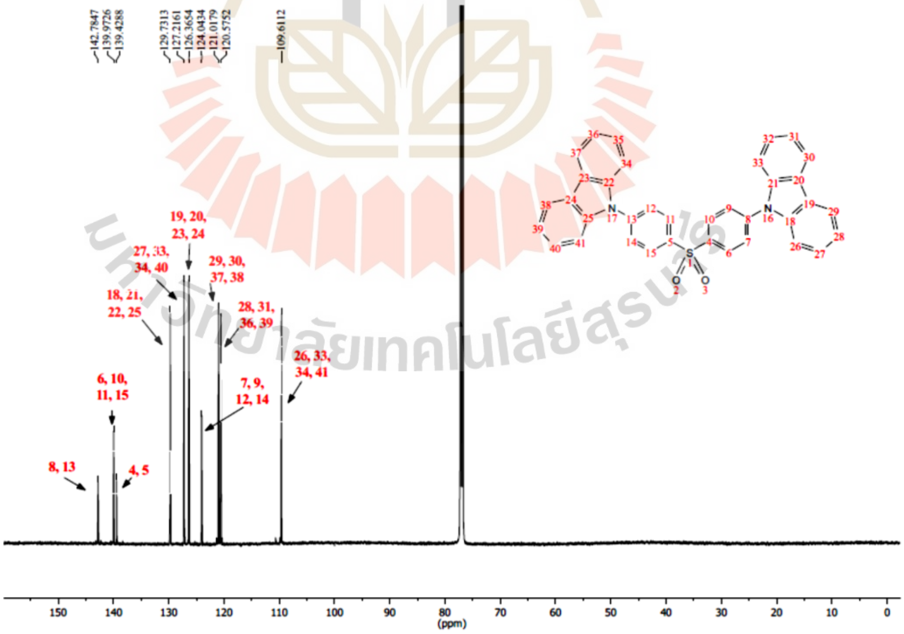

^{13}C-NMR (150 MHz, $CDCl_3$)

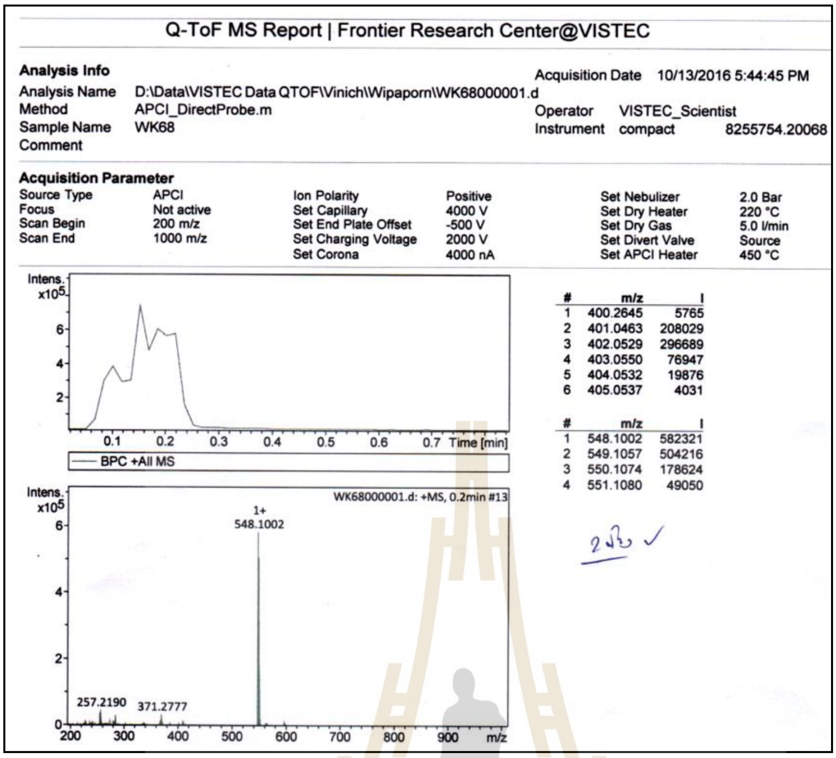

Q-ToF MS Report | Frontier Research Center@VISTEC

Analysis Info

Analysis Name	D:\Data\VISTEC Data QTOF\Vinich\Wipaporn\WK68000001.d	Acquisition Date	10/13/2016 5:44:45 PM
Method	APCI_DirectProbe.m	Operator	VISTEC_Scientist
Sample Name	WK68	Instrument	compact 8255754.20068
Comment			

Acquisition Parameter

Source Type	APCI	Ion Polarity	Positive	Set Nebulizer	2.0 Bar
Focus	Not active	Set Capillary	4000 V	Set Dry Heater	220 °C
Scan Begin	200 m/z	Set End Plate Offset	-500 V	Set Dry Gas	5.0 l/min
Scan End	1000 m/z	Set Charging Voltage	2000 V	Set Divert Valve	Source
		Set Corona	4000 nA	Set APCI Heater	450 °C

#	m/z	I
1	400.2645	5765
2	401.0463	208029
3	402.0529	296689
4	403.0550	76947
5	404.0532	19876
6	405.0537	4031

#	m/z	I
1	548.1002	582321
2	549.1057	504216
3	550.1074	178624
4	551.1080	49050

2 [illegible] ✓

Intens.
x10^5
6
4
2
0.1
0.2
0.3
0.4
0.5
0.6
0.7
Time [min]
BPC +All MS
Intens.
x10^5
6
4
2
0
WK68000001.d: +MS, 0.2min #13
1+
548.1002
257.2190
371.2777
200
300
400
500
600
700
800
900
m/z

Q-TOF

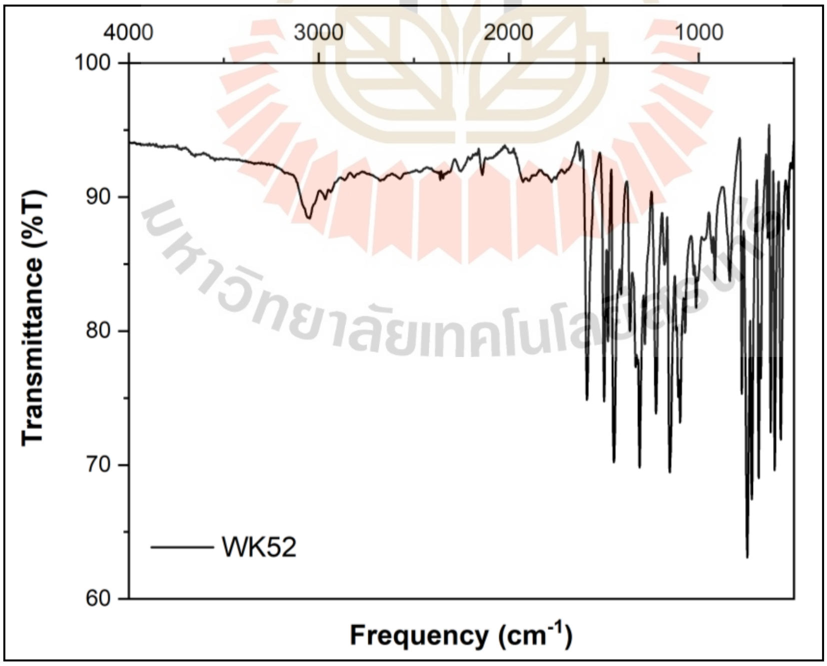

FT-IR

G1-DPS (5)

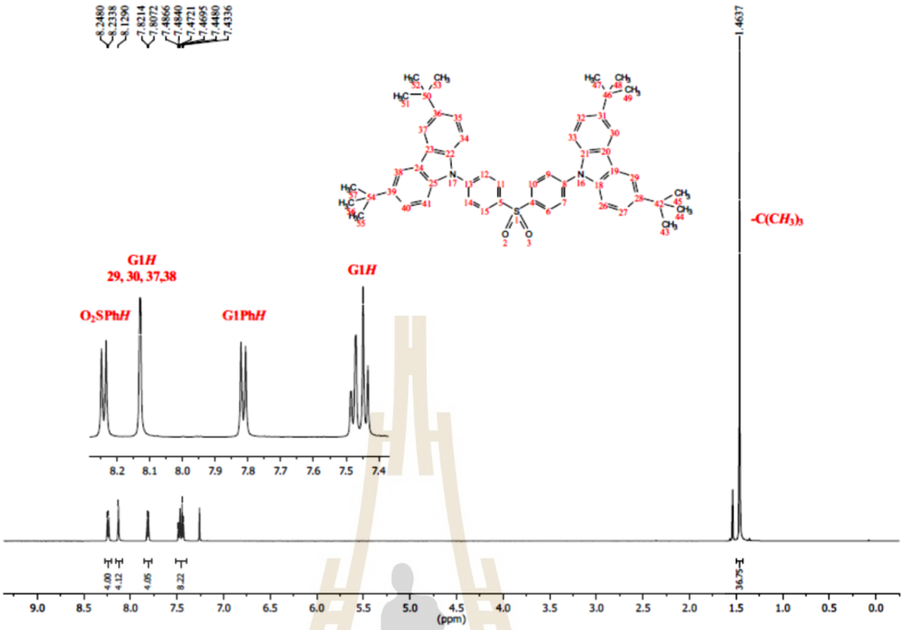

^{1}H-NMR (600 MHz, CDCl$_3$)

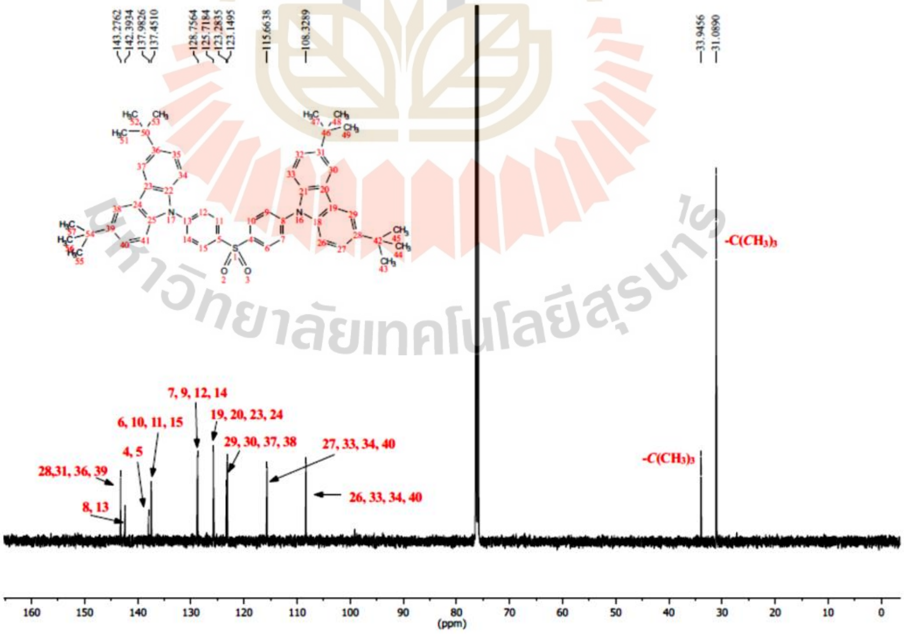

^{13}C-NMR (150 MHz, CDCl$_3$)

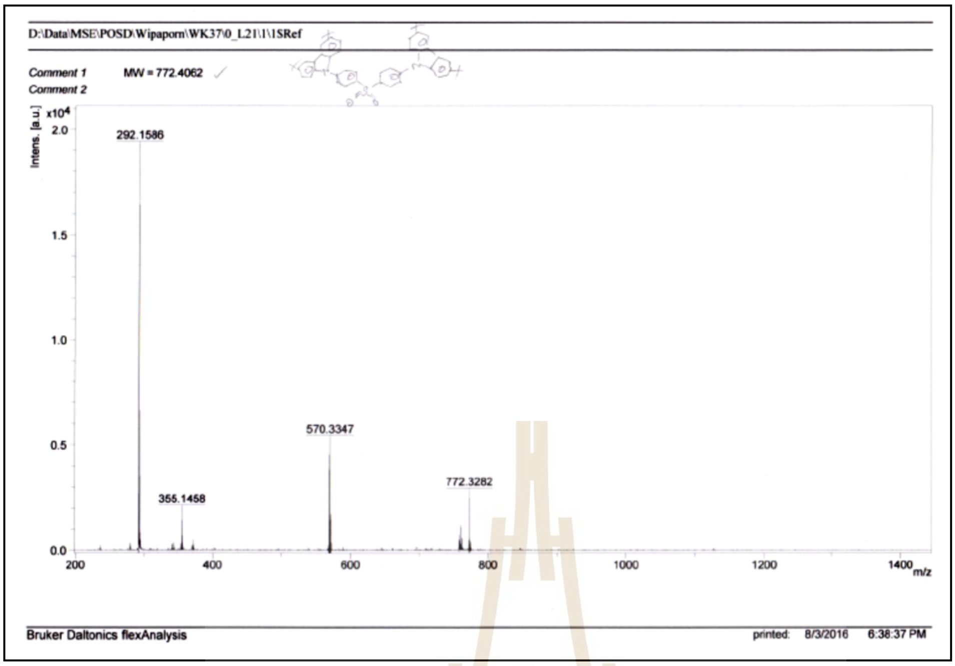

MALDI-TOF

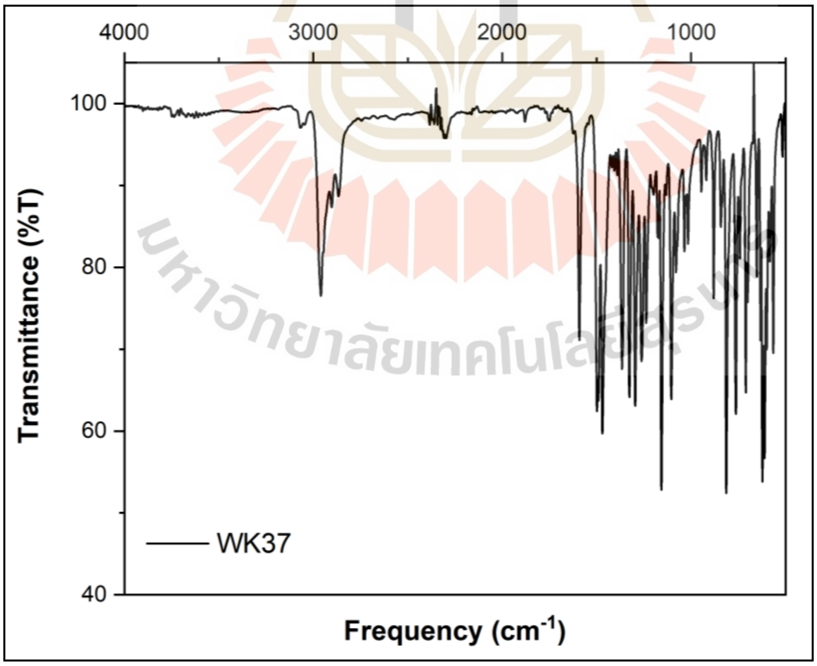

FT-IR

3,6-diPhCz-DPS (6)

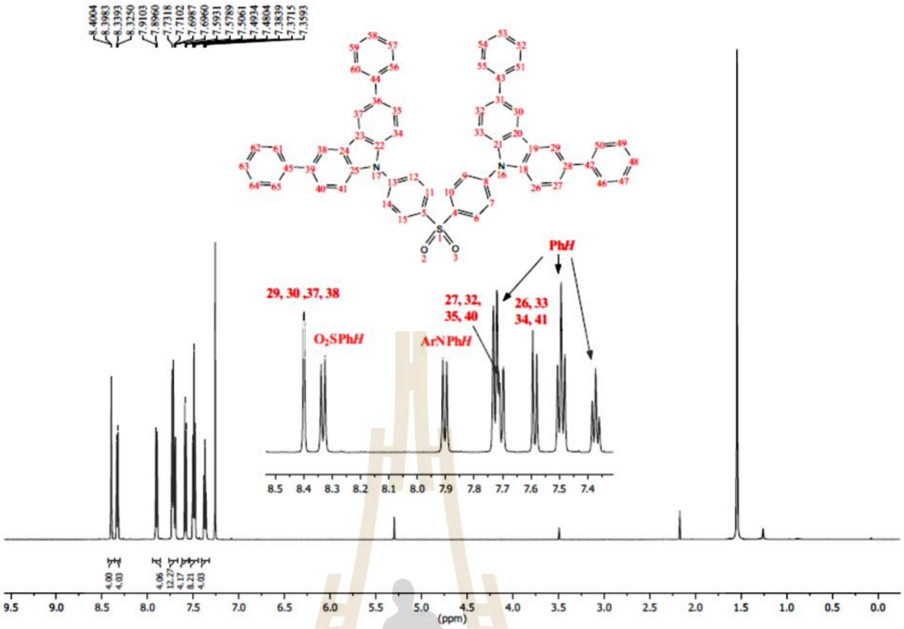

^{1}H-NMR (600 MHz, CDCl$_3$)

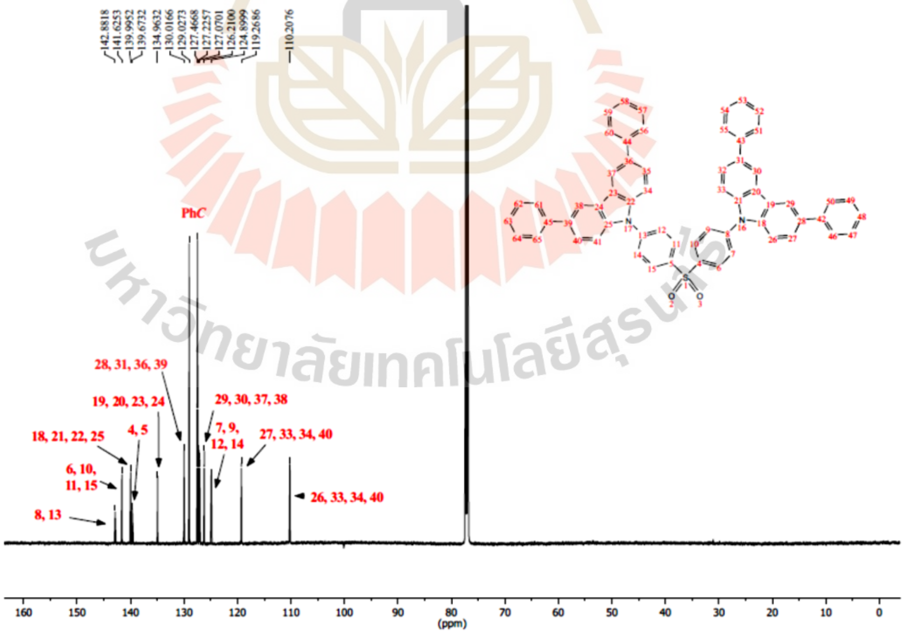

^{13}C-NMR (150 MHz, CDCl$_3$)

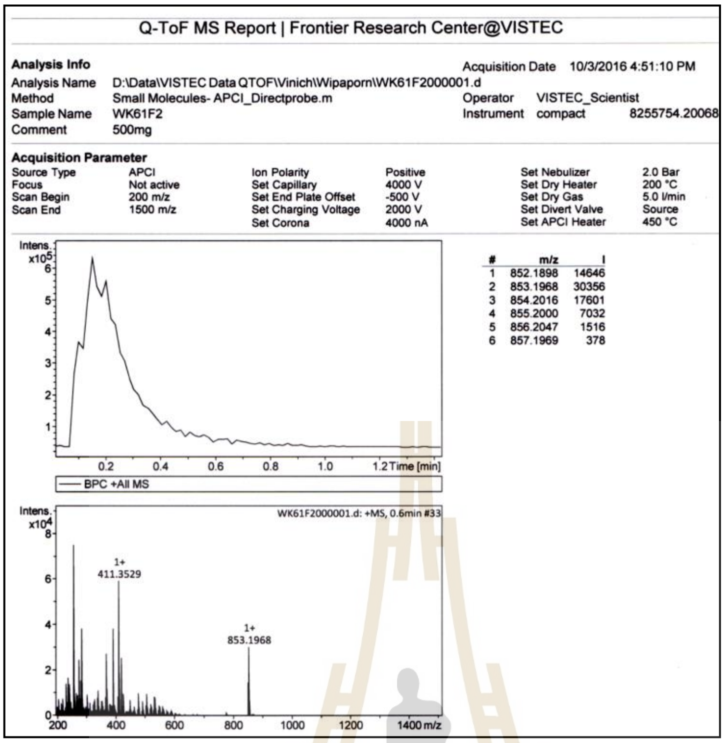

Q-ToF MS Report | Frontier Research Center@VISTEC

Analysis Info

Acquisition Date 10/3/2016 4:51:10 PM

Analysis Name D:\Data\VISTEC Data QTOF\Vinich\Wipaporn\WK61F2000001.d
Method Small Molecules- APCI_Directprobe.m
Sample Name WK61F2
Comment 500mg

Operator VISTEC_Scientist
Instrument compact 8255754.20068

Acquisition Parameter

Source Type APCI
Focus Not active
Scan Begin 200 m/z
Scan End 1500 m/z

Ion Polarity Positive
Set Capillary 4000 V
Set End Plate Offset -500 V
Set Charging Voltage 2000 V
Set Corona 4000 nA

Set Nebulizer 2.0 Bar
Set Dry Heater 200 °C
Set Dry Gas 5.0 l/min
Set Divert Valve Source
Set APCI Heater 450 °C

#	m/z	I
1	852.1898	14646
2	853.1968	30356
3	854.2016	17601
4	855.2000	7032
5	856.2047	1516
6	857.1969	378

WK61F2000001.d: +MS, 0.6min #33

Intens.
x10^5
6
5
4
3
2
1
0.2
0.4
0.6
0.8
1.0
1.2 Time [min]
BPC +All MS
Intens.
x10^4
8
6
4
2
0
1+
411.3529
1+
853.1968
200
400
600
800
1000
1200
1400 m/z

Q-TOF

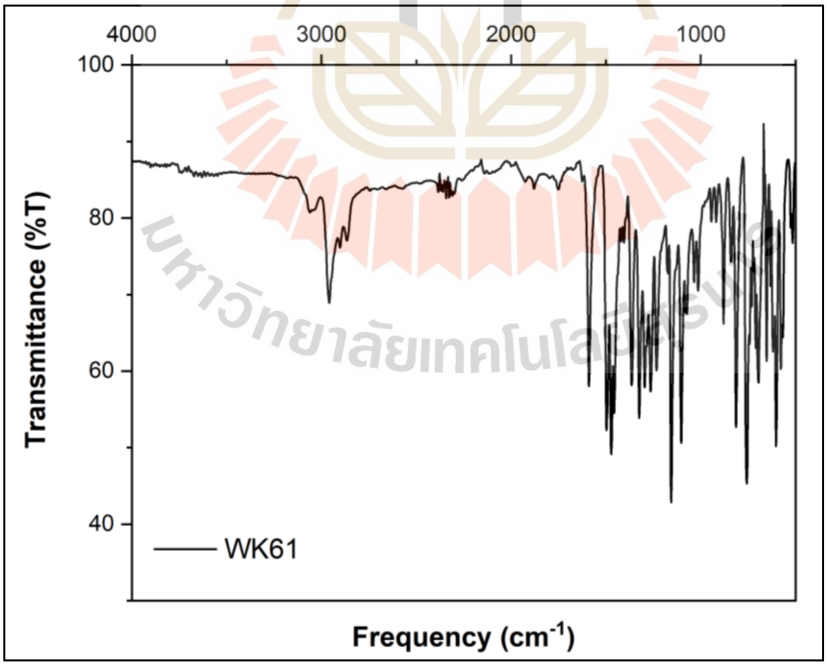

FT-IR

2,7-diPhCz-DPS (7)

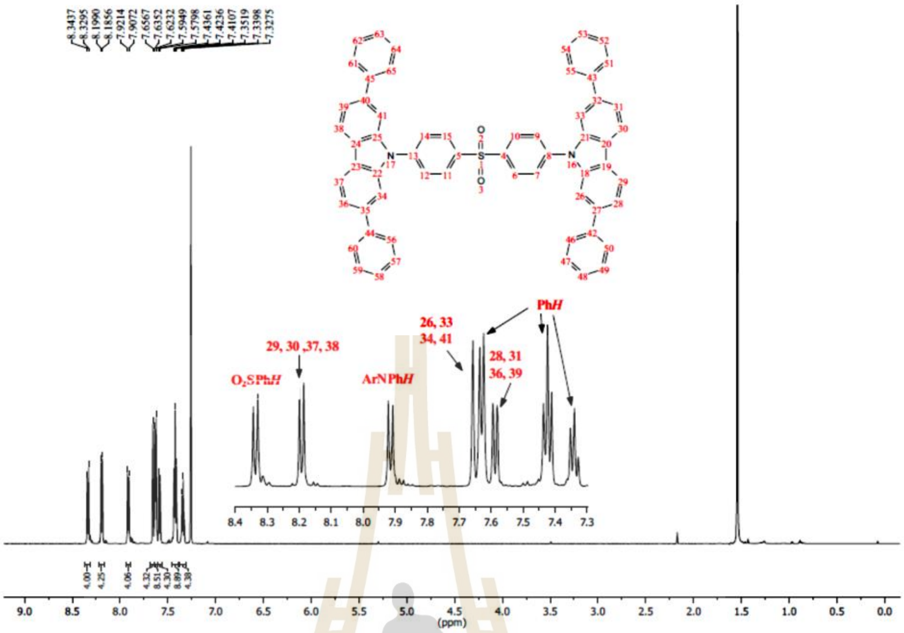

^{1}H-NMR (600 MHz, CDCl$_3$)

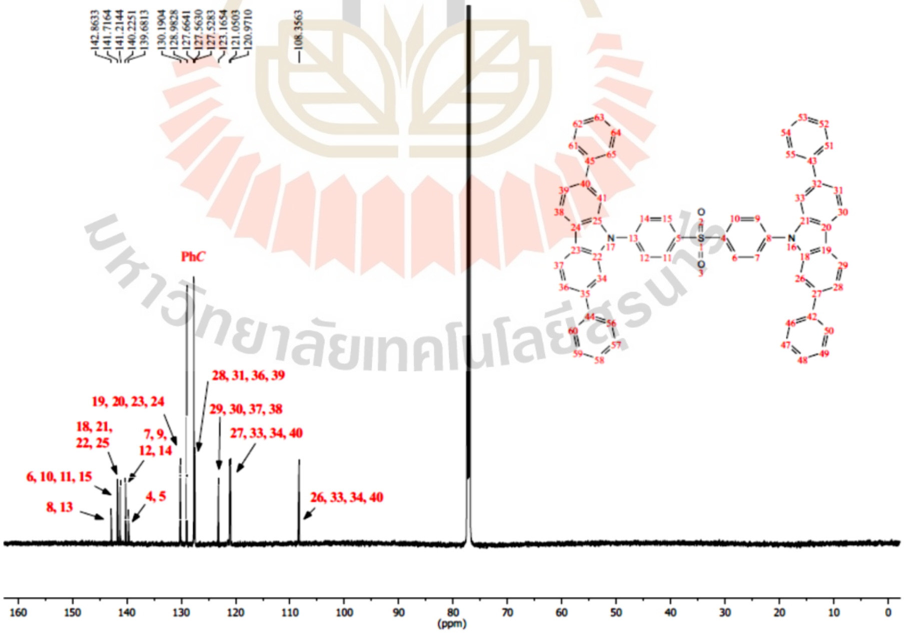

^{13}C-NMR (150 MHz, CDCl$_3$)

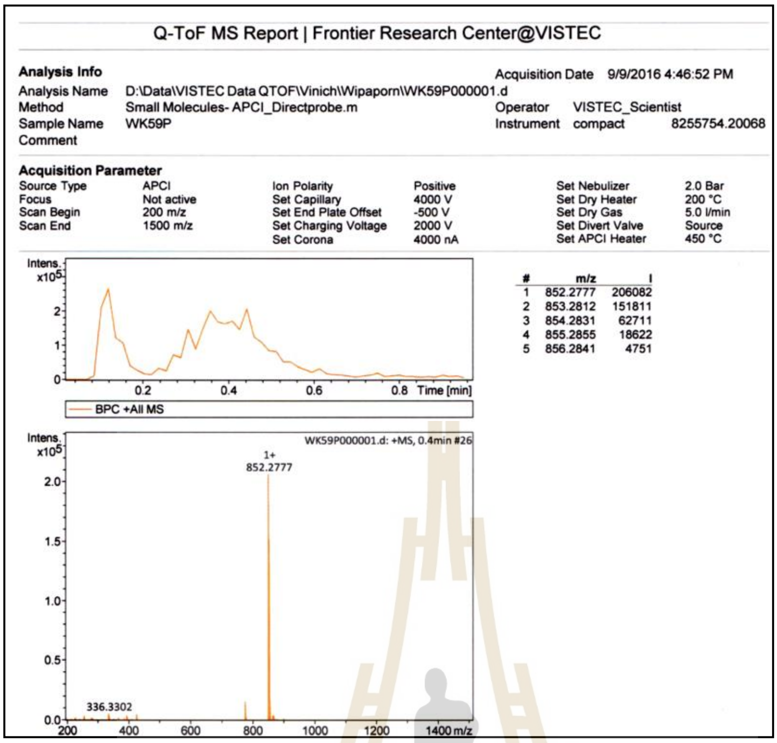

Q-ToF MS Report | Frontier Research Center@VISTEC

Analysis Info

Analysis Name	D:\Data\VISTEC Data QTOF\Vinich\Wipaporn\WK59P000001.d	Acquisition Date	9/9/2016 4:46:52 PM
Method	Small Molecules- APCI_Directprobe.m	Operator	VISTEC_Scientist
Sample Name	WK59P	Instrument	compact 8255754.20068
Comment			

Acquisition Parameter

Source Type	APCI	Ion Polarity	Positive	Set Nebulizer	2.0 Bar
Focus	Not active	Set Capillary	4000 V	Set Dry Heater	200 °C
Scan Begin	200 m/z	Set End Plate Offset	-500 V	Set Dry Gas	5.0 l/min
Scan End	1500 m/z	Set Charging Voltage	2000 V	Set Divert Valve	Source
		Set Corona	4000 nA	Set APCI Heater	450 °C

#	m/z	I
1	852.2777	206082
2	853.2812	151811
3	854.2831	62711
4	855.2855	18622
5	856.2841	4751

Intens.
x10^5
2
1
0
0.2
0.4
0.6
0.8
Time [min]
BPC +All MS
Intens.
x10^5
WK59P000001.d: +MS, 0.4min #26
1+
852.2777
2.0
1.5
1.0
0.5
0.0
336.3302
200
400
600
800
1000
1200
1400 m/z

Q-TOF

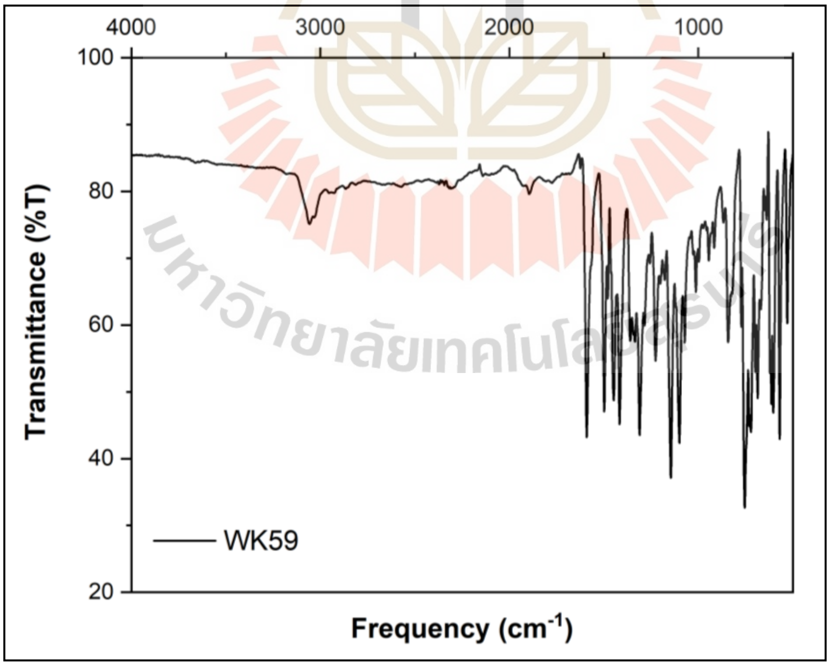

FT-IR

G1-2Ph-DPS (8)

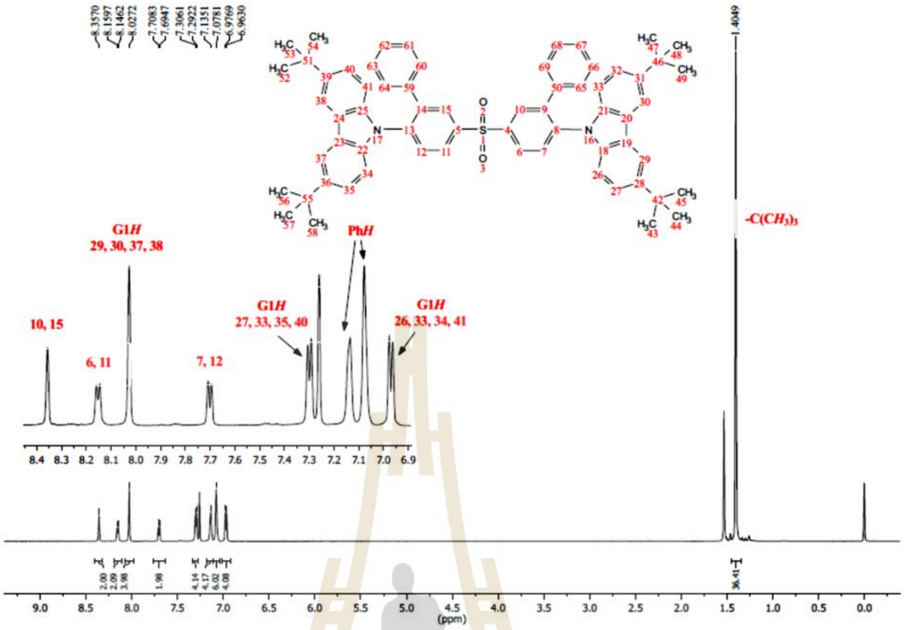

^{1}H-NMR (600 MHz, CDCl$_3$)

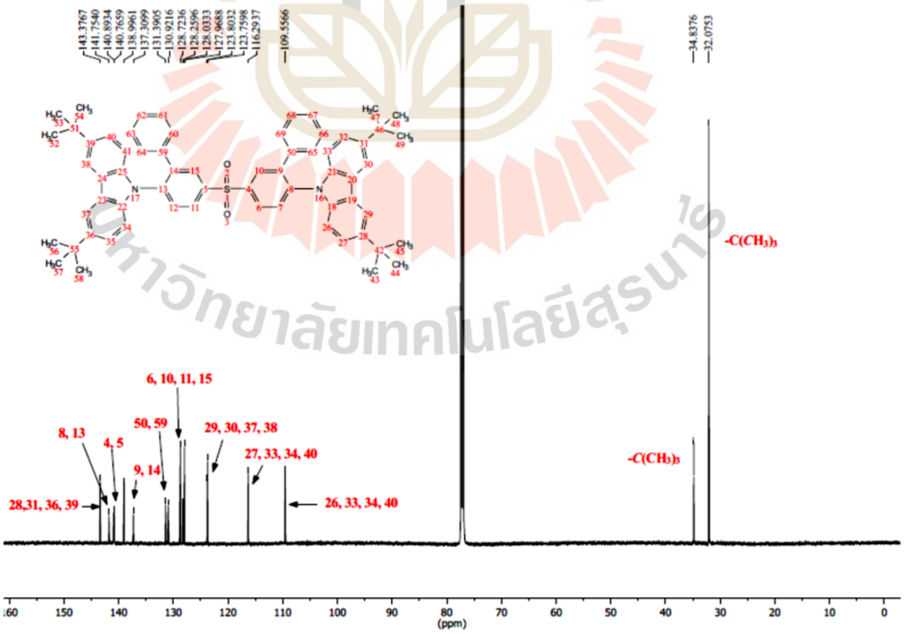

^{13}C-NMR (150 MHz, CDCl$_3$)

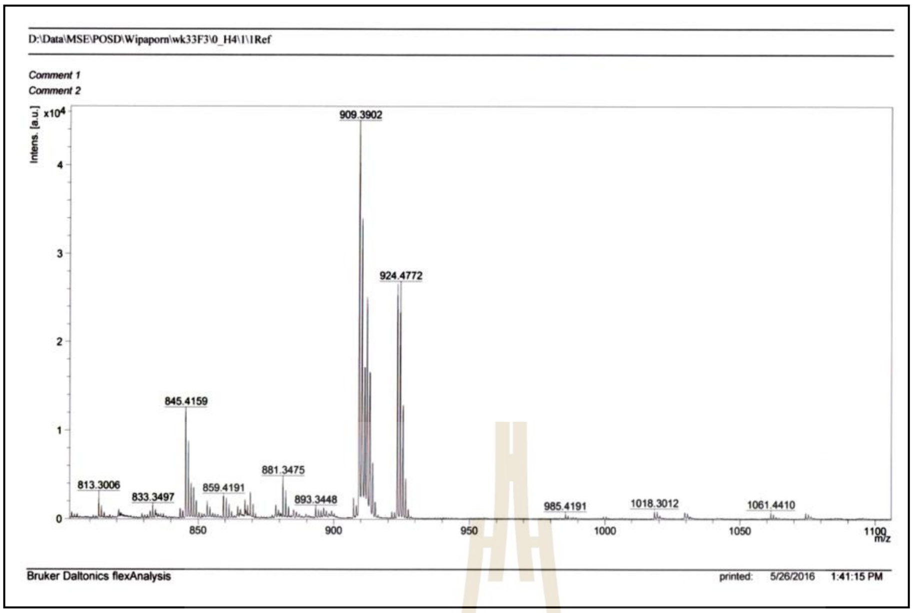

MALDI-TOF

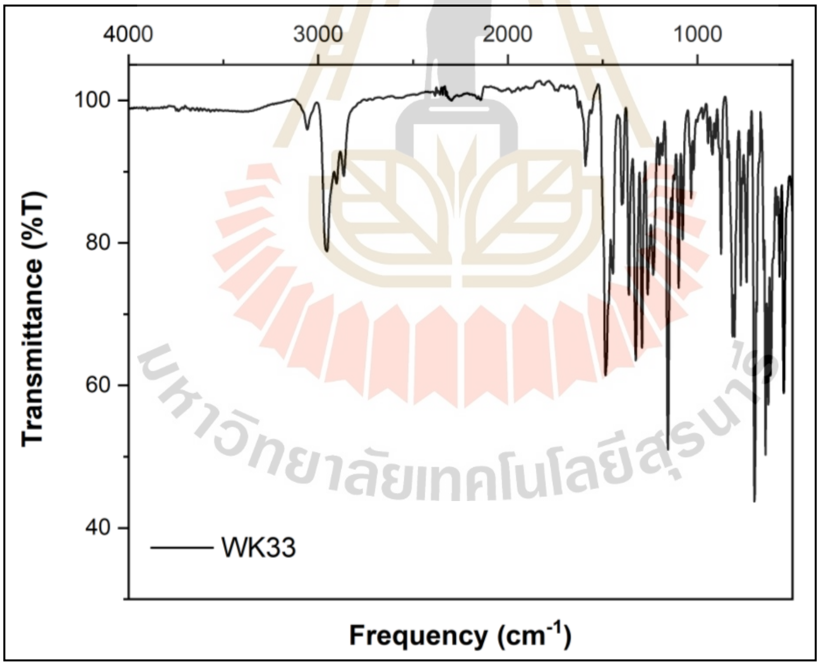

FT-IR

G2-2Ph-DPS (9)

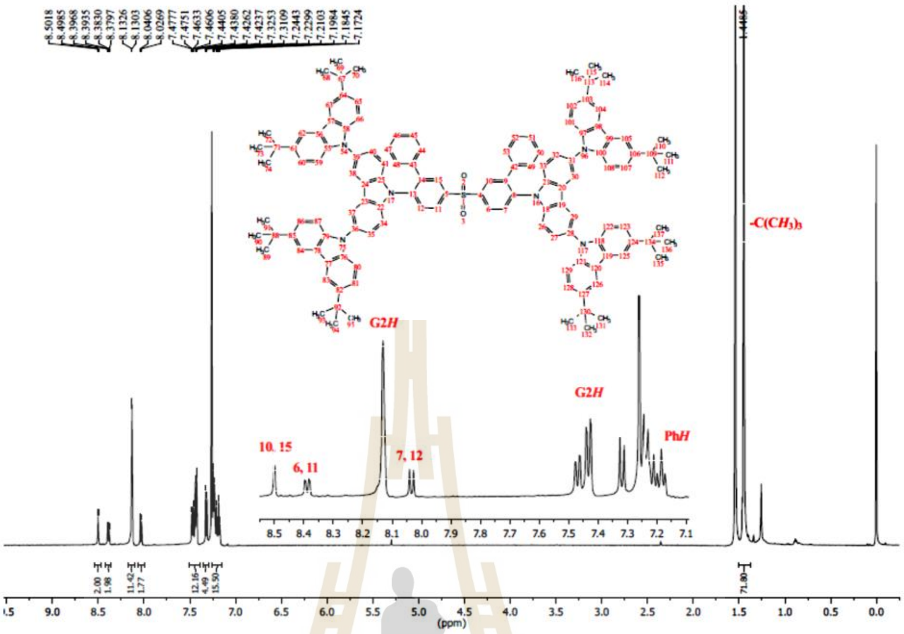

^{1}H-NMR (600 MHz, CDCl$_3$)

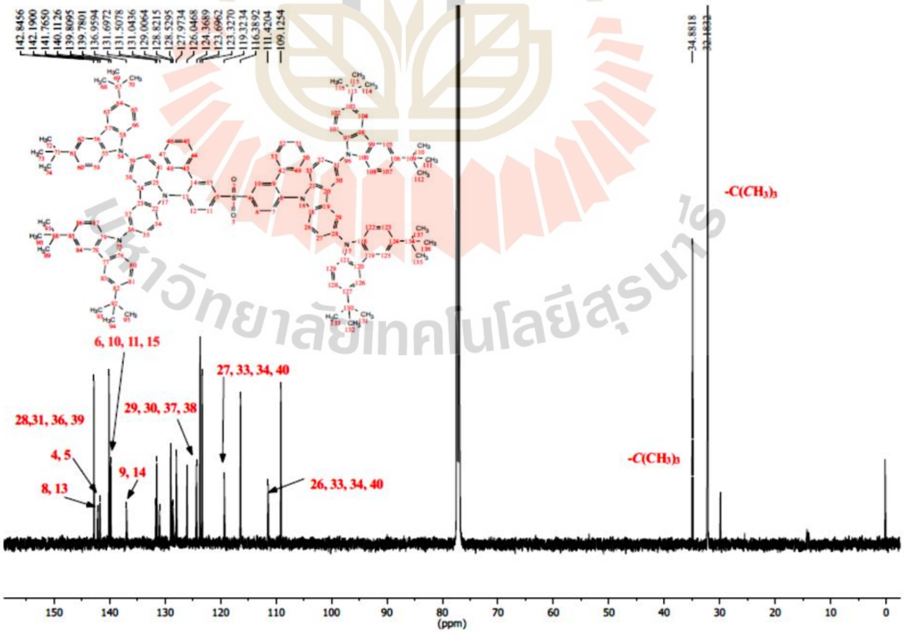

^{13}C-NMR (150 MHz, CDCl$_3$)

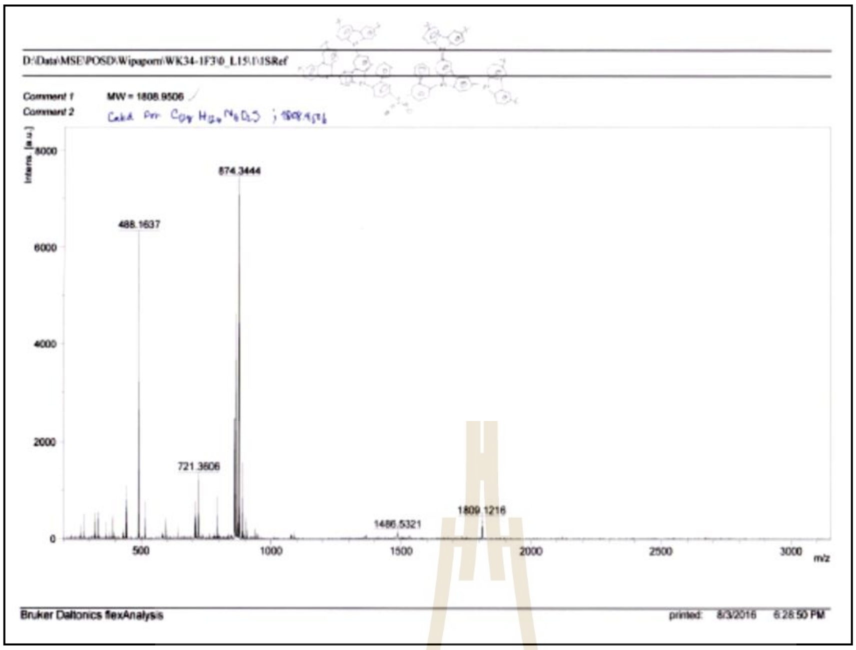

MALDI-TOF

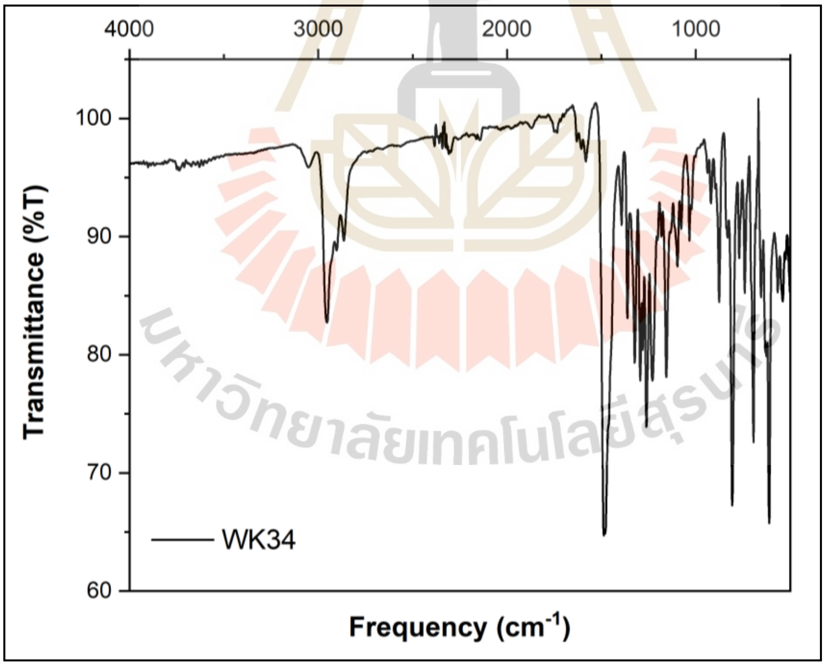

FT-IR

G14Ph-DPS (10)

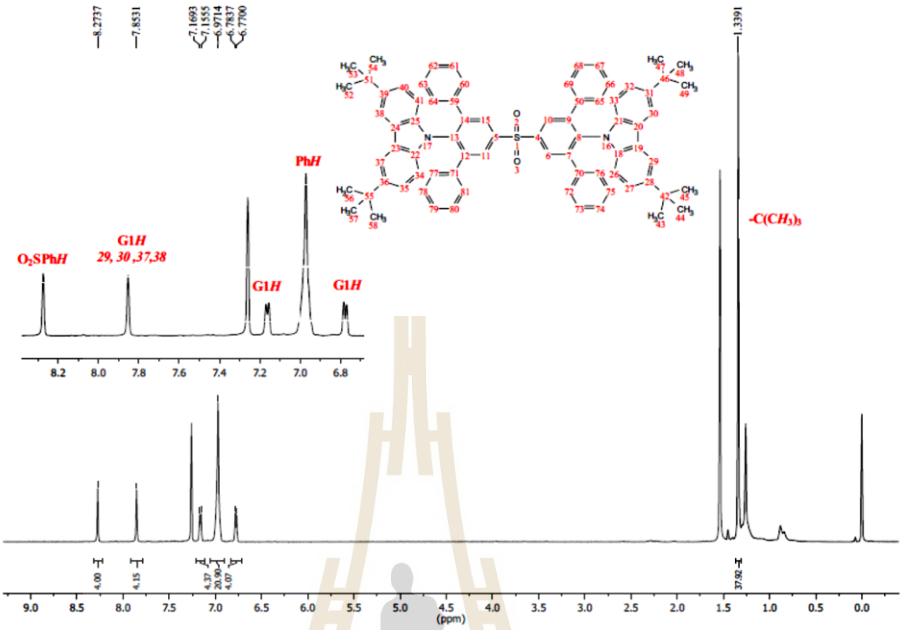

^{1}H-NMR (600 MHz, $CDCl_3$)

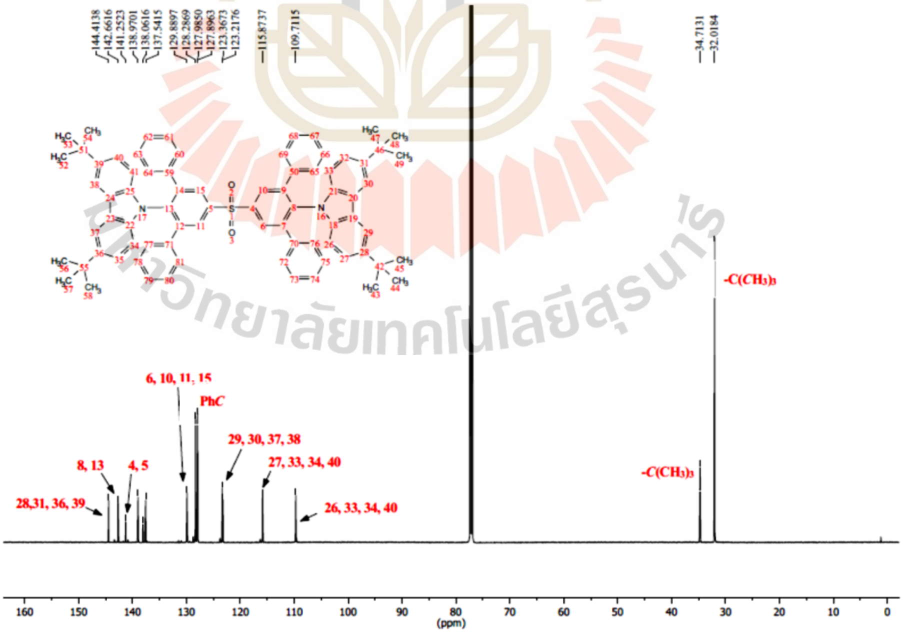

^{13}C-NMR (150 MHz, $CDCl_3$)

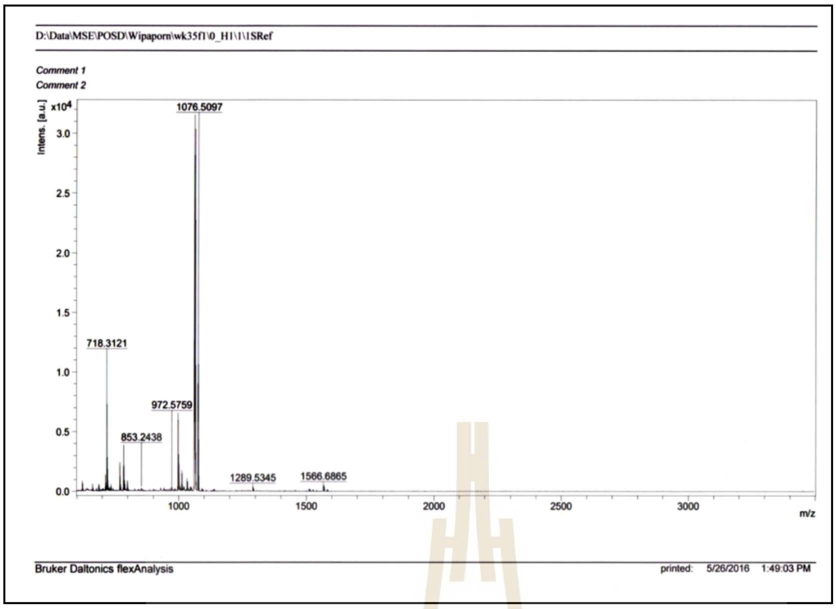

MALDI-TOF

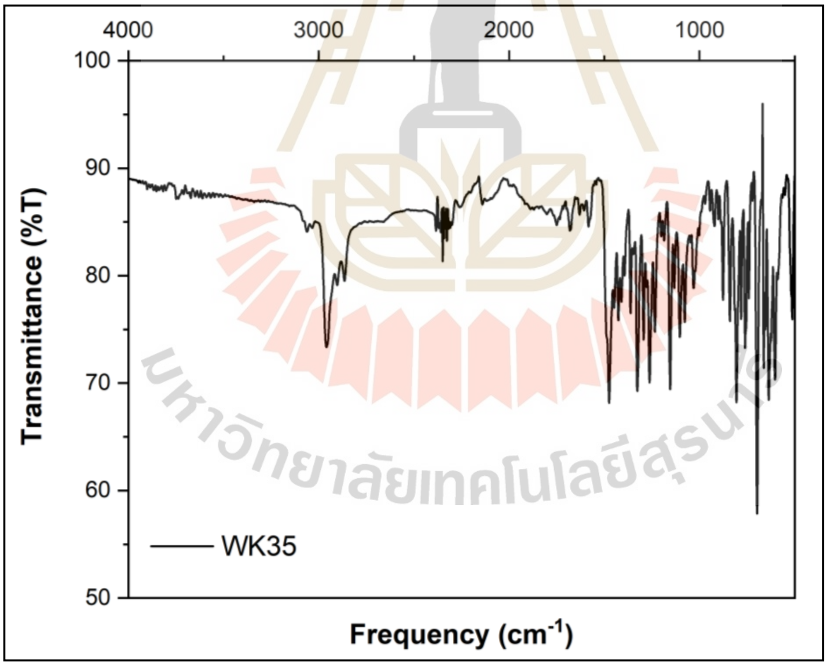

FT-IR

G2-4Ph-DPS (11)

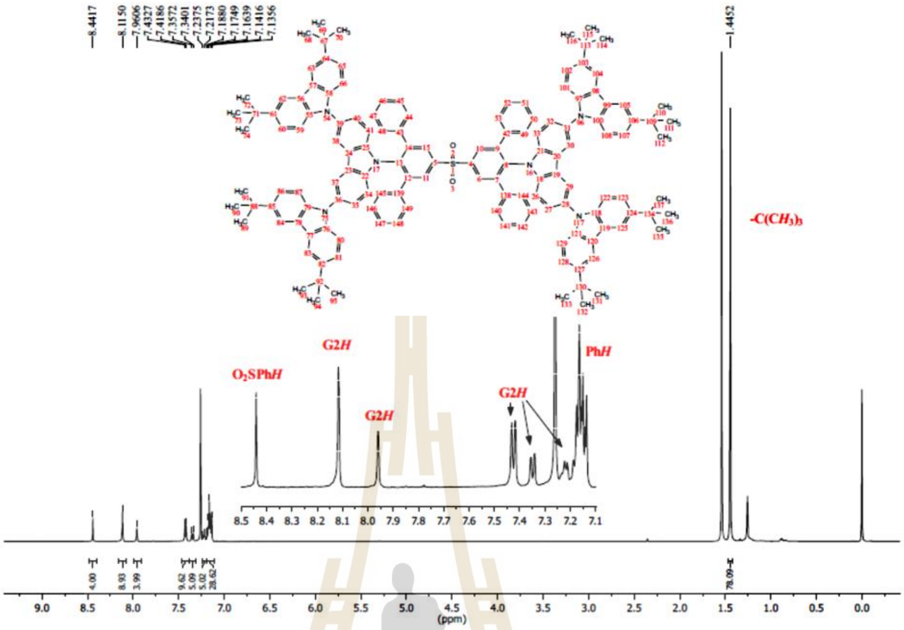

^{1}H-NMR (600 MHz, CDCl$_3$)

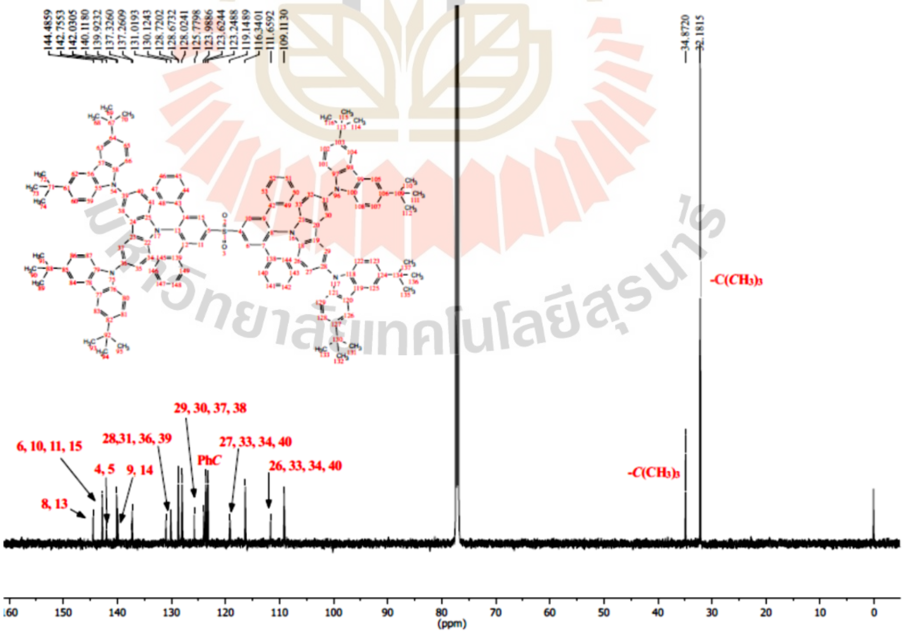

^{13}C-NMR (150 MHz, CDCl$_3$)

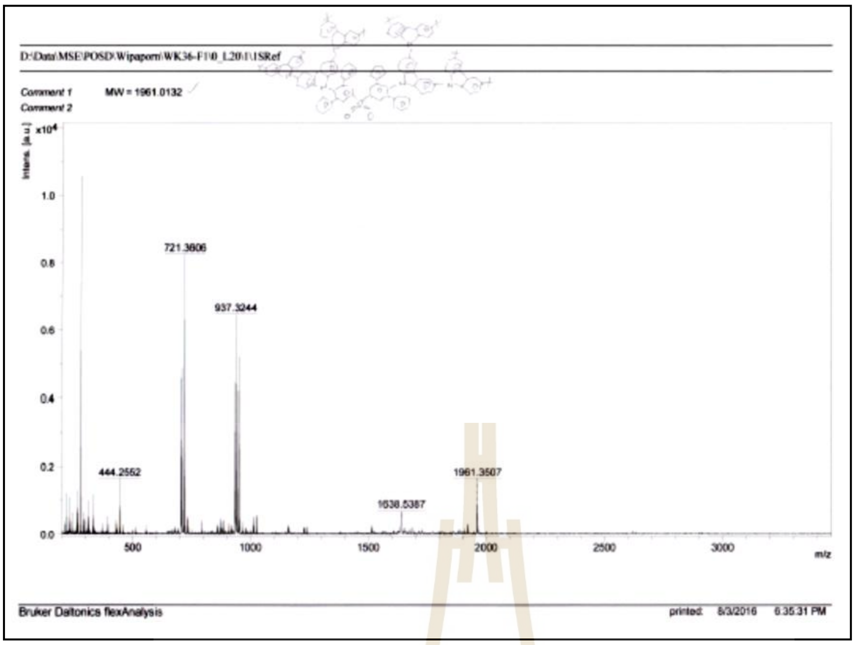

D:\Data\MSE\POSD\Wipaporn\WK36-F1\0_L20\1\1SRef

Comment 1 MW = 1961.0132

Comment 2

Bruker Daltonics flexAnalysis printed: 8/3/2016 6:35:31 PM

MALDI-TOF

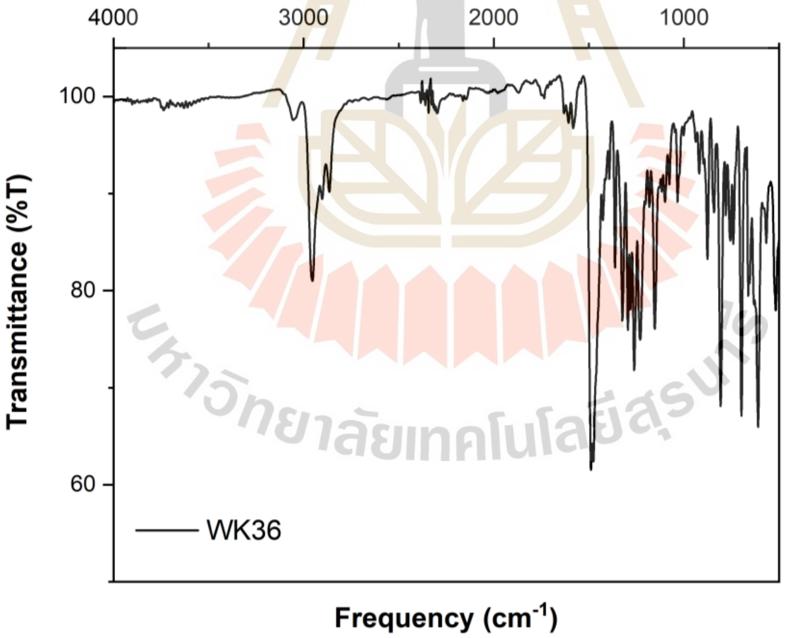

FT-IR

3,6-diPhCz-4Ph-DPS (12)

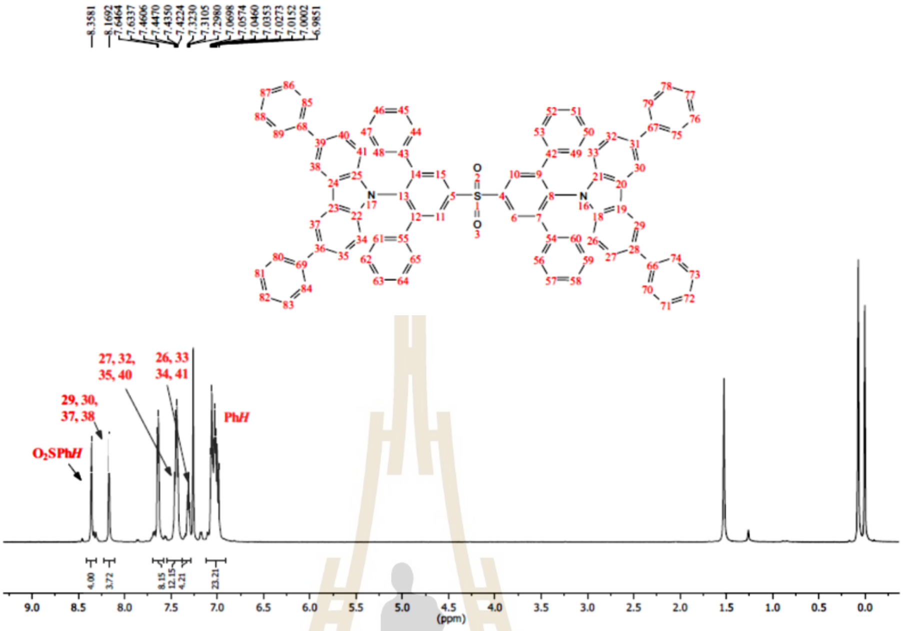

^{1}H-NMR (600 MHz, CDCl$_3$)

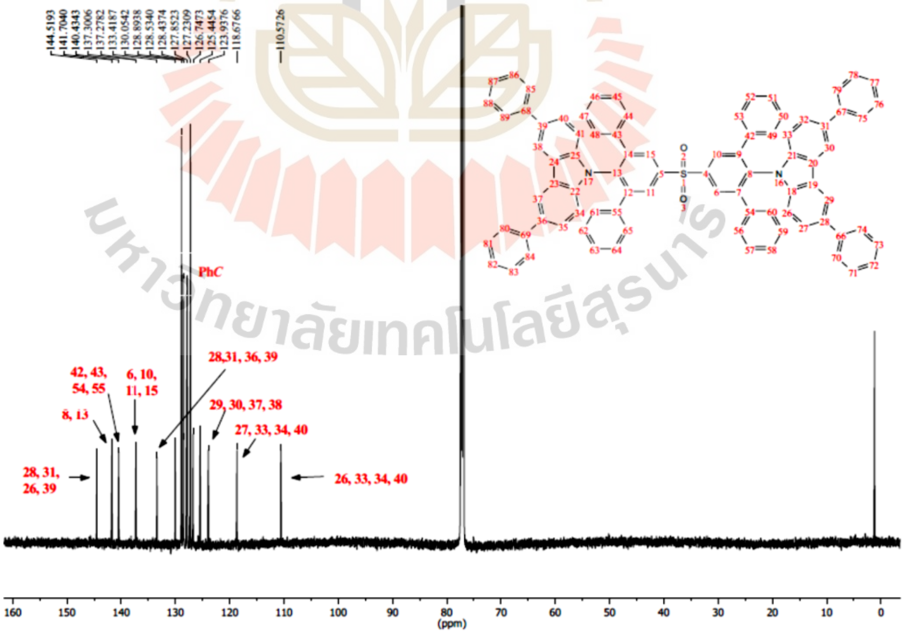

^{13}C-NMR (150 MHz, CDCl$_3$)

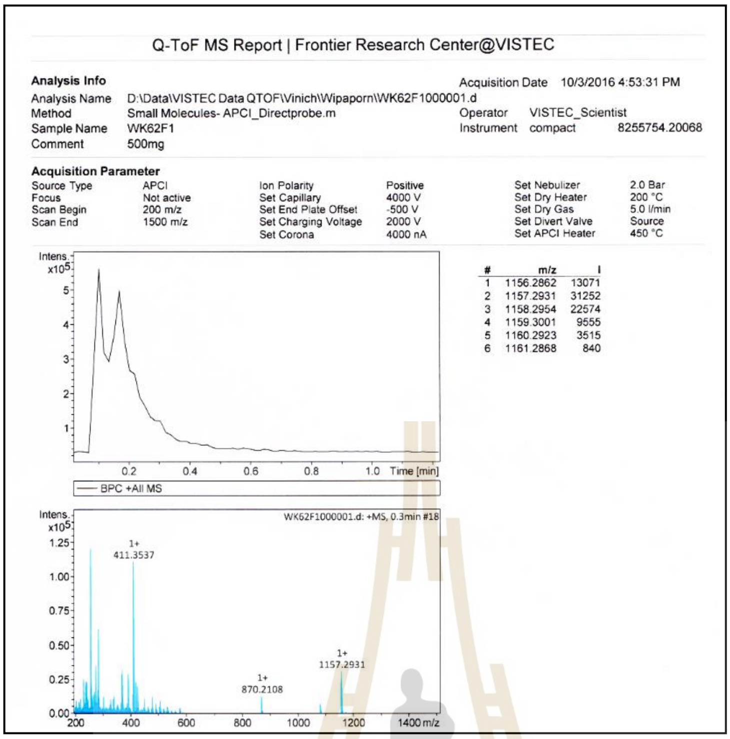

Q-ToF MS Report | Frontier Research Center@VISTEC

Analysis Info

Analysis Name	D:\Data\VISTEC Data QTOF\Vinich\Wipaporn\WK62F1000001.d	Acquisition Date	10/3/2016 4:53:31 PM
Method	Small Molecules- APCI_Directprobe.m	Operator	VISTEC_Scientist
Sample Name	WK62F1	Instrument	compact 8255754.20068
Comment	500mg		

Acquisition Parameter

Source Type	APCI	Ion Polarity	Positive	Set Nebulizer	2.0 Bar
Focus	Not active	Set Capillary	4000 V	Set Dry Heater	200 °C
Scan Begin	200 m/z	Set End Plate Offset	-500 V	Set Dry Gas	5.0 l/min
Scan End	1500 m/z	Set Charging Voltage	2000 V	Set Divert Valve	Source
		Set Corona	4000 nA	Set APCI Heater	450 °C

#	m/z	I
1	1156.2862	13071
2	1157.2931	31252
3	1158.2954	22574
4	1159.3001	9555
5	1160.2923	3515
6	1161.2868	840

Intens.
x10^5
5
4
3
2
1
0.2
0.4
0.6
0.8
1.0
Time [min]
BPC +All MS
Intens.
x10^5
WK62F1000001.d: +MS, 0.3min #18
1.25
1.00
0.75
0.50
0.25
0.00
1+
411.3537
1+
870.2108
1+
1157.2931
200
400
600
800
1000
1200
1400 m/z

APCI (Q-TOF)

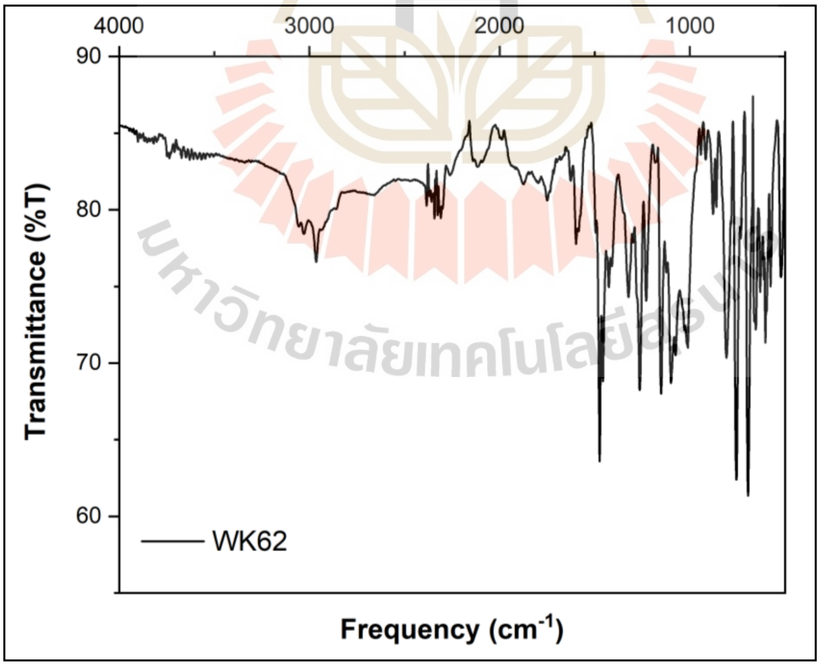

FT-IR

2,7-diPhCz-4Ph-DPS (13)

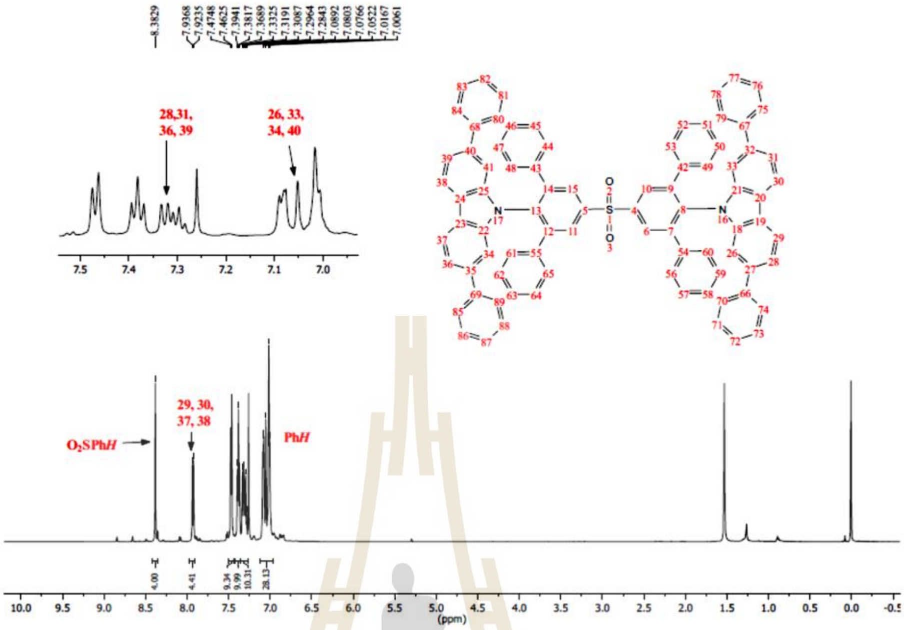

^{1}H-NMR (600 MHz, CDCl$_3$)

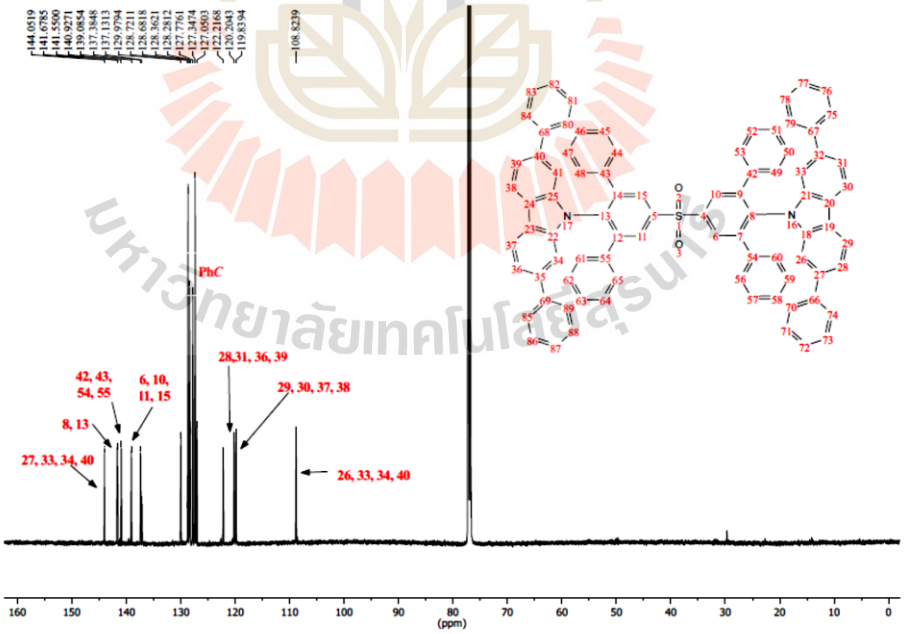

^{13}C-NMR (150 MHz, CDCl$_3$)

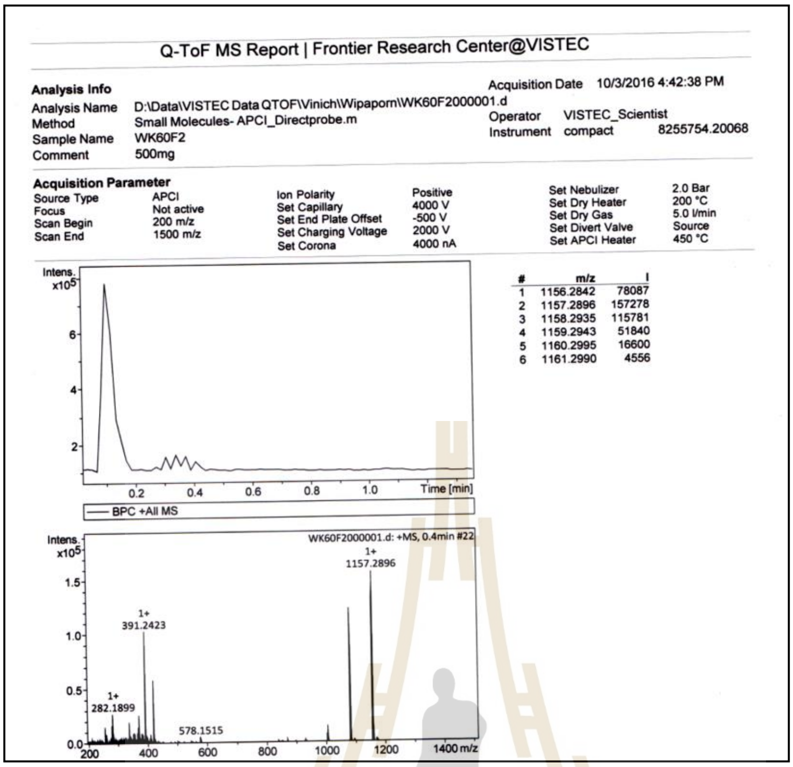

Q-ToF MS Report | Frontier Research Center@VISTEC

Analysis Info

Analysis Name D:\Data\VISTEC Data QTOF\Vinich\Wipaporn\WK60F2000001.d
Method Small Molecules- APCI_Directprobe.m
Sample Name WK60F2
Comment 500mg

Acquisition Date 10/3/2016 4:42:38 PM
Operator VISTEC_Scientist
Instrument compact 8255754.20068

Acquisition Parameter

Source Type APCI
Focus Not active
Scan Begin 200 m/z
Scan End 1500 m/z
Ion Polarity Positive
Set Capillary 4000 V
Set End Plate Offset -500 V
Set Charging Voltage 2000 V
Set Corona 4000 nA
Set Nebulizer 2.0 Bar
Set Dry Heater 200 °C
Set Dry Gas 5.0 l/min
Set Divert Valve Source
Set APCI Heater 450 °C

#	m/z	I
1	1156.2842	78087
2	1157.2896	157278
3	1158.2935	115781
4	1159.2943	51840
5	1160.2995	16600
6	1161.2990	4556

Intens.
x10^5
6
4
2
0.2
0.4
0.6
0.8
1.0
Time [min]
BPC +All MS
Intens.
x10^5
WK60F2000001.d: +MS, 0.4min #22
1+
1157.2896
1.5
1.0
0.5
0.0
1+
391.2423
1+
282.1899
578.1515
200
400
600
800
1000
1200
1400 m/z

APCI (Q-TOF)

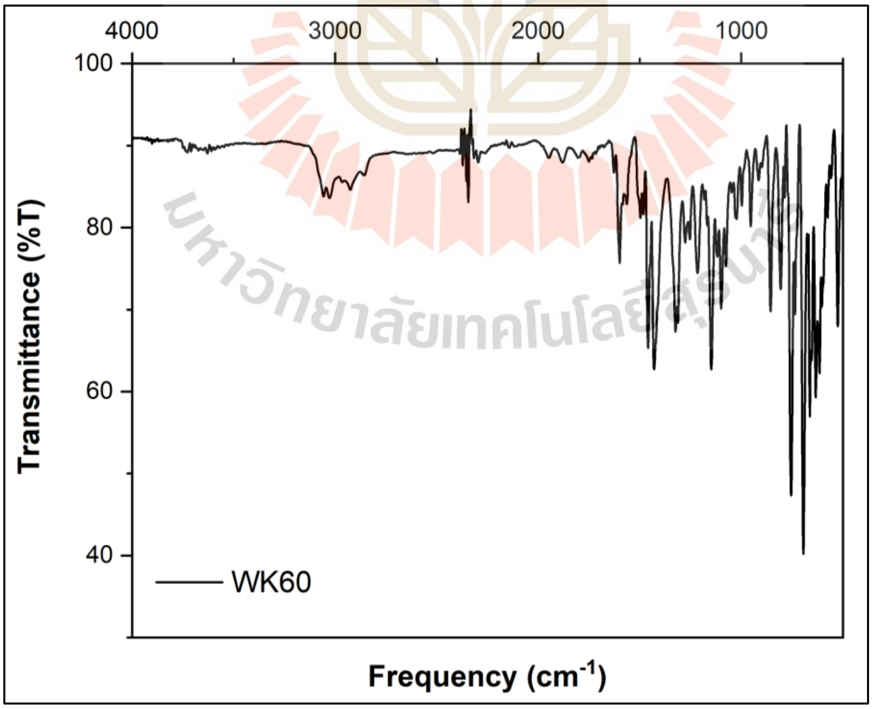

FT-IR

6.4.3 The synthesis of TADF dendrimers

Bis(4-(2,7-dibromocarbazole)phenyl) sulfone (160)

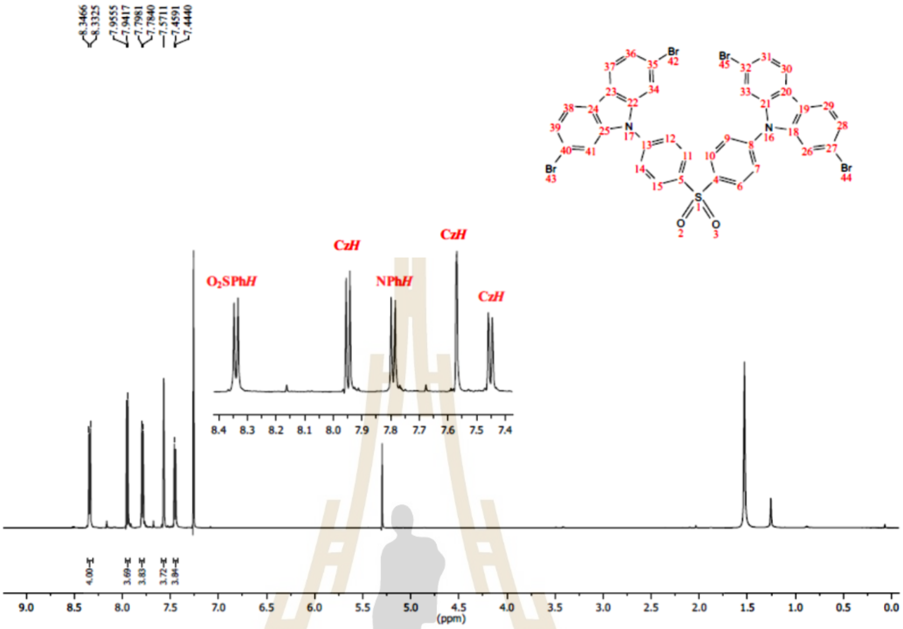

^{1}H-NMR (600 MHz, CDCl$_3$)

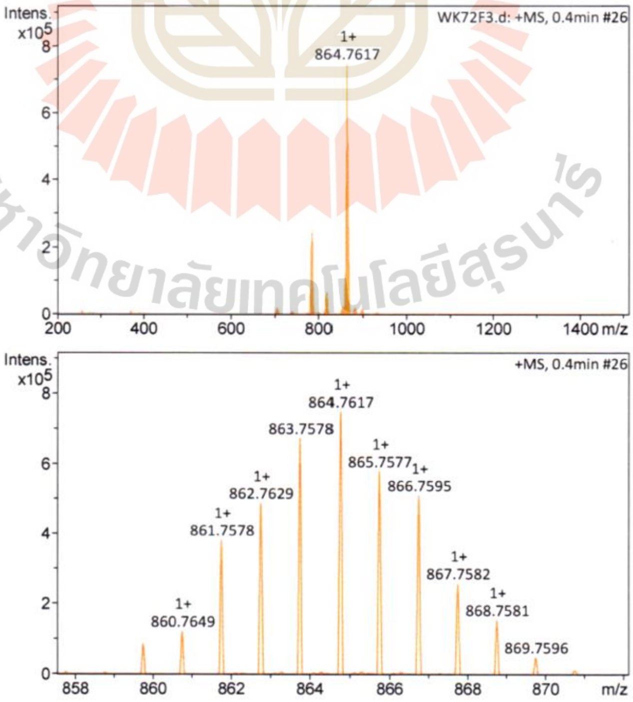

Q-TOF

2-bromo fluorene (162)

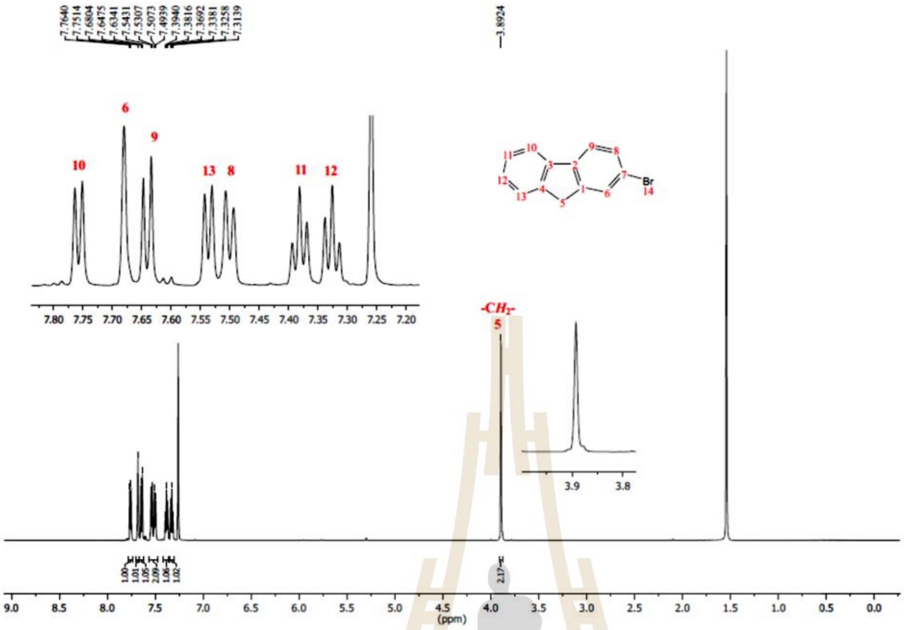

^{1}H-NMR (600 MHz, CDCl$_3$)

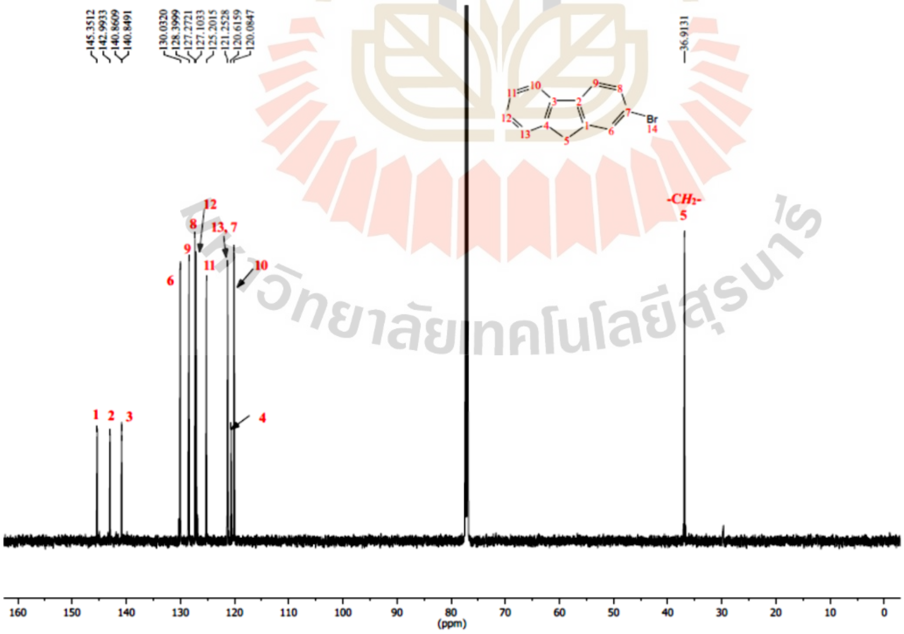

^{13}C-NMR (150 MHz, CDCl$_3$)

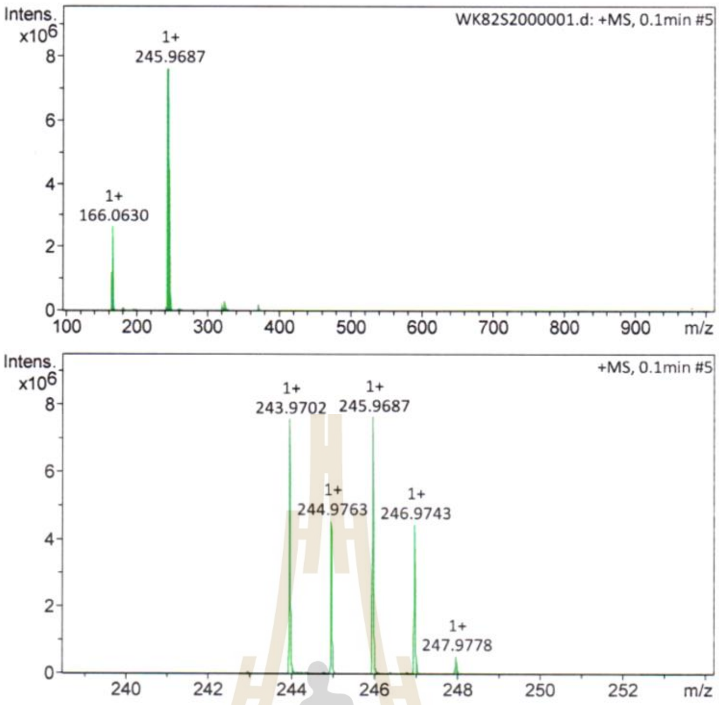

Q-TOF

Dibromohexyl-2-bromo fluorene (164)

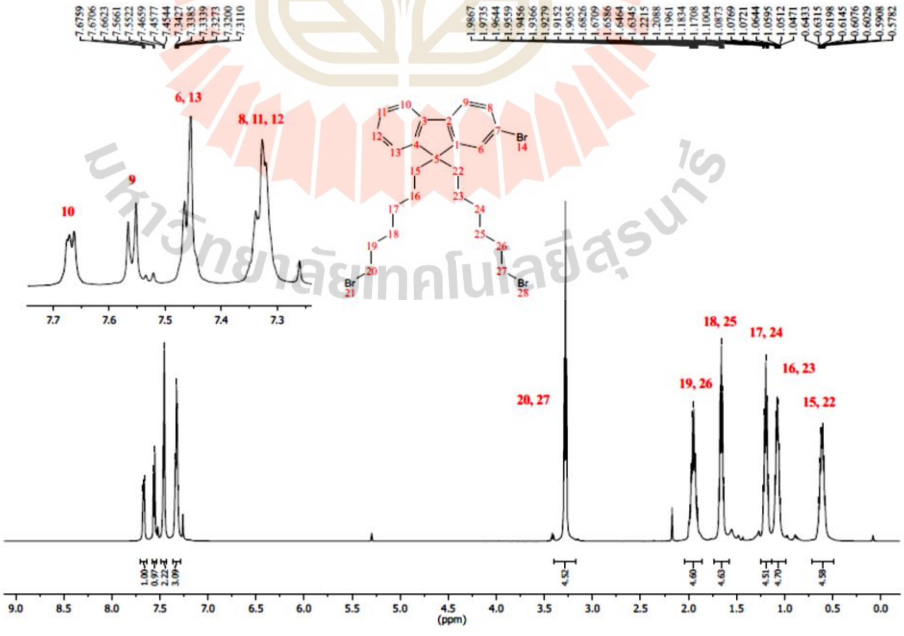

^{1}H-NMR (600 MHz, $CDCl_3$)

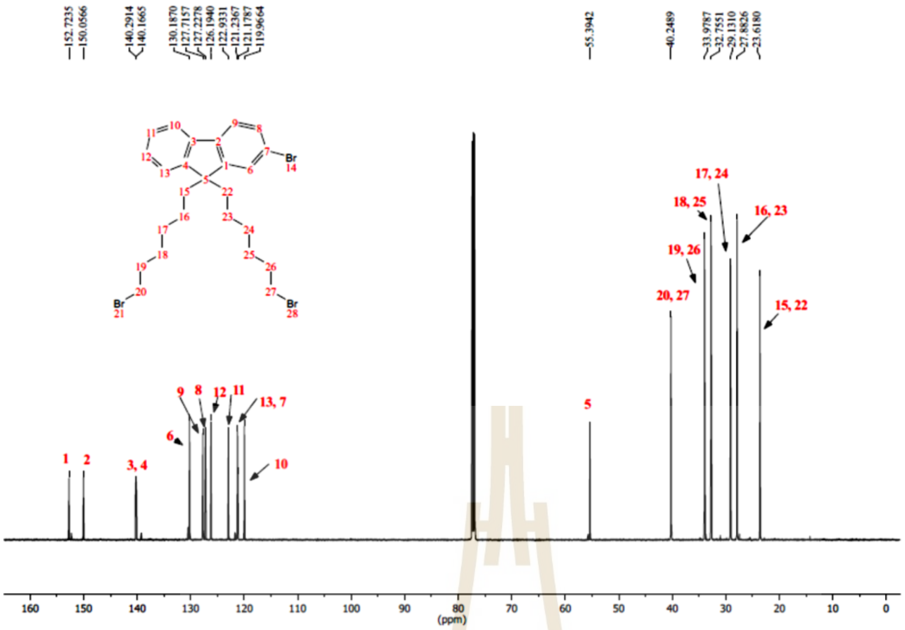

^{13}C-NMR (150 MHz, $CDCl_3$)

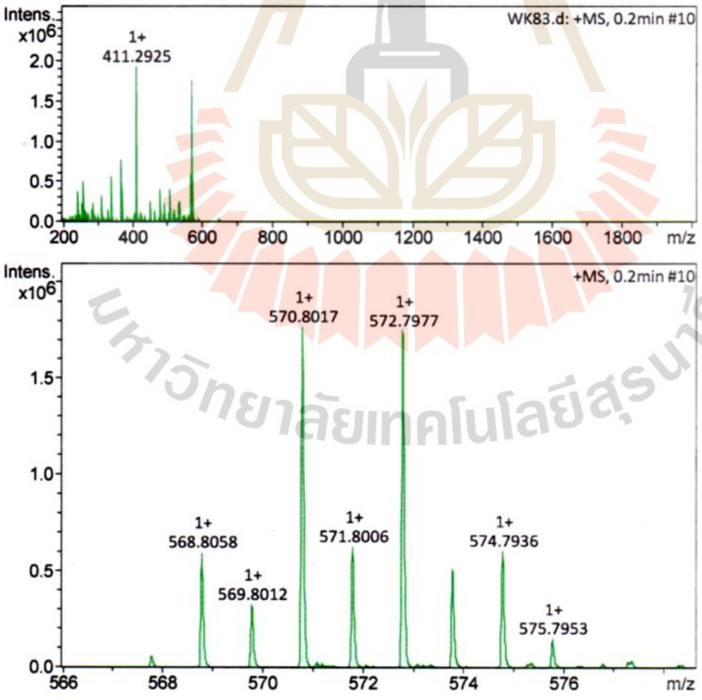

Q-TOF

G1hexyl-2-bromo fluorene (165)

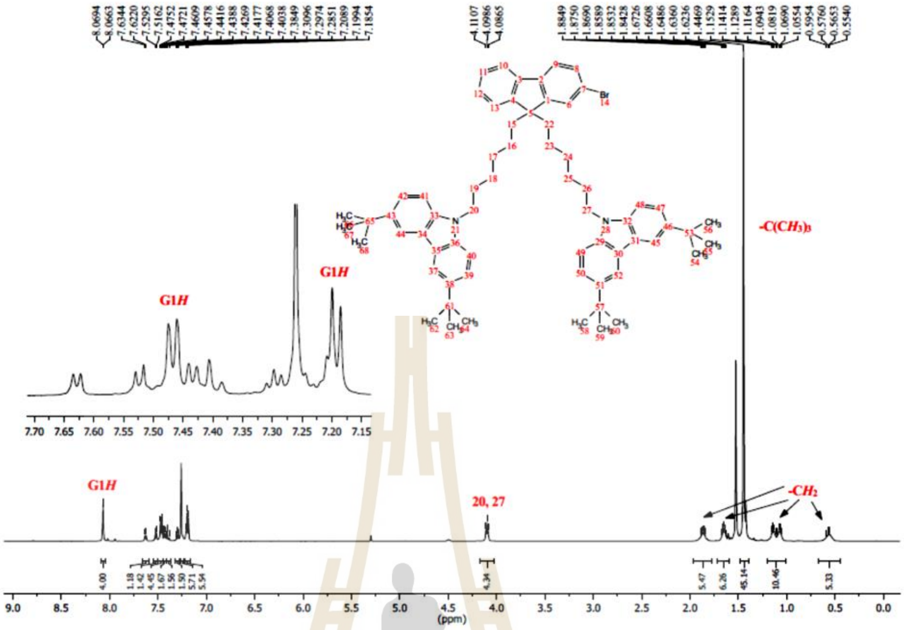

^{1}H-NMR (600 MHz, $CDCl_3$)

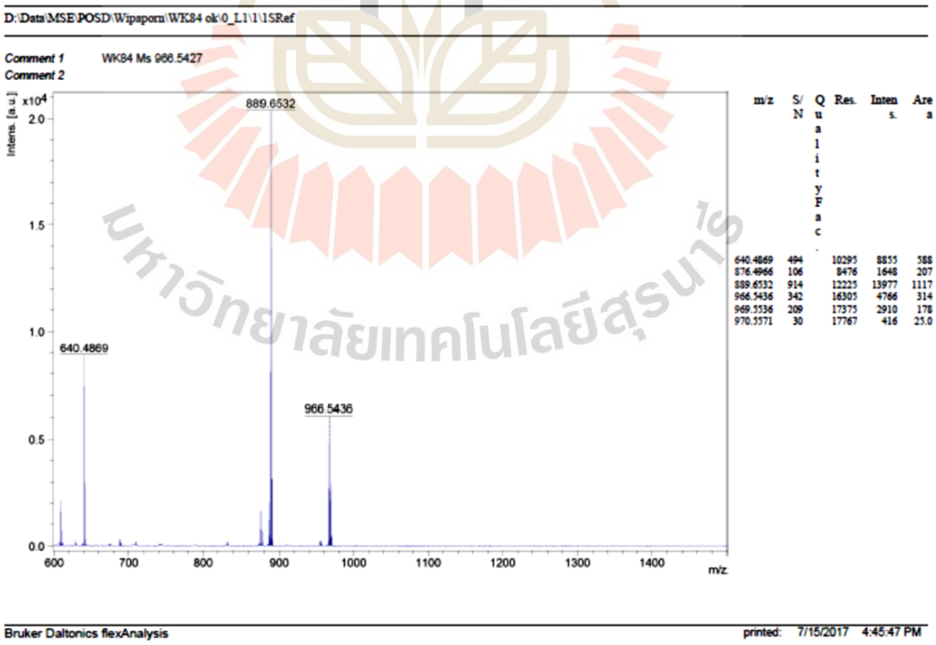

D:\Data\MSE\POSD\Wipaporn\WK84 ok\0_L1\1\1SRef

Comment 1 WK84 Ms 966.5427
Comment 2

m/z	S/N	QualityFac.	Res.	Intens.	Area
640.4869	494		10295	8855	588
876.4966	106		8476	1648	207
889.6532	914		12225	13977	1117
966.5436	342		16305	4766	314
969.5536	209		17375	2910	178
970.5571	30		17767	416	25.0

Bruker Daltonics flexAnalysis printed: 7/15/2017 4:45:47 PM

MALDI-TOF

TPA-2-bromo fluorene (167)

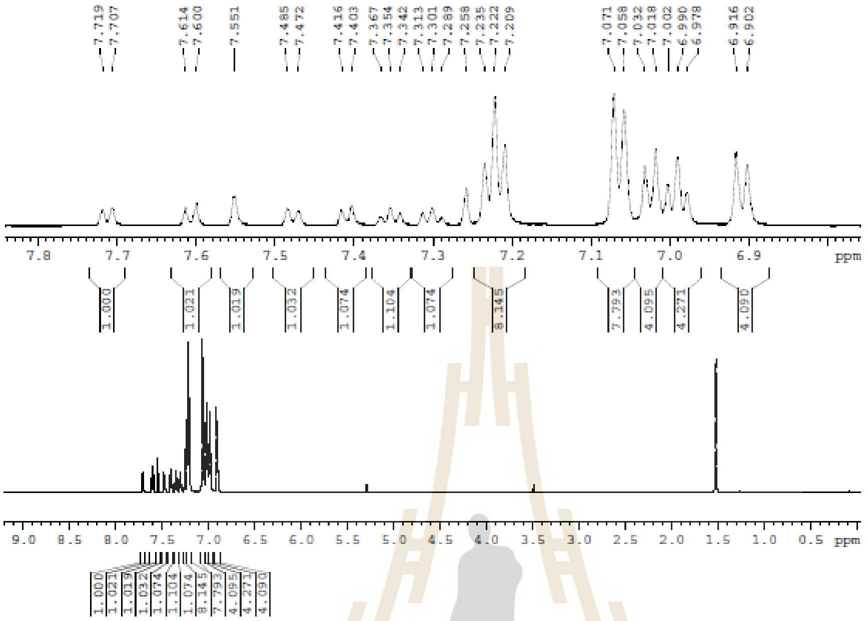

^{1}H-NMR (600 MHz, CDCl$_3$)

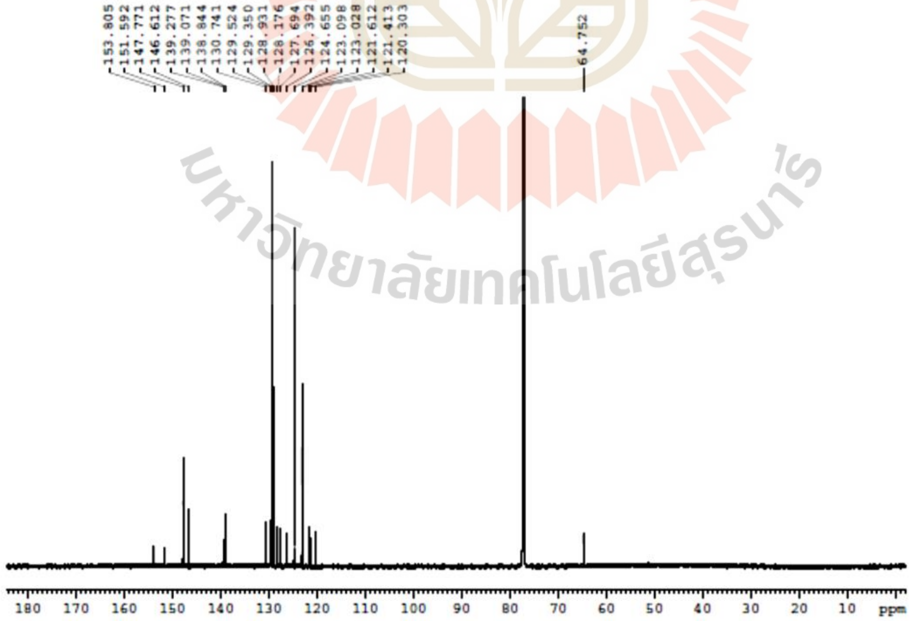

^{13}C-NMR (150 MHz, CDCl$_3$)

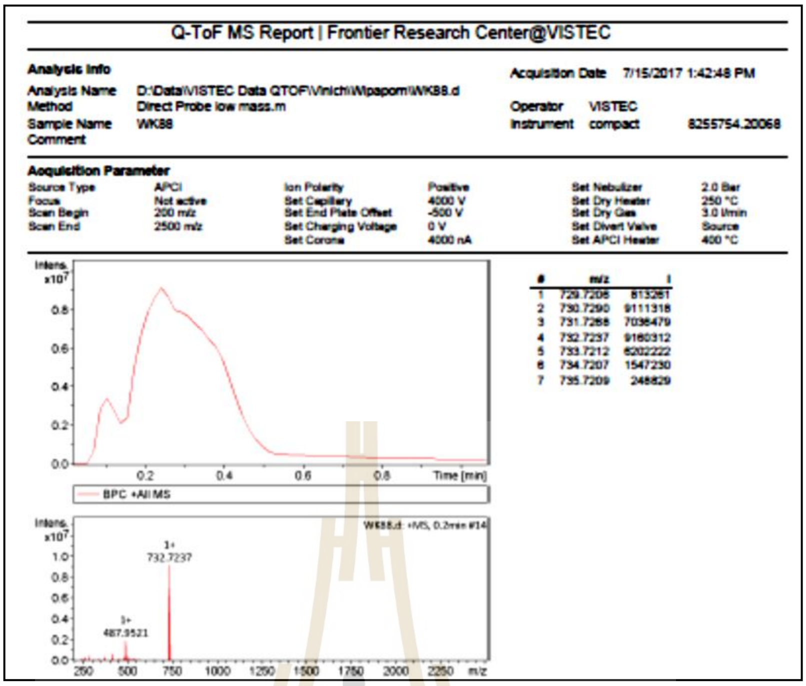

Q-ToF MS Report | Frontier Research Center@VISTEC

Analysis Info

Analysis Name D:\Data\VISTEC Data QTOF\Vinich\Wipaporn\WK88.d
Method Direct Probe low mass.m
Sample Name WK88
Comment

Acquisition Date 7/15/2017 1:42:48 PM

Operator VISTEC
Instrument compact 8255754.20068

Acquisition Parameter

Source Type	APCI	Ion Polarity	Positive	Set Nebulizer	2.0 Bar
Focus	Not active	Set Capillary	4000 V	Set Dry Heater	250 °C
Scan Begin	200 m/z	Set End Plate Offset	-500 V	Set Dry Gas	3.0 l/min
Scan End	2500 m/z	Set Charging Voltage	0 V	Set Divert Valve	Source
		Set Corona	4000 nA	Set APCI Heater	400 °C

#	m/z	I
1	729.7206	813261
2	730.7290	9111318
3	731.7268	7036479
4	732.7237	9160312
5	733.7212	6202222
6	734.7207	1547230
7	735.7209	248829

Intens. x10^7
0.8
0.6
0.4
0.2
0.0
0.2
0.4
0.6
0.8
Time [min]
BPC +All MS
Intens. x10^7
WK88.d: +MS, 0.2min #14
1+
732.7237
1+
487.9521
1.0
0.8
0.6
0.4
0.2
0.0
250
500
750
1000
1250
1500
1750
2000
2250
m/z

Q-TOF

G1hexyl fluorene boronate (170)

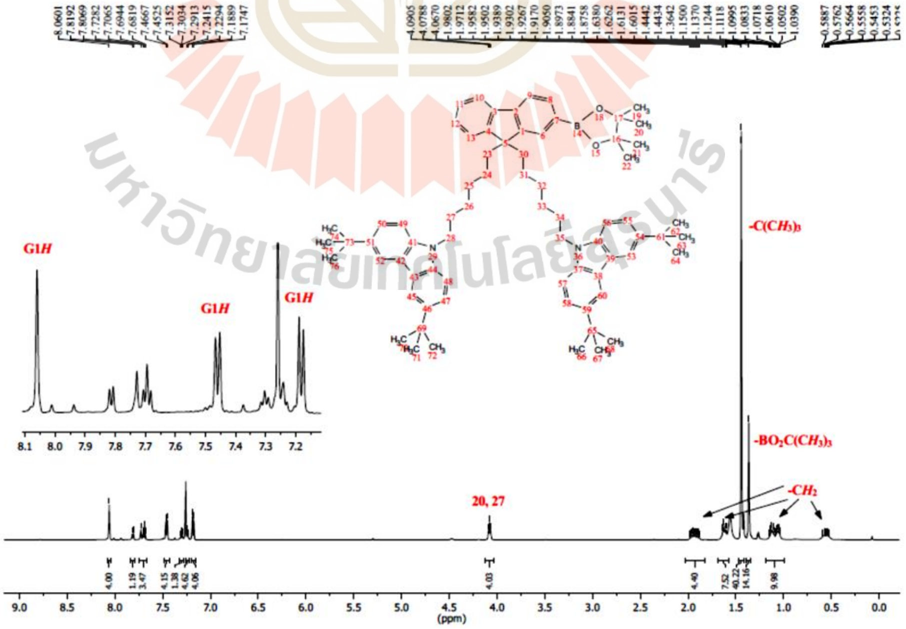

^{1}H-NMR (600 MHz, CDCl$_3$)

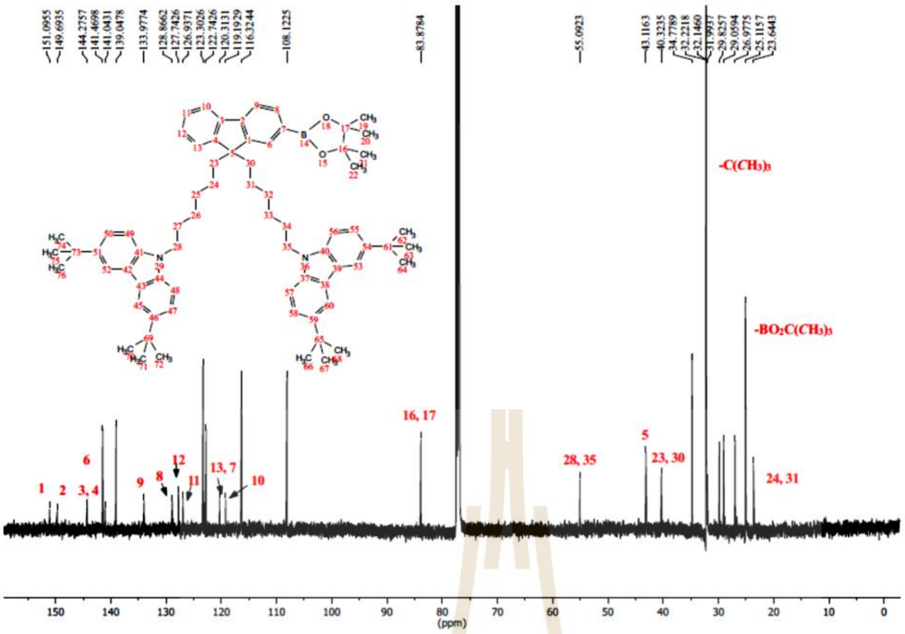

^{13}C-NMR (150 MHz, CDCl$_3$)

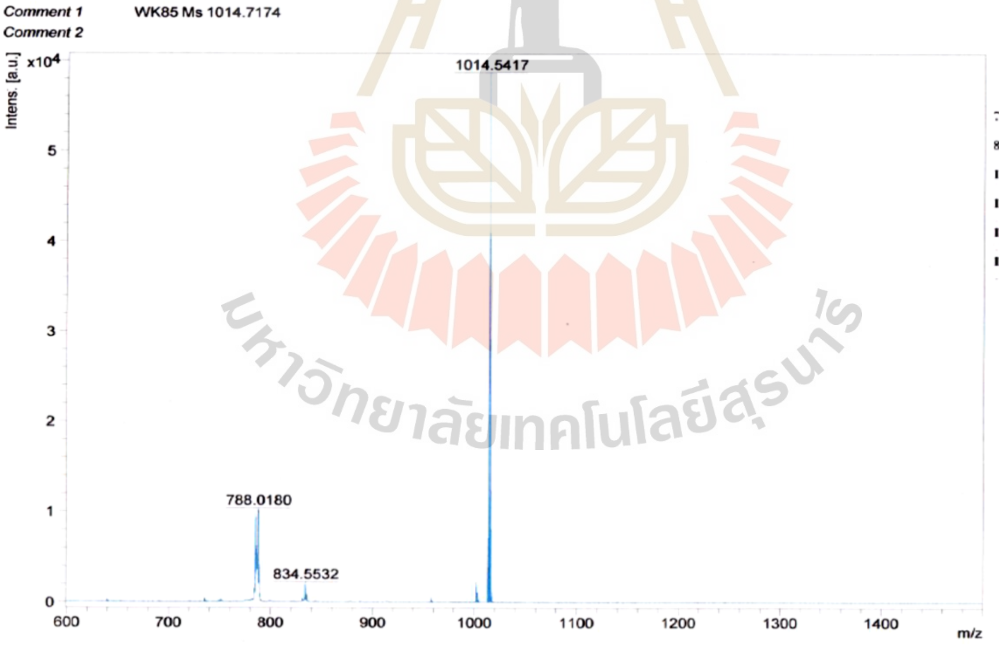

MALDI-TOF

TPA fluorene boronate (172)

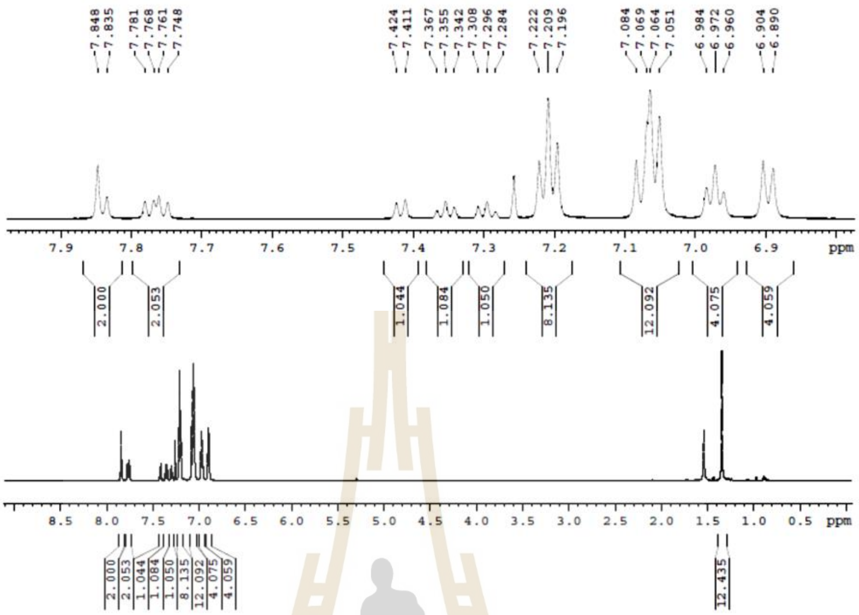

^{1}H-NMR (600 MHz, $CDCl_3$)

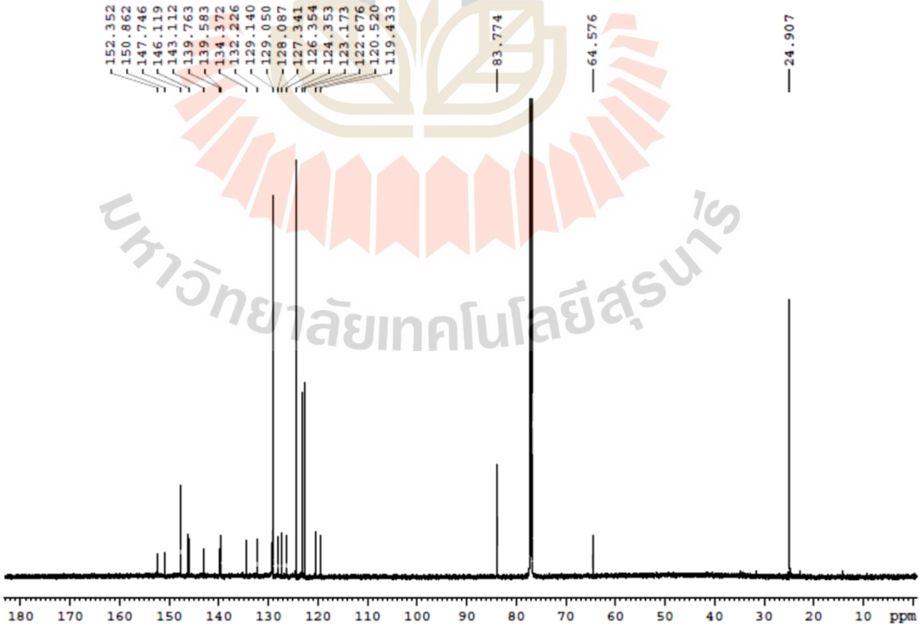

^{13}C-NMR (150 MHz, $CDCl_3$)

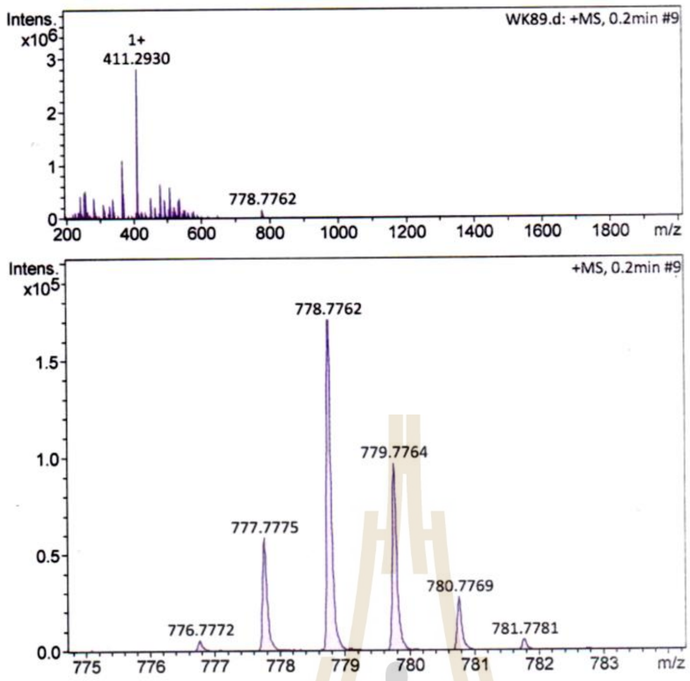

Q-TOF

TADF dendrimers (14)

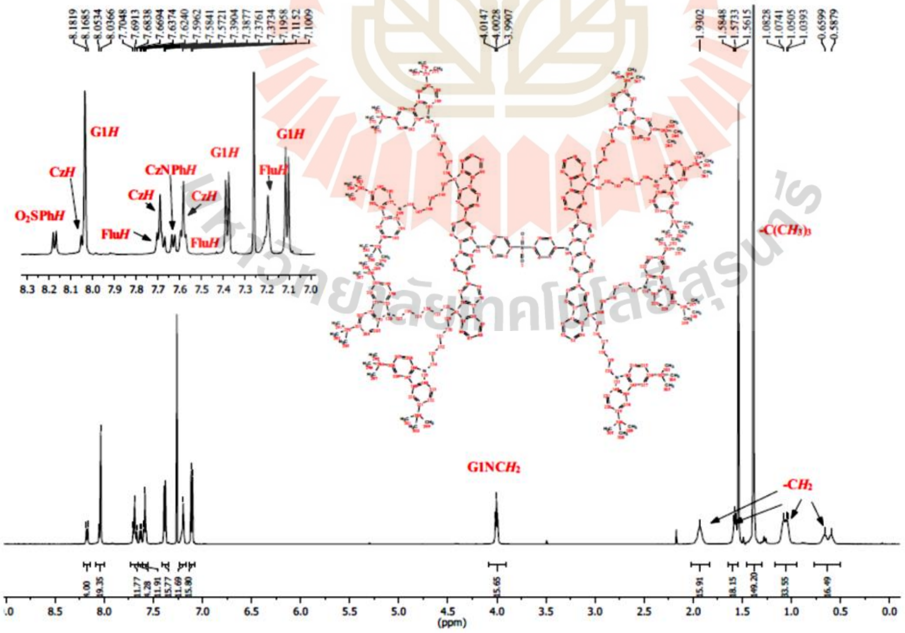

^{1}H-NMR (600 MHz, $CDCl_3$)

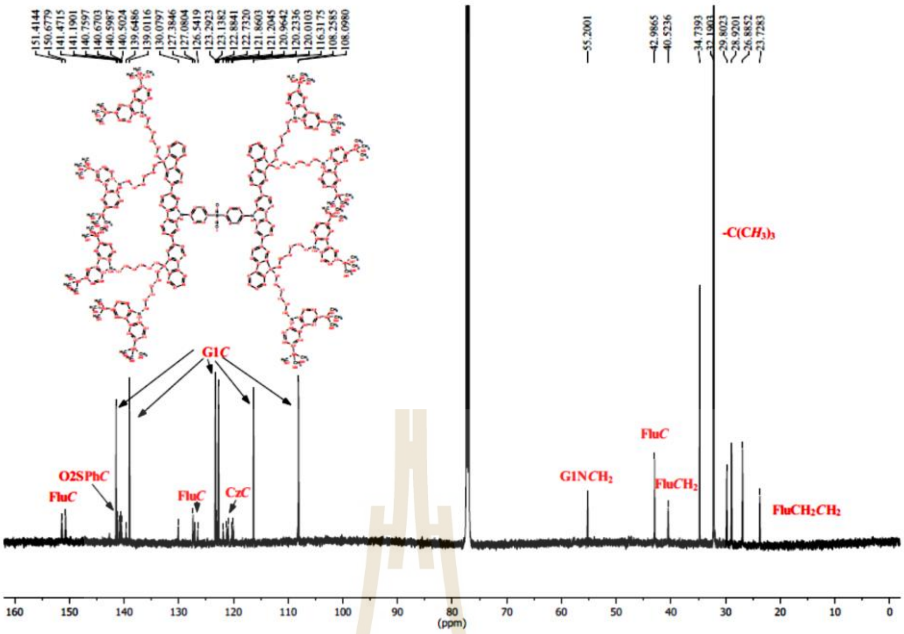

^{13}C-NMR (150 MHz, CDCl$_3$)

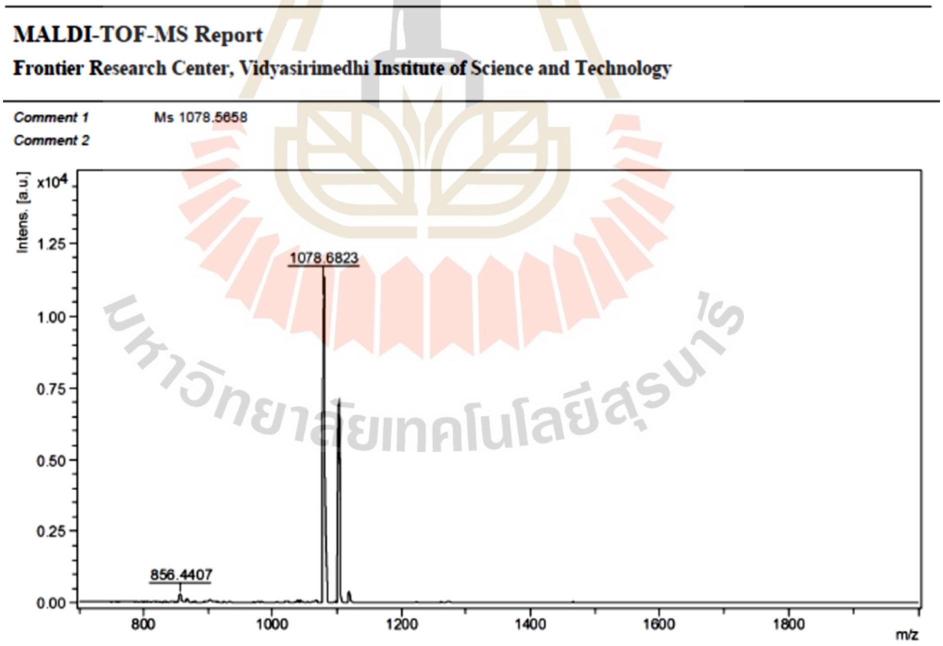

MALDI-TOF-MS Report

Frontier Research Center, Vidyasirimedhi Institute of Science and Technology

Comment 1 Ms 1078.5658

Comment 2

MALDI-TOF

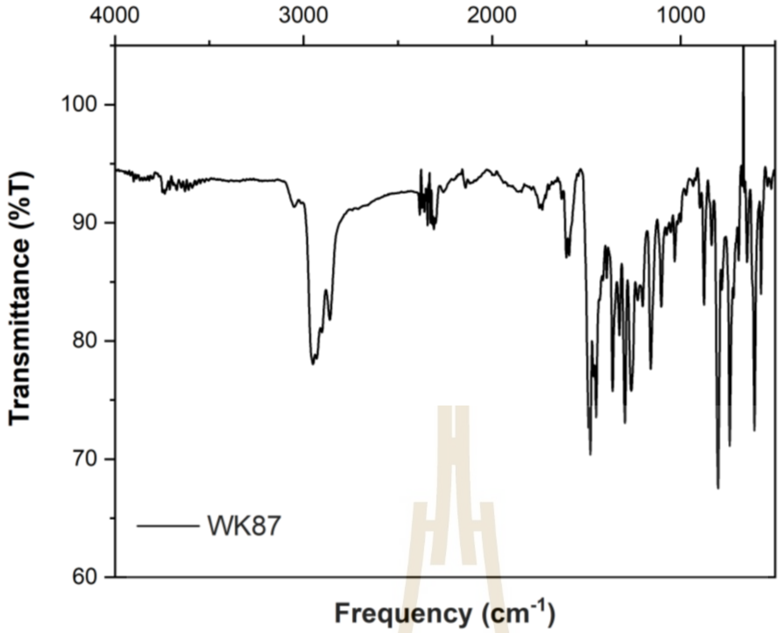

FT-IR

TADF dendrimers (15)

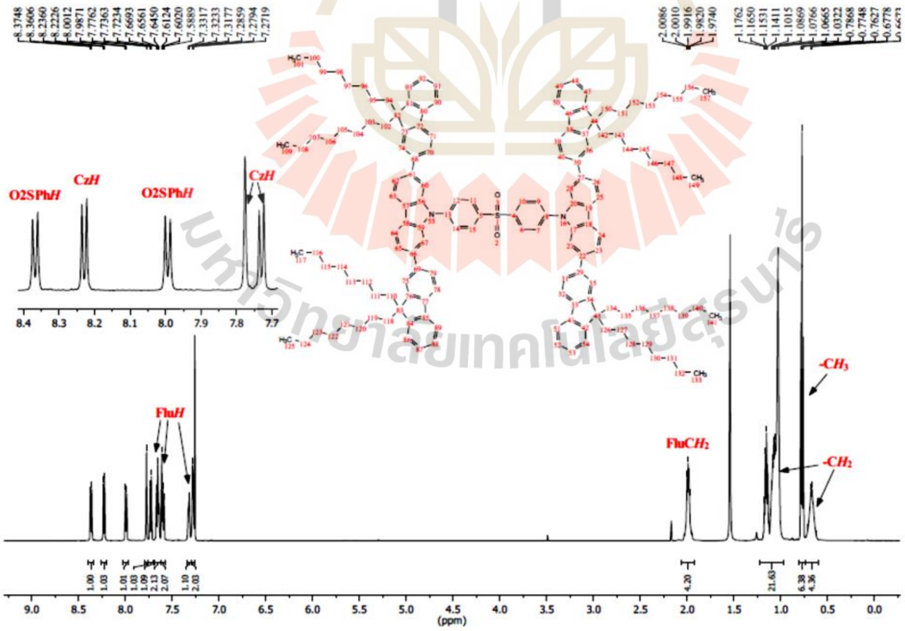

^{1}H-NMR (600 MHz, $CDCl_3$)

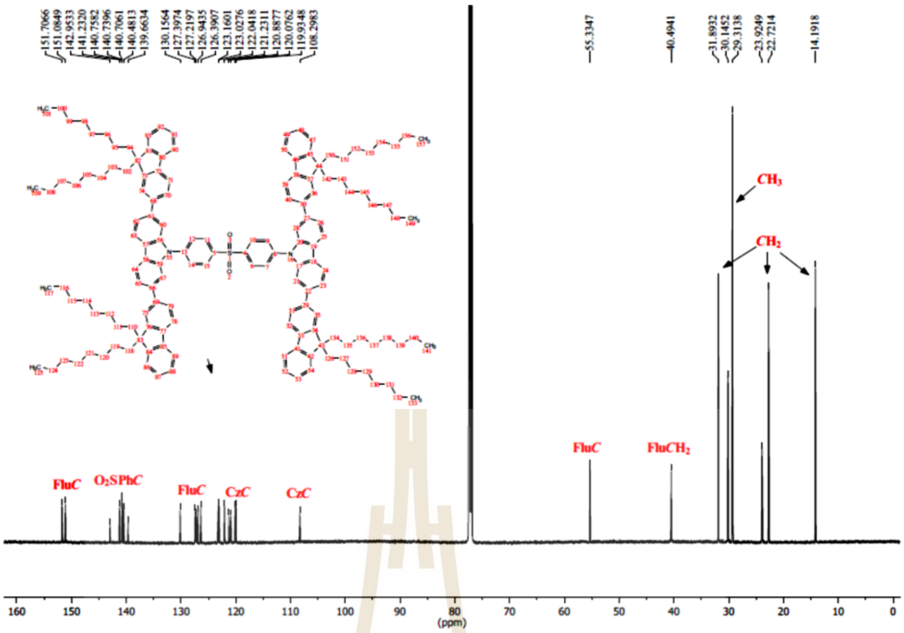

^{13}C-NMR (150 MHz, CDCl$_3$)

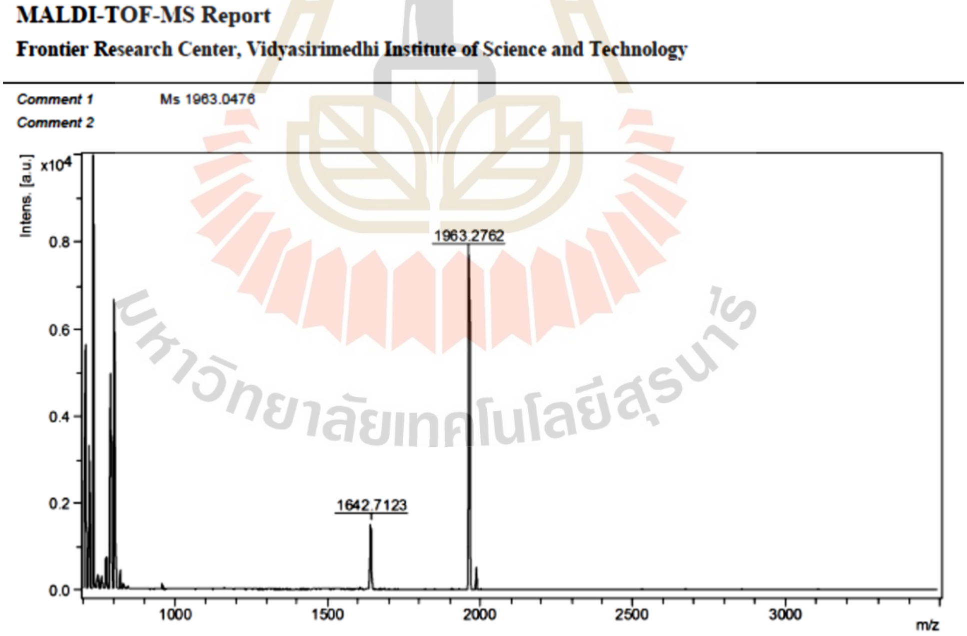

MALDI-TOF-MS Report

Frontier Research Center, Vidyasirimedhi Institute of Science and Technology

Comment 1 Ms 1963.0476

Comment 2

MALDI-TOF

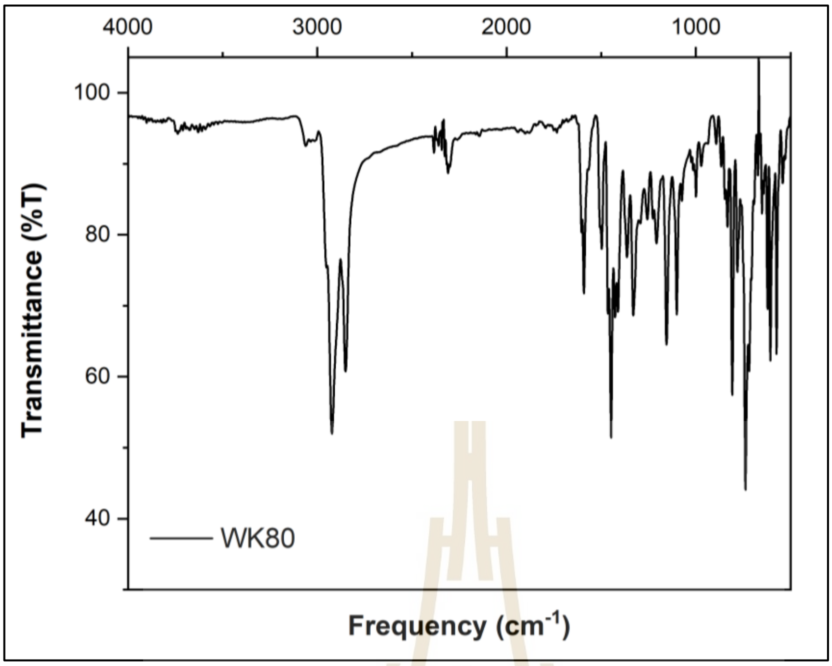

FT-IR

TADF dendrimers (16)

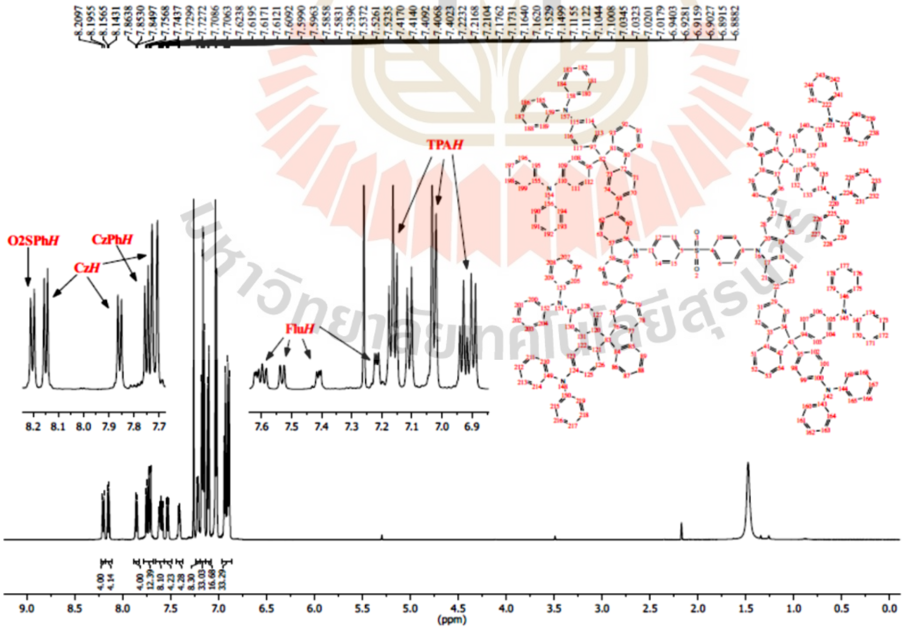

^{1}H-NMR (600 MHz, $CDCl_3$)

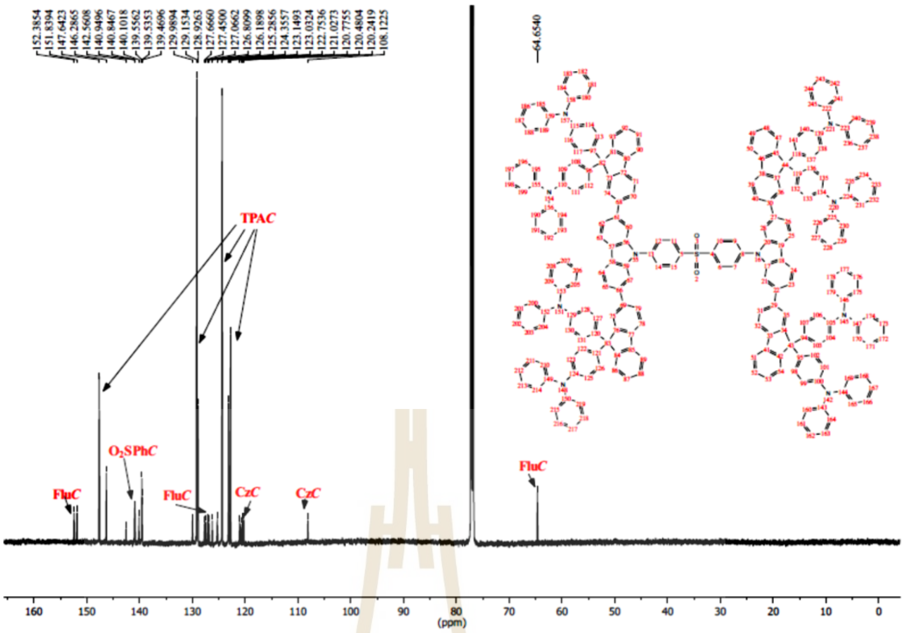

^{13}C-NMR (150 MHz, $CDCl_3$)

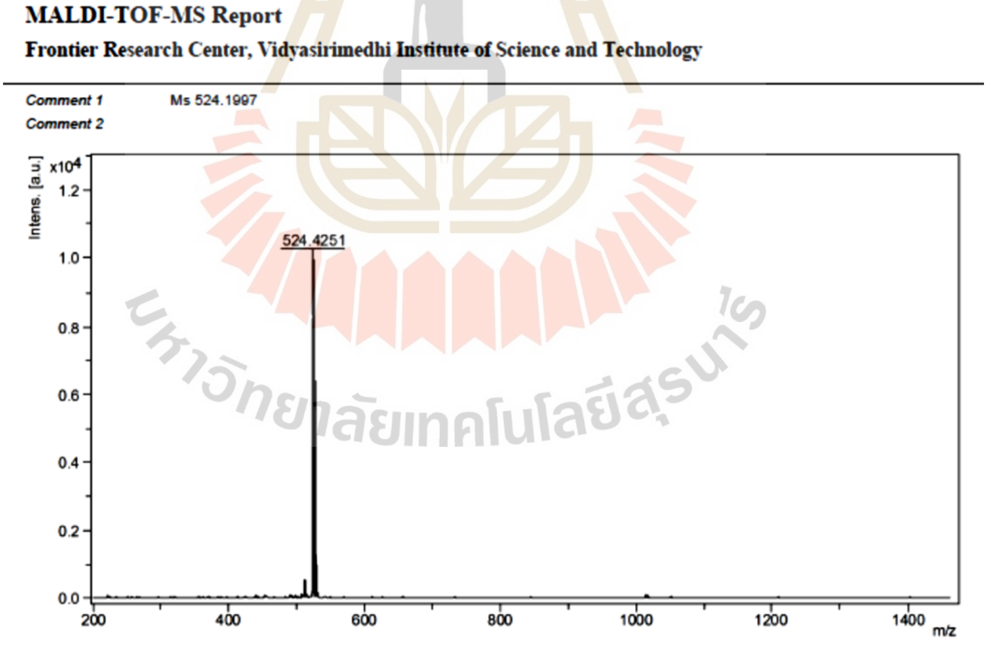

MALDI-TOF-MS Report

Frontier Research Center, Vidyasirimedhi Institute of Science and Technology

Comment 1 Ms 524.1997

Comment 2

MALDI-TOF

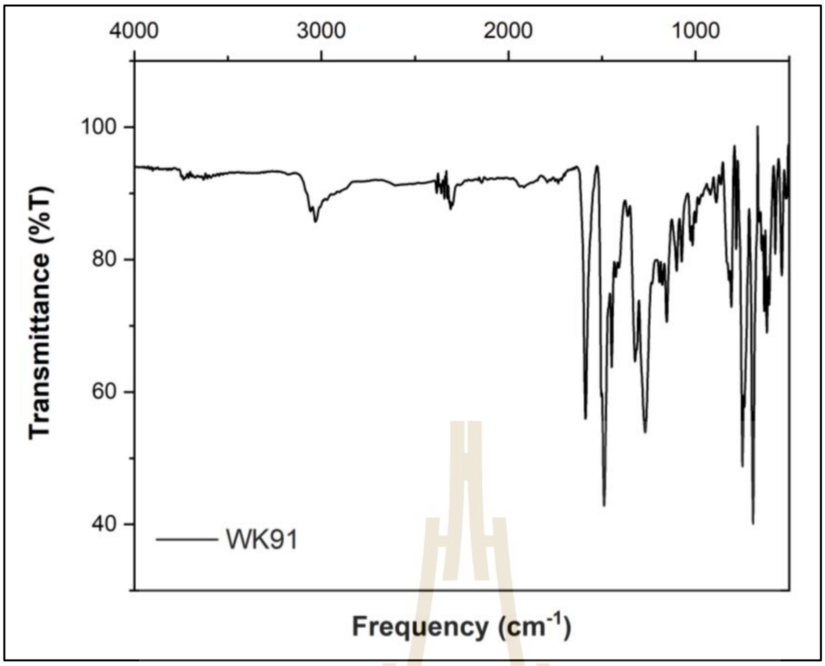

FT-IR

6.4.4 The synthesis of AIE emitters

TPEH dioxaborolane (202)

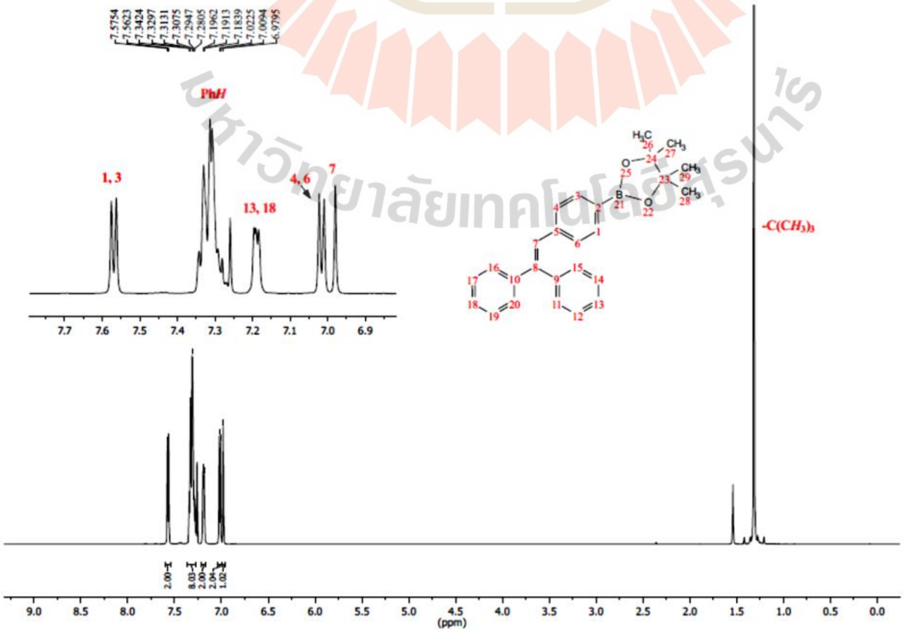

^{1}H-NMR (600 MHz, $CDCl_3$)

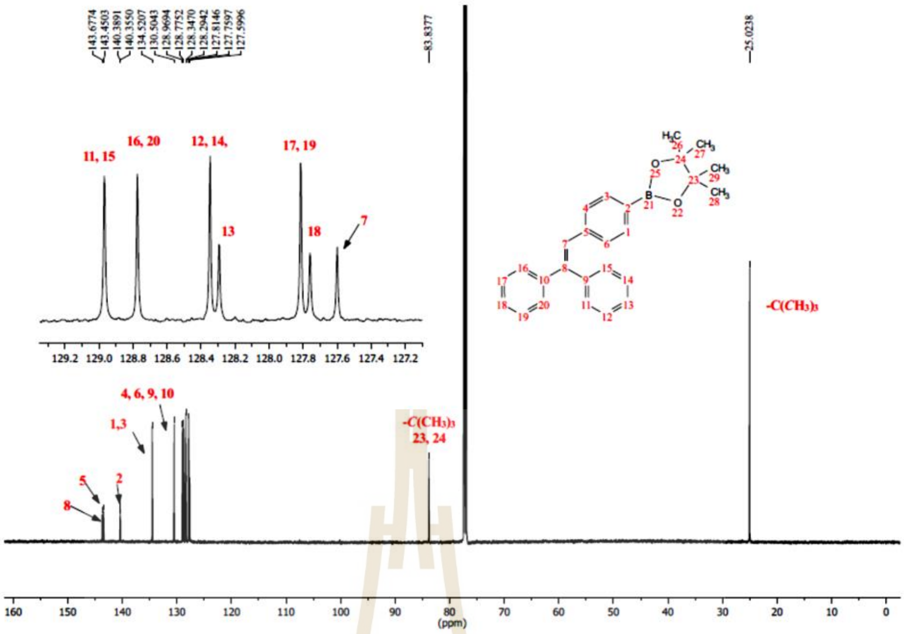

^{13}C-NMR (150 MHz, $CDCl_3$)

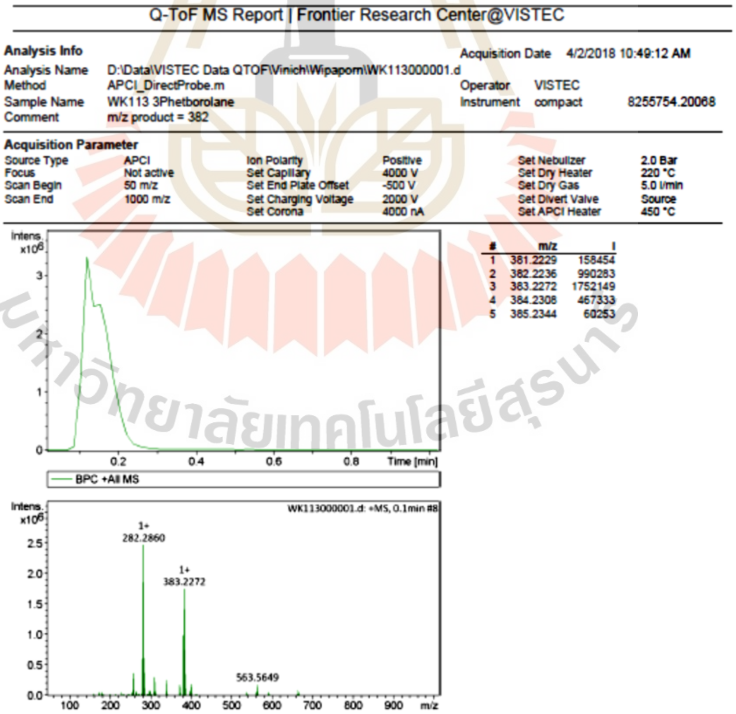

Q-ToF MS Report | Frontier Research Center@VISTEC

Analysis Info

Analysis Name D:\Data\VISTEC Data QTOF\Vinich\Wipaporn\WK113000001.d
Method APCI_DirectProbe.m
Sample Name WK113 3Phetborolane
Comment m/z product = 382

Acquisition Date 4/2/2018 10:49:12 AM
Operator VISTEC
Instrument compact 8255754.20068

Acquisition Parameter

Source Type	APCI	Ion Polarity	Positive	Set Nebulizer	2.0 Bar
Focus	Not active	Set Capillary	4000 V	Set Dry Heater	220 °C
Scan Begin	50 m/z	Set End Plate Offset	-500 V	Set Dry Gas	5.0 l/min
Scan End	1000 m/z	Set Charging Voltage	2000 V	Set Divert Valve	Source
		Set Corona	4000 nA	Set APCI Heater	450 °C

#	m/z	I
1	381.2229	158454
2	382.2236	990283
3	383.2272	1752149
4	384.2308	467333
5	385.2344	60253

Intens.
x10^6
3
2
1
0
0.2
0.4
0.6
0.8
Time [min]
BPC +All MS
Intens.
x10^6
WK113000001.d: +MS, 0.1min #8
1+
282.2860
1+
383.2272
563.5649
2.5
2.0
1.5
1.0
0.5
0.0
100 200 300 400 500 600 700 800 900 m/z

Q-TOF

TPE dioxaborolane (203)

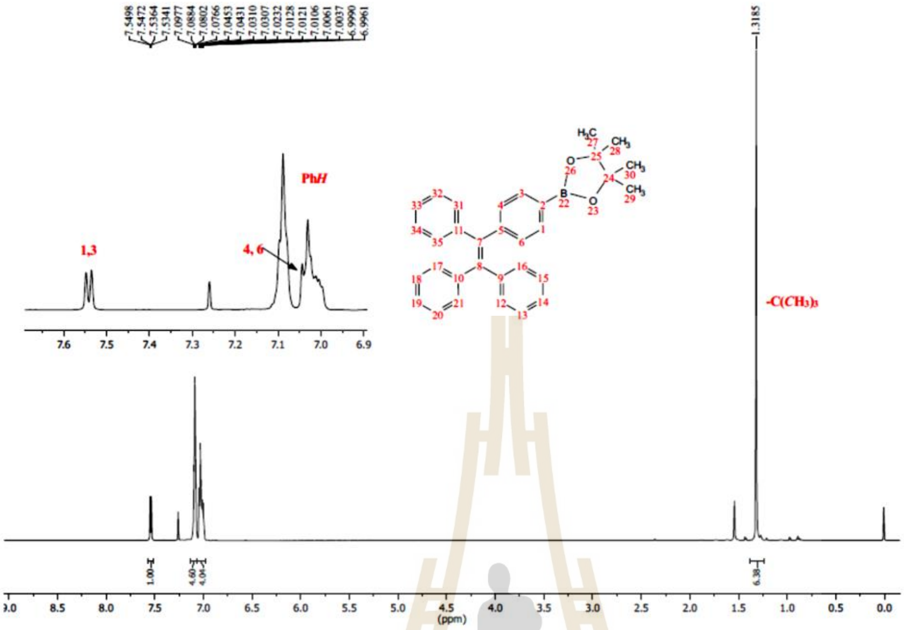

^{1}H-NMR (600 MHz, CDCl$_3$)

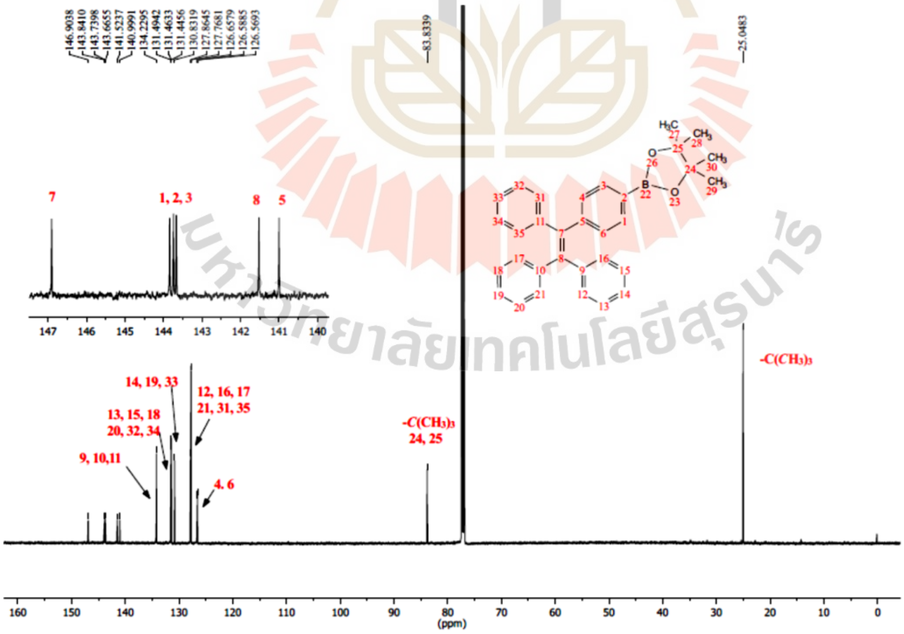

^{13}C-NMR (150 MHz, CDCl$_3$)

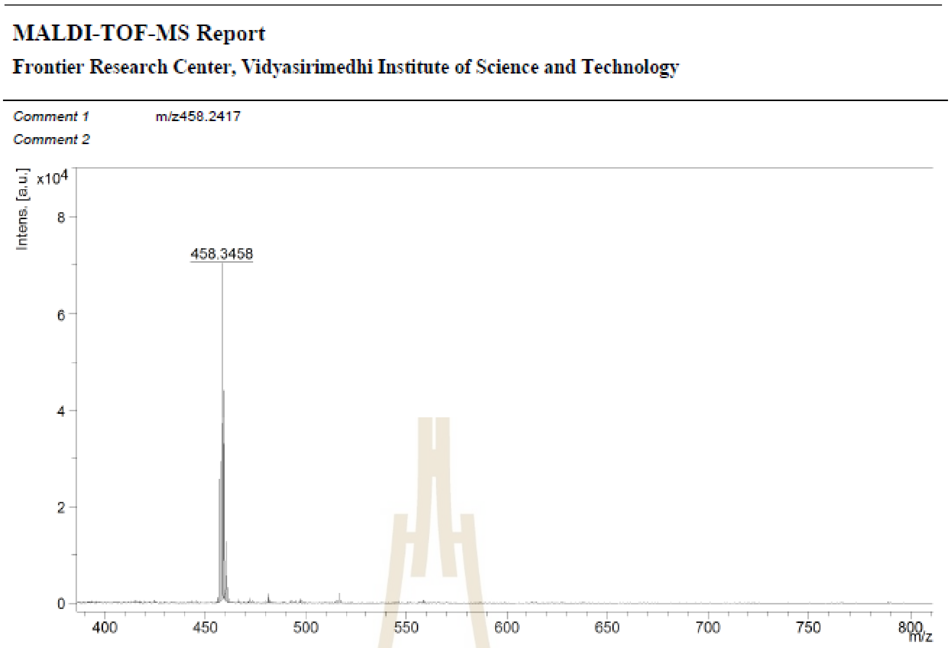

MALDI-TOF-MS Report
Frontier Research Center, Vidyasirimedhi Institute of Science and Technology

Comment 1 m/z458.2417
Comment 2

MALDI-TOF

BT-2TPE (17)

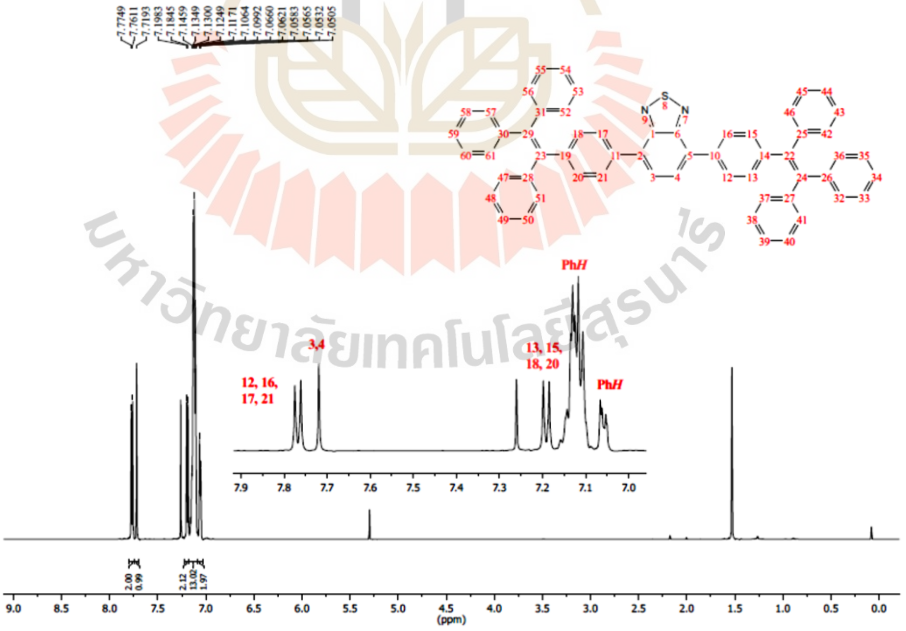

^{1}H-NMR (600 MHz, CDCl$_3$)

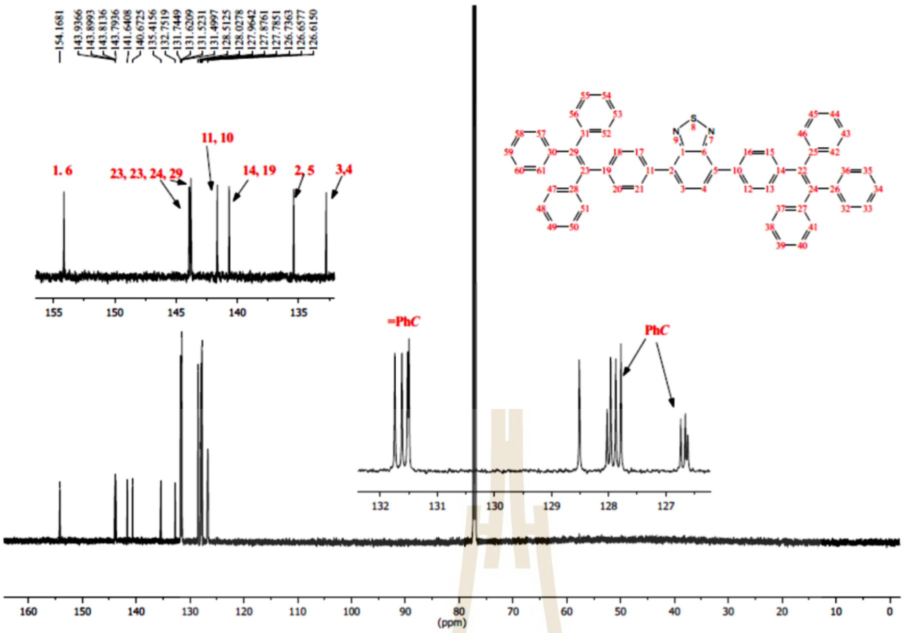

^{13}C-NMR (150 MHz, CDCl$_3$)

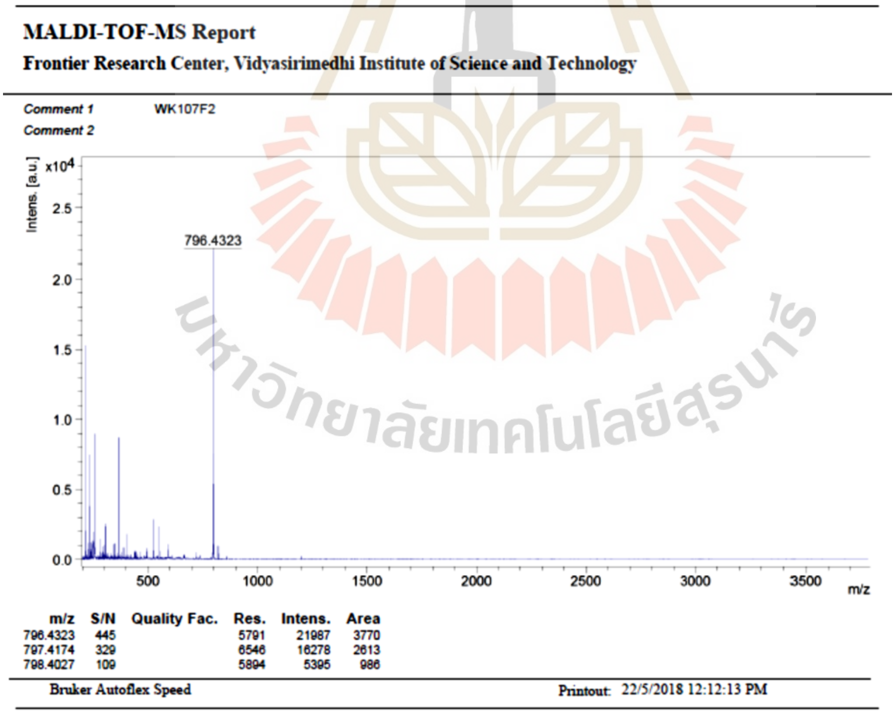

MALDI-TOF-MS Report

Frontier Research Center, Vidyasirimedhi Institute of Science and Technology

Comment 1 WK107F2

Comment 2

m/z	S/N	Quality Fac.	Res.	Intens.	Area
796.4323	445		5791	21987	3770
797.4174	329		6546	16278	2613
798.4027	109		5894	5395	986

Bruker Autoflex Speed

Printout: 22/5/2018 12:12:13 PM

MALDI-TOF

NT-2TPE (18)

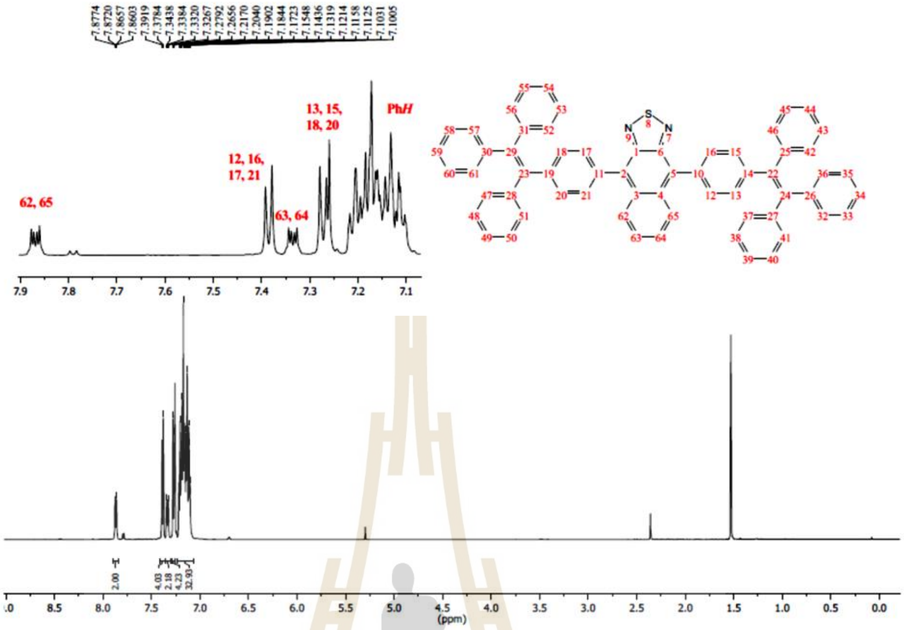

^{1}H-NMR (600 MHz, $CDCl_3$)

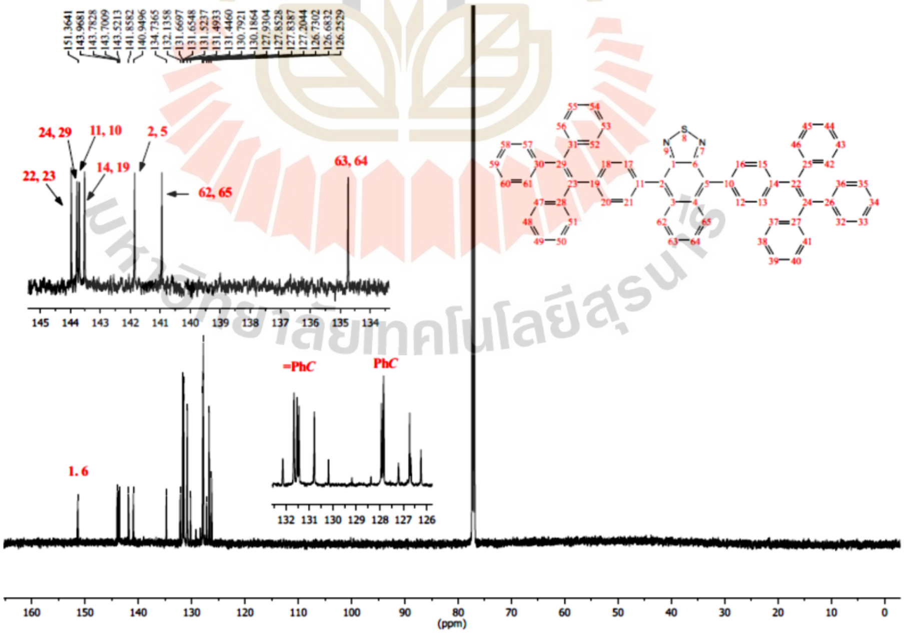

^{13}C-NMR (150 MHz, $CDCl_3$)

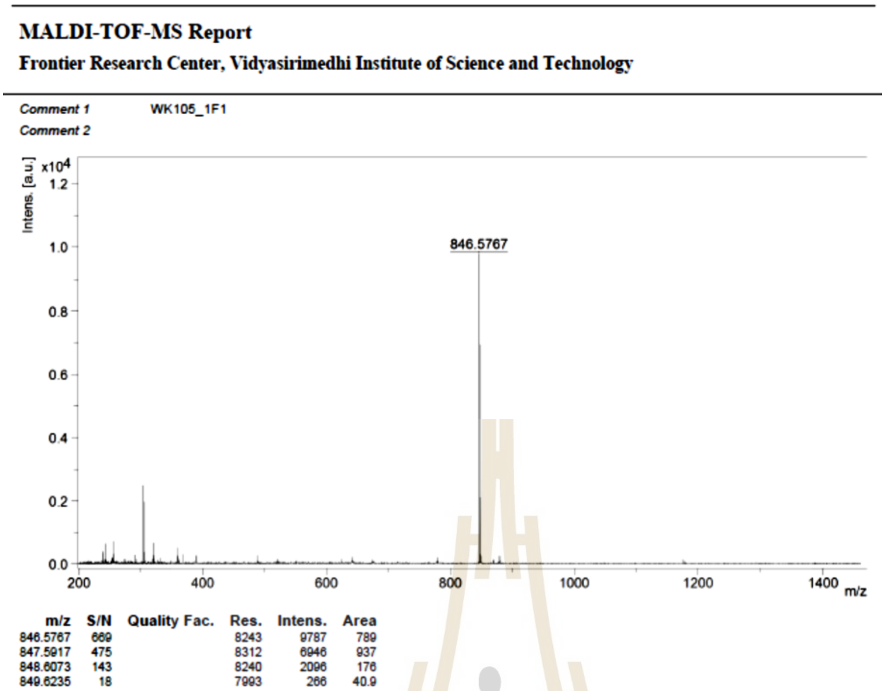

MALDI-TOF-MS Report

Frontier Research Center, Vidyasirimedhi Institute of Science and Technology

Comment 1 WK105_1F1

Comment 2

m/z	S/N	Quality Fac.	Res.	Intens.	Area
846.5767	669		8243	9787	789
847.5917	475		8312	6946	937
848.6073	143		8240	2096	176
849.6235	18		7993	266	40.9

MALDI-TOF

NT-TPETPA (19)

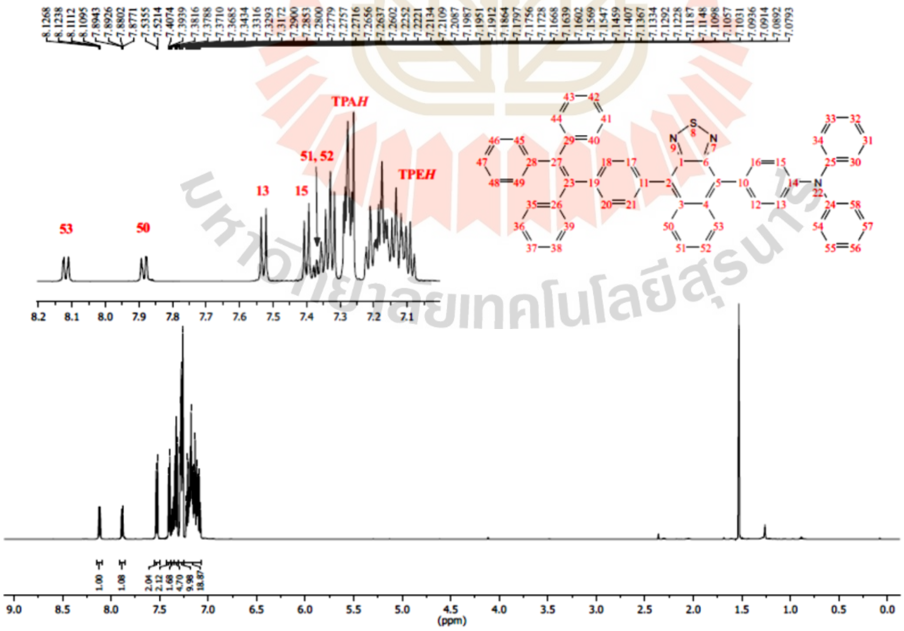

^{1}H-NMR (600 MHz, CDCl$_3$)

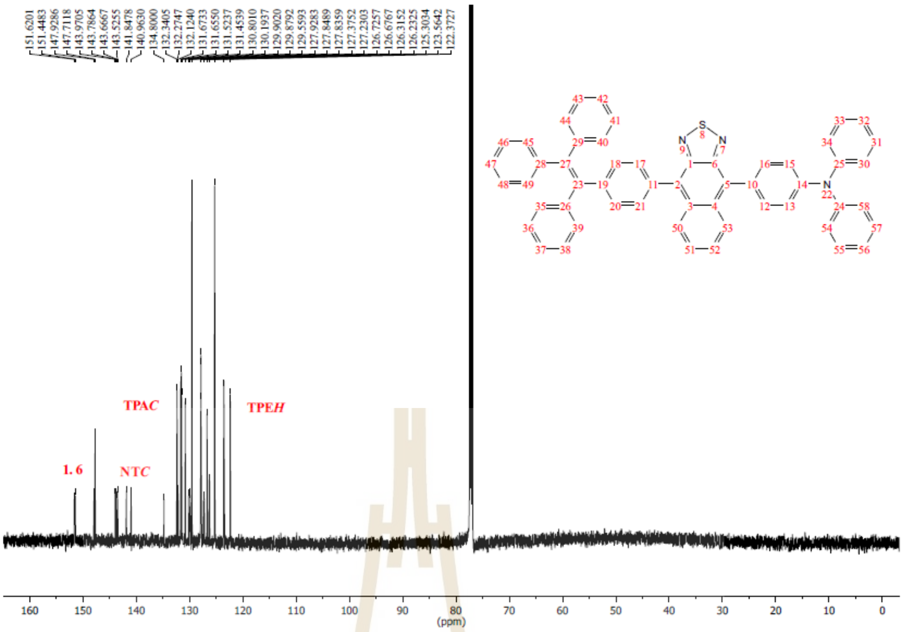

^{13}C-NMR (150 MHz, $CDCl_3$)

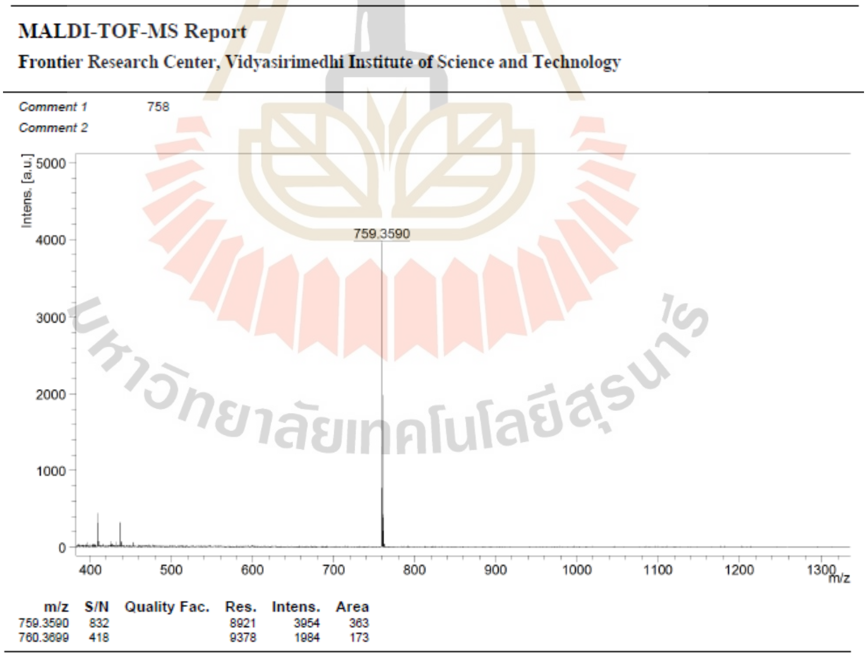

MALDI-TOF-MS Report

Frontier Research Center, Vidyasirimedhi Institute of Science and Technology

Comment 1 758

Comment 2

m/z	S/N	Quality Fac.	Res.	Intens.	Area
759.3590	832		8921	3954	363
760.3699	418		9378	1984	173

MALDI-TOF

BT-2TPEH (20)

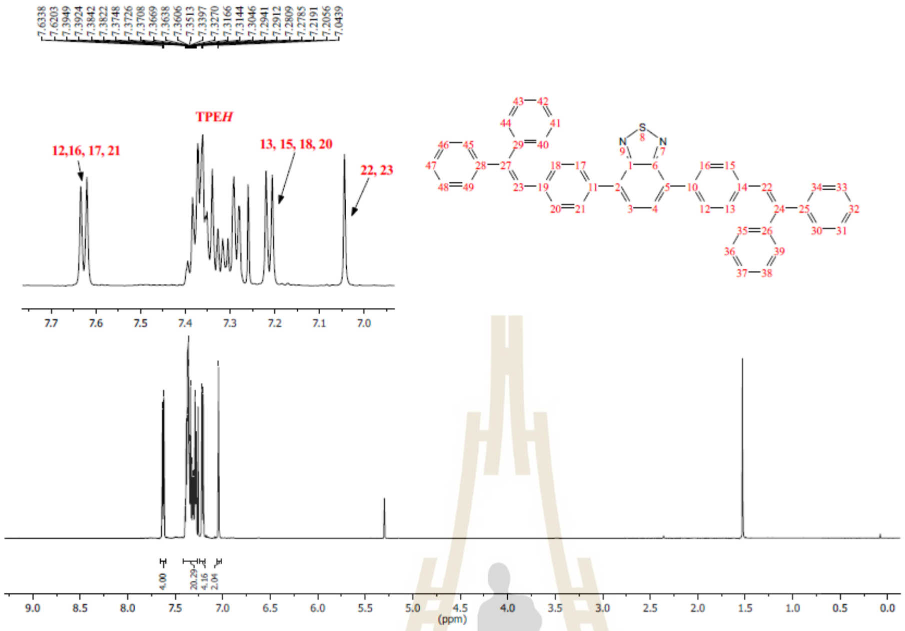

^{1}H-NMR (600 MHz, CDCl$_3$)

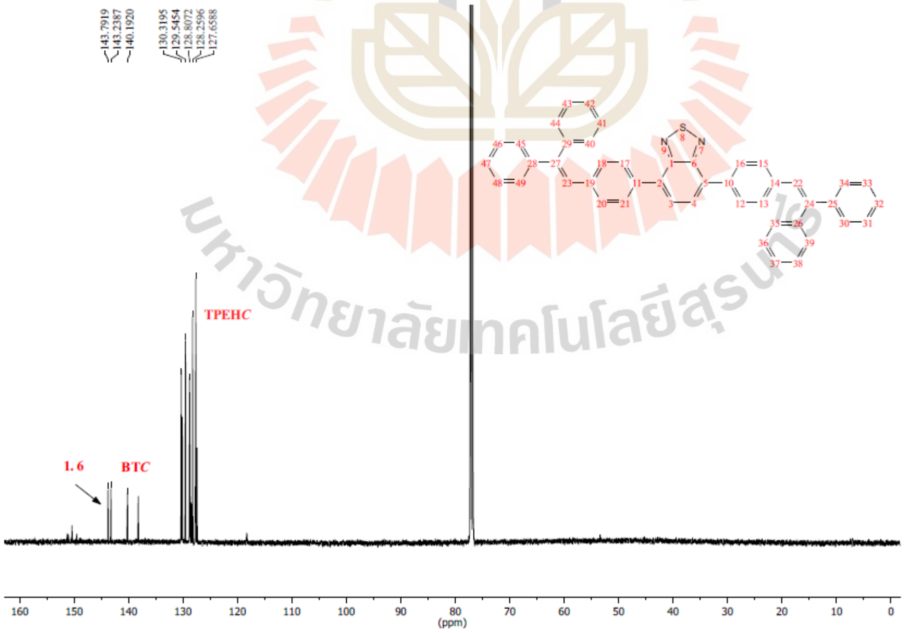

^{13}C-NMR (150 MHz, CDCl$_3$)

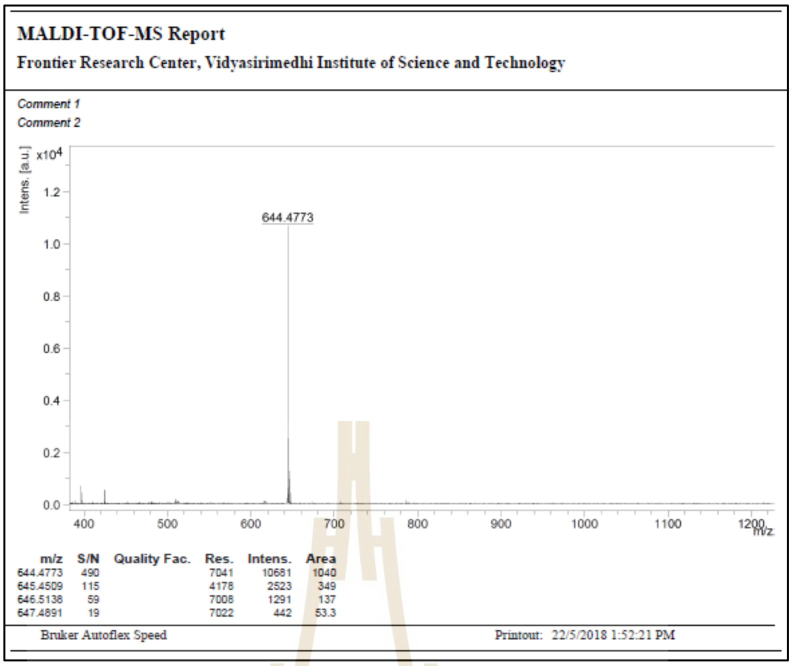

MALDI-TOF-MS Report

Frontier Research Center, Vidyasirimedhi Institute of Science and Technology

Comment 1
Comment 2

m/z	S/N	Quality Fac.	Res.	Intens.	Area
644.4773	490		7041	10681	1040
645.4509	115		4178	2523	349
646.5138	59		7008	1291	137
647.4891	19		7022	442	53.3

Bruker Autoflex Speed   Printout: 22/5/2018 1:52:21 PM

MALDI-TOF

BT-TPETPA (21)

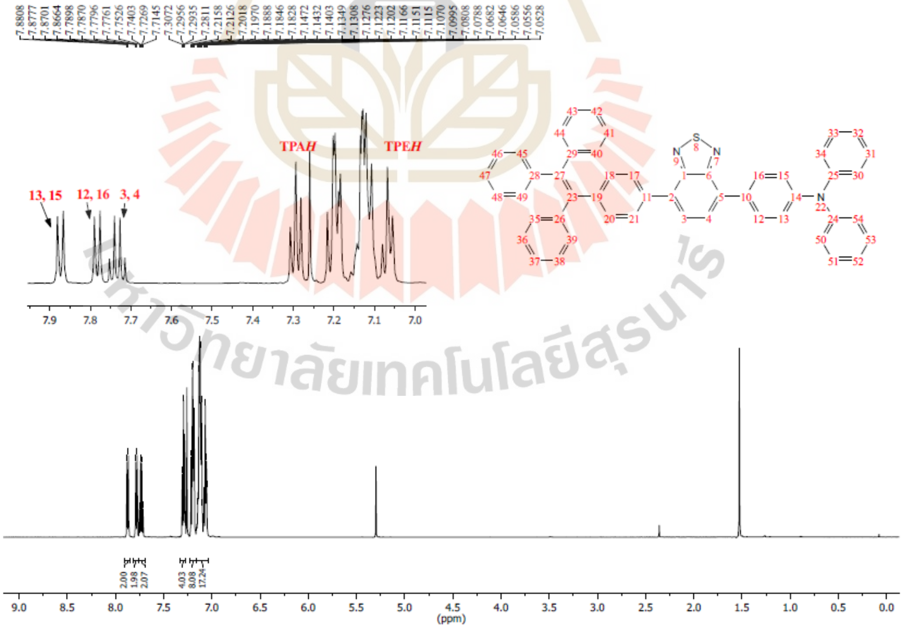

^{1}H-NMR (600 MHz, $CDCl_3$)

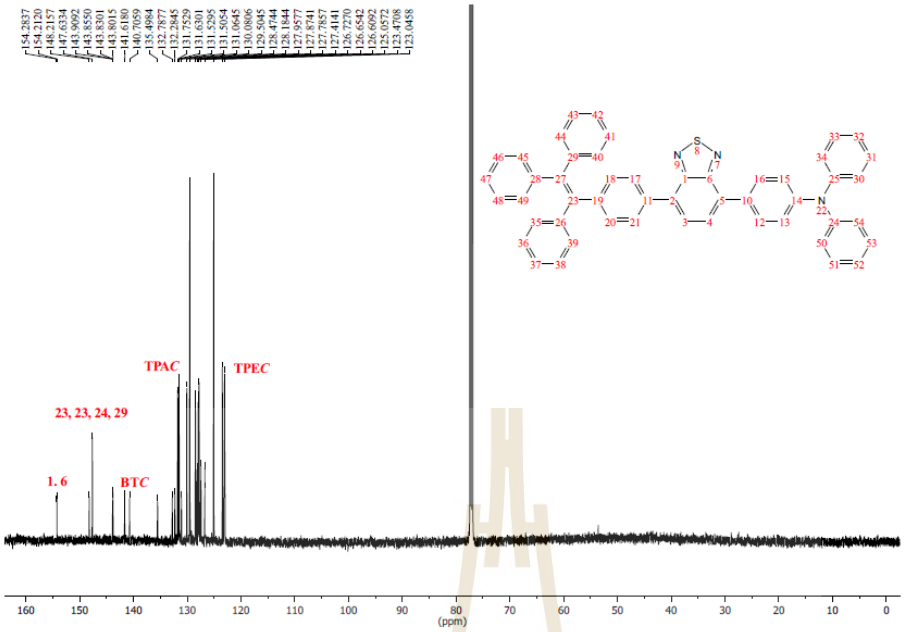

^{13}C-NMR (150 MHz, CDCl$_3$)

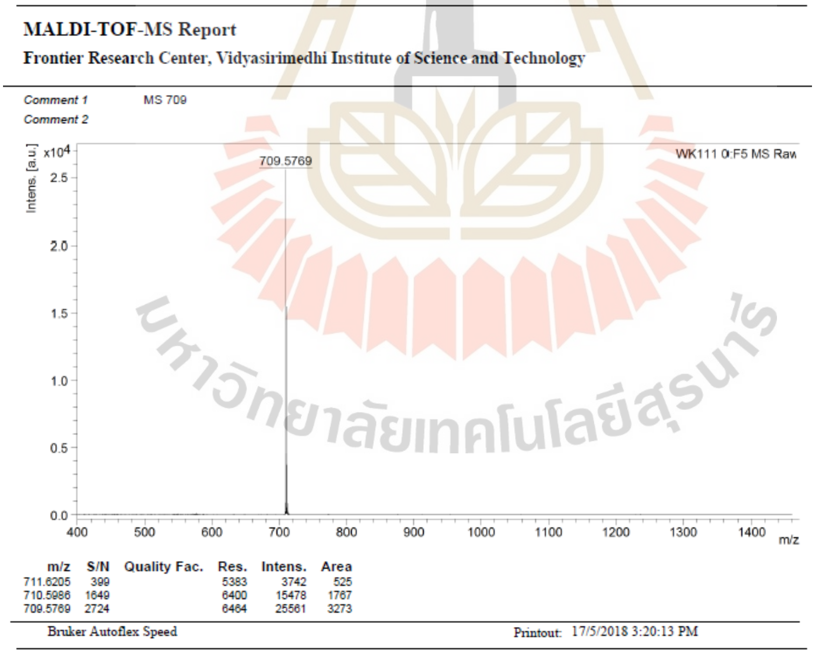

MALDI-TOF-MS Report

Frontier Research Center, Vidyasirimedhi Institute of Science and Technology

Comment 1 MS 709

Comment 2

m/z	S/N	Quality Fac.	Res.	Intens.	Area
711.6205	399		5383	3742	525
710.5986	1649		6400	15478	1767
709.5769	2724		6464	25561	3273

Bruker Autoflex Speed Printout: 17/5/2018 3:20:13 PM

MALDI-TOF

FBT-2TPE (22)

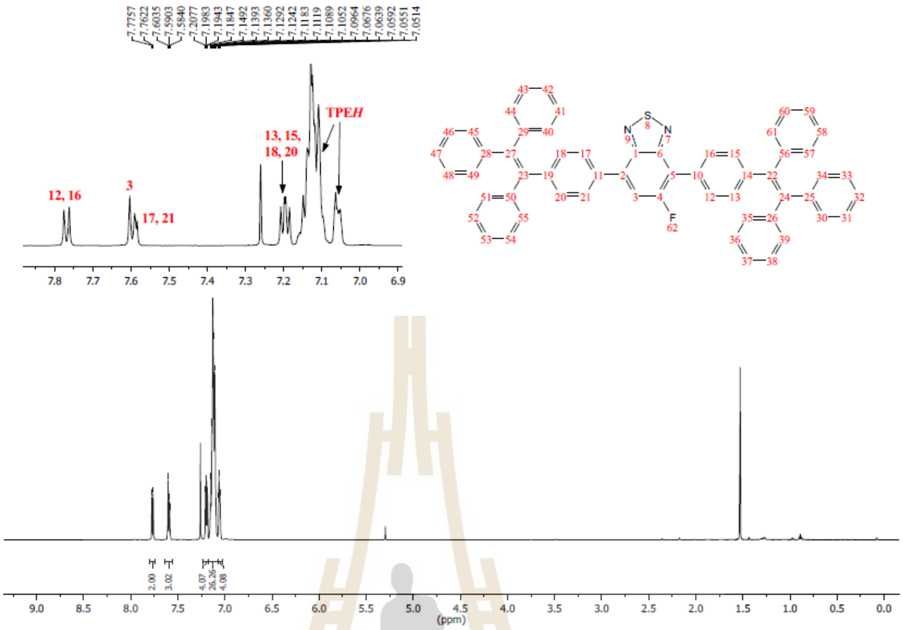

^{1}H-NMR (600 MHz, $CDCl_3$)

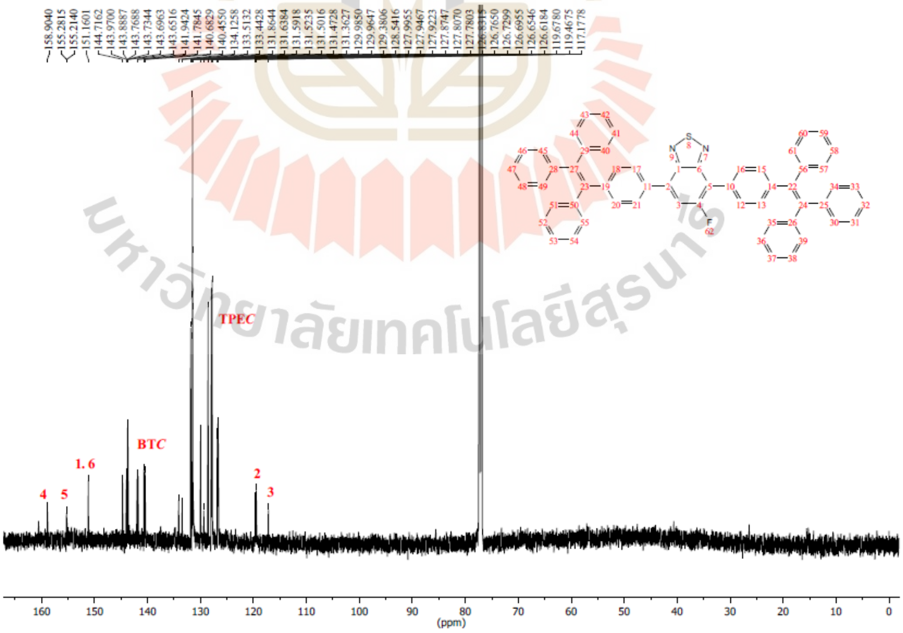

^{13}C-NMR (150 MHz, $CDCl_3$)

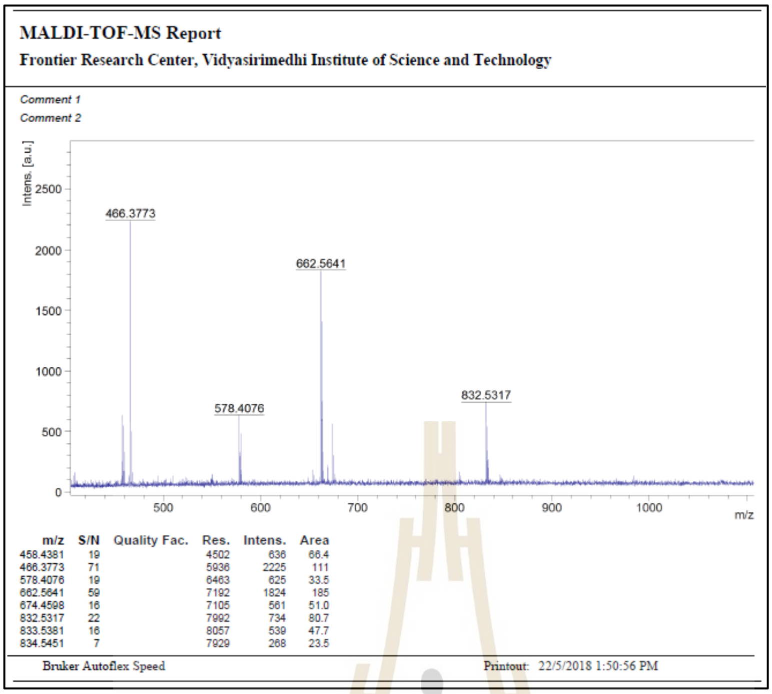

MALDI-TOF-MS Report

Frontier Research Center, Vidyasirimedhi Institute of Science and Technology

Comment 1

Comment 2

m/z	S/N	Quality Fac.	Res.	Intens.	Area
458.4381	19		4502	636	66.4
466.3773	71		5936	2225	111
578.4076	19		6463	625	33.5
662.5641	59		7192	1824	185
674.4598	16		7105	561	51.0
832.5317	22		7992	734	80.7
833.5381	16		8057	539	47.7
834.5451	7		7929	268	23.5

Bruker Autoflex Speed

Printout: 22/5/2018 1:50:56 PM

MALDI-TOF

2FBT-2TPE (23)

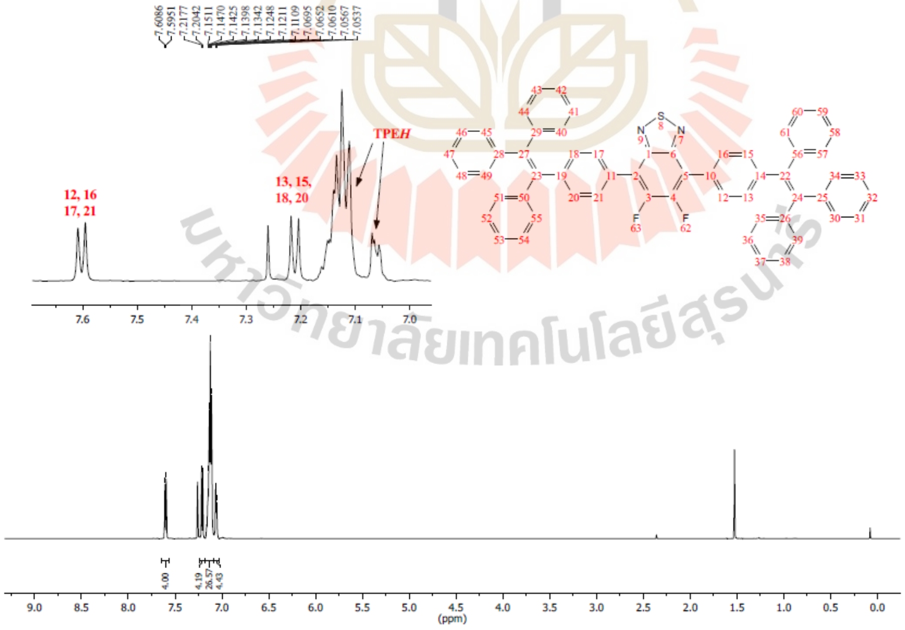

^{1}H-NMR (600 MHz, $CDCl_3$)

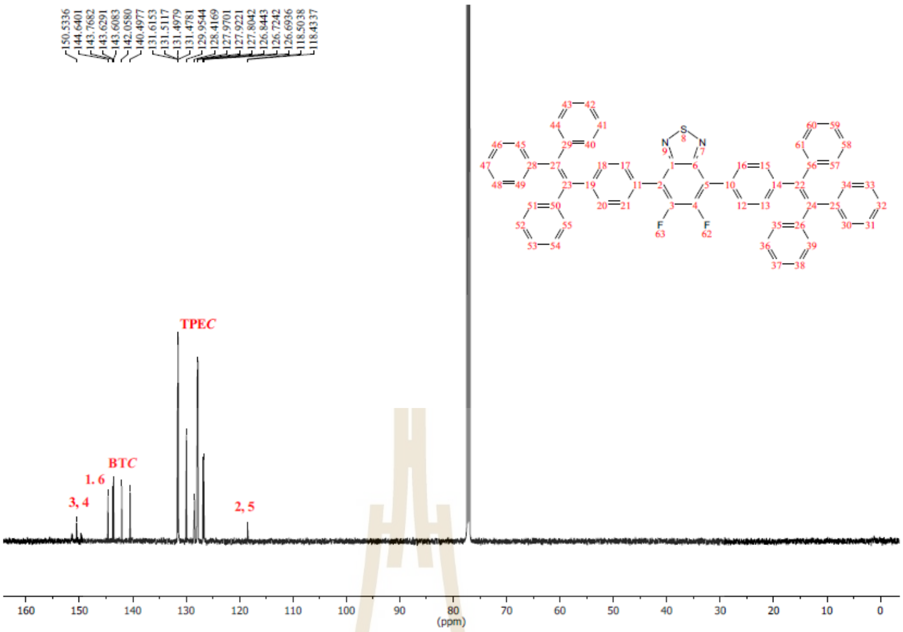

^{13}C-NMR (150 MHz, CDCl$_3$)

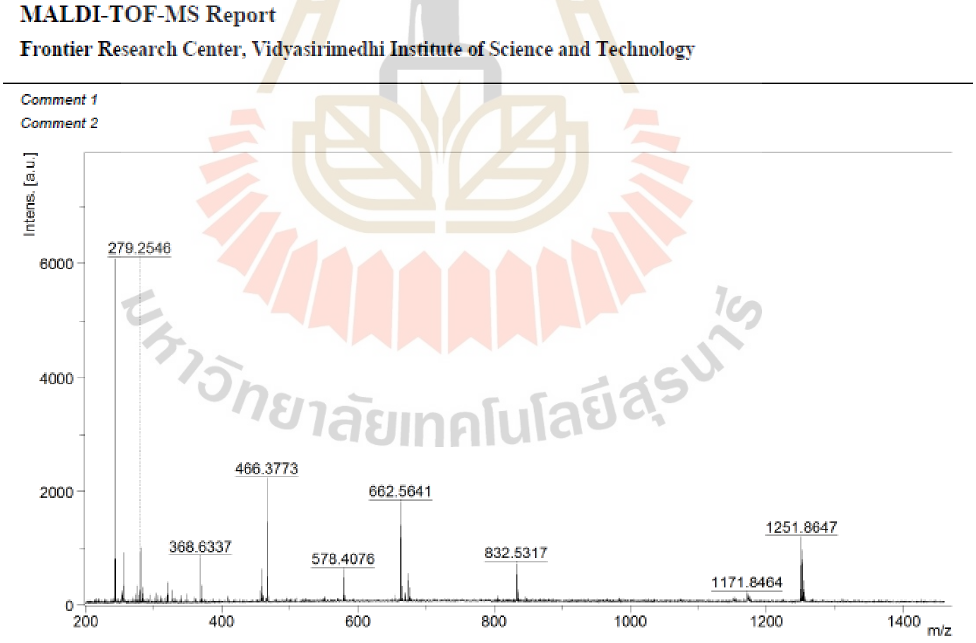

MALDI-TOF-MS Report

Frontier Research Center, Vidyasirimedhi Institute of Science and Technology

Comment 1

Comment 2

MALDI-TOF

2FBT-2TPEH (24)

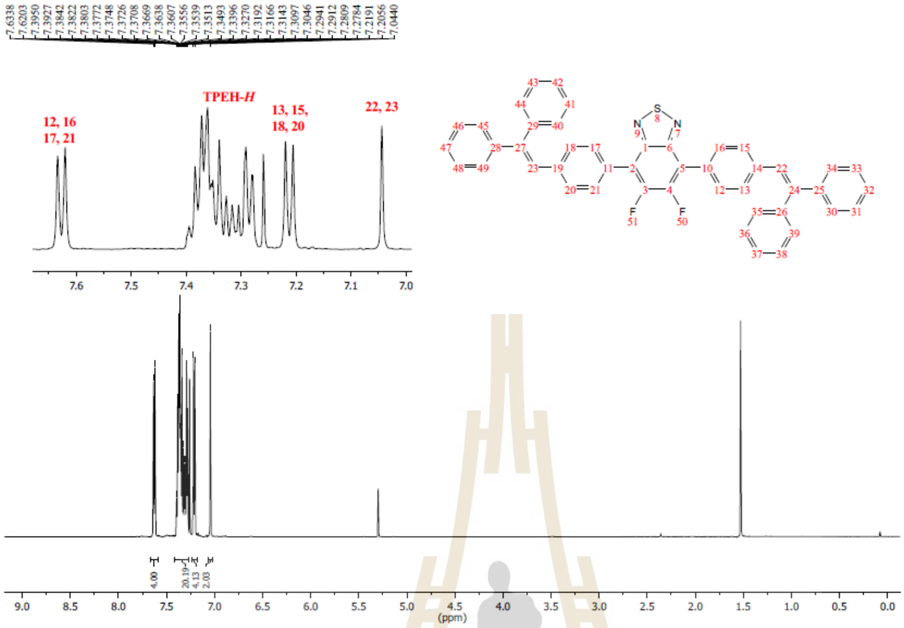

^{1}H-NMR (600 MHz, CDCl$_3$)

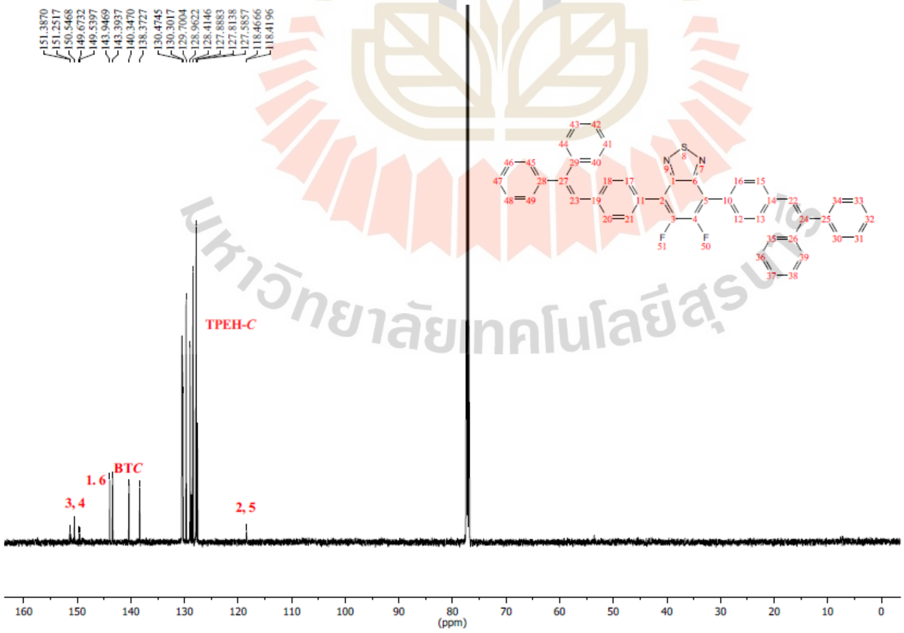

^{13}C-NMR (150 MHz, CDCl$_3$)

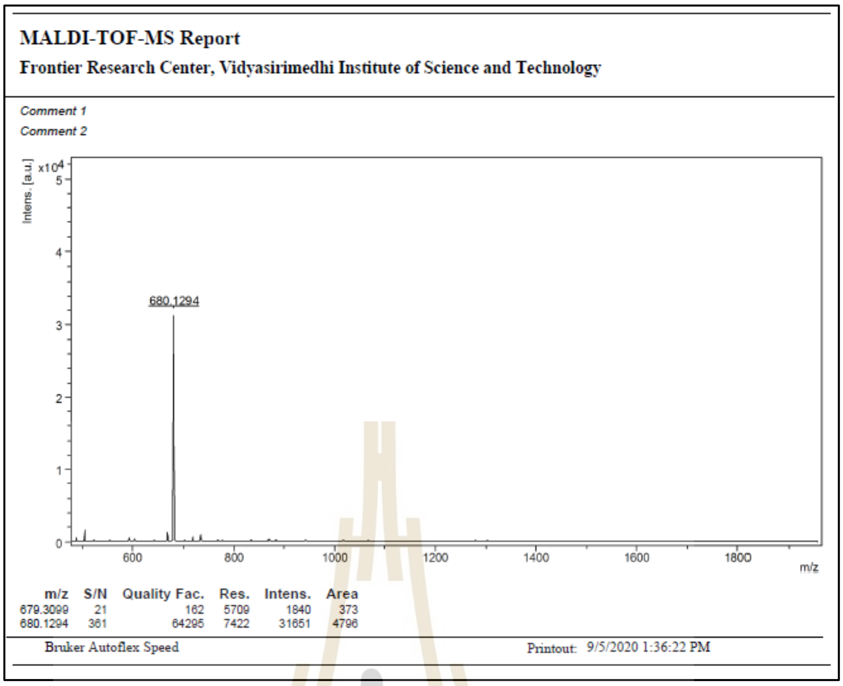

MALDI-TOF-MS Report

Frontier Research Center, Vidyasirimedhi Institute of Science and Technology

Comment 1

Comment 2

m/z	S/N	Quality Fac.	Res.	Intens.	Area
679.3099	21	162	5709	1840	373
680.1294	361	64295	7422	31651	4796

Bruker Autoflex Speed

Printout: 9/5/2020 1:36:22 PM

MALDI-TOF

NBT-2TPE (25)

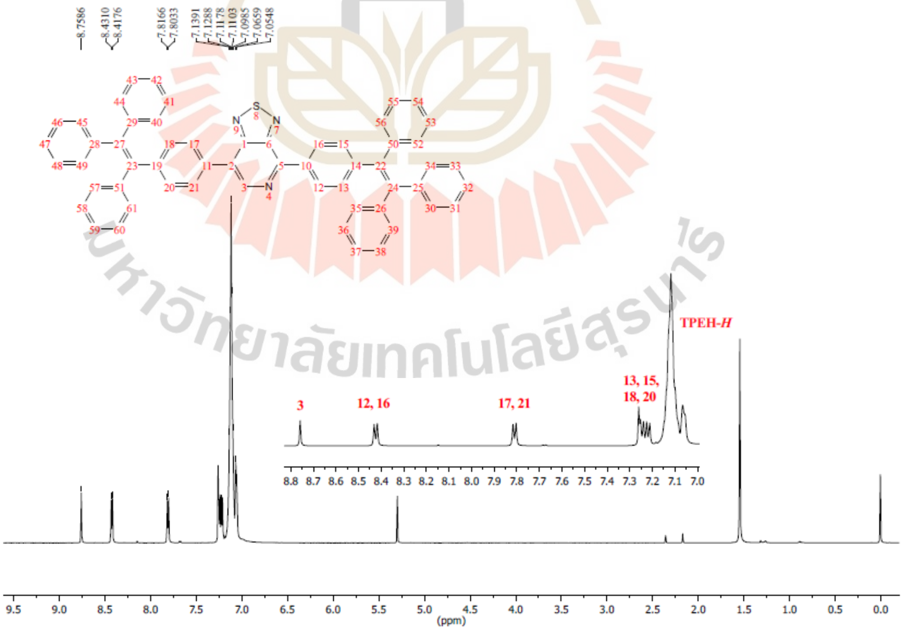

^{1}H-NMR (600 MHz, $CDCl_3$)

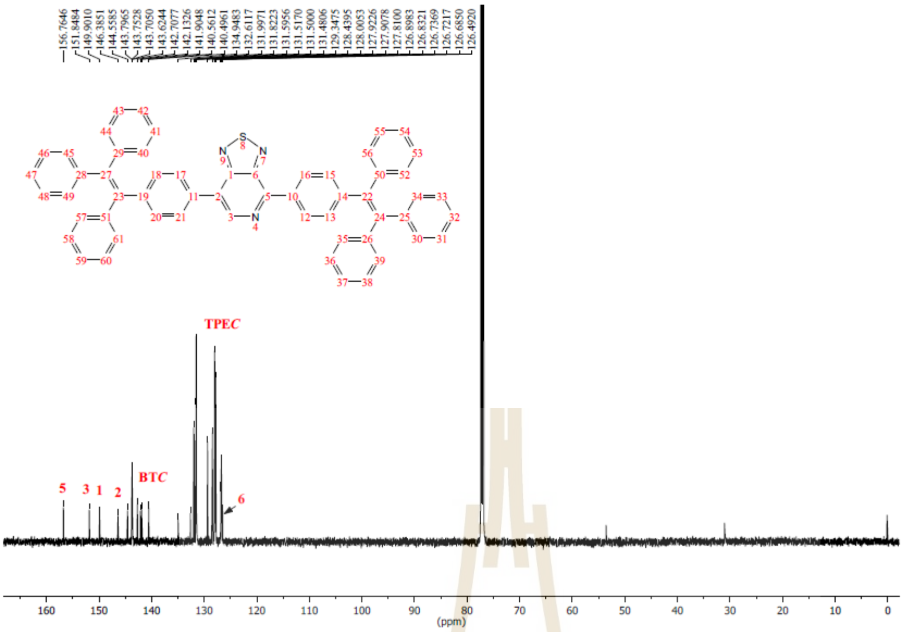

^{13}C-NMR (150 MHz, $CDCl_3$)

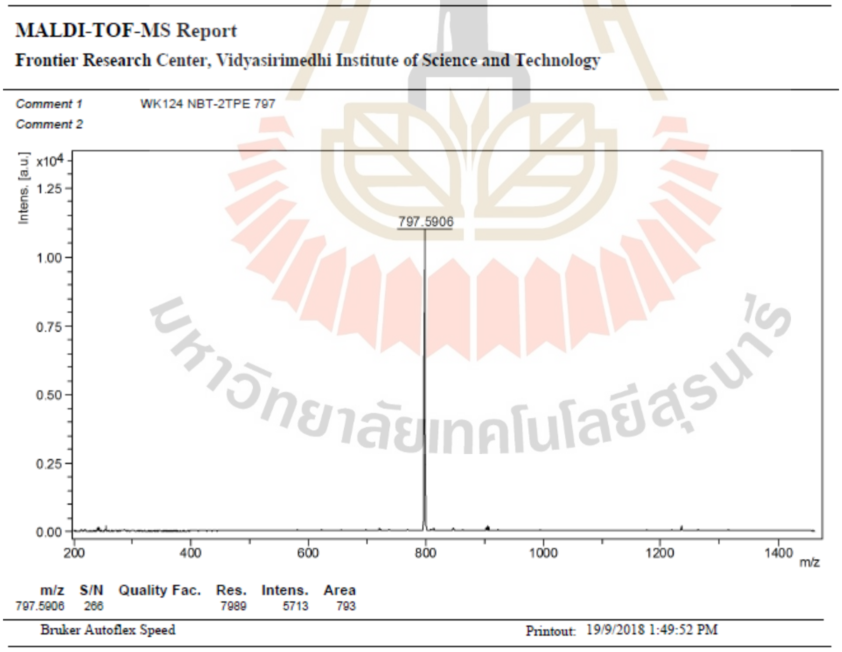

MALDI-TOF-MS Report

Frontier Research Center, Vidyasirimedhi Institute of Science and Technology

Comment 1 WK124 NBT-2TPE 797

Comment 2

m/z	S/N	Quality Fac.	Res.	Intens.	Area
797.5906	266		7989	5713	793

Bruker Autoflex Speed Printout: 19/9/2018 1:49:52 PM

MALDI-TOF

BNT-2TPE (26)

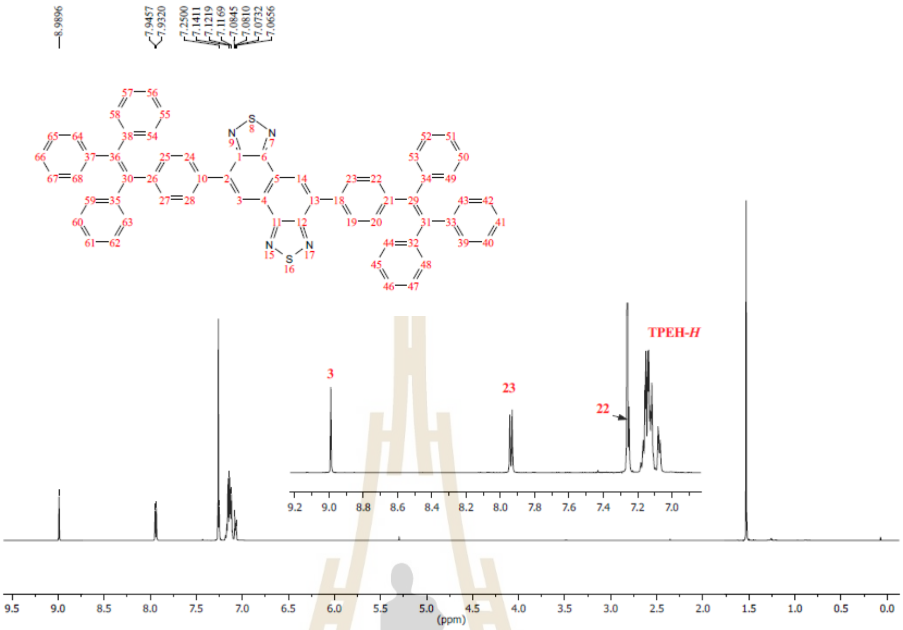

^{1}H-NMR (600 MHz, $CDCl_3$)

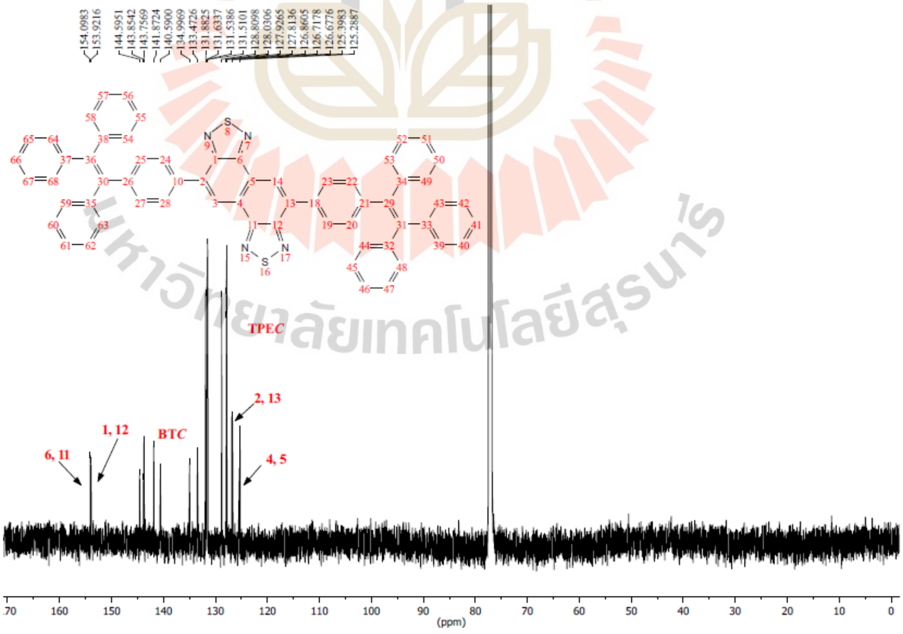

^{13}C-NMR (150 MHz, $CDCl_3$)

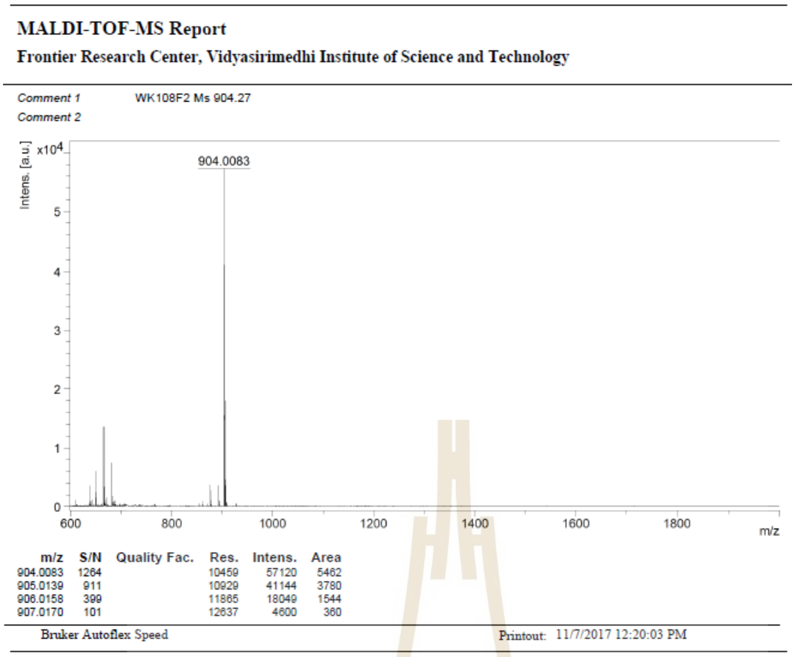

MALDI-TOF-MS Report

Frontier Research Center, Vidyasirimedhi Institute of Science and Technology

Comment 1 WK108F2 Ms 904.27

Comment 2

m/z	S/N	Quality Fac.	Res.	Intens.	Area
904.0083	1264		10459	57120	5462
905.0139	911		10929	41144	3780
906.0158	399		11865	18049	1544
907.0170	101		12637	4600	360

Bruker Autoflex Speed Printout: 11/7/2017 12:20:03 PM

MALDI-TOF

CHAPTER VII

CONCLUSION

In summary, we demonstrated the design strategy and synthesis of novel organic emitters based on D-A-D type with the unique character in each molecule as discussed in detail below;

In the first series, we design and synthesize the red emitters containing diketopyrrolopyrrole linked to the end-capped dendronized carbazole via the alkyl chain. From the study, we success to synthesize the target molecules by using the N-alkylation reaction with the moderate yield. We obtain emitters with high solubility, high emissive ability and reduce the π-π stacking interaction of DPP fluorophore as well as improve amorphous glass-forming ability and thermal stability of the material (T_{5d} = 333, 411, and 416°C, for G0DPP (**1**), G1DPP (**2**), and G2DPP (**3**)), respectively. The devices based on G1DPP as an emitter achieve the EQE of 2.90%, and the CIE coordinates of (0.415, 0.483).

In the second series, we designed the target molecules with the TADF characteristic, that molecular structure composed of D-π-A-π-D system which behaves like a "push-pull" architecture to obtain a small ΔE_{ST} and separated the HOMO and LUMO. Novel TADF emitters consist of *bis*(4-carbazolephenyl) sulfone as an acceptor core and carbazole derivatives as a donor moiety, and benzene as the π-linker. All emitters exhibited deep blue emission with strong ICT and showed a slight red shift when changing the donor moieties to a more strongly electron-donating group.

To further demonstrate the character of TADF, the emission decays in dilute toluene solution under argon and oxygen atmosphere and time-resolved emission spectrum (TRES) of these TADF compounds were investigated. The results revealed that the photoluminescence quantum yield of all compounds decreased when exposed to oxygen and the lifetimes were estimated to be 4-19 ns for prompt fluorescence and 36-600 ns for delayed fluorescence under argon atmosphere.

Moreover, from TRES measurement, the prompt component and the delayed component are identical, which can be concluded that the delayed component is originated from the fluorescence. Therefore, we can conclude that this strategy for designed TADF molecules is an effective method to achieve efficient TADF.

After that, the third series, the TADF dendrimers was designed and synthesized. The generation of carbazole dendrons leads three-dimensional molecular conformations and the spatial distribution of the HOMO and LUMO of the molecule. All TADF dendrimers can be dissolved in an organic solvent and exhibited blue emission with strong fluorescence intensity. However, only TPAfluorene-DPS (**16**) reveal the ICT characteristic, which might be from the more spatial distribution of the HOMO and LUMO of G1hexylfluorene (**14**) and octylfluorene (**15**). In addition, their dendritic structure, which arises from G1 and TPA moieties leads to increased Tg resulting in the thermal property of these materials.

In the last series, we designed the emitters by using the AIEgens to solve the strong aggregation-caused quenching effect. The Suzuki-Miyaura cross-coupling reaction of benzothiadiazole, naphthothiadiazole, and *bis*- naphthothiadiazole with the AIE activator such as TPE, TPEH as the donor moieties to afford the AIE emitters. The results revealed that the AIE molecules containing the TPE linked to a variety of acceptors exhibited the different emission colors from yellow to red with the strong ICT in solution and showed a strong PL intensity when the molecules were aggregated in a high ratio of water fraction. The OLEDs device based on AIE emitters exhibited a high external quantum efficiency of 3.14-4.66%. We believe that our results could provide a useful guide to design the highly efficient emitter with a high PL intensity in solid-state to be suitable for applications in OLEDs devices.

REFERENCES

REFERENCES

Adachi, C. (2014). Third-generation organic electroluminescence materials. **Japanese Journal of Applied Physics**. 53(6).

Aizawa, N., Pu, Y. J., Watanabe, M.; Chiba, T., Ideta, K., Toyota, N., Igarashi, M., Suzuri, Y., Sasabe, H., and Kido, J. (2014). Solution-processed multilayer small-molecule light-emitting devices with high-efficiency white-light emission. **Nature Communications**. 5: 5756.

Albrecht, K., Matsuoka, K., Fujita, K., and Yamamoto, K. (2018). A dendrimer emitter doped in a dendrimer host: efficient thermally activated delayed fluorescence OLEDs with fully-solution processed organic-layers. **Materials Chemistry Frontiers**. 2(6): 1097-1103.

Bagher, A. M. (2014). OLED Display Technology. **American Journal of Optics and Photonics**. 2(3).

Baleizao, C., and Berberan-Santos, M. N. (2008). Thermally activated delayed fluorescence in fullerenes. **Annals of the New York Academy of Sciences**. 1130: 224-234.

Berberan-Santos, M. N., and Garcia, J. M. M. (1996). Unusually Strong Delayed Fluorescence of C70. **Journal of the American Chemical Society**. 118(39): 9391-9394.

Blasse, G., and McMillin, D. R. (1980). On the luminescence of bis (triphenyl phosphine) phenanthroline copper (I). **Chemical Physics Letters**. 70(1): 1-3.

Chen, M., Li, L., Nie, H., Tong, J., Yan, L., Xu, B., Sun, J. Z., Tian, W., Zhao, Z., Qin, A., and Tang, B. Z. (2015). Tetraphenylpyrazine-based AIEgens: facile preparation and tunable light emission. **Chemical Science**. 6(3): 1932-1937.

Chow, W. K., Yuen, O. Y., Choy, P. Y., So, C. M., Lau, C. P., Wong, W. T., and Kwong, F. Y. (2013). A decade advancement of transition metal-catalyzed borylation of aryl halides and sulfonates. **RSC Advances**. 3(31).

Data, P., Kurowska, A., Pluczyk, S., Zassowski, P., Pander, P., Jedrysiak, R., Czwartosz, M., Otulakowski, L., Suwinski, J., Lapkowski, M., and Monkman, A. P. (2016). Exciplex Enhancement as a Tool to Increase OLED Device Efficiency. **The Journal of Physical Chemistry C**. 120(4): 2070-2078.

David, J., Weiter, M., Vala, M., Vyňuchal, J., and Kučerík, J. (2011). Stability and structural aspects of diketopyrrolopyrrole pigment and its N-alkyl derivatives. **Dyes and Pigments**. 89(2): 137-143.

Dawei Ma, Q. C., and Hui Zhang. (2003). Mild Method for Ullmann Coupling Reaction of Amines and Aryl Halides. **Organic Letters**. 5(14).

Dimitrakopoulos, C. D., and Malenfant, P. R. L. (2002). Organic Thin Film Transistors for Large Area Electronics. **Advanced Materials**. 14(2): 99-117.

Du, X., Qi, J., Zhang, Z., Ma, D., and Wang, Z. Y. (2012). Efficient Non-doped Near Infrared Organic Light-Emitting Devices Based on Fluorophores with Aggregation-Induced Emission Enhancement. **Chemistry of Materials**. 24(11): 2178-2185.

Endo, A., Ogasawara, M., Takahashi, A., Yokoyama, D., Kato, Y., and Adachi, C. (2009). Thermally activated delayed fluorescence from Sn(4+)-porphyrin complexes and their application to organic light emitting diodes-a novel mechanism for electroluminescence. **Advanced Materials**. 21(47): 4802-4806.

Endo, A., Sato, K., Yoshimura, K., Kai, T., Kawada, A., Miyazaki, H., and Adachi, C. (2011). Efficient up-conversion of triplet excitons into a singlet state and its application for organic light emitting diodes. **Applied Physics Letters**. 98(8).

Strieter, E. R., Bhayana, B., and Buchwald, S. L. (2009). Mechanistic Studies on the Copper-Catalyzed N-Arylation of Amides. **Journal of the American Chemical Society**. 231(1).

Farré, Y., Zhang, L., Pellegrin, Y., Planchat, A., Blart, E., Boujtita, M. Hammarström, L., Jacquemin, D., and Odobel, F. (2016). Second Generation of Diketopyrrolopyrrole Dyes for NiO-Based Dye-Sensitized Solar Cells. **The Journal of Physical Chemistry C**. 120(15): 7923-7940.

Ftouni, H., Bolze, F., de Rocquigny, H., and Nicoud, J.-F. (2013). Functionalized Two-Photon Absorbing Diketopyrrolopyrrole-Based Fluorophores for Living Cells Fluorescent Microscopy. **Bioconjugate Chemistry**. 24(6): 942-950.

Goushi, K., Yoshida, K., Sato, K., and Adachi, C. (2012). Organic light-emitting diodes employing efficient reverse intersystem crossing for triplet-to-singlet state conversion. **Nature Photonics**. 6(4): 253-258.

Hao, Z., and Iqbal, A. (1997). Some aspects of organic pigments **Chemical Society Reviews**. 26: 203-213.

Hu, Q., Gao, M., Feng, G., Chen, X., and Liu, B. (2015). A cell apoptosis probe based on fluorogen with aggregation induced emission characteristics. **ACS Applied Materials & Interfaces**. 7(8): 4875-4882.

Huang, J., Sun, N., Chen, P., Tang, R., Li, Q., Ma, D., and Li, Z. (2014). Largely blue-shifted emission through minor structural modifications: molecular design, synthesis, aggregation-induced emission and deep-blue OLED application. **Chemical communications**. 50(17): 2136-2138.

Ji, K., Xue, Y., and Cui, Z., (2015). A new method for colors characterization of colored stainless steel using CIE and Munsell color systems. **Optical Materials**. 47: 180-184.

Jin, R., Zhang, X., Xiao, W., and Irfan, A. (2018). Rational design of diketopyrrolo pyrrole-based multifunctional materials for organic light-emitting diodes and organic solar cells. **Theoretical Chemistry Accounts**. 137(11): 145.

Jürgensen, N., Kretzschmar, A., Höfle, S., Freudenberg, J., Bunz, U. H. F., and Hernandez-Sosa, G. (2017). Sulfone-Based Deep Blue Thermally Activated Delayed Fluorescence Emitters: Solution-Processed Organic Light-Emitting Diodes with High Efficiency and Brightness. **Chemistry of Materials**. 29(21): 9154-9161.

Kaur, M., and Choi, D. H. (2015). Diketopyrrolopyrrole: brilliant red pigment dye-based fluorescent probes and their applications. **Chemical Society Reviews**. 44(1): 58-77.

Kawamura, Y., Goushi, K., Brooks, J., Brown, J. J., Sasabe, H., and Adachi, C. (2005). 100% phosphorescence quantum efficiency of Ir(III) complexes in organic semiconductor films. **Applied Physics Letters**. 86(7).

Kim, H. J., Shin, M. H., Kim, J. S., Kim, S. E., and Kim, Y. J. (2017). High efficient OLED displays prepared with the air-gapped bridges on quantum dot patterns for optical recycling. **Scientific Reports**. 7: 43063.

Kim, J. G., Lee, J. E., Jo, S. M., Chin, B. D., Baek, J. Y., Ahn, K. J., Kang, S. J., and Kim, H. K. (2018). Room temperature processed high mobility W-doped In_2O_3 electrodes coated via in-line arc plasma ion plating for flexible OLEDs and quantum dots LEDs. **Scientific Reports**. 8(1): 12019.

Kwon, T. W., Alam, M. M., and Jenekhe, S. A. (2004). n-Type Conjugated Dendrimers: Convergent Synthesis, Photophysics, Electroluminescence, and Use as Electron-Transport Materials for Light-Emitting Diodes. **Chemistry of Materials**, 16(23): 4657-4666.

Lee, G. H., and Kim, Y. S. (2016). Diphenylsulphone derivatives for a blue thermally activated delayed fluorescence. **Polymer Bulletin**. 73(9): 2439-2446.

Lee, G. H., and Kim, Y. S. (2016). High-efficiency diphenylsulfon derivative-based organic light-emitting diode exhibiting thermally-activated delayed fluorescence. **Journal of the Korean Physical Society**. 69(3): 398-401.

Li, C., Zhang, A., Wang, Z., Liu, F., Zhou, Y., Russell, T. P., Li, Y., and Li, W. (2016). All polymer solar cells with diketopyrrolopyrrole-polymers as electron donor and a naphthalenediimide-polymer as electron acceptor. **RSC Advances**. 6(42): 35677-35683.

Li, J., Liao, X., Xu, H., Li, L., Zhang, J., Wang, H., and Xu, B. (2017). Deep-blue thermally activated delayed fluorescence dendrimers with reduced singlet-triplet energy gap for low roll-off non-doped solution-processed organic light-emitting diodes. **Dyes and Pigments**. 140: 79-86.

Li, N., Shin, D. W., Hwang, D. S., Lee, Y. M., and Guiver, M. D. (2010). Polymer Electrolyte Membranes Derived from New Sulfone Monomers with Pendent Sulfonic Acid Groups. **Macromolecules**. 43(23): 9810-9820.

Li, Y., Xie, G., Gong, S., Wu, K., and Yang, C. (2016). Dendronized delayed fluorescence emitters for non-doped, solution-processed organic light-emitting diodes with high efficiency and low efficiency roll-off simultaneously: two parallel emissive channels. **Chemical Science**. 7(8): 5441-5447.

Li, Y., Xu, Z., Zhu, X., Chen, B., Wang, Z., Xiao, B., Lam, J. W. Y., Zhao, Z., Ma, D., and Tang, B. Z. (2019). Creation of Efficient Blue Aggregation-Induced Emission Luminogens for High-Performance Nondoped Blue OLEDs and Hybrid White OLEDs. **ACS Applied Materials & Interfaces**. 11(19): 17592-17601.

Liu, T., Zhu, L., Zhong, C., Xie, G., Gong, S., Fang, J., Ma, D., and Yang, C. (2017). Naphthothiadiazole-Based Near-Infrared Emitter with a Photoluminescence Quantum Yield of 60% in Neat Film and External Quantum Efficiencies of up to 3.9% in Nondoped OLEDs. **Advanced Functional Materials**. 27(12).

Liu, Y., Chen, S., Lam, J. W. Y., Lu, P., Kwok, R. T. K., Mahtab, F., Kwok, H. S., and Tang, B. Z. (2011). Tuning the Electronic Nature of Aggregation-Induced Emission Luminogens with Enhanced Hole-Transporting Property. **Chemistry of Materials**. 23(10): 2536-2544.

Luo, J., Xie, Z., Lam, J. W., Cheng, L., Chen, H., Qiu, C., Kwok, H. S., Zhan, X., Liu, Y., Zhu, D., and Tang, B. Z. (2001). Aggregation-induced emission of 1-methyl-1,2,3,4,5-pentaphenylsilole. **Chemical Communications**. 18: 1740-1741.

Ma, C. Q., Zhang, L. Q., Zhou, J. H., Wang, X. S., Zhang, B. W., Cao, Y., Bugnon, P., Schaer, M., Nüesch, F., Zhang, D. Q., and Qiu, Y. (2002). 1,3-Diphenyl-5-(9-phenanthryl)-4,5-dihydro-1H-pyrazole (DPPhP): structure, properties, and application in organic light-emitting diodes. **Journal of Materials Chemistry** 12(12): 3481-3486.

Maasoumi, F., Jansen-van Vuuren, R. D., Shaw, P. E., Puttock, E. V., Nagiri, R. C. R., McEwan, J. A., Bown, M., O'Connell, J. L., Dunn, C. J., Burn, P. L., and Namdas, E. B. (2018). An external quantum efficiency of >20% from solution-processed poly(dendrimer) organic light-emitting diodes. **npj Flexible Electronics**. 2(1).

Más-Montoya, M., and Janssen, R. A. J. (2017). The Effect of H- and J-Aggregation on the Photophysical and Photovoltaic Properties of Small Thiophene-Pyridine-DPP Molecules for Bulk-Heterojunction Solar Cells. **Advanced Functional Materials**. 27(16).

Mehes, G., Nomura, H., Zhang, Q., Nakagawa, T., and Adachi, C. (2012). Enhanced electroluminescence efficiency in a spiro-acridine derivative through thermally activated delayed fluorescence. **Angewandte Chemie International Edition in English**. 51(45): 11311-11315.

Minaev, B., Baryshnikov, G., and Agren, H. (2014). Principles of phosphorescent organic light emitting devices. **Physical Chemistry Chemical Physics**. 16(5): 1719-1758.

Mitschke, U., and Bäuerle, P., (2000). The electroluminescence of organic materials. **Journal of Materials Chemistry**. 10(7): 1471-1507.

Monçalves, M., Rampon, D. d. S., Schneider, P. H., Rodembusch, F. S., and Silveira, C. d. C. (2014). Divinyl sulfides/sulfones-based D–π–A–π–D dyes as efficient non-aromatic bridges for π-conjugated compounds. **Dyes and Pigments**. 102: 71-78.

Mondal, S. (2016). Recent advancement of Ullmann-type coupling reactions in the formation of C–C bond. **ChemTexts**. 2(4).

Moonsin, P., Prachumrak, N., Rattanawan, R., Keawin, T., Jungsuttiwong, S., Sudyoadsuk, T., and Promarak, V. (2012). Carbazole dendronised triphenylamines as solution processed high Tg amorphous hole-transporting materials for organic electroluminescent devices. **Chemical Communications**. 48(28): 3382-3384.

Nakagawa, T., Ku, S. Y., Wong, K. T., and Adachi, C. (2012). Electroluminescence based on thermally activated delayed fluorescence generated by a spirobifluorene donor-acceptor structure. **Chemical Communications**. 48(77): 9580-9582.

Nelson, T. L., Young, T. M., Liu, J., Mishra, S. P., Belot, J. A., Balliet, C. L., Javier, A. E., Kowalewski, T., and McCullough, R. D. (2010). Transistor paint: high mobilities in small bandgap polymer semiconductor based on the strong acceptor, diketopyrrolopyrrole and strong donor, dithienopyrrole. **Advanced Materials**. 22(41): 4617-4621.

Parker, C. A., and Hatchard, C. G. (1961). Triplet-singlet emission in fluid solutions. Phosphorescence of eosin. **Transactions of the Faraday Society**. 57: 1894-1904.

Peng, L., Xu, S., Zheng, X., Cheng, X., Zhang, R., Liu, J., Liu, B., and Tong, A. (2017). Rational Design of a Red-Emissive Fluorophore with AIE and ESIPT Characteristics and Its Application in Light-Up Sensing of Esterase. **Analytical Chemistry**. 89(5): 3162-3168.

Podlesny, J., Dokladalova, L., Pytela, O., Urbanec, A., Klikar, M., Almonasy, N., Mikysek, T., Jedryka, J., Kityk, I. V., and Bures, F. (2017). Structure-property relationships and third-order nonlinearities in diketopyrrolopyrrole based D-pi-A-pi-D molecules. **Beilstein Journal of Organic Chemistry**. 13: 2374-2384.

Prachumrak, N., Pojanasopa, S., Namuangruk, S., Kaewin, T., Jungsuttiwong, S., Sudyoadsuk,T., and Promarak, V. (2013). Novel bis[5-(fluoren-2-yl)thiophen-2-yl]benzothiadiazole end-capped with carbazole dendrons as highly efficient solution-processed nondoped red emitters for organic light-emitting diodes. **ACS Applied Materials & Interfaces**. 5(17): 8694-8703.

Qu, S., and Tian, H. (2012). Diketopyrrolopyrrole (DPP)-based materials for organic photovoltaics. **Chemical Communications**. 48(25): 3039-3051.

Qu, Y., Wu, Y., Gao, Y., Qu, S., Yang, L., and Hua, J. (2014). Diketopyrrolopyrrole-based fluorescent conjugated polymer for application of sensing fluoride ion and bioimaging. **Sensors and Actuators B: Chemical**. 197: 13-19.

Rajamalli, P., Senthilkumar, N., Gandeepan, P., Ren-Wu, C.-C., Lin, H.-W., and Cheng, C.-H. (2016). A Method for Reducing the Singlet–Triplet Energy Gaps of TADF Materials for Improving the Blue OLED Efficiency. **ACS Applied Materials & Interfaces**. 8(40): 27026-27034.

Sassi, M., Buccheri, N., Rooney, M., Botta, C., Bruni, F., Giovanella, U., Brovelli, S., and Beverina, L. (2016). Near-infrared roll-off-free electroluminescence from highly stable diketopyrrolopyrrole light emitting diodes. **Scientific Reports**. 6: 34096.

Schmidbauer, S., Hohenleutner, A., and Konig, B. (2013). Studies on the photodegradation of red, green and blue phosphorescent OLED emitters. **Beilstein Journal of Organic Chemistry**. 9: 2088-2096.

Sharma, G., Marri, A., Koyyada, G., Singh, S., and Malapaka, C. (2014). Indole and triisopropyl phenyl as capping units for a diketopyrrolopyrrole (DPP) acceptor central unit: An efficient D-A-D type small mo A dendrimer emitter doped in a dendrimer lecule for organic solar cells. **RSC Advances**. 4: 732-742.

So, F., Kido, J., and Burrows, P. (2008). Organic Light-Emitting Devices for Solid-State Lighting. **MRS Bulletin**. 33(7): 663-669.

Sovdat, B., Kadunc, M., Batič, M., and Milčinski, G. (2019). Natural color representation of Sentinel-2 data. **Remote Sensing of Environment**. 225: 392-402.

Sudyoadsuk, T., Moonsin, P., Prachumrak, N., Namuangruk, S., Jungsuttiwong, S., Keawin, T., and Promarak, V. (2014). Carbazole dendrimers containing oligoarylfluorene cores as solution-processed hole-transporting non-doped emitters for efficient pure red, green, blue and white organic light-emitting diodes. **Polymer Chemistry**. 5(13).

Sun, K., Sun, Y., Tian, W., Liu, D., Feng, Y., Sun, Y., and Jiang, W. (2018). Thermally activated delayed fluorescence dendrimers with exciplex-forming dendrons for low-voltage-driving and power-efficient solution-processed OLEDs. **Journal of Materials Chemistry C**. 6(1): 43-49.

Tang, C. W. and VanSlyke, S. A. (1987). Organic Electroluminescent Diodes. **Applied Physics Letters**. 51(12): 913-915.

Thejo Kalyani, N., and Dhoble, S. J. (2014). Novel approaches for energy efficient solid state lighting by RGB organic light emitting diodes – A review. **Renewable and Sustainable Energy Reviews**. 32: 448-467.

Thejo Kalyani, N., and Dhoble, S. J. (2015). Novel materials for fabrication and encapsulation of OLEDs. **Renewable and Sustainable Energy Reviews**. 44, 319-347.

Udagawa, K., Sasabe, H., Cai, C., and Kido, J. (2014). Low-driving-voltage blue phosphorescent organic light-emitting devices with external quantum efficiency of 30%. **Advanced Materials**. 26(29): 5062-5066.

Uoyama, H., Goushi, K., Shizu, K., Nomura, H., and Adachi, C. (2012). Highly efficient organic light-emitting diodes from delayed fluorescence. **Nature**. 492(7428): 234-238.

Vala, M., Weiter, M., Vynuchal, J., Toman, P., and Lunak, S., Jr., (2008). Comparative studies of diphenyl-diketo-pyrrolopyrrole derivatives for electroluminescence applications. **Journal of Fluorescence**. 18(6): 1181-1186.

Wang, H., Xie, L., Peng, Q., Meng, L., Wang, Y., Yi, Y., and Wang, P. (2014). Novel thermally activated delayed fluorescence materials-thioxanthone derivatives and their applications for highly efficient OLEDs. **Advanced Materials**. 26(30): 5198-5204.

Wei, P., Duan, L., Zhang, D., Qiao, J., Wang, L., Wang, R., Dong, G., and Qiu, Y. (2008). A new type of light-emitting naphtho[2,3-c][1,2,5]thiadiazole derivatives: synthesis, photophysical characterization and transporting properties. **Journal of Materials Chemistry**. 18(7).

Wei, X., Chen, Y., Duan, R., Liu, J., Wang, R., Liu, Y., Li, Z., Yi, Y., Yamada-Takamura, Y., Wang, P., and Wang, Y. (2017). Triplet decay-induced negative temperature dependence of the transient photoluminescence decay of thermally activated delayed fluorescence emitter. **Journal of Materials Chemistry C**. 5(46): 12077-12084.

Wu, S., Aonuma, M., Zhang, Q., Huang, S., Nakagawa, T., Kuwabara, K., and Adachi, C. (2014). High-efficiency deep-blue organic light-emitting diodes based on a thermally activated delayed fluorescence emitter. **Journal of Materials Chemistry C**. 2(3): 421-424.

Yang, Y., Wang, L., Cao, H., Li, Q., Li, Y., Han, M., Wang, H., and Li, J. (2019). Photodynamic Therapy with Liposomes Encapsulating Photosensitizers with Aggregation-Induced Emission. **Nano Letters**. 19(3): 1821-1826.

Yao, L., Zhang, S., Wang, R., Li, W., Shen, F., Yang, B., and Ma, Y. (2014). Highly efficient near-infrared organic light-emitting diode based on a butterfly-shaped donor-acceptor chromophore with strong solid-state fluorescence and a large proportion of radiative excitons. **Angewandte Chemie International Edition in English**. 53(8): 2119-2123.

Yu, C.-Y., Hsu, C.-C., and Weng, H.-C. (2018). Synthesis, characterization, aggregation-induced emission, solvatochromism and mechanochromism of fluorinated benzothiadiazole bonded to tetraphenylethenes. **RSC Advances**. 8(23): 12619-12627.

Zhang, G., Auer-Berger, M., Gehrig, D. W., Blom, P. W., Baumgarten, M., Schollmeyer, D., List-Kratochvil, E. J., and Mullen, K. (2016). Blue Light

Emitting Polyphenylene Dendrimers with Bipolar Charge Transport Moieties. **Molecules**. 21(10).

Zhang, Q., Li, B., Huang, S., Nomura, H., Tanaka, H., and Adachi, C. (2014). Efficient blue organic light-emitting diodes employing thermally activated delayed fluorescence. **Nature Photonics**. 8(4): 326-332.

Zhang, Q., Li, J., Shizu, K., Huang, S., Hirata, S., Miyazaki, H., and Adachi, C. (2012). Design of Efficient Thermally Activated Delayed Fluorescence Materials for Pure Blue Organic Light Emitting Diodes. **Journal of the American Chemical Society**. 134(36): 14706-14709.

Zhang, X., Zhang, Y., Zhang, H., Quan, Y., Li, Y., Cheng, Y., and Ye, S. (2019). High Brightness Circularly Polarized Organic Light-Emitting Diodes Based on Nondoped Aggregation-Induced Emission (AIE)-Active Chiral Binaphthyl Emitters. **Organic Letters**. 21(2): 439-443.

Zhao, C., Guo, Y., Zhang, Y., Yan, N., You, S., and Li, W. (2019). Diketopyrrolo pyrrole-based conjugated materials for non-fullerene organic solar cells. **Journal of Materials Chemistry A**. 7(17): 10174-10199.

Zhao, Z., Chen, S., Shen, X., Mahtab, F., Yu, Y., Lu, P., Lam, J. W., Kwok, H. S., and Tang, B. Z. (2010). Aggregation-induced emission, self-assembly, and electroluminescence of 4,4'-bis(1,2,2-triphenylvinyl)biphenyl. **Chemical Communications**. 46(5): 686-688.

Zhao, Z., Deng, C., Chen, S., Lam, J. W., Qin, W., Lu, P., Wang, Z., Kwok, H. S., Ma, Y., Qiu, H., and Tang, B. Z. (2011). Full emission color tuning in luminogens constructed from tetraphenylethene, benzo-2,1,3-thiadiazole and thiophene building blocks. **Chemical Communications**. 47(31): 8847-8849.

Zhu, Y., Rabindranath, A. R., Beyerlein, T., and Tieke, B. (2007). Highly Luminescent 1,4-Diketo-3,6-diphenylpyrrolo[3,4-c]pyrrole- (DPP-) Based Conjugated Polymers Prepared Upon Suzuki Coupling. **Macromolecules**. 40(19): 6981-6989.

APPENDICES

APPENDIX A

THE SYNTHESIS OF DPP EMITTERS

Table 1 The UV-vis data of DPP emitters.

Parameter	G0DPP	G1DPP	G2DPP
Conc.	2.5 x 10^{-05}	1.0 x 10^{-05}	6.0 x 10^{-06}
λmax (nm)	476	478	478
A	0.5159	0.2932	0.1129
ε	20634.4	19547.3	18816.0
log ε	4.31	4.29	4.27
λ_{onset}	531	530	527
E_g	2.33	2.34	2.35

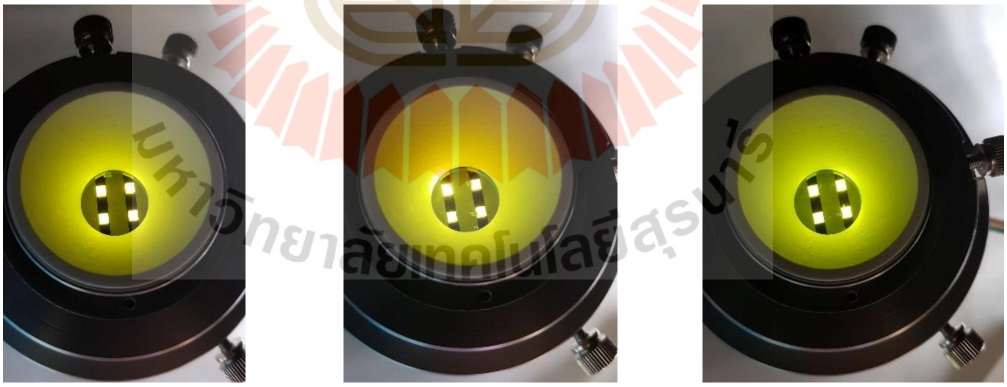

G0DPP **G1DPP** **G2DPP**

Figure 1 The emission colors of devices based on the DPP emitters under applied voltage.

APPENDIX B

THE SYNTHESIS OF THERMALLY ACTIVATED DELAYED FLUORESCENCE MATERIALS

Table 1 The data for Lippert Mataga equation of TADF emitters.

Compounds		**Solution**		**λuv-λem (nm)**	**λuv*lem (nm)**	**Stokes shift (Δn, nm)**	**Stokes shift (Δn, cm^{-1})**	**function of the solvent polarity parameter (Δ*f*)**
		λ_{UV} (nm)	**λ_{em} (nm)**					
G1-2Ph-DPS	**toluene**	344	403	59	138632	0.000425587	4256	0.01
	CHCl3	344	443	99	152392	0.00064964	6496	0.15
	DCB	344	452	108	155488	0.000694587	6946	0.19
	THF	343	443	100	151949	0.000658116	6581	0.21
	ACN	343	486	143	166698	0.000857839	8578	0.30
G2-2Ph-DPS	**toluene**	349	450	101	157050	0.000643107	6431	0.01
	CHCl3	349	478	129	166822	0.000773279	7733	0.15
	DCB	350	496	146	173600	0.000841014	8410	0.19
	THF	348	478	130	166344	0.000781513	7815	0.21
	ACN	347	556	209	192932	0.001083283	10833	0.30
G1-4Ph-DPS	**toluene**	343	389	46	133427	0.000344758	3448	0.01
	CHCl3	343	449	106	154007	0.00068828	6883	0.15
	DCB	343	457	114	156751	0.000727268	7273	0.19
	THF	343	449	106	154007	0.00068828	6883	0.21
	ACN	343	488	145	167384	0.000866272	8663	0.30
G2-4Ph-DPS	**toluene**	350	455	105	159250	0.000659341	6593	0.01
	CHCl3	350	482	132	168700	0.000782454	7825	0.15
	DCB	350	502	152	175700	0.000865111	8651	0.19
	THF	350	485	135	169750	0.000795287	7953	0.21
	ACN	-	455	455	0	0	0	0.30

Table 1 The data for Lippert Mataga equation of TADF emitters (Continued).

Compounds		Solution		λuv-λem (nm)	λuv*lem (nm)	Stokes shift (Δn, nm)	Stokes shift (Δn, cm^{-1})	function of the solvent polarity parameter (Δ*f*)
		λ_{UV} (nm)	λ_{em} (nm)					
G1DPS	**toluene**	347	403	56	139841	0.000400455	4005	0.01
	CHCl3	347	434	87	150598	0.000577697	5777	0.15
	DCB	347	439	92	152333	0.00060394	6039	0.19
	THF	345	427	82	147315	0.00055663	5566	0.21
	ACN	345	472	127	162840	0.000779907	7799	0.30
CzDPS	**toluene**	339	387	48	131193	0.000365873	3659	0.01
	CHCl3	339	407	68	137973	0.00049285	4929	0.15
	DCB	340	415	75	141100	0.000531538	5315	0.19
	THF	338	407	69	137566	0.000501577	5016	0.21
	ACN	337	448	111	150976	0.000735216	7352	0.30
3,6-diPhCz-DPS	**toluene**	324	376	52	121824	0.000426845	4268	0.01
	CHCl3	324	406	82	131544	0.000623366	6234	0.15
	DCB	324	407	83	131868	0.000629417	6294	0.19
	THF	322	392	70	126224	0.00055457	5546	0.21
	ACN	320	443	123	141760	0.000867664	8677	0.30
3,6-diPhCz-4Ph-DPS	**toluene**	324	397	73	128628	0.000567528	5675	0.01
	CHCl3	324	420	96	136080	0.000705467	7055	0.15
	DCB	324	428	104	138672	0.000749971	7500	0.19
	THF	324	420	96	136080	0.000705467	7055	0.21
	ACN	324	451	127	146124	0.000869125	8691	0.30
2,7-diPhCz-DPS	**toluene**	355	405	50	143775	0.000347766	3478	0.01
	CHCl3	355	434	79	154070	0.000512754	5128	0.15
	DCB	358	440	82	157520	0.000520569	5206	0.19
	THF	349	431	82	150419	0.000545144	5451	0.21
	ACN	344	470	126	161680	0.000779317	7793	0.30

Table 1 The data for Lippert Mataga equation of TADF emitters (Continued).

Compounds		Solution		λuv-λem (nm)	λuv*lem (nm)	Stokes shift (Δn, nm)	Stokes shift (Δn, cm^{-1})	function of the solvent polarity parameter (Δ*f*)
		λ_{UV} (nm)	λ_{em} (nm)					
2,7-diPhCz-4Ph-DPS	**toluene**	356	424	68	150944	0.000450498	4505	0.01
	CHCl3	356	446	90	158776	0.000566836	5668	0.15
	DCB	356	460	104	163760	0.000635076	6351	0.19
	THF	356	450	94	160200	0.000586767	5868	0.21
	ACN	356	490	134	174440	0.000768172	7682	0.30

APPENDIX C

THE SYNTHESIS OF TADF DENDRIMERS

Table 1 The data for Lippert Mataga equation of TADF dendrimers.

Compounds		**Solution**		**λuv-λem (nm)**	**λuv*lem (nm)**	**Stokes shift (Δn, nm)**	**Stokes shift (Δn, cm^{-1})**	**function of the solvent polarity parameter (Δ*f*)**
		λ$_{\mathrm{UV}}$ (nm)	**λ$_{\mathrm{em}}$ (nm)**					
G1hexylfluorene-DPS (14)	**toluene**	353	392	39	138376	0.000281841	2818	0.01
	CHCl3	354	394	40	139476	0.000286788	2868	0.15
	DCB		396	396	0	#DIV/0!	#DIV/0!	0.19
	THF	352	392	40	137984	0.000289889	2899	0.21
	ACN	386	399	13	154014	8.44079E-05	844	0.30
hexylfluorene-DPS (15)	**toluene**	350	392	42	137200	0.000306122	3061	0.01
	CHCl3	353	384	31	135552	0.000228695	2287	0.15
	DCB	355	385	30	136675	0.000219499	2195	0.19
	THF	350	382	32	133700	0.000239342	2393	0.21
	ACN	351	380	29	133380	0.000217424	2174	0.30
TPAfluorene-DPS (16)	**toluene**	310	394	84	122140	0.000687735	6877	0.01
	CHCl3	315	397	82	125055	0.000655711	6557	0.15
	DCB	300	400	100	120000	0.000833333	8333	0.19
	THF	302	395	93	119290	0.000779613	7796	0.21
	ACN	274	404	130	110696	0.001174388	11744	0.30

APPENDIX D

THE SYNTHESIS OF AIE EMITTERS

Table 1 The data for Lippert Mataga equation of AIE emitters.

Compounds		**Solution**		**λuv-λem (nm)**	**λuv*lem (nm)**	**Stokes shift (Δn, nm)**	**Stokes shift (Δn, cm^{-1})**	**function of the solvent polarity parameter (Δ*f*)**
		λ_{UV} (nm)	**λ_{em} (nm)**					
BT-2TPE(17)	hexane	416	517	101	215072	0.00046961	4696	0.00
	toluene	417	535	118	223095	0.000528923	5289	0.01
	DCM	414	570	156	235980	0.000661073	6611	0.22
	THF	417	552	135	230184	0.000586487	5865	0.21
	ACN	406	593	187	240758	0.000776714	7767	0.30
NT-2TPE (18)	hexane	485	579	94	280815	0.00033474	3347	0.00
	toluene	489	597	108	291933	0.000369948	3699	0.01
	DCM	487	624	137	303888	0.000450824	4508	0.22
	THF	481	616	135	296296	0.000455625	4556	0.21
	ACN	477	630	153	300510	0.000509134	5091	0.30
NT-TPETPA (19)	hexane	497	640	143	318080	0.000449572	4496	0.00
	toluene	514	663	149	340782	0.00043723	4372	0.01
	DCM	509	706	197	359354	0.000548206	5482	0.22
	THF	506	689	183	348634	0.000524906	5249	0.21
	ACN	495	629	134	311355	0.000430377	4304	0.30
BT-2TPEH (20)	hexane	417	517	100	215589	0.000463846	4638	0.00
	toluene	422	535	113	225770	0.000500509	5005	0.01
	DCM	418	558	140	233244	0.00060023	6002	0.22
	THF	422	549	127	231678	0.000548175	5482	0.21
	ACN	408	566	158	230928	0.000684196	6842	0.30

Table 1 The data for Lippert Mataga equation of AIE emitters (Continued).

Compounds		**Solution**		**λuv-λem (nm)**	**λuv*lem (nm)**	**Stokes shift (Δn, nm)**	**Stokes shift (Δn, cm^{-1})**	**function of the solvent polarity parameter (Δ*f*)**
		λ$_{UV}$ (nm)	**λ$_{em}$ (nm)**					
BT-TPETPA (21)	hexane	444	545	101	241980	0.00041739	4174	0.00
	toluene	447	581	134	259707	0.000515966	5160	0.01
	DCM	444	647	203	287268	0.000706657	7067	0.22
	THF	444	613	169	272172	0.000620931	6209	0.21
	ACN	433	641	208	277553	0.000749406	7494	0.30
FBT-2TPE (22)	hexane	408	512	104	208896	0.000497855	4979	0.00
	toluene	411	529	118	217419	0.000542731	5427	0.01
	DCM	405	578	173	234090	0.000739032	7390	0.22
	THF	407	556	149	226292	0.000658441	6584	0.21
	ACN	393	614	221	241302	0.000915865	9159	0.30
2FBT-2TPE(23)	hexane	397	504	107	200088	0.000534765	5348	0.00
	toluene	400	523	123	209200	0.000587954	5880	0.01
	DCM	393	586	193	230298	0.000838045	8380	0.22
	THF	393	564	171	221652	0.00077148	7715	0.21
	ACN	379	606	227	229674	0.000988357	9884	0.30
2FBT-2TPEH (24)	hexane	400	502	102	200800	0.000507968	5080	0.00
	toluene	402	516	114	207432	0.000549578	5496	0.01
	DCM	394	541	147	213154	0.000689642	6896	0.22
	THF	395	517	122	204215	0.00059741	5974	0.21
	ACN	382	564	182	215448	0.000844751	8448	0.30
NBT-2TPE (25)	hexane	449	562	113	252338	0.000447812	4478	0.00
	toluene	447	583	136	260601	0.000521871	5219	0.01
	DCM	442	644	202	284648	0.000709648	7096	0.22
	THF	445	616	171	274120	0.000623814	6238	0.21
	ACN	427	680	253	290360	0.000871332	8713	0.30

Table 1 The data for Lippert Mataga equation of AIE emitters (Continued).

Compounds		Solution		λuv-λem (nm)	λuv*lem (nm)	Stokes shift (Δn, nm)	Stokes shift (Δn, cm^{-1})	function of the solvent polarity parameter (Δf)
		λ_{UV} (nm)	λ_{em} (nm)					
BNT-2TPE(26)	hexane	418	513	95	214434	0.000443027	4430	0.00
	toluene	424	545	121	231080	0.000523628	5236	0.01
	DCM	449	590	141	264910	0.000532256	5323	0.22
	THF	417	605	188	252285	0.000745189	7452	0.21
	ACN	407	601	194	244607	0.000793109	7931	0.30

CURRICULUM VITAE

Name	Wipaporn Kitisriworaphan
Date of Birth	8 May 1980
Place of Birth	Tha Uthen district, Nakhon Phanom
Education	2002 Bachelor's degree in Chemistry at Mahasarakham University 2008 Master's degree in Organic Chemistry at Khon Kaen University
Grants and Fellowships	The National Research Council of Thailand (NRCT) in 2018
Position and Place of Work	Lecturer at Udon Thani Rajabhat University